Bull. Spec. Astrophys. Obs., 2001, 52, 5-133

Results of investigation of radio galaxies of the survey "Cold": photometry, colour redshifts and the age of the stellar population

O.V. Verkhodanov[a], Yu.N. Parijskij[a], N.S. Soboleva[b], A.I. Kopylov[a], A.V. Temirova[b], O.P. Zhelenkova[a], W.V. Goss[c]

[a] Special Astrophysical Observatory of the Russian AS, Nizhnij Arkhyz 369167, Russia
[b] St.Petersburg branch of SAO RAS, St.Petersburg, Russia
[c] National Radio Astronomical Observatory, Soccoro, USA

Received November 14, 2001; accepted December 1, 2001.

Abstract. BVRI data for the majority of the objects of the RC catalogue with steep spectra and $m_R < 24^m$ are presented. These data have been used to estimate colour redshifts and the age of stellar systems of host galaxies. By way of example of distant radio galaxies it is shown that this approach gives an accuracy of redshift estimates close to that for field galaxies ($\sim 20\,\%$). The age estimates are less confident, however, the lower age limit for not too distant ($z < 1.5$) objects is determined quite reliably. Several galaxies have been detected that have an age above that of the Universe at the given z in a simple CDM model of the Universe. A possibility of using such objects to specify the part played by "dark energy" is discussed. This paradox disappears in a model with the Λ-term equal to 0.6–0.8.

Key words: radio continuum: galaxies — surveys: galaxies — galaxies: fundamental parameters

1. Introduction

A population of powerful radio galaxies is observable with the available facilities practically to any distances. This allows one to follow the evolution of this population in the radio range from the moment it originated up to the present time.

However, a good deal of effort has to be undertaken to find new objects at $z > 3$ with application of rigorous methods of selection by radio, optical and infrared properties, which leads to inhomogeneous samples with regard to different parameters.

It is customary to assume that a population of very powerful radio galaxies of type FR II owes its origin to giant elliptical galaxies having supermassive ($10^9 M_\odot$) black holes at the centre. That is why the evolution of this population is related to the problem of formation of the largest stellar systems and to the problem of evolution of massive black holes. Besides, these objects are often associated with clusters and groups of galaxies and can be indicators of distant clusters formed in the nodes of the large-scale structure. At last, there is a number of suggestions for using them in estimation of parameters of their environment and even of the geometry of the Universe and its dynamics (Parijskij et al., 1998; Daly, 1994).

In contrast to quasar, in radio galaxies one can study in details the stellar population. As a rule, in objects with medium and weak energy release of the active nucleus in the optical and near infrared ranges, radiation of stars rather than gas dominates at $z < 1 - 1.5$. For this reason, one may attempt to apply the method of stellar evolution and evolution of synthetic colours of the stellar population to determination of "colour" redshifts and the age of the stellar population. When lucky, one can define the moment of star formation (z).

In the generally accepted scheme of the Unified Theory of active objects, radio galaxies of type FR II differ from quasars, BL Lac objects and other populations with powerful nucleus activity only in that at what angle the axis of rotation of the gas-dust tore, that screens the accretion disk around the black hole, is located with respect to the observer. And the data on evolution of these objects can be applied to other classes of objects.

At last, powerful galaxies with active nuclei (radio galaxies and quasars, predominantly "radio quiet") supply much UV radiation to the Universe, and in combination with the integral optical depth by Thomson scattering of relic photons of the 3K background permit the moment of secondary ionization of the

© Special Astrophysical Observatory of the Russian AS, 2002

Universe to be refined.

Deep optical investigations of host galaxies in this class of objects are impeded by the fact that their spatial density is by 5–6 orders of magnitude less than that of background galaxies, and this is why they are virtually lacking in ultimately deep frames of small size. In the HDF (Hubble Deep Fields) there is found but one distant ($z = 4.42$) radio galaxy of medium power. For this reason, sampling of fields for such investigations has to be started with preliminary selection on radio astronomy data with allowance made for all possible indirect criteria. The principles of selection of candidates for distant objects in the "Big Trio" project (Parijskij et al., 1994, 1096a,b) are similar to universally adopted (McCarthy, 1993). The list of objects presented below has been derived from the catalogue of the "Cold" survey (Parijskij et al., 1991, 1992) as a result of several selection steps: selection of comparatively faint sources having steep spectra ($\alpha < -1.0 S \sim \nu^{\alpha}$) and being of the FR II morphological type (Fanaroff, Riley, 1974) in the cm range (10–100 mJy). Further selection was done according to the procedure described below.

The labour input for acquisition of quality spectroscopic data on distant and faint galaxies and radio galaxies forces to search for indirect methods for determination of the redshift and other characteristic features of these objects. With regard to the powerful radio galaxies, even photometric estimates proved to be helpful and they have so far been widely used (McCarthy, 1993; Benn et al., 1989; Parijskij et al., 2000a, b).

Over the last few years, colour characteristics of faint galaxies have come to be used in addition to the methods of photometric evaluation of the redshift, and this approach forms a basis for a number of major projects (e.g. see Szalay, 1996). As we have already noted, the colours of stellar systems make it possible to estimate their age as well. Generally speaking, the legitimacy of using colours for such estimations of evolution characteristics of the population of powerful radio galaxies requires a separate study because the effect the nuclear activity in these objects has on the colour characteristics is not sufficiently understood. The sites of "secondary" star formation may also tell upon the colour characteristics.

The present paper is a continuation of our programme of investigation of the radio galaxies detected in the RATAN-600 survey "Cold" with involvement of multicolour photometry data for assessment of colour redshifts and ages of stellar systems of host galaxies. Current use of these data is practically inevitable. Direct spectroscopy of faint objects required until recently a great deal of the 6 m telescope observational time when working with objects fainter than 20^m. So, in 1995–1996 we managed to measure the spectroscopic redshift but in four bright objects (three quasars and one galaxy, all being brighter than $m_R = 20.5^m$) and only in one faint galaxy, $m_R = 23^m$ (Dodonov et al., 1999). The redshift of the latter, $z = 2.73$, was estimated from the only emission line. It is independently confirmed by our colour data: the negative B–V colour index agrees with identification of a strong line as Ly_{α}, which is typical of radio galaxies.

During the last time, in connection with placing in service of more efficient spectral tools in SAO RAS, spectroscopy of faint objects is expected to substantionally improve. The spectra of another two objects, radio galaxy RCJ 0908+0451 and quasar RCJ 1154+0431, were obtained at the 6 m telescope in 2001 March with the aid of new equipment SCORPIO (Afanasiev and Moiseev, *http://www.sao.ru/~moisav/scorpio/scorpio.html*). The spectral redshift for the radio galaxy is practically the same as the colour redshift. The data on the colour redshift will help improve the efficiency of spectroscopic observations.

This paper has the following structure. In the first section we present the data of multicolour BVRI photometry and also the latest results of identifications of the "Cold" survey radio sources. Further we describe the procedures of obtaining colour redshifts and ages of stellar systems from BVRI magnitudes with the use of present-day models of spectral energy distribution (SED). In the sections that follow we discuss the results obtained, evaluate model differences in the estimates of redshifts and propose new steps to improve the accuracy of estimations.

2. Multicolour photometry of RC objects

By the present time observations of about 60 RC objects (radio galaxies and quasars) of our sample have been carried out with the 6 m telescope of SAO RAS in four filters (B, V, R, I). In this paper we present the photometry results for 50 radio galaxies. The observations were made in 1994–1998. A CCD ISD015A of 580×520 pixels with a pixel size of $0.205'' \times 0.154''$ was employed in the 1994–1995 observations, and a CCD ISD017A (1160×1040, $0.137'' \times 0.137''$) was used in observations of 1996–1998. When reading the latter, the initial elements of the matrix were summed up to produce the output elements twice as large in both coordinates. The exposure time was defined in the course of observations, proceeding from brightness and colour of objects, from 1200–1800 s (total) in the B band to 400–800 s in the R band for a typical object of our sample having $R = 22^m - 23^m$, so that the resulting signal-to-noise ratio would be no worse than 4–5 in all the filters. At a seeing worse than $2''$, we had to increase the exposure time by a factor of

Table 1: *A list of RC objects classified as QSO and excluded from this study*

Name	RA(2000.0)	Dec(2000.0)
RC J0038+0449	00 38 34.65	+04 50 50.5
RC J0042+0504	00 42 27.17	+05 05 24.7
RC J0126+0502	01 26 16.11	+05 02 09.9
RC J0143+0505	01 43 33.89	+05 07 57.4
RC J0226+0512	02 26 19.80	+04 46 32.5
RC J0459+0456	04 59 04.28	+04 55 54.4
RC J0506+0558	05 06 25.00	+05 08 19.3
RC J1154+0431	11 54 53.50	+04 24 12.5
RC J1740+0502	17 40 33.96	+05 02 42.3
RC J2013+0508	20 13 23.48	+05 10 30.5
RC J2036+0451	20 36 56.93	+04 49 52.7

1.5–2.

Identifications of RC objects are presented in Fig. 5 (see after the references). The radio isophotes were plotted from the data of VLA observations and superimposed on the images of galaxies obtained with the 6 m telescope in the R filter. The VLA radio observations were carried out in the 1990s with different antenna configurations (Parijskij et al., 1996a). Besides, the VLA data for the RC objects from the MIT survey (Fletcher et al., 1996) and the FIRST survey (White et al., 1997) data were used. Images are also presented for the objects that we classified as QSO and which are excluded from the present study. The list of the objects is given in Table 1.

The processing of optical images was accomplished using the standard procedure in the MIDAS system. Subtraction of the averaged dark frame and element-by-element correction with the use of twilight sky frames were performed. The residual background inhomogeneity in the I filter, which is due to interference of night sky emission lines, was removed by means of the procedure of subtraction of the median sum of all working frames of a given night or several nights of one observing run. The calibration of photometric measurements for their conversion to the standard Johnson–Cousins system was done using the stars from Landolt's (1992) list, which were observed several times during a night. To do photometry of the selected object, a circular aperture of one and the same size was used when measuring in different filters. The aperture size was chosen to be between $3''$ and $12''$, depending on the object luminosity. The typical size was $4'' - 5''$. The background was measured with a circular aperture of sufficiently large radius in order not to cover the outer regions of the object being measured. When necessary, the neighbouring objects were removed by the procedure of interpolation of the surrounding background. The photometry accuracy was generally not worse than 0.1^m for galaxies brighter than 21^m. It dropped down to $0.2^m - 0.25^m$ for $23^m - 24^m$ and was as low as $0.3^m - 0.5^m$ for galaxies fainter than $25^m - 25.5^m$.

Table 2: *Characteristics of photometric bands*

Filter name	λ_{eff}	$A/E(B-V)$	C
Landolt B	4400	4.315	3.620
Landolt V	5500	3.315	3.564
Landolt R	6500	2.673	3.487
Landolt I	8000	1.940	3.388

To provide for the Galactic extinction, we used the charts from the paper "Maps of Dust IR Emission for Use in Estimation of Reddening and CMBR Foregrounds" (Schlegel et al., 1998), written in the form of FITS files. The conversion of stellar magnitudes to flux densities was implemented via the formula $S(Jy) = 10^{C-0.4m}$ (von Hoerner, 1974). The values of the constant C for different filters are listed in Table 2, where the following characteristics are also given: name of filter, effective wavelength, coefficient $A/E(B-V)$ of change-over from distribution of dust radiation to extinction in a given band under the assumption of extinction curve $R_V = 3.1$.

The stellar magnitudes of 50 galaxies of our sample, which were corrected for extinction in the four filters, are presented in Table 3.

3. Models of energy distribution in the spectra of host galaxies

In the late 1980s and early 1990s, attempts were made to use colour characteristics of radio galaxies for estimation of redshifts and ages of systems of host galaxies. There appeared numerous evolution models with which observational data were compared and results largely differing from one another were obtained (Arimoto & Yoshii, 1987; Chambers & Charlot, 1990; Lilly, 1987, 1990; Parijskij et al., 1996a). Over the past few years the models like PEGASE: Project de'Etude des Galaxies par Synthese Evolutive (Fioc & Rocca-Volmerange, 1997), and GISSEL'98 (Bruzual, Charlot, 1993; Bolzonella et al., 2000), in which an attempt was made to eliminate the shortcomings of the preceding versions, have been most commonly used.

In the "Big Trio" experiment (Parijskij et al., 1996a), we also tried to apply these methods to distant steep spectrum objects of the RC catalogue, for which we measured the magnitudes in the four filters (BVRI). This paper is distinguished from the paper of Parijskij et al. (1996a) by using more reliable identifications of radio sources, new photometric data and new models of energy distribution. Besides, we used in our work the smoothing procedure that makes it possible to model and predict the flux in the given filter at the specified SED with allowance for the fil-

Table 3: *Stellar magnitudes of the sample radio galaxies corrected for extinction*

Source	B	V	R	I	Source	B	V	R	I
	m	m	m	m		m	m	m	m
0015+0503a	23.89	22.97	22.20	21.36	1155+0444	21.36	19.83	18.90	18.20
0015+0501	24.82	23.91	23.37	22.22	1213+0500	23.55	22.90	22.04	21.32
0034+0513	25.28	24.79	23.25	21.79	1235+0435b	24.15	22.81	21.59	20.35
0039+0454	24.81	24.00	22.69	21.22	1322+0449	23.68	22.52	20.77	19.17
0105+0501	24.00	22.48	22.78	22.43	1333+0452	24.87	24.44	23.56	22.46
0135+0450	20.49	19.16	18.42	17.82	1339+0445	25.05	23.72	22.70	21.55
0152+0453	23.31	23.02	22.47	21.70	1357+0453	22.98	21.85	21.10	20.11
0159+0448	22.65	21.72	21.23	20.65	1429+0501	25.57	23.24	21.64	20.50
0209+0501a	20.37	19.19	18.43	17.78	1436+0501	23.90	23.86	23.39	22.70
0209+0501b	25.72	24.09	23.12	21.63	1446+0507	21.48	20.03	19.17	18.54
0318+0456	25.64	23.98	22.61	20.99	1503+0456	24.02	23.67	23.14	22.24
0444+0501	23.48	23.70	23.33	23.13	1510+0438	24.98	23.73	22.57	21.25
0457+0452	22.01	20.86	20.05	19.37	1551+0458	25.57	25.34	24.43	23.30
0836+0511	23.68	23.53	23.09	22.44	1626+0448	22.32	23.07	22.73	22.63
0837+0446	23.03	23.29	22.99	22.11	1638+0450	22.86	22.33	22.14	21.04
0845+0444	24.72	22.42	21.09	19.77	1646+0501	24.01	22.44	20.97	19.76
0908+0451	21.63	20.72	19.85	19.07	1703+0502	24.22	23.39	23.12	22.26
0909+0445	22.60	21.53	20.50	19.59	1706+0502	24.73	24.19	23.25	21.88
0934+0505	25.29	24.45	24.67	23.61	1722+0442	22.30	21.59	20.63	19.44
1011+0502	23.71	23.18	22.47	22.60	2029+0456	22.85	22.24	21.66	20.53
1031+0443	23.93	22.79	22.09	20.85	2219+0458	24.80	25.03	23.72	22.25
1043+0443	23.98	23.57	22.51	21.70	2224+0513	23.16	22.31	21.43	20.32
1124+0456	20.30	18.79	17.85	17.07	2247+0507	23.64	23.18	22.53	21.43
1142+0455	24.83	22.53	21.38	20.39	2348+0507	23.89	23.79	23.56	23.08
1152+0449	23.86	23.66	22.39	21.00					

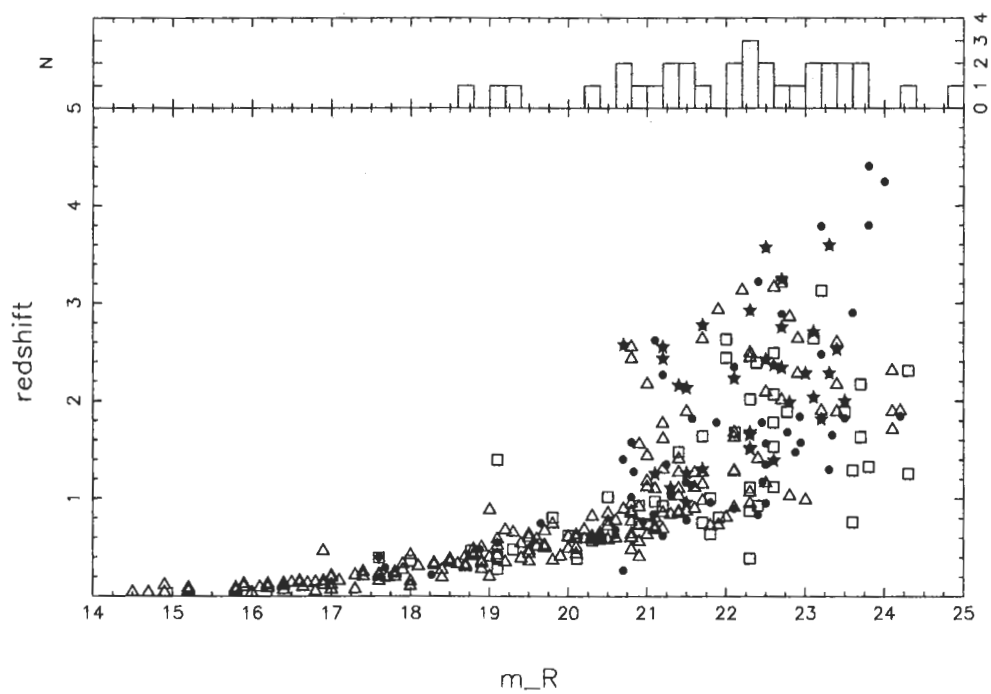

Figure 1: *Hubble diagram R-value vrs redshift for different radio galaxies taken from literature. The figure is reproduced from Pursimo et al. (1999).*

ter throughput curve and also for the redshift effect. These changes in the procedure enabled making the results of estimation more reliable as compared to our previous work.

We (Verkhodanov et al., 1999) preliminarily discussed applicability of the new methods to a population of distant ($z > 1$) radio galaxies with known redshifts, for which we managed to find in literature more or less reliable data of multicolour photometry in the optical and near infrared ranges in no fewer than three filters. It is shown, in particular, that redshifts can be estimated with an accuracy of 25–30 % at $1 < z < 4$, given measured stellar magnitudes in more than three filters. And given at least one luminosity estimate in the infrared region, it suffices to use measurement in three filters. Estimates were made for two evolution models.

As one of the SED models the evolution model PEGASE (Fioc & Rocca-Volmerange, 1997) was employed for galaxies of the Hubble sequence both star forming and evolving in a passive fashion. One of the principal merits of this model is the extension to the near infrared range (NIR) of the atlas of synthetic spectra of Rocca-Volmerange & Guiderdoni (1988) with the revised stellar library including parameters of cool stars. The model covers a range from 220 Å to 5 microns. According to the authors the algorithm of the model makes it possible to follow rapid evolution phases such as red supergiants or AGB in the near IR. We used a wide set of SED curves from this model in a range of ages from 7×10^6 years to 19×10^9 years for massive elliptical galaxies.

From the library of synthetic spectra of the model GISSEL'98 (Bolzonella et al., 2000) derived with the aid of the evolution models of Bruzual & Charlot (1993, 1996), we used the computations for elliptical galaxies. The library of synthetic spectra was constructed with the following star formation parameters: simple stellar population (SSP), the duration of starburst activity is 1 billion years, the starburst activity decays exponentially. The solar metallicity was used in the model. The initial mass function (IMF) with an upper limit of 125 solar masses was taken from Miller & Scalo (1979). As Bolzonella et al. (2000) show the choice of IMF has no effect on the accuracy of redshift measurements. The mode tracks are computed in a wavelength range from 200 to 95800 Å. We used the range specified by a redshift limit of 0 to 6 in our calculations.

The sets of evolution models employed are available at *http://sed.sao.ru* (Verkhodanov et al., 2000).

4. Estimation of age and redshift

Before using the model transmission curves we performed their smoothing with the filter via applying the algorithm

$$S_{ik} = \frac{\sum\limits_{j=0}^{n} s_{i-n/2+j} f_{jk}(z)}{\sum\limits_{j=0}^{n} f_{jk}(z)},$$

where s_i is the initial model curve of SED, S_{ik} is the model curve of SED smoothed by the kth filter, $f_k(z)$ is the curve of transmission of the kth filter "compressed" $(1+z)$ times when "moving" along the wavelength axis of the SED curve, $j = 1, n$ is the number of the pixel in the filter transmission curve. From the k curves of SED thus formed (there are four of them in our case), we constructed a two-dimensional array (λ, filter) of smoothed spectra for further computations.

The evaluation of ages and redshifts was carried out by the method of choosing an "optimum" location of photometric magnitudes obtained in photometric observations of radio galaxies in different filters on the SED curves. We used the already computed and table-specified SED curves for different ages. The algorithm of selection of the optimum location on the curve was briefly as follows (for details see Verkhodanov, 1996): by way of shifting the points lengthwise (along the wavelength axis) and transverse (along the intensity axis) the SED curves, we defined the location at which the sum of squares of deviations of points from the corresponding smoothed curves is a minimum, i.e. the minimum of χ^2 is actually calculated:

$$\chi^2 = \sum_{k=1}^{Nfilters} \left(\frac{F_{obs,k} - p \cdot \mathrm{SED}_k(z)}{\sigma_k} \right),$$

where $F_{obs,k}$ is the observed stellar magnitude in the kth filter, $\mathrm{SED}_k(z)$ is the model stellar magnitude for the given spectral distribution in the kth filter at a given z, p is the free coefficient, σ_k is the measurement error.

The redshift was found from the shift of location of the observed magnitudes at their best location on the SED curves from the "rest frame" position (position at $z = 0$). From the total set of curves for different ages we chose the ones on which the sum of squares of deviations for the given observations turned out to be a minimum.

Fig. 6 (see at the end of the paper) gives the results of the most plausible choice of evolution models for the photometry data and the corresponding function of plausibility.

5. Photometric redshifts for RC catalogue radio galaxies

To examine the potentialities of the method for determination of redshift and ages of the stellar population

of host galaxies from the data of multicolour photometry, we selected 40 remote radio galaxies with known redshifts, for which stellar magnitudes in no fewer than three filters are available in literature (Verkhodanov et al., 1998b, 1999).

It should be noted that literature photometric data are most inhomogeneous: they were obtained by different authors, different tools, with different filters; measurements for one and the same object were not always made in the same apertures, etc. This is why, only 42 out of 300 radio galaxies of the original sample remained. The subsamples of objects (3C, 4C, B2) with relatively homogeneous data are not large enough to be statistically compared. At first, using the collected photometric data obtained with the aid of the models PEGASE and GISSEL'98, only the ages of the stellar population of host galaxies with a fixed known redshift were derived. After that, a search for an optimum model SED curve, for the redshift and age of the stellar population simultaneously, was carried out, and the derived values were compared.

Thus, we estimated both the galaxy age and the redshift within the frames of the specified models (see Verkhodanov et al., 1998a, 1999). It is clear from general considerations that the reliability of the result at large redshifts shows a significant dependence on the availability of infrared data (up to the R range), because when fitting, we "cover" the region of rapid spectrum change (a jump) before the optical range of SED and thereby can reliably (with a well defined maximum of the plausibility curve) determine the location of our data. This can be proved as follows. When the available points are removed (to check the reliability of the procedure) with retaining only 3 points (one of which is in the K range), we obtain in fitting the same result on the curve of deviations as for 4 or 5 points. If the infrared range is not used, the result will then be more uncertain. However, as we show (Verkhodanov et al., 1999) the version of "tight" positioning of the four filters, as in our case of BVRI photometry, gave a good result in a sample of 6 galaxies, which is a good fit to the result obtained with using all the filters, including the infrared range.

A similar procedure was employed to estimate the redshift and the age for galaxies of the RC catalogue. The common distinction from the papers by Verkhodanov et al., 1998b, 1999) is that our observations were made only in 4 filters, B V R I, so, the infrared data are lacking.

Table 4 presents redshift and age estimates for the stellar systems of radio galaxies from the RC catalogue. The redshift z_c, the age of the radio galaxy t, the discrepancy ε and the age of the Universe T at $z = z_c$ ($H = 65, \Omega_m = 0.3, \Omega_\Lambda = 0.7$ for standard Friedmann-Lemaître-Robertson-Walker cosmology (Thomas & Kantowski, 2000)) are given in the table columns for the models GISSEL and PEGASE, respectively.

Table 4: *Colour redshifts and ages of stellar systems for the RC Catalogue radio galaxies*

Object RC J	GISSEL'98				PEGASE			
	z_c	t[Myr]	ε	T[Myr]	z_c	t[Myr]	ε	T[Myr]
1	2	3	4	5	6	7	8	9
0015+0503a	0.73	900	0.0412	7546	0.48	3000	0.0299	9237
	0.07	16000	0.0342	13512	4.91	16000	0.0199	1273
0015+0501	0.81	1000	0.0334	7103	0.87	3250	0.0358	6797
0034+0513	0.98	16000	0.0729	6286	1.29	10000	0.0374	5130
					1.11	15000	0.0196	5755
0039+0454	0.95	16000	0.0346	6419	0.99	7000	0.0057	6242
0105+0501	0.28	500	0.0852	11032	4.21	9250	0.0839	1537
0135+0450	0.35	2500	0.0106	10350	0.10	7250	0.0018	13112
	0.12	16000	0.0072	12855				
0152+0453	0.75	400	0.0051	7431	0.81	640	0.0016	7103
	1.15	900	0.0113	5606				
0159+0448	0.13	2000	0.0093	12729	0.41	1900	0.0093	9813
					0.09	5000	0.0090	13244
					4.75	15000	0.0060	1326
0209+0501a	0.39	1800	0.0067	9988	0.39	3500	0.0063	9988
					0.09	6750	0.0088	13244
					0.07	9250	0.0097	13512

Table 4: *Colour redshifts and ages of stellar systems for the RC Catalogue radio galaxies (continued)*

1	2	3	4	5	6	7	8	9
					0.07	16000	0.0058	13512
0209+0601b	0.69	13000	0.0400	7783	0.70	6000	0.0483	7723
0318+0456	0.67	16000	0.0491	7906	0.71	6500	0.0071	7663
0444+0501	1.17	200	0.0365	5534	2.42	13000	0.0419	2870
0457+0452	0.40	2000	0.0092	9900	0.41	3500	0.0068	9813
0836+0511	0.77	250	0.0058	7319	0.81	286	0.0094	7103
	1.14	600	0.0028	5643	1.21	2100	0.0037	5394
	1.93	2500	0.0229	3599	1.37	2400	0.0021	4886
0837+0446	0.98	200	0.0490	6286	0.99	202	0.0494	6242
	1.91	6000	0.0697	3636	1.92	9250	0.0635	3617
0845+044	5.29	16000	0.1139	1160	0.66	8750	0.0560	7969
0908+0451	0.49	1400	0.0322	9159	0.48	3250	0.0193	9237
					4.99	16000	0.0125	1248
0909+0445	0.67	1800	0.0145	7906	0.64	4000	0.0168	8096
0934+0505	1.72	1200	0.0785	4010	1.79	4250	0.0728	3865
					1.79	16000	0.0727	3865
1011+0502	0.46	300	0.0501	9397	0.50	453	0.0624	9082
1031+0443	0.86	2500	0.0188	6846	0.87	4250	0.0275	6797
1043+0443	1.19	3000	0.0138	5463	0.72	2200	0.0250	7604
					1.23	4500	0.0171	5326
					5.98	8500	0.0181	993
1124+0456	0.35	10000	0.0025	10350	0.35	5750	0.0115	10350
1142+0455	5.20	16000	0.1082	1185	4.99	571	0.0386	1248
					0.35	14000	0.0421	10350
1152+0449	1.17	16000	0.0619	5534	1.33	8000	0.0069	5006
					1.30	15250	0.0079	5099
1155+0444	4.18	500	0.1161	1550	0.33	5750	0.0179	10538
	0.35	9000	0.0091	10350				
1213+0500	0.70	700	0.0201	7723	0.68	2100	0.0162	7844
	1.08	2000	0.0334	5871	5.15	15500	0.0118	1200
	0.07	9000	0.0522	13512				
1235+0435b	0.64	11000	0.0042	8096	0.68	5750	0.0083	7844
1322+0449	0.65	16000	0.1129	8032	0.78	7250	0.0702	7264
					0.99	14000	0.0037	6242
1333+0452	1.04	1400	0.0158	6032	1.08	4000	0.0062	5871
1339+0445	0.67	4500	0.0217	7906	0.71	5000	0.0136	7663
1357+0453	0.73	1400	0.0421	7546	0.41	4000	0.0409	9813
1429+0501	5.38	450	0.0827	1135	0.61	11500	0.0483	8294
1436+0501	1.35	800	0.0157	4945	1.15	1680	0.0136	5606
	1.93	3000	0.0318	3599	1.18	1900	0.0127	5499
1446+0507	0.35	5000	0.0140	10350	0.24	5750	0.0191	11451
					4.99	6750	0.0189	1248
					0.11	14500	0.0144	12983
1503+0456	0.78	500	0.0065	7264	0.83	1015	0.0023	6998
1510+0438	0.66	8000	0.0110	7969	0.75	5750	0.0074	7431
1551+0458	1.05	1200	0.0341	5991	1.11	4000	0.0294	5755
	1.32	6000	0.0099	5036	1.32	5750	0.0129	5036
1626+0448	0.04	200	0.1268	13930	0.03	202	0.1282	14073
	2.31	6000	0.1642	3011	2.30	3000	0.1814	3025

Table 4: *Colour redshifts and ages of stellar systems for the RC Catalogue radio galaxies (continued)*

1	2	3	4	5	6	7	8	9
1638+0450	0.84	500	0.0315	6947	0.89	1015	0.0388	6699
	1.67	2000	0.0284	4119	1.78	4750	0.0134	3885
1646+0501	0.65	>5000	0.1171	8032	0.64	6750	0.0106	8096
1703+0502	0.81	600	0.0692	7103	3.56	640	0.0567	1874
	0.07	2500	0.0431	13512	0.35	1680	0.0508	10350
	0.00	6000	0.0452	14515	0.00	5500	0.0363	14515
1706+0502	0.96	1800	0.0339	6374	1.06	5750	0.0293	5951
	1.17	16000	0.0317	5534				
1722+0442	1.02	4000	0.0033	6115	1.01	4500	0.0033	6157
2029+0456	0.81	800	0.0094	7103	0.88	2600	0.0107	6747
2219+0458	0.98	1200	0.1271	6286	1.36	7750	0.0555	4916
	1.22	16000	0.0987	5360				
2224+0513	0.73	1200	0.0101	7546	0.77	3500	0.0072	7319
2247+0507	0.78	700	0.0094	7264	0.93	2500	0.0068	6510
	1.38	3000	0.0253	4857	1.45	4750	0.0134	4660
2348+0507	1.43	450	0.0016	4715	1.24	571	0.0030	5293
					2.07	3000	0.0291	3362

Notes to Table 4

0034+0513 — the age of the stellar system in the two alternatives from the model GISSEL'98 is greater than that of the Universe at the given z; we choose the age where the difference is smaller despite a somewhat greater error.

0039+0454 — the age of the stellar system from the PEGASE model is inadmissively large, it is about 3 times as large as that of the Universe at a given z. The same is observed in a number of other sources (0209+0501, 0845+0454, 1142+0455, 1152+0449, 1235+0435b, 1322+0449, 1510+0438, 1646+0501, 2219+0454). The cause of this has not been understood yet.

0105+0501 — in contrast to the majority of objects of our sample the redshift and the age from the two models are not consistent. Besides, the computation gives large errors in this case. The optical images (Soboleva et al., 2000) show that the bright line $Ly\alpha$ falls in the V filter. For this reason, the stellar magnitude is strongly corrupted.

0135+0450 — the redshift value lies between 0.34 and 0.10, but closer to 0.34. Note that from the GISSEL'98 model there is another minimum at $z = 0.17$ with the age 5750 Myr and a deviation of 0.0105. The values at the absolute minimum are discarded in the two models because of the discrepancy between the age of the system and that of the Universe.

0159+0448 — $z = 0.09$ (GISSEL'98) and $z = 0.13$ (PEGASE) lie outside the region of permissible values in the plane $z - R$ (see Fig. 1; Pursimo et al., 1999). The age 15000 Myr in the GISSEL model does not conform to reality. We consider the alternative with $z = 0.41$ to be more reliable.

0209+0501a — $z = 0.39$ for both models. The age derived does not conform to real fact for a minimum deviation 0.0058 in the GISSEL model. Two other estimates yield a larger value of deviation.

0318+0456 — close redshifts for the models GISSEL'98 ($z = 0.71$) and PEGASE ($z = 0.67$). The age turns out to be ultimately small for both models.

0444+0501 — although to the value $z = 1.17$ for the PEGASE model corresponds a minimum deviation, the closest to the spectroscopic redshift ($z = 2.73$) is obtained in the GISSEL model ($z = 2.42$). The estimated age proves to be too great to be real, although z is close to real.

0836+0511 — the values $z = 1.21$ (GISSEL'98) and $z = 1.14$ (PEGASE) are close (to an accuracy of 6%) and practically have a minimal deviation. One can see here that the age of stellar systems turns out to be older in the GISSEL models.

0845+0444 — $z = 5.29$ (PEGASE) is not admissible both by age and by position in the plane $z - R$.

0908+0451 — the colour redshift ($z_{ph} = 0.48$) is confirmed by spectral measurements at the 6 m telescope of SAO RAS ($z_{sp} = 0.5$).

1142+9455 — $z = 4.99$ (GISSEL'98) and $z = 5.20$ (PEGASE) do not fall within the range of admissible values in the plane $z-R$. We choose $z = 0.35$, though in this case the age of the stellar system, according to the criterion of minimum of squares of deviations, proves to be somewhat larger than the age of the Universe.

1213+0500 — $z = 5.15$ (GISSEL) is outside of the region of acceptable values in the plane $z-R$, and the age of the stellar system in this case is 10 times that of the Universe. There are close redshift values in the region $z = 0.7$ for both models, a minimum χ^2

being consistent with this solution in the PEGASE model.

1322+0449 — the variant with $z = 0.99$ in the GISSEL model is unsuitable because the age of the stellar system is twice that of the Universe. A similar situation also occurs in the PEGASE model where the solution goes beyond the limits of acceptable age values. There is a stable minimum for $z = 0.78$ in the PEGASE model. In all the cases the redshift proves to be less than 1.

1357+0453 — assume $z = 0.73$ from PEGASE model. $z = 0.41$, however, for GISSEL model falls out of the plane $z - R$. Note that there is one more local minimum for the GISSEL model, which corresponds to $z = 3.86$ in the plane of distribution of deviations, but the value of this minimum is 3 times as large as for $z = 0.41$, and the corresponding point also falls out of the plane $z - R$.

1429+0501 — we fail to find acceptable values of the parameters for either model. This may be due to difficulties of separating a radio galaxy from a nearby star in the optical range (Parijskij et al., 1996a).

1436+0501 — accept the alternatives $z = 1.18$ (GISSEL) and $z = 1.35$ (PEGASE) with errors close to minimum. The difference between the redshifts in these models is then about 12 %.

1446+0507 — at $z = 0.11$ the age of the galaxy in the GISSEL model turns out to be larger than the age of the Universe at a minimum of deviations, at $z = 4.99$ with a minimum error it does not fall within the range of admissible values in the plane $z - R$ for radio galaxies, and the age of the stellar system is 5 times the age of the Universe. We retain $z = 0.35$ for PEGASE and $z = 0.24$ for GISSEL as possible alternatives.

1626+0448 — spectroscopic redshift for this object is $z = 2.66$ (Afanasiev et al., 2002). The current calculations have been carried out with no provision for the line $Ly\,\alpha$. The data obtained show that $z = 0.03$ and $z = 0.04$ do not fall in the interval of acceptable values for radio galaxies in the plane $z-R$. In all the cases the large errors are due to the fact that the bright line $Ly\,\alpha$ falls on the B band (Parijskij et al., 1996a). The z values equal to 2.31 for PEGASE and 2.30 for GISSEL are quite close to the true values. When the line $Ly\,\alpha$ is taken into account in the computations, the redshift value then turns out to be equal to the spectroscopic.

1638+0450 — choose $z = 1.78$ (GISSEL'98) and $z = 1.67$ (PEGASE), though $z = 0.89$ (GISSEL'98) and $z = 0.84$ (PEGASE) cannot be rejected either.

1703+0502 — the stellar magnitudes in all the filters can be affected by a nearby bright star (Parijskij et al., 1996a).

1722+0442 — the spectroscopic $z = 0.7$ (Afanasiev et al., 2002) is by 30 % lower than the value derived by photometry for both models.

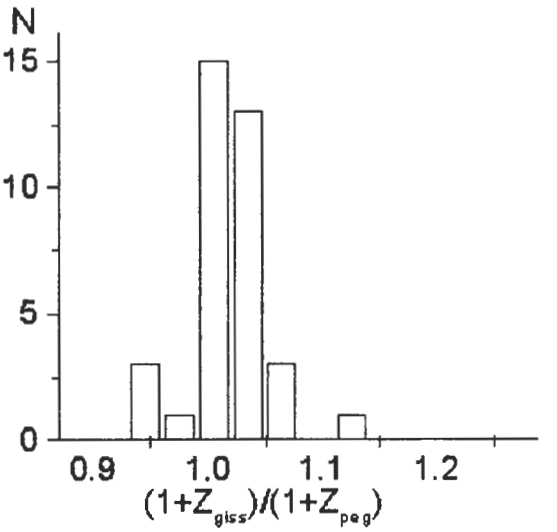

Figure 2: *Histogram characterizing the distribution of the ratio of colour redshifts from the GISSEL'98 (z_{giss}) and PEGASE (z_{peg}) models. The central part of the histogram, within which 80 % of objects fall, is presented.*

2247+0507 — there are two minima in the two models. The z values less than 1 differ for the models by less than 20 %. The difference is less than 10 % for z of about 1.4, however, the age of the stellar system is the same as the age of the Universe for the model GISSEL. By the criterion χ^2 we choose the former alternative in both models.

2348+0507 — the stellar magnitudes in all the filters can be affected by a nearby bright star (Parijskij et al., 1996a).

6. Discussion and results

1. The problem of colour redshifts of distant galaxies

As it was shown earlier (Verkhodanov et al., 1999), the model PEGASE yielded satisfactory results over 40 objects for which spectral measurements of redshifts are available. Analysis of Table 4 shows that the new model CISSEL often gives results only slightly differing from the PEGASE model (see also Verkhodanov et al., 2001a, b).

Fig. 2 presents a histogram of the ratio $(1 + z_{GISSEL})/(1 + z_{PEGASE})$. The distribution of errors is not normal, there is a nucleus with very small model errors, in which most of the objects (80 %) fall, but 20 % of the objects have very large errors. As a rule, the large errors are caused by getting of the strong line ($Ly\,\alpha$) in one of the filters, illumination from a nearby bright object and complicated cases of SED deviation from the model. A number of such examples are described in notes to Table 4.

It should be noted that we use the standard set of filters of the 6 m telescope, BVRI, which is satisfactory for not too distant objects (the colours of which have been measured yet). Measurements have to be extended to the H and K ranges. In a considerable number of cases, this will enable elimination of uncertainties in the estimates. The situation may change for ultimately distant objects with R> 24^m, and we have to wait until the observations are completed, prior to giving recommendations. It is clear from general considerations that there is a danger from "right" and "left", that is, the secondary star formation sites may distort the blue region of the spectrum, but the dust at very great redshifts may deform the IR region. It can easily be shown that large discrepancies may point to possibilities of luminosity distortion by strong lines, and we hope to take this into account in the future. For $z > 2$, it is necessary to take into account, at least, the line $Ly\,\alpha$. Considerable errors may arise because of the periodicity of series in Bor's model, but here simple energetic considerations may be helpful (discrepancies in the colour and photometric estimates). This can be illustrated by the RC object J1703+0502 formally having a zero redshift. When adopting this estimate, the optical luminosity of this object will then prove to be so low that it cannot produce any perceptible radio radiation (note that $P_{radio} \sim L_{opt}^{2.5}$; Iskudarian & Parijskij, 1964; Franceschini et al., 1998). When making use of the secondary criteria, we sometimes have to reject the variant with the smallest discrepancies and take the next one.

2. The age of stellar systems of host galaxies

As it is known, the age is much more difficult to assess than the redshift. The older the stellar population the larger the error may be. We have made a histogram (Fig. 3) of differences of ages determined from the models GISSEL (t_{giss}) and PEGASE (t_{peg}) for one and the same object. They are normalized to the age of the Universe with $\Lambda = 0.7$ (T) for the moment that corresponds to the measured redshift $(t_{giss} - t_{peg})/2T$. The distribution of differences of ages derived from different models are far from normal, but there is a nucleus where 70 % of objects fall. The "model" dispersion for them is close to 20 %. Large departures were detected in 9 out of 50 objects with the use of PEGASE. The measured age of host stellar systems for them is far larger than that of the Universe even at redshifts close to GISSEL. For this reason, we consider the GISSEL model to be more trustworthy. A systematic difference between the models has been discovered, which increases with rising redshift (see Fig. 4). When the difference is taken into account, the dispersion of ages drops to < 10 % for objects with close redshifts in both models.

It is essential that not a single GISSEL model

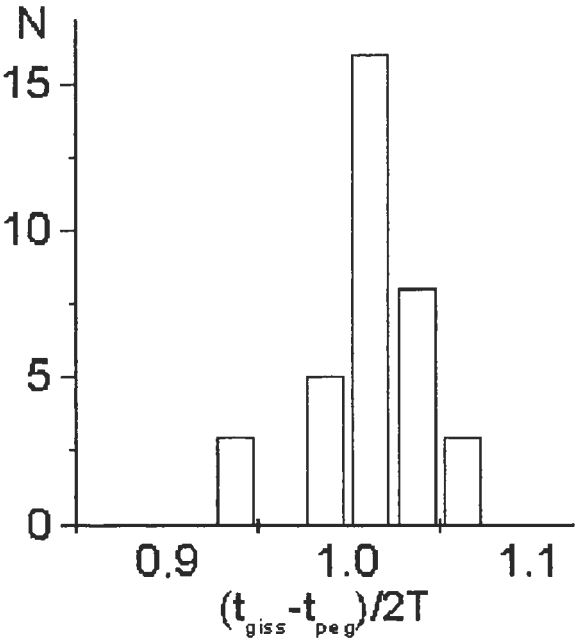

Figure 3: *Histogram of half-difference of colour ages of host stellar systems obtained from the models GISSEL'98 (t_{giss}) and PEGASE (t_{peg}) vrs the age of the Universe with $\Lambda = 0.7$ (T) for the moment corresponding to the measured redshift. The central part of the histogram is shown where 80 % of objects fall.*

galaxy is older within the errors than the Universe in the model with the Λ-term equal to 0.7–0.8. There are more than ten such galaxies in the old model SCDM, and they can be used for independent assessment of the behaviour of $H(z)$, Λ-term and quintessence (suggestion of Starobinsky (1998), see Saini et al. (2000); Parijskij et al. (1998)). The average age of galaxies is a few billion years, however, there is a subgroup of galaxies having the age that coincides within the errors with the age of the Universe at a corresponding redshift, and a group of formally very young (some hundred million years) stellar systems. The formers are likely to belong to the first generation of galaxies in the Universe which formed at $z \gg 1$ ($z \sim 5 - 10$). The situation of the galaxies with "young" objects is more complicated, their colour can be distorted by repeated star-formation bursts at merging of galaxies or under the action of close passings. The variant of "young" galaxy cannot be accepted, since we deal with powerful radio galaxies, for functioning of which a supermassive black hole is necessary (DMO — Dark Massive Object, Salucci et al., 1999) with the mass of about $10^9 M_\odot$, that is not possible within the standard models of black hole formation (Franceschini et al., 1998). Only the primary black holes with masses $10^4 - 10^6 M_\odot$, round of which galaxies form later on,

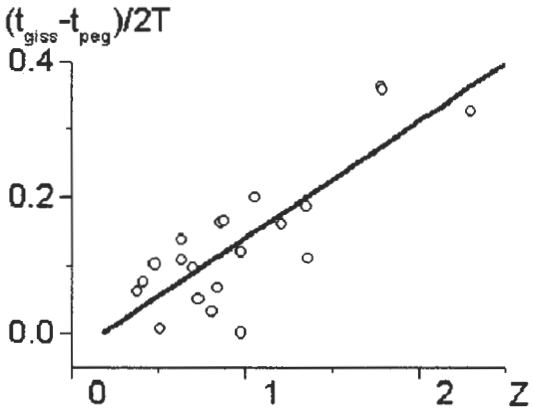

Figure 4: *Systematic difference between ages of stellar systems from GISSEL'98 (t_{giss}) and PEGASE (t_{peg}) models normalized to the age of the Universe with $\Lambda = 0.7$ (T) for the moment of the corresponding redshift as a function of redshift. The departures from the relationship derived are 6 %.*

may be the alternatives of "merging".

As a result, a careful conclusion can be drawn that at least the statistical estimates of the redshift and age for population of powerful radio galaxies give satisfactory results. The GISSEL model can be recommended not only for radio-quiet galaxies but also for powerful radio galaxies. It is advantageous to use all available data on the objects to obtain more reliable estimates, this will decrease the errors.

In conclusion we enumerate the results obtained.

1. The largest currently available body of data on BVRI magnitudes of host galaxies responsible for the origin of powerful radio galaxies is presented.

2. The colour redshifts for powerful radio galaxies show a satisfactory agreement with the spectral ones (the error is 10–20 % with a small fraction of large errors). The recent 2001 spectral observations of the RC objects RC J0908+0451, RC J1154+0431, RC J1626+0448 RC J1722+0442 gave errors of redshift measurement by the techniques described above within 10–15 % (Afanasiev et al., 2002).

3. The limited number of closely spaced filters as in our BVRI case may also yield satisfactory results even for large redshifts.

4. The redshift distribution for the studied objects of our sample (the subgroup of objects brighter than $m_R = 23.5^m$) shows a maximum near $z{\sim}1$, i.e. in the range of maximum radio activity of the Universe. The group of objects with large colour redshifts ($z > 2.5-3$) requires a separate analysis. In any case, we do not consider yet the gap in the population of the region ($1.5 < z < 2.5$) to be real.

5. The colour data are generally not at variance with the stellar magnitudes in the filter R (Parijskij et al., 1996a) when $R < 22.5^m$. Fainter objects show a higher dispersion of photometric redshifts at one and the same value of R. One can notice here two branches in the plane $(z - R)$ (Pursimo et al., 1999). The search for differences in the morphology, radio luminosity, spectral indices has given no final result. Note that the objects with the steepest spectra and a large radio-to-optical luminosity ratio occur in the branch with large redshifts. However, further investigations are needed. Objects with low relative radio luminosity, as it was to be expected, prove to be either quasars or nearby galaxies.

6. The age of galaxies is determined less reliably, and results turn out to be of low significance for larger z. However, in practice one can always indicate the lower limit of the age of galaxies and, therefore, the minimum redshift of their formation. This age is always larger than the standard estimate of the object lifetime, and in a number of cases it exceeds the age of the Universe at an object redshift in a simple CDM model. There are no such galaxies in a model with a Λ-term of 0.6–0.8 (e.g. de Bernardis et al., 2000).

7. A programme has been developed and tested of automatic determination of colour redshifts and ages of galaxies, which is applicable to any redshifts with provision for transformation of the shape of the filters when changing over from the rest to the moving system of reading, available through the server *http://sed.sao.ru*.

We contemplate further investigation of colour and photometric techniques as applied to the population of distant radio galaxies. New more realistic models of colour evolution and refined methods of age evaluation in stellar systems will make it possible to obtain more reliable results for a great number of objects.

Acknowledgements. The work was done with partial support from the SSTP "Astronomy" (projects 1.2.1.2 1.2.2.4), through the grants of RFBR 99-02-17114, INTAS 97-1192, Integration project 578, 206. OVV, AIK and OPZh thank RFBR (grant 99-07-90334) for support in the creation of a server for calculation of redshifts and ages of radio galaxies (*http://sed.sao.ru*). Thanks are due to the editor-in-chief, N.F. Vojkhanskaya, and also to the referee for remarks, recommendations and discussions.

References

Afanasiev V.L., Moiseev A.V., Dodonov S.N., Verkhodanov O.V., Kopylov A.I., Parijskij Yu.N., Soboleva N.S., Temirova A.V., Zhelenkova O.P., Goss W.M., 2002, Astron. Zh., in preparation

Arimoto N., Yoshii Y., 1987, Astron. Astrophys., **179**, 23

Benn C.R., Wall J., Vigotti M., Grueff G., 1989, Mon. Not. R. Astron. Soc., **235**, 465

Bolzonella M., Miralles J.-M., Pelló R., 2000, Astron. Astrophys., **363**, 476, astro-ph/0003380

Bruzual G., Charlot S., 1993, Astrophys. J., **405**, 538

Bruzual G., Charlot S., 1996, anonymous@ftp://gemini.tuc.noao.edu/pub/charlot/bc96

Chambers K., Charlot S., 1990, Astrophys. J. Lett., **348**, L1

Daly R.A., 1994, Astrophys. J., **426**, 38

de Bernardis P., Ade P.A.R., Bock J.J. et al., 2000, Nature **404**, 955

Dodonov S.N., Parijskij Yu.N., Goss W.M., Kopylov A.I., Soboleva N.S., Temirova A.V., Verkhodanov O.V., Zhelenkova O.P., 1999, Astron. Zh., **76**, 323

Fanaroff B.L., Riley J.M., 1974, Mon. Not. R. Astron. Soc., **167**, 31P

Fioc M., Rocca-Volmerange B., 1997, Astron. Astrophys., **326**, 950

Fletcher A., Conner S., Crawford F., Cartwright J., Burke B., Pariiskij Yu.N., Soboleva N.S., Kopylov A.I., Temirova A.V., Verkhodanov O.V., Naugol'naya M.N., 1996, Astronomy Reports, **40**, No. 6, 759 (in Russian: 1996, Astron. Zh. **73**, No. 6, 835)

Franceschini A., Vercellone S., Fabian A., 1998, Mon. Not. R. Astron. Soc., **297**, 817

Iskudarian S., Parijskij Yu.N., 1964, Izv. MAO, **182**

Landolt A.U., 1992, Astron. J., **104**, 340

Lilly S., 1987, Mon. Not. R. Astron. Soc., **229**, 573

Lilly S., 1990, in: "Evolution of the Universe", ed.: Kron R.G., Astron. Soc. Pacific, 344

Miller G.E., Scalo J.M., 1979, Astrophys. J. Suppl. Ser., **41**, 513

McCarthy P.J., 1993, Annu. Rev. Astron. Astrophys., **31**, 639

Parijskij Yu.N., Bursov N.N., Lipovka N.M., Soboleva N.S., Temirova A.V., 1991, Astron. Astrophys. Suppl. Ser., **87**, 1

Parijskij Yu.N., Bursov N.N., Lipovka N.M., Soboleva N.S., Temirova A.V., Chepurnov A.V., 1992, Astron. Astrophys. Suppl. Ser., **96**, 583

Parijskij Yu. N., Kopylov A.I., Zhelenkova O.P., Naugolnaya M.N., Soboleva N.S., Temirova A.V., Vitkovskij V.V., 1994, Turkish Journal of Physics, **18**, No. 8, 894

Parijskij Yu. N., Goss W.M., Kopylov A.I., Soboleva N.S., Temirova A.V., Verkhodanov O.V., Zhelenkova O.P., Naugolnaya M.N., 1996a, Bull. Spec. Astrophys. Obs., **40**, 5

Parijskij Yu.N., Soboleva N.S., Goss W.M., Kopylov A.I., Verkhodanov O.V., Temirova A.V., Zhelenkova O.P., 1996b, in: IAU Symp. No. 175, 591

Parijskij Yu.N., Kopylov A.I., Soboleva N.S., Verkhodanov O.V., Temirova A.V., Zhelenkova O.P., Tsibulev P.G., Chepurnov A.V., Stolarov V.A., 1998, "Dark Ages" of the Universe, in: International School of Aph. "D Chalonge" 5th Course, Current topics in Astrofundamental Physics, NATO ASI series, **511**, 443

Parijskij Yu.N., Goss W.M., Kopylov A.I., Soboleva N.S., Temirova A.V., Verkhodanov O.V., Zhelenkova O.P., 2000a, Astron. and Astrophys. Transactions, **19**, 297

Parijskij Yu.N., Soboleva N.S., Kopylov A.I., Verkhodanov O.V., Temirova A.V., Zhelenkova O.P., Winn J., Fletcher A., Burke B., 2000b, Pis'ma Astron. Zh., **26**, No. 7, 493

Pursimo T., Nelson K., Teerikorpi P., Kopylov A., Soboleva N., Parijskij Yu., Baryshev Yu., Verkhodanov O., Temirova A., Zhelenkova O., Goss W., Sillanpaa A., Takalo L., 1999, Astron. Astrophys. Suppl. Ser., **134**, 505

Rocca-Volmerange B., Guiderdoni B., 1988, Astron. Astrophys. Suppl. Ser., **75**, 93

Salucci P., Szuszkievicz E., Monaco P., Danese L., 1999, astro-ph/9811102

Saini T., Raychaudhury S., Sahni V., Starobinsky A., 2000, asrto-ph/9910231

Schlegel D., Finkbeiner D., Davis M., 1998, Astrophys. J., **500**, 525

Soboleva N.S., Goss V.M., Verkhodanov O.V., Zhelenkova O.P., Temirova A.V., Kopylov A.I., Parijskij Yu.N., 2000, Pis'ma Astron. Zh., **26**, No. 10, 723

Starobinsky A.A., 1998, JETF lett., **68**, 757

Szalay A.S., 1996, in: "Cosmology and Large Scale Structure", Les Houches, Session 60 1-28, 1993, ed.: R.Shaeffer et al., 253

Thomas R.C., Kantowski R., 2000, astro-ph/0003463

von Hoerner S., 1974, in: "Galactic and extragalactic radio astronomy", eds.: G.L. Verschuur & K.I. Kellermann, Springer-Verlag

Verkhodanov O.V., 1996, Bull. Spec. Astrophys. Obs., **41**, 149

Verkhodanov O.V., Kopylov A.I., Parijskij Yu.N., Soboleva N.S., Temirova A.V., 1998a, in: "Aktualnye problemy vnegalakticheskoi astronomii", ("Current Problems of Extragalactic Astronomy"), Proc. XV Conf., Pushchino, May 25–29, Pushchino Sci. Center, 24

Verkhodanov O.V., Kopylov A.I., Parijskij Yu.N., Soboleva N.S., Temirova A.V., Zhelenkova O.P., 1998b, in: "Prospects of Astronomy and Astrophysics For the New Millennium", Joint European and National Astronomical Meeting, JENAM'98, 7th Europ. & 65th Ann. Czech Astron. Conf., Prague, 9-12 Sept., 302

Verkhodanov O.V., Kopylov A.I., Parijskij Yu.N., Soboleva N.S., Temirova A.V., 1999, Bull. Spec. Astrophys. Obs., **48**, 41, astro-ph/9910559

Verkhodanov O.V., Kopylov A.I., Zhelenkova O.P., Verkhodanova N.V., Chernenkov V.N., Parijskij Yu.N., Soboleva N.S., Temirova A.V., 2000, Atsron. Astrophys. Trans., **19**, No 3-4, 662, astro-ph/9912359, http://sed.sao.ru

Verkhodanov O.V., Kopylov A.I., Parijskij Yu.N., Soboleva N.S., Temirova A.V., Zhelenkova O.P., 2001a, Preprint No. 135, SPb, (St.Petersburg branch of SAO)

Verkhodanov O.V., Kopylov A.I., Parijskij Yu.N., Soboleva N.S., Temirova A.V., Zhelenkova O.P., 2001b, Preprint No. 136 SPb, (St.Petersburg branch of SAO)

White R.L., Becker R.H., Helfand D.J., Gregg M.D., 1997, Astrophys. J., **475**, 479

Fig. 5. Oprical identifications of RC sources: VLA radio isophotes overlaid on the 6 m telescope R-band images, and R-band isolines overalaid on the VLA images.

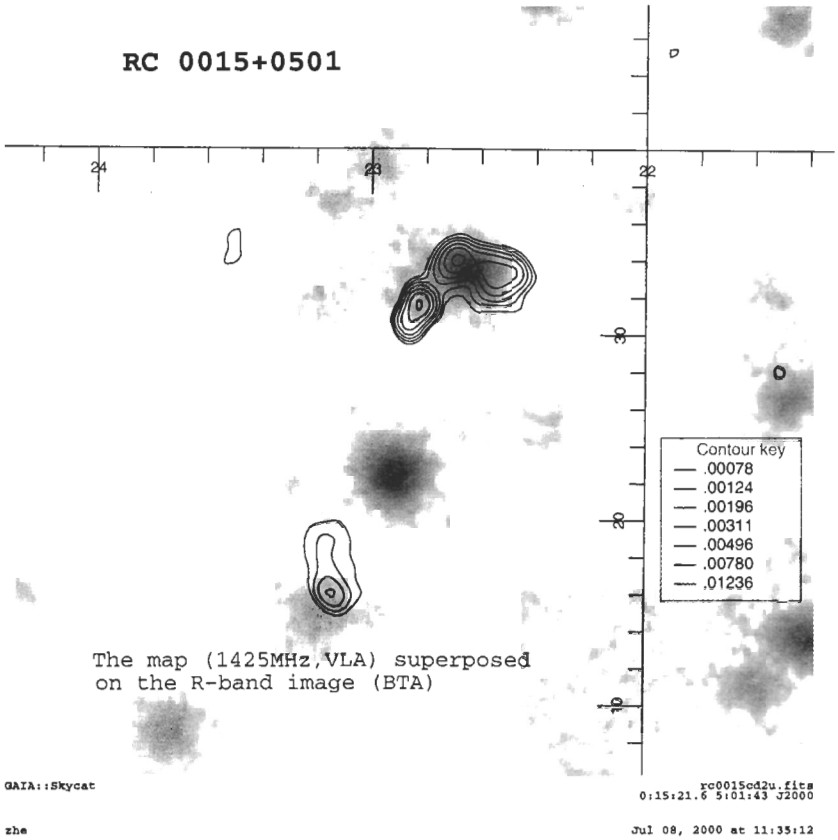

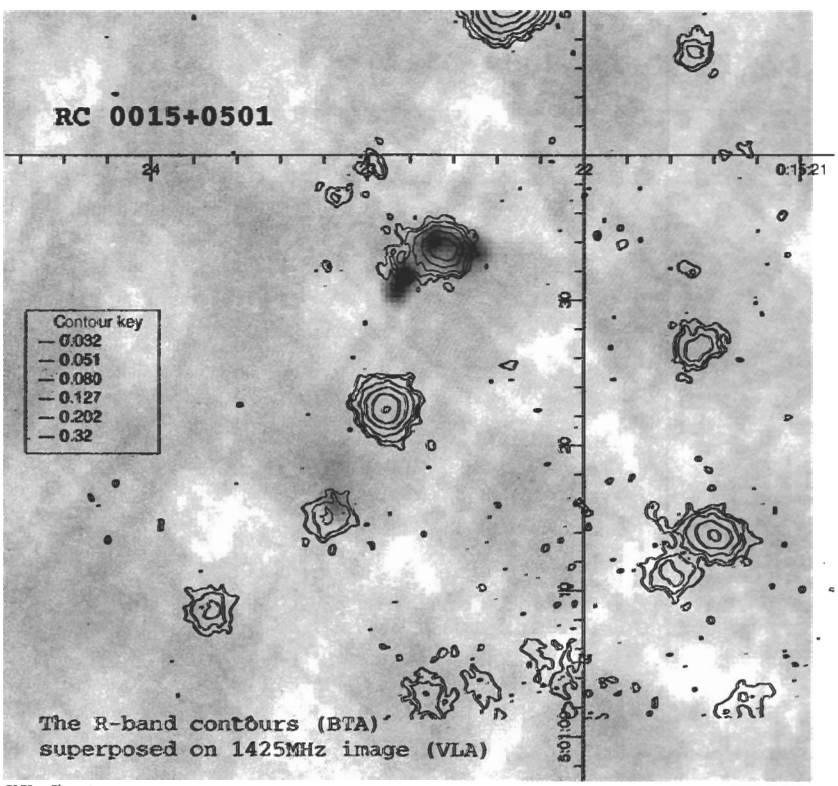

БИБЛИОТЕКА
Специальной

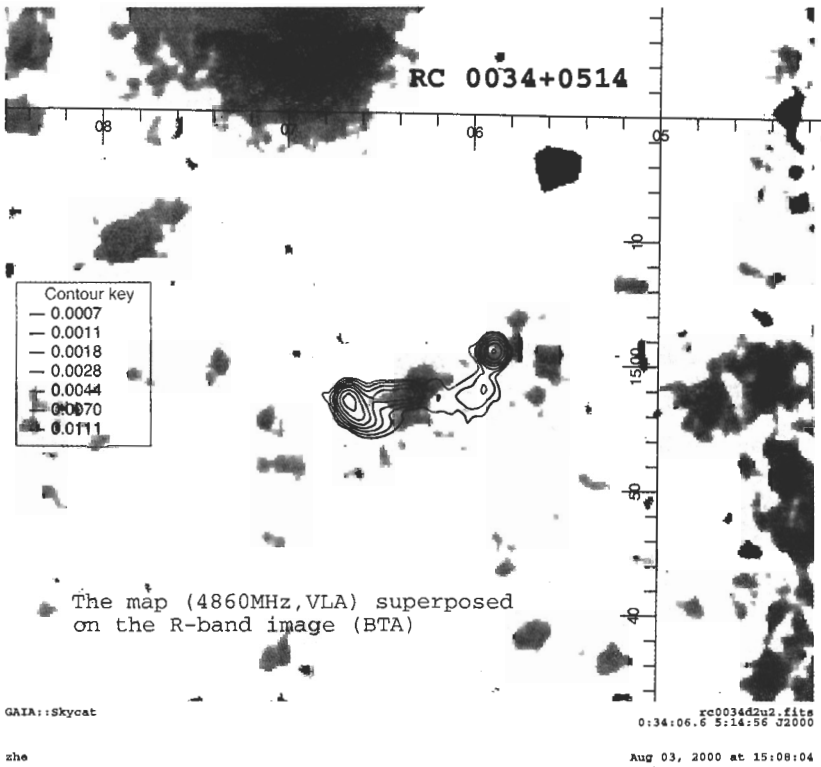
RC 0034+0514
Contour key
— 0.0007
— 0.0011
— 0.0018
— 0.0028
— 0.0044
— 0.0070
— 0.0111
The map (4860MHz,VLA) superposed
on the R-band image (BTA)
GAIA::Skycat
rc0034d2u2.fits
0:34:06.6 5:14:56 J2000
zhe
Aug 03, 2000 at 15:08:04

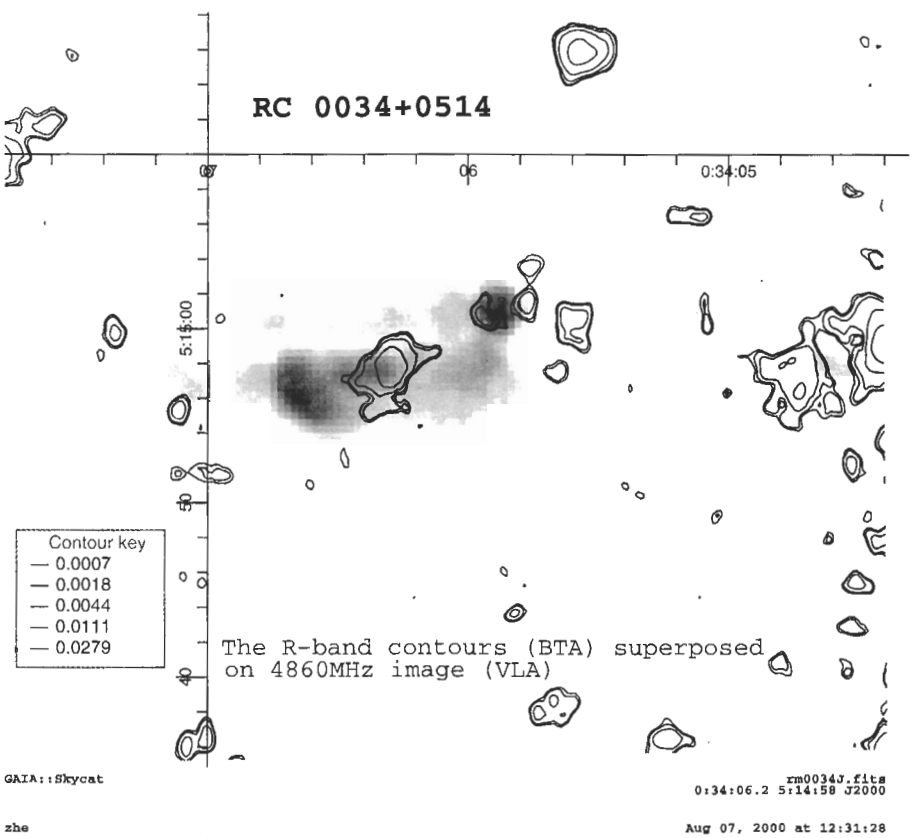
RC 0034+0514
0:34:05
Contour key
— 0.0007
— 0.0018
— 0.0044
— 0.0111
— 0.0279
The R-band contours (BTA) superposed
on 4860MHz image (VLA)
GAIA::Skycat
rm0034J.fits
0:34:06.2 5:14:58 J2000
zhe
Aug 07, 2000 at 12:31:28

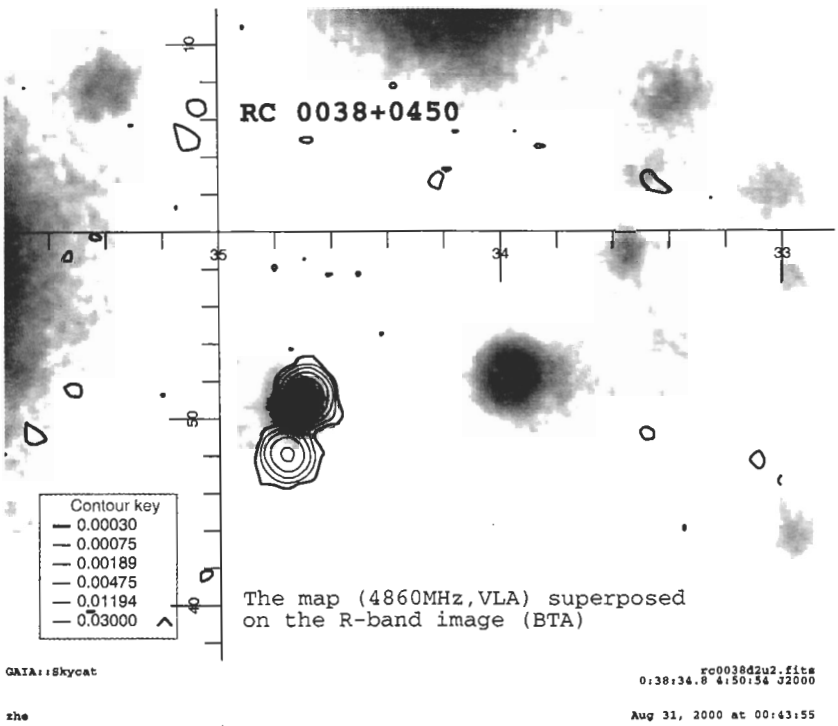

The map (4860MHz,VLA) superposed on the R-band image (BTA)

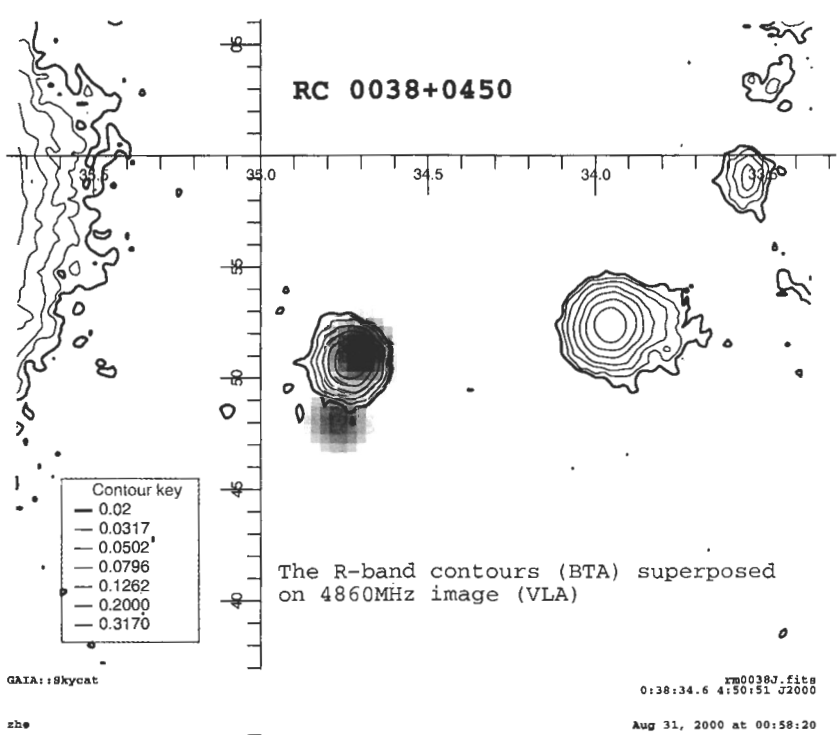

The R-band contours (BTA) superposed on 4860MHz image (VLA)

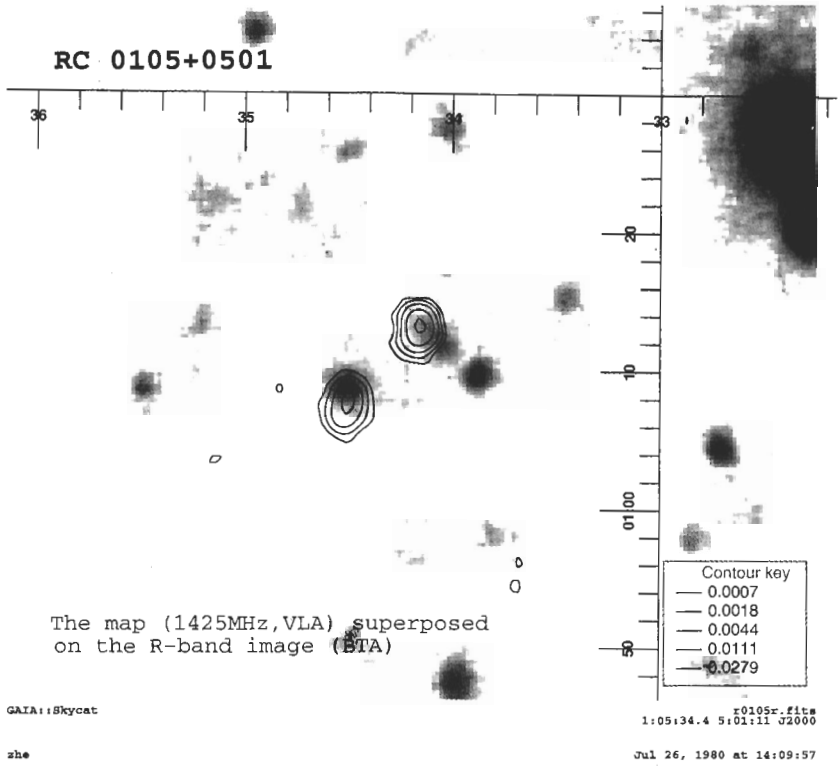

The map (1425MHz,VLA) superposed on the R-band image (BTA)

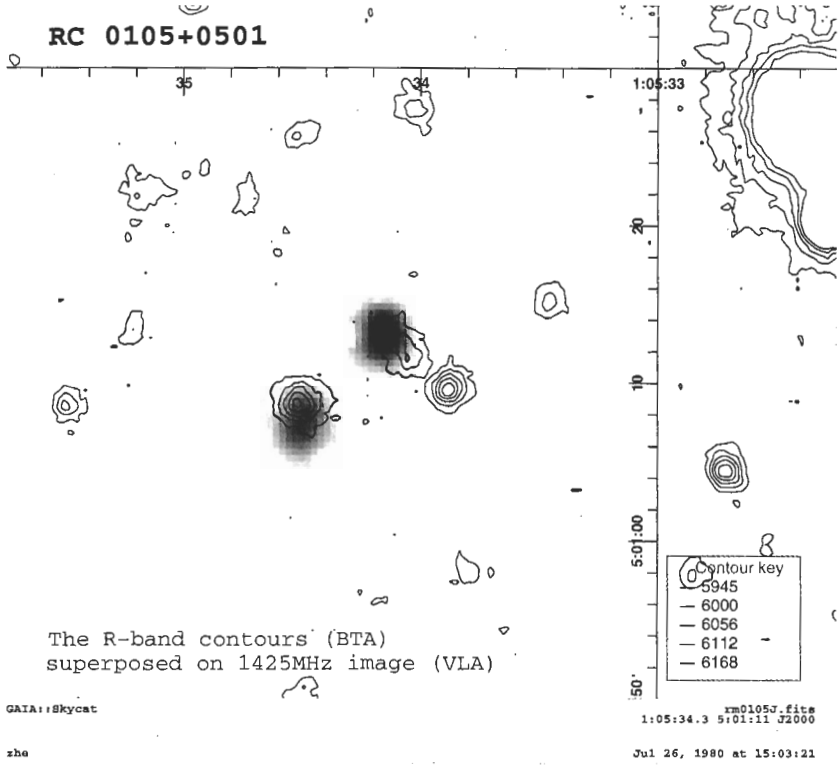

The R-band contours (BTA) superposed on 1425MHz image (VLA)

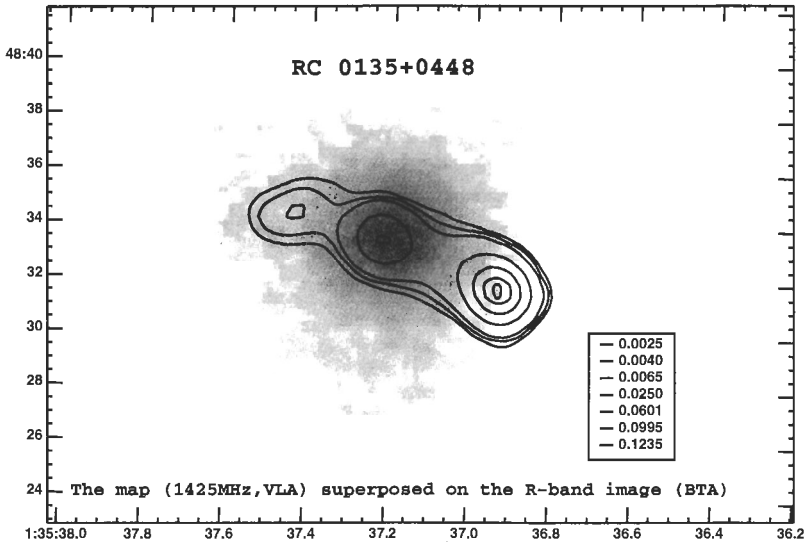
RC 0135+0448
48:40
38
36
34
32
30
28
26
24
0.0025
0.0040
0.0065
0.0250
0.0601
0.0995
0.1235
The map (1425MHz,VLA) superposed on the R-band image (BTA)
1:35:38.0
37.8
37.6
37.4
37.2
37.0
36.8
36.6
36.4
36.2

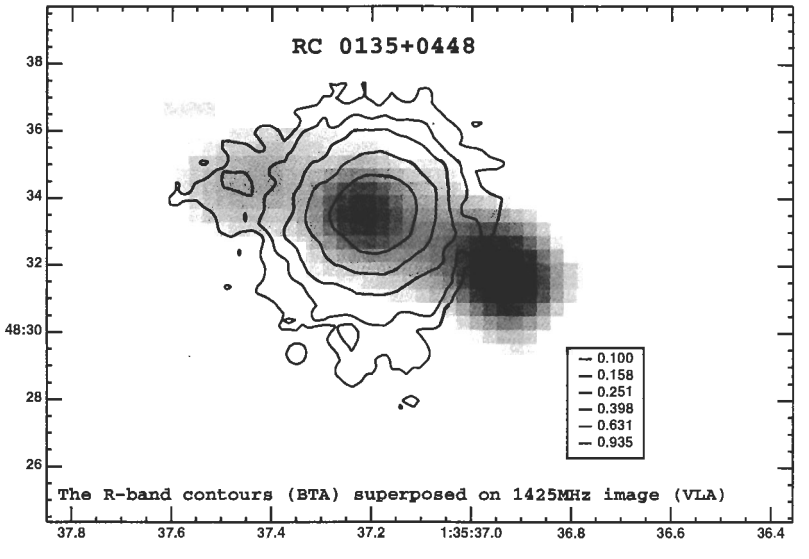
RC 0135+0448
38
36
34
32
48:30
28
26
0.100
0.158
0.251
0.398
0.631
0.935
The R-band contours (BTA) superposed on 1425MHz image (VLA)
37.8
37.6
37.4
37.2
1:35:37.0
36.8
36.6
36.4

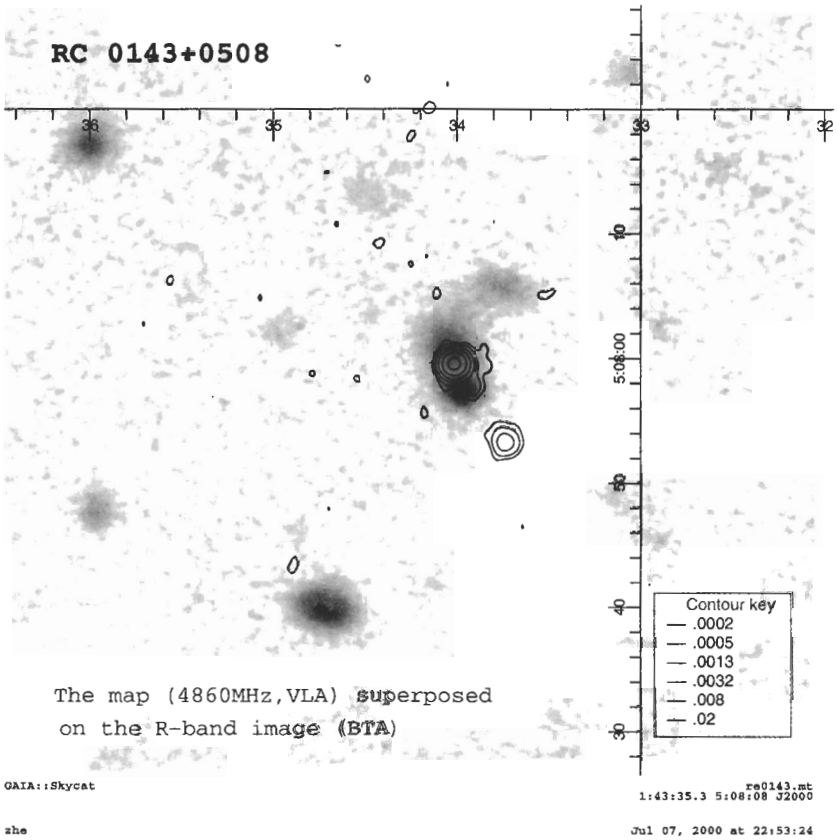

The map (4860MHz,VLA) superposed on the R-band image (BTA)

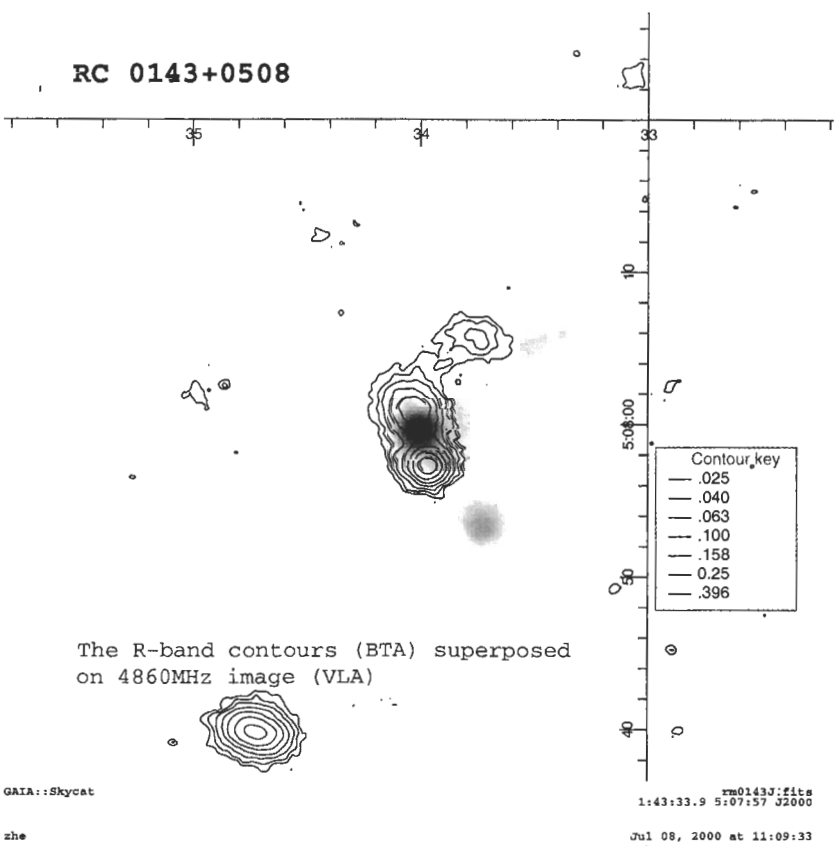

The R-band contours (BTA) superposed on 4860MHz image (VLA)

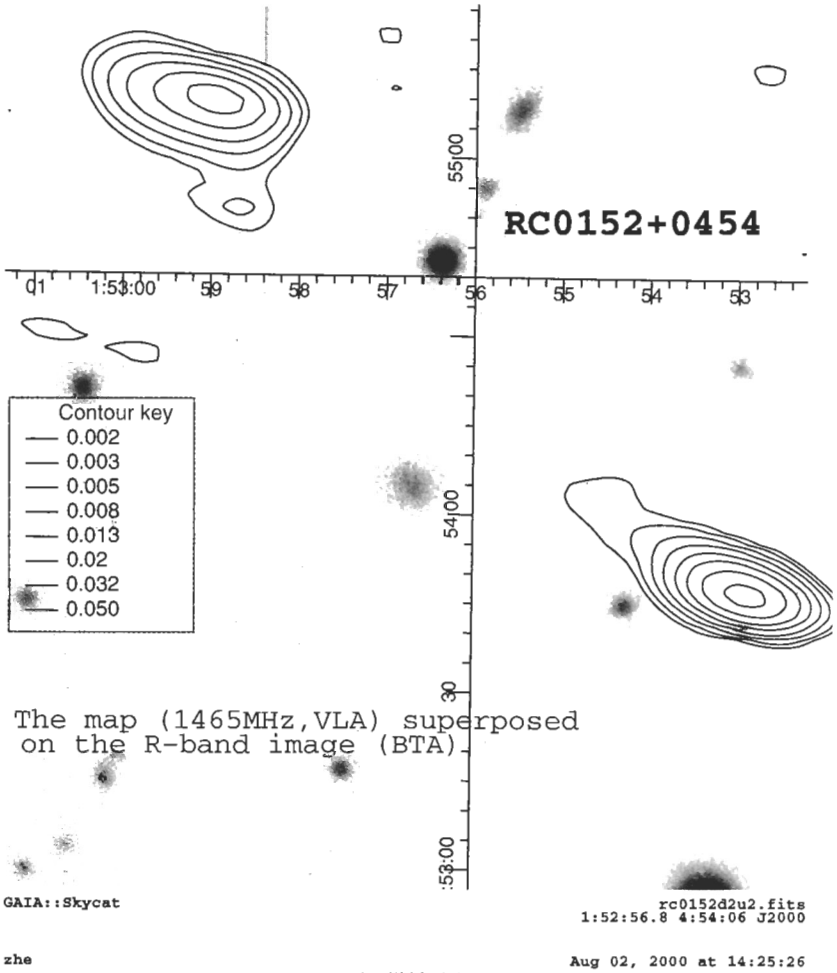

The map (1465MHz,VLA) superposed on the R-band image (BTA).

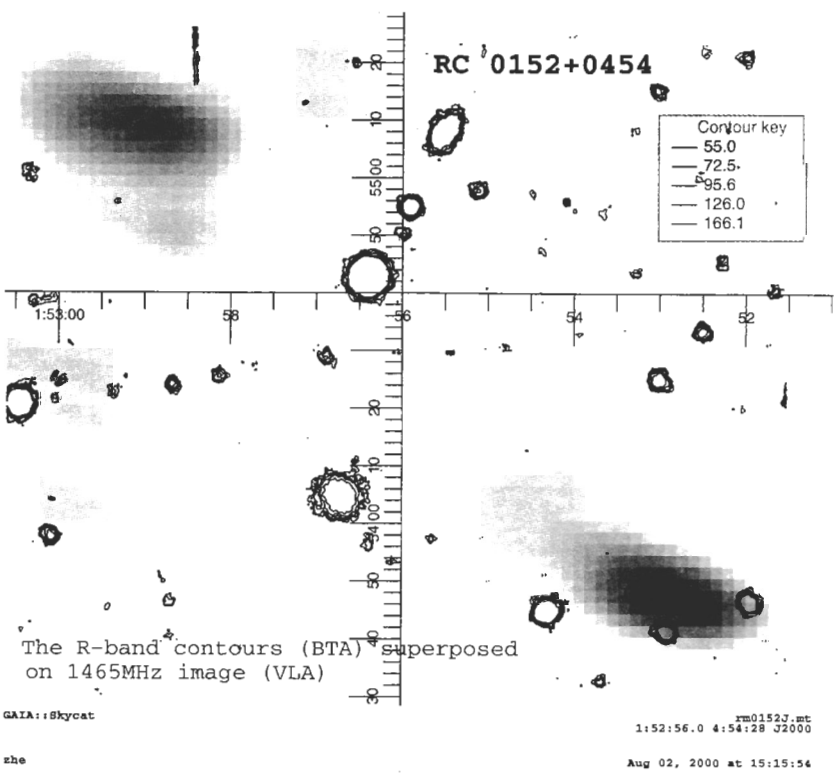

The R-band contours (BTA) superposed on 1465MHz image (VLA)

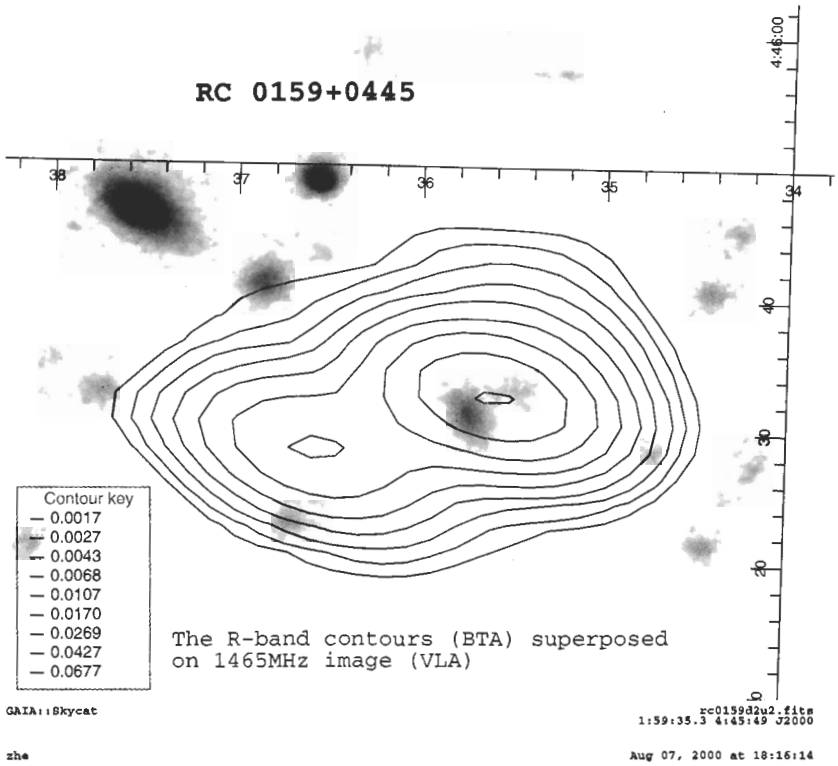
RC 0159+0445
Contour key
— 0.0017
— 0.0027
— 0.0043
— 0.0068
— 0.0107
— 0.0170
— 0.0269
— 0.0427
— 0.0677
The R-band contours (BTA) superposed
on 1465MHz image (VLA)
GAIA::Skycat
rc0159d2u2.fits
1:59:35.3 4:45:49 J2000
zhe
Aug 07, 2000 at 18:16:14

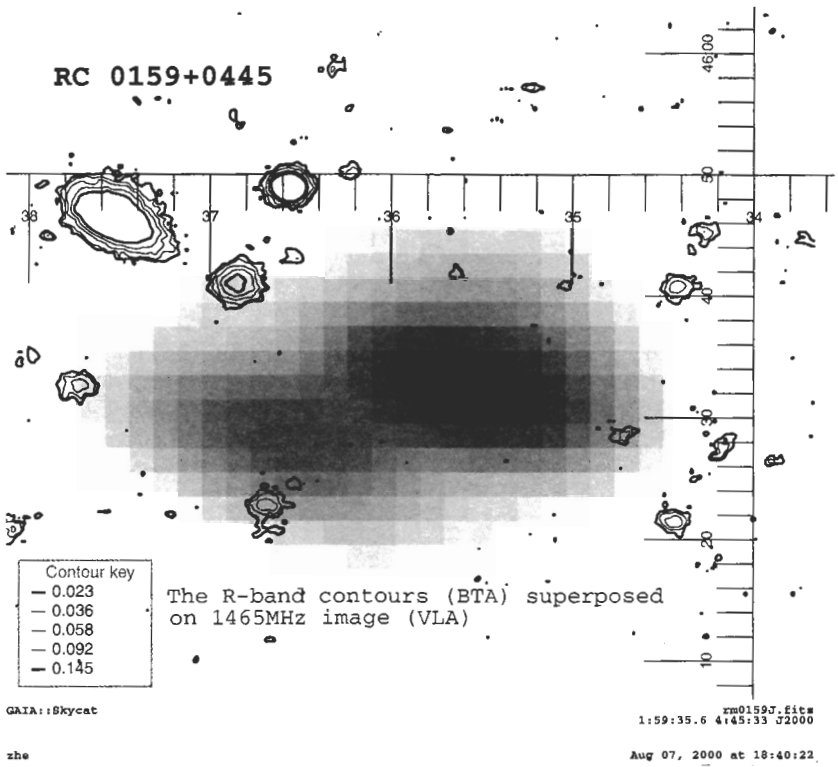
RC 0159+0445
Contour key
— 0.023
— 0.036
— 0.058
— 0.092
— 0.145
The R-band contours (BTA) superposed
on 1465MHz image (VLA)
GAIA::Skycat
rm0159J.fits
1:59:35.6 4:45:33 J2000
zhe
Aug 07, 2000 at 18:40:22

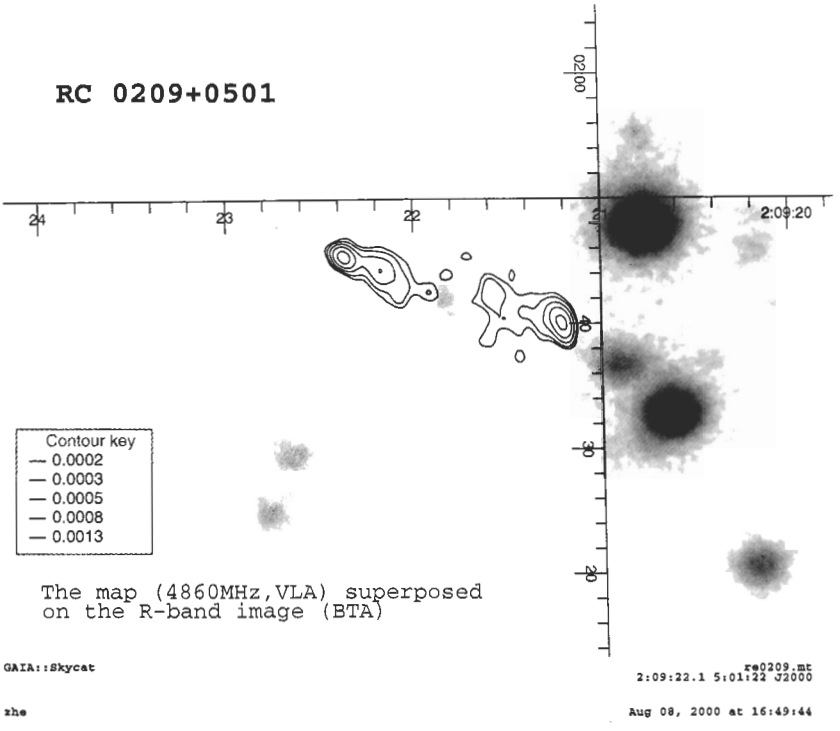
RC 0209+0501
02'00
24
23
22
21
2:09:20
Contour key
— 0.0002
— 0.0003
— 0.0005
— 0.0008
— 0.0013
The map (4860MHz,VLA) superposed
on the R-band image (BTA)
GAIA::Skycat
rm0209.mt
2:09:22.1 5:01:22 J2000
zhe
Aug 08, 2000 at 16:49:44

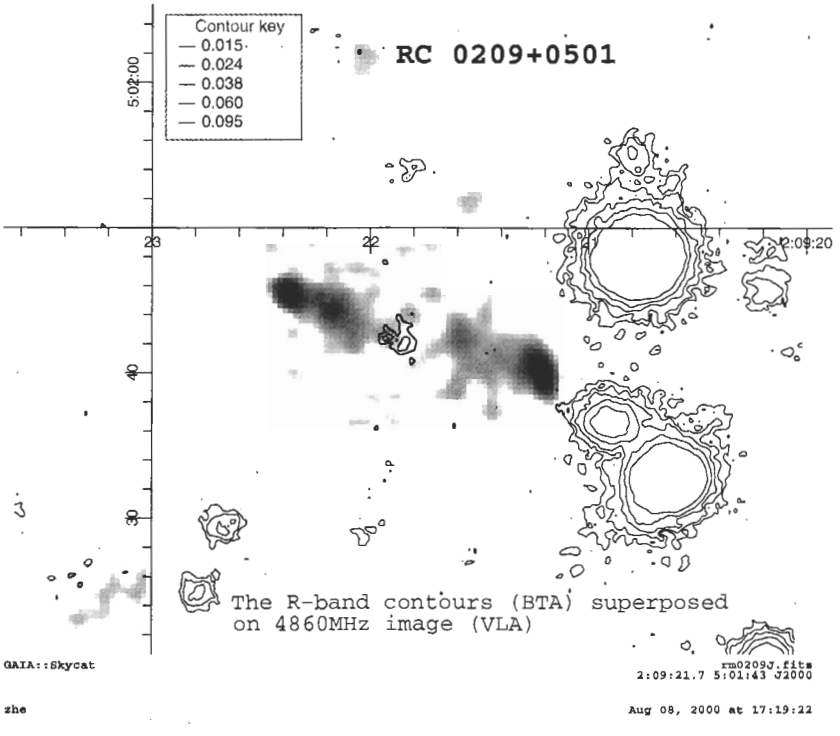
Contour key
— 0.015
— 0.024
— 0.038
— 0.060
— 0.095
RC 0209+0501
5:02:00
23
22
2:09:20
40
30
The R-band contours (BTA) superposed
on 4860MHz image (VLA)
GAIA::Skycat
rm0209J.fits
2:09:21.7 5:01:43 J2000
zhe
Aug 08, 2000 at 17:19:22

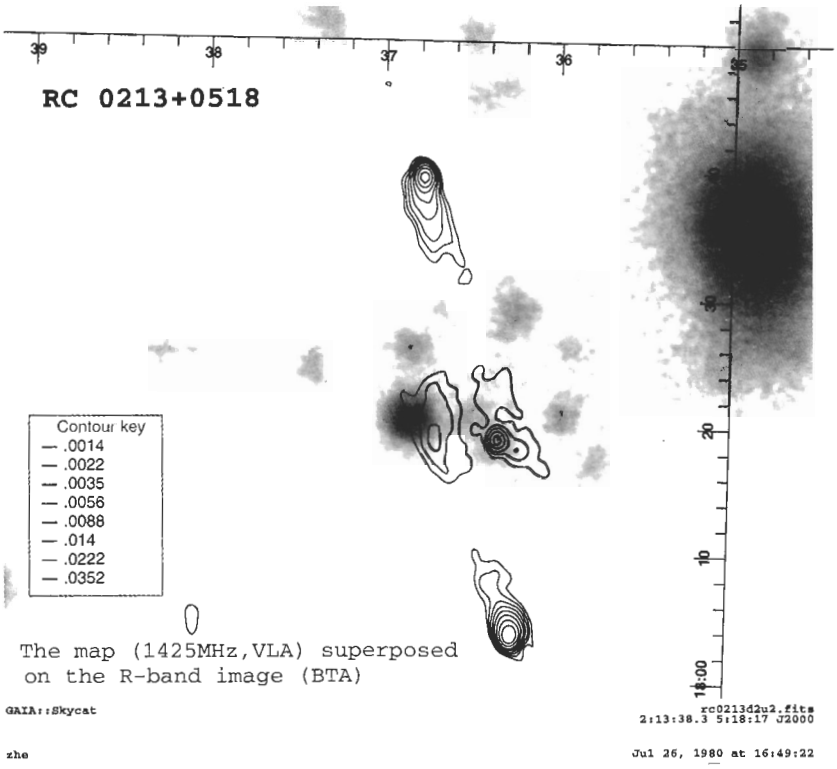

The map (1425MHz,VLA) superposed on the R-band image (BTA)

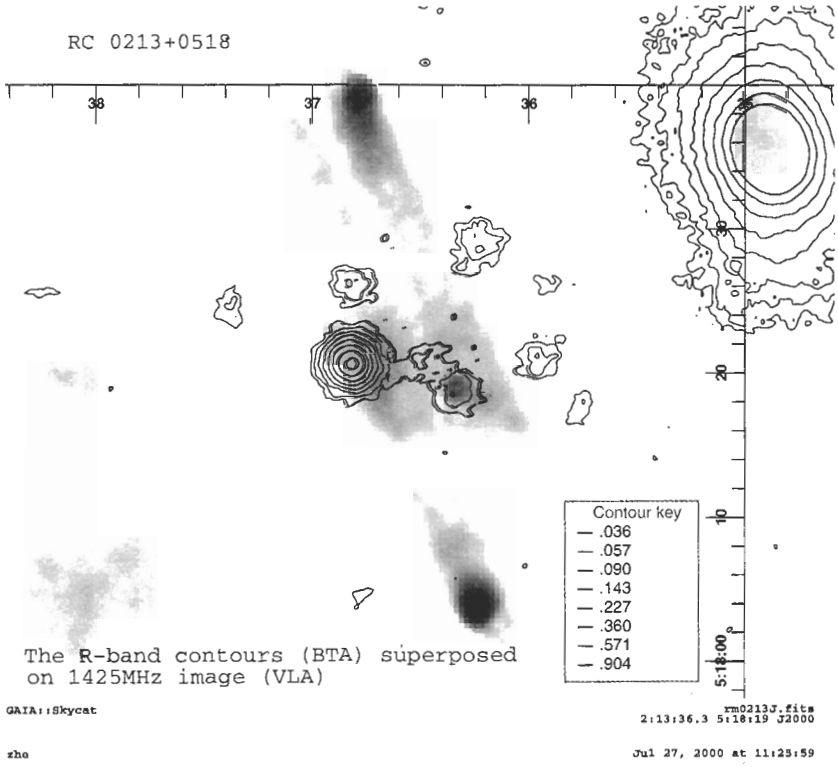

The R-band contours (BTA) superposed on 1425MHz image (VLA)

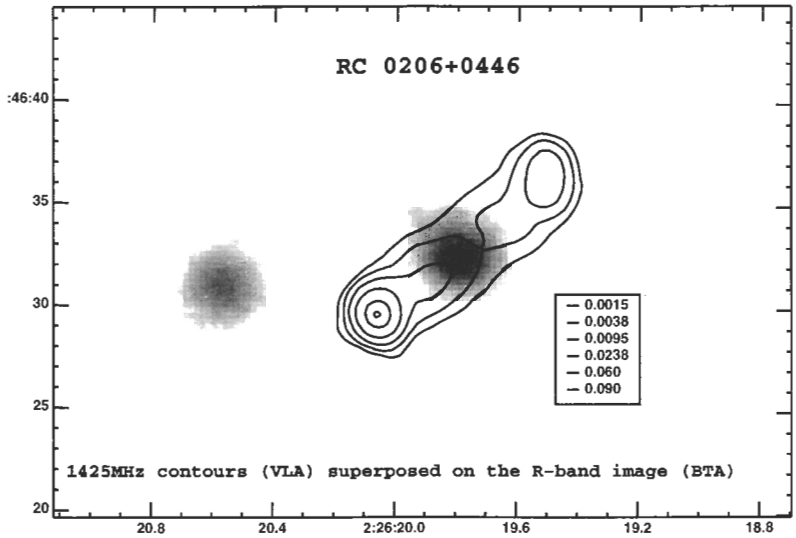
RC 0206+0446
:46:40
35
30
25
20
20.8
20.4
2:26:20.0
19.6
19.2
18.8
0.0015
0.0038
0.0095
0.0238
0.060
0.090
1425MHz contours (VLA) superposed on the R-band image (BTA)

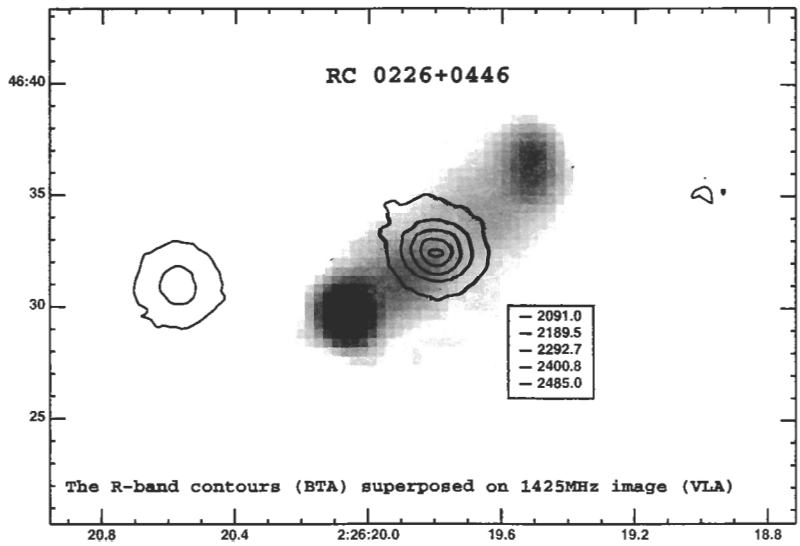
RC 0226+0446
46:40
35
30
25
20.8
20.4
2:26:20.0
19.6
19.2
18.8
2091.0
2189.5
2292.7
2400.8
2485.0
The R-band contours (BTA) superposed on 1425MHz image (VLA)

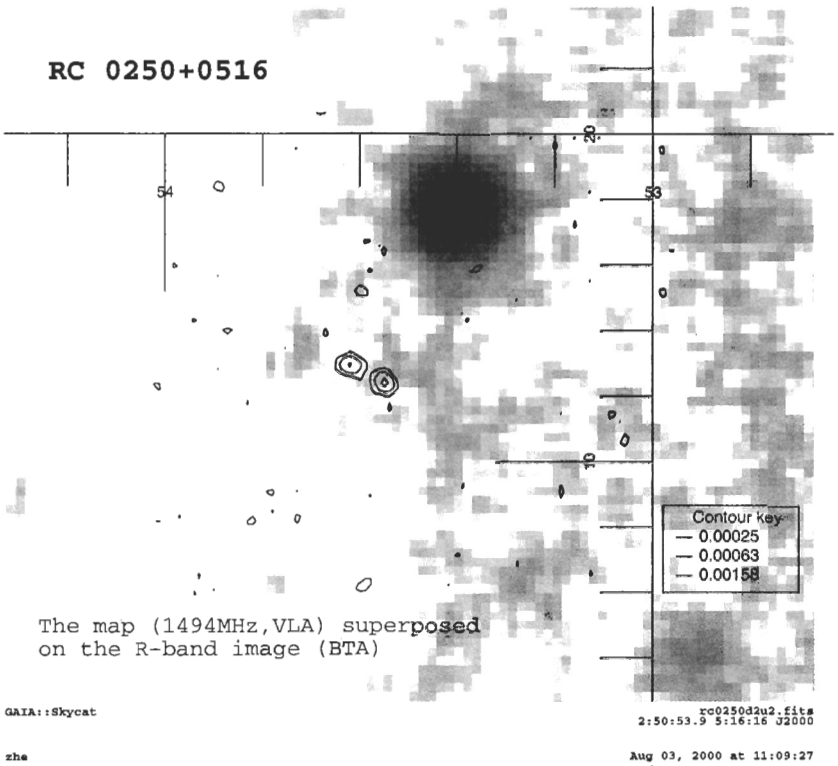

The map (1494MHz,VLA) superposed on the R-band image (BTA)

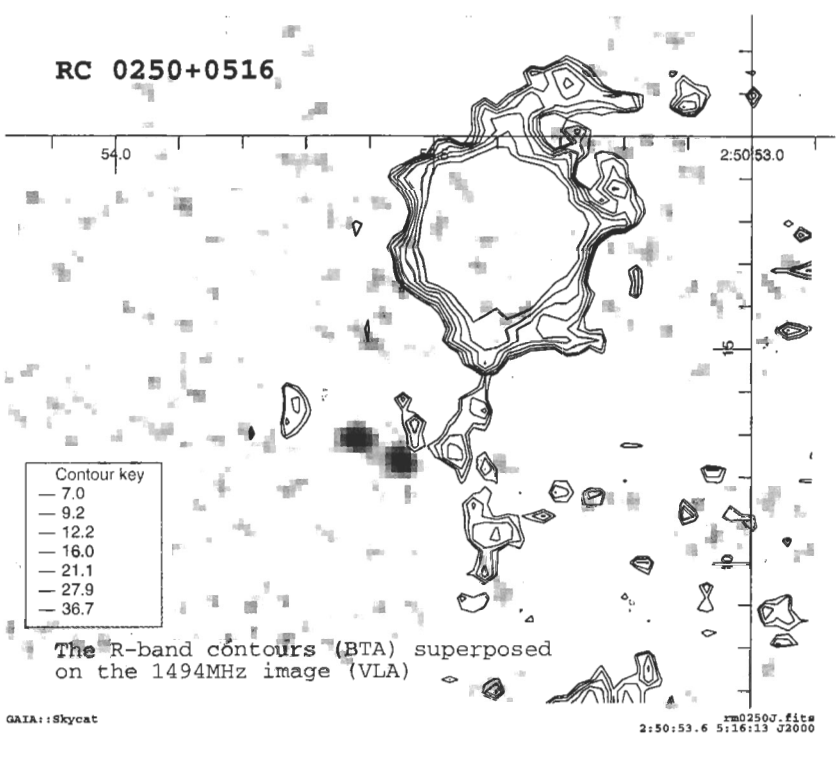

The R-band contours (BTA) superposed on the 1494MHz image (VLA)

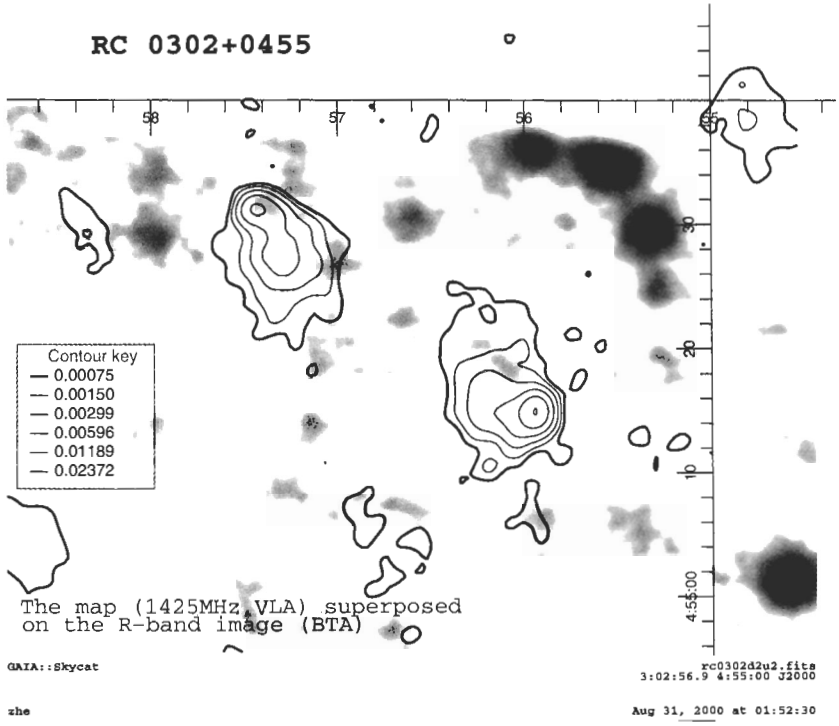
RC 0302+0455
58
57
56
55
30
20
10
4:55:00
Contour key
0.00075
0.00150
0.00299
0.00596
0.01189
0.02372
The map (1425MHz,VLA) superposed
on the R-band image (BTA)
GAIA::Skycat
rc0302d2u2.fits
3:02:56.9 4:55:00 J2000
zhe
Aug 31, 2000 at 01:52:30

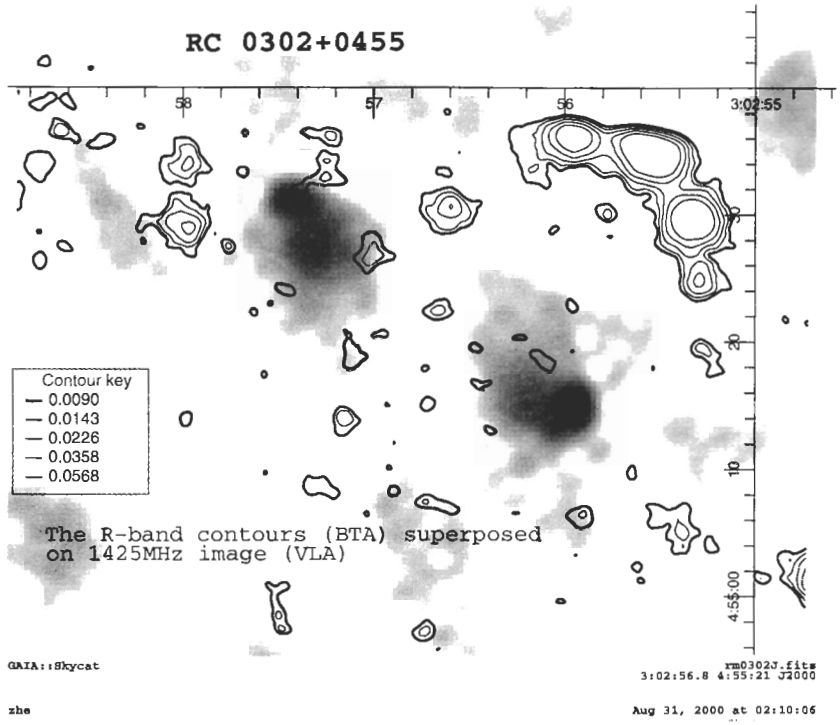
RC 0302+0455
58
57
56
3:02:55
30
20
10
4:55:00
Contour key
0.0090
0.0143
0.0226
0.0358
0.0568
The R-band contours (BTA) superposed
on 1425MHz image (VLA)
GAIA::Skycat
rm0302J.fits
3:02:56.8 4:55:21 J2000
zhe
Aug 31, 2000 at 02:10:06

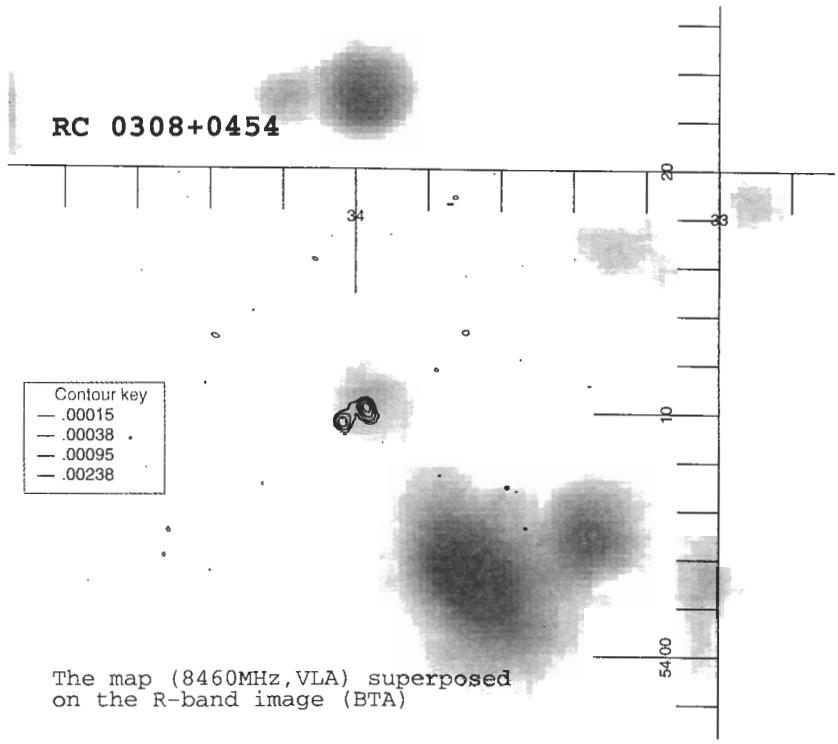
RC 0308+0454
34
33
20
10
54.00
Contour key
— .00015
— .00038
— .00095
— .00238
The map (8460MHz,VLA) superposed
on the R-band image (BTA)
GAIA::Skycat
agg.fits
3:08:34.7 4:54:18 J2000
zhe
Jul 27, 2000 at 17:33:30

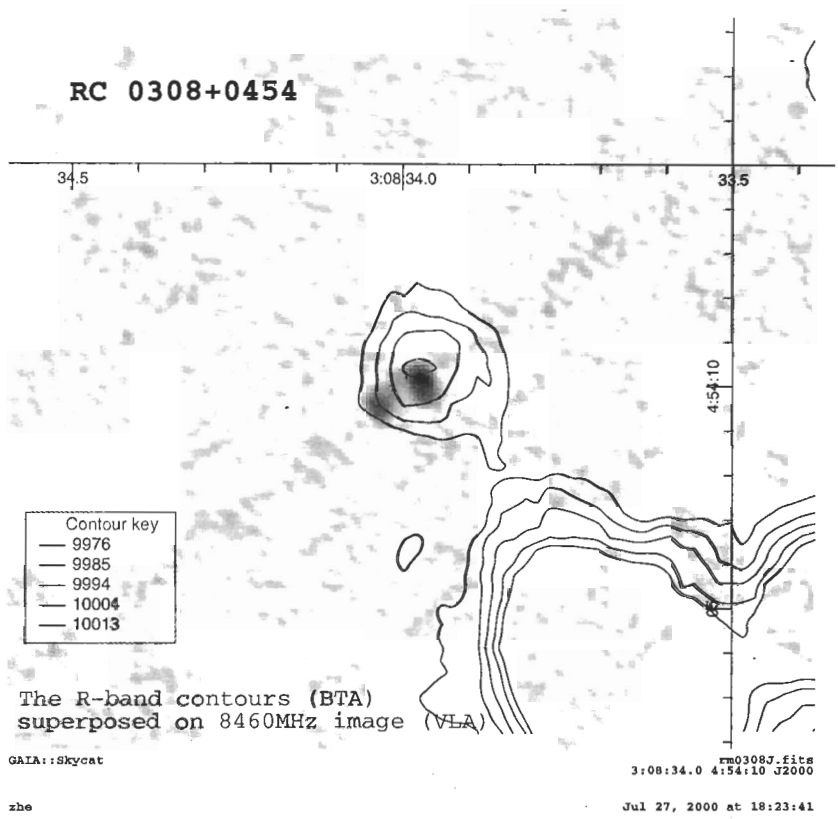
RC 0308+0454
34.5
3:08:34.0
33.5
4:54:10
Contour key
— 9976
— 9985
— 9994
— 10004
— 10013
The R-band contours (BTA)
superposed on 8460MHz image (VLA)
GAIA::Skycat
rm0308J.fits
3:08:34.0 4:54:10 J2000
zhe
Jul 27, 2000 at 18:23:41

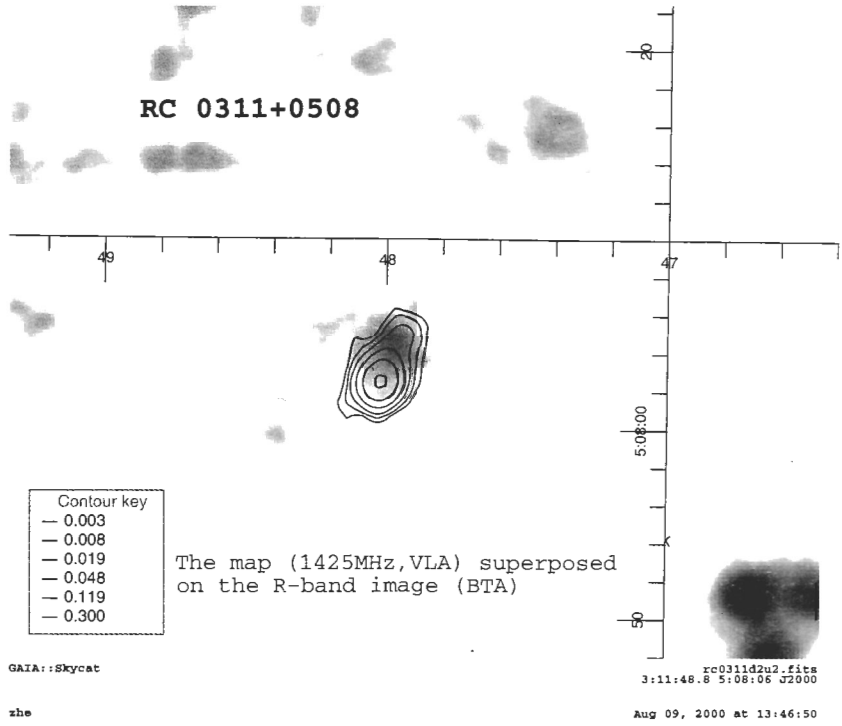

The map (1425MHz,VLA) superposed on the R-band image (BTA)

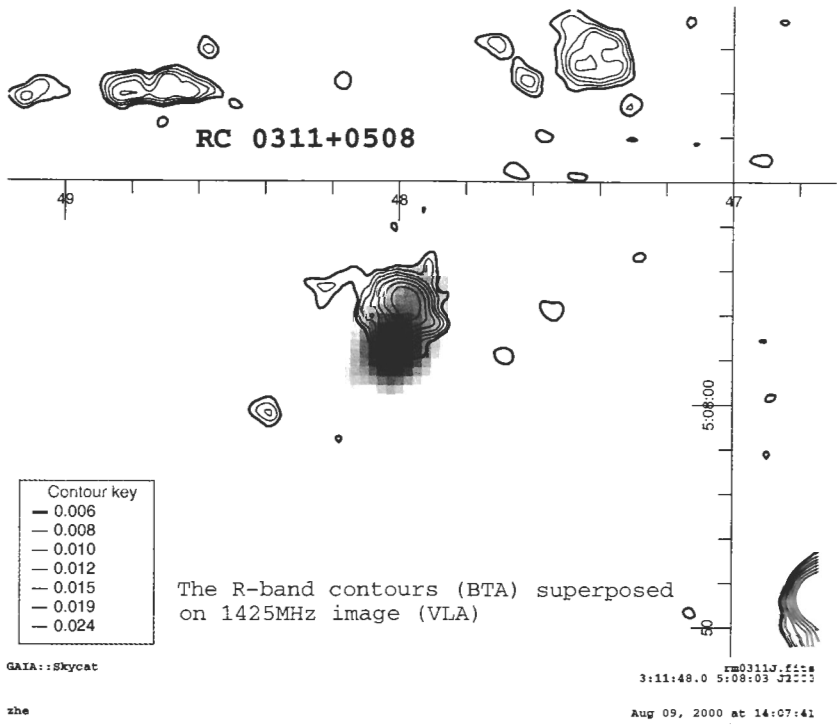

The R-band contours (BTA) superposed on 1425MHz image (VLA)

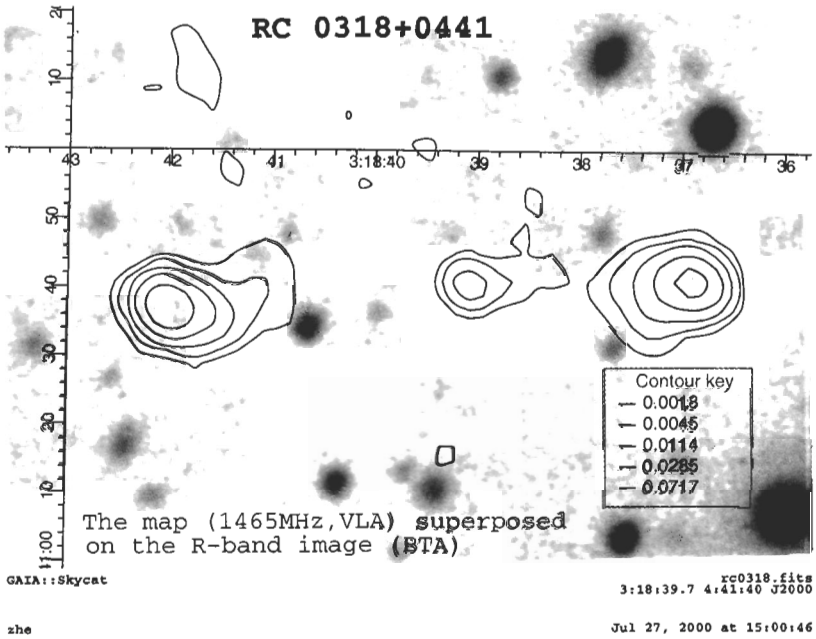
RC 0318+0441
Contour key
0.0018
0.0045
0.0114
0.0285
0.0717
The map (1465MHz,VLA) superposed
on the R-band image (BTA)
GAIA::Skycat
rc0318.fits
3:18:39.7 4:41:40 J2000
zhe
Jul 27, 2000 at 15:00:46

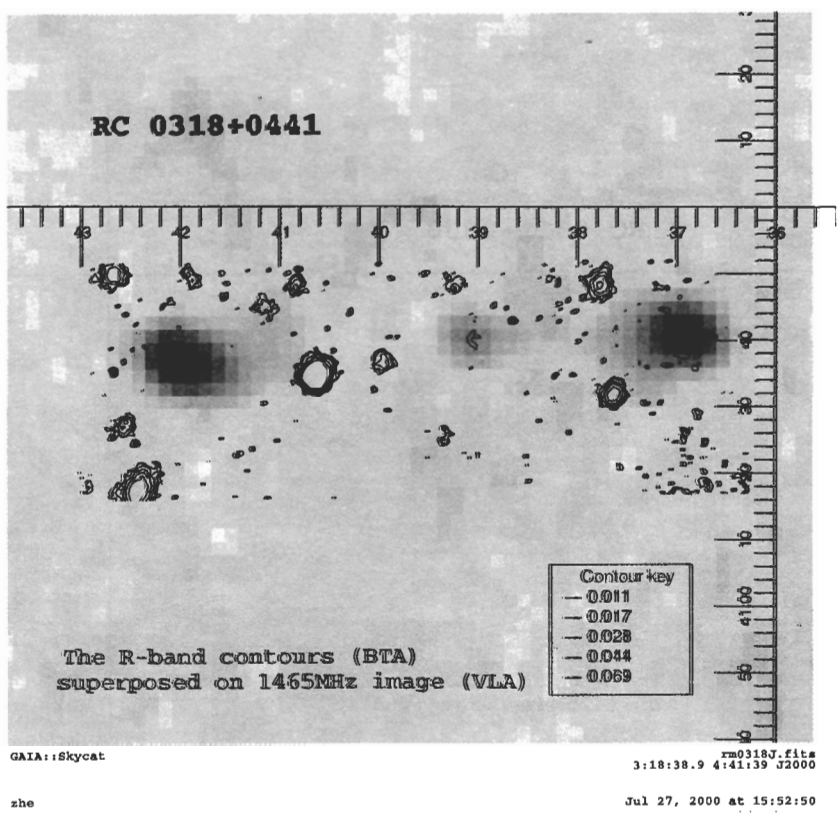
RC 0318+0441
Contour key
0.011
0.017
0.028
0.044
0.069
The R-band contours (BTA)
superposed on 1465MHz image (VLA)
GAIA::Skycat
rm0318J.fits
3:18:38.9 4:41:39 J2000
zhe
Jul 27, 2000 at 15:52:50

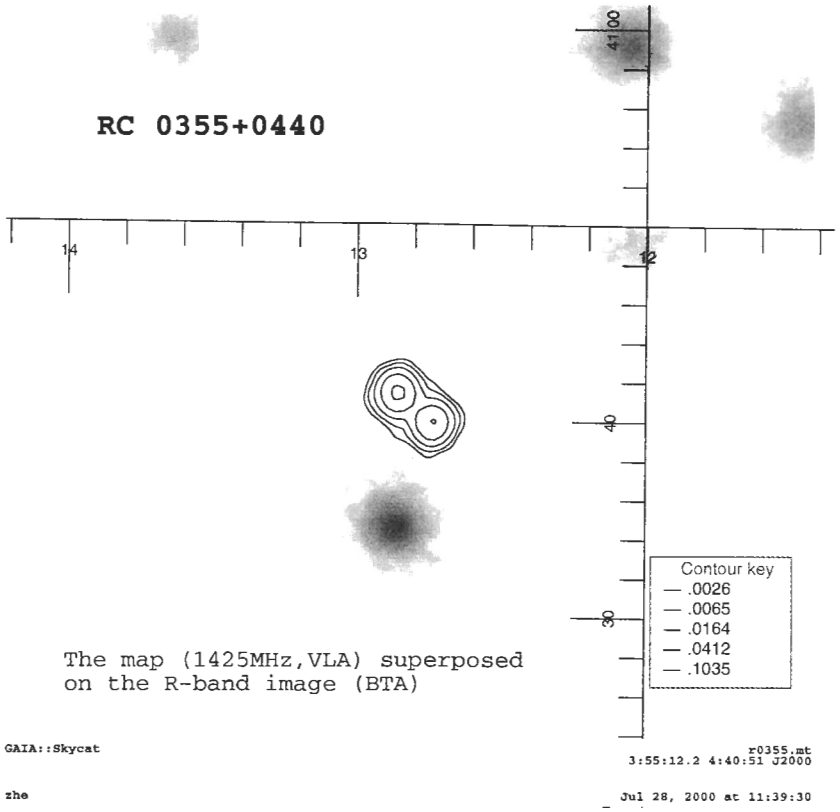
RC 0355+0440
41'00
40
30
14
13
12
Contour key
— .0026
— .0065
— .0164
— .0412
— .1035
The map (1425MHz,VLA) superposed
on the R-band image (BTA)
GAIA::Skycat
zhe
r0355.mt
3:55:12.2 4:40:51 J2000
Jul 28, 2000 at 11:39:30

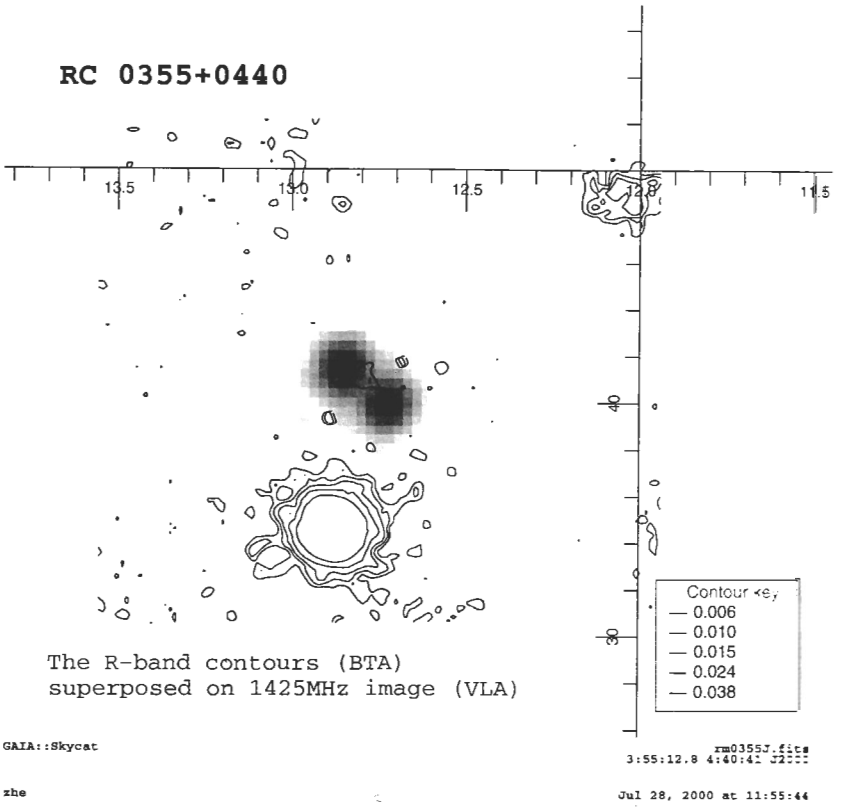
RC 0355+0440
13.5
13.0
12.5
12.0
11.5
40
30
Contour key
— 0.006
— 0.010
— 0.015
— 0.024
— 0.038
The R-band contours (BTA)
superposed on 1425MHz image (VLA)
GAIA::Skycat
zhe
rm0355J.fits
3:55:12.8 4:40:41 J2000
Jul 28, 2000 at 11:55:44

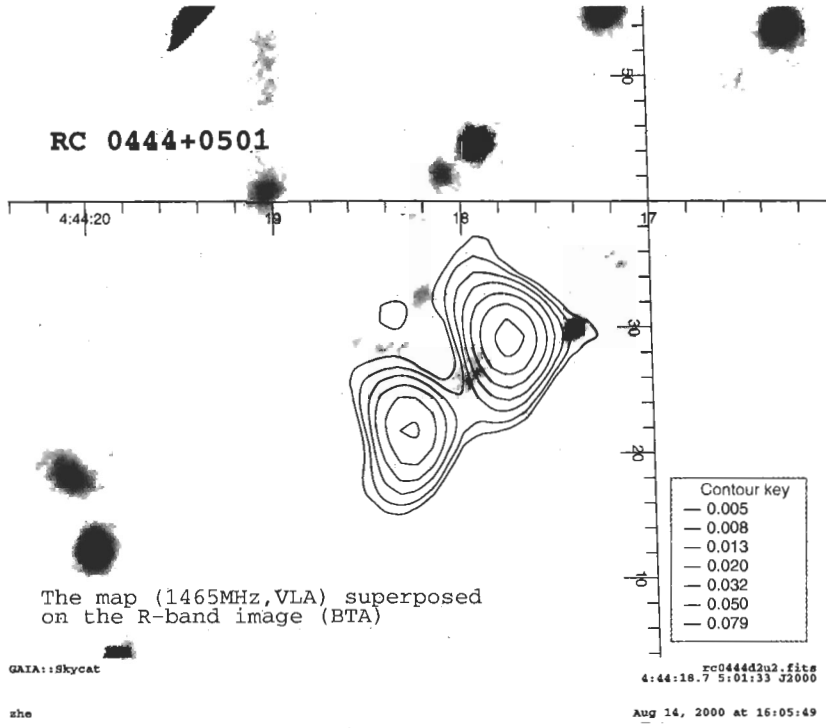
RC 0444+0501
4:44:20
19
18
17
50
40
30
20
10
Contour key
— 0.005
— 0.008
— 0.013
— 0.020
— 0.032
— 0.050
— 0.079
The map (1465MHz,VLA) superposed
on the R-band image (BTA)
GAIA::Skycat
rc0444d2u2.fits
4:44:18.7 5:01:33 J2000
zhe
Aug 14, 2000 at 16:05:49

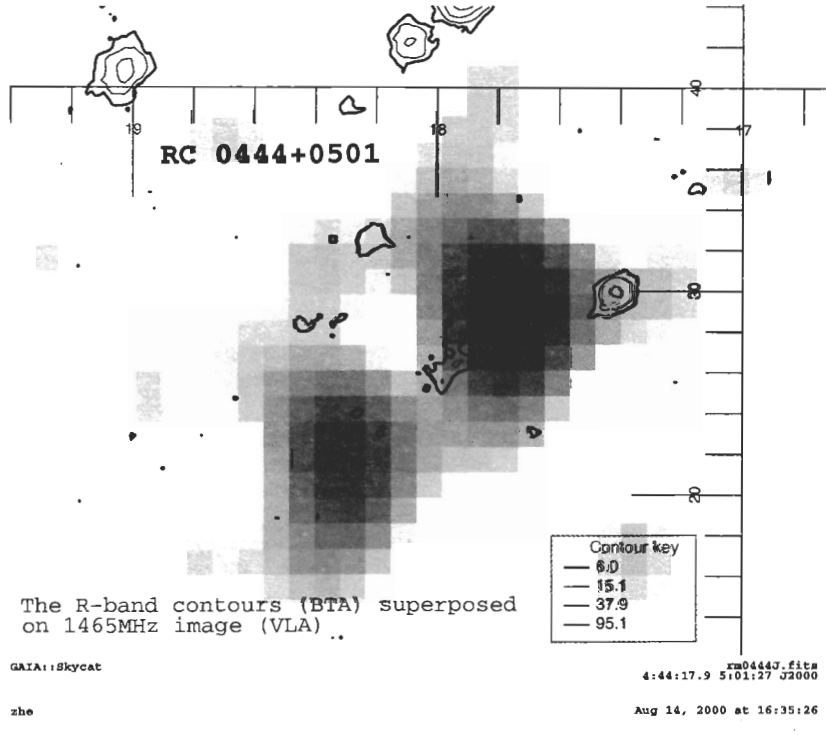
RC 0444+0501
19
18
17
40
30
20
Contour key
— 6.0
— 15.1
— 37.9
— 95.1
The R-band contours (BTA) superposed
on 1465MHz image (VLA)
GAIA::Skycat
rm0444J.fits
4:44:17.9 5:01:27 J2000
zhe
Aug 14, 2000 at 16:35:26

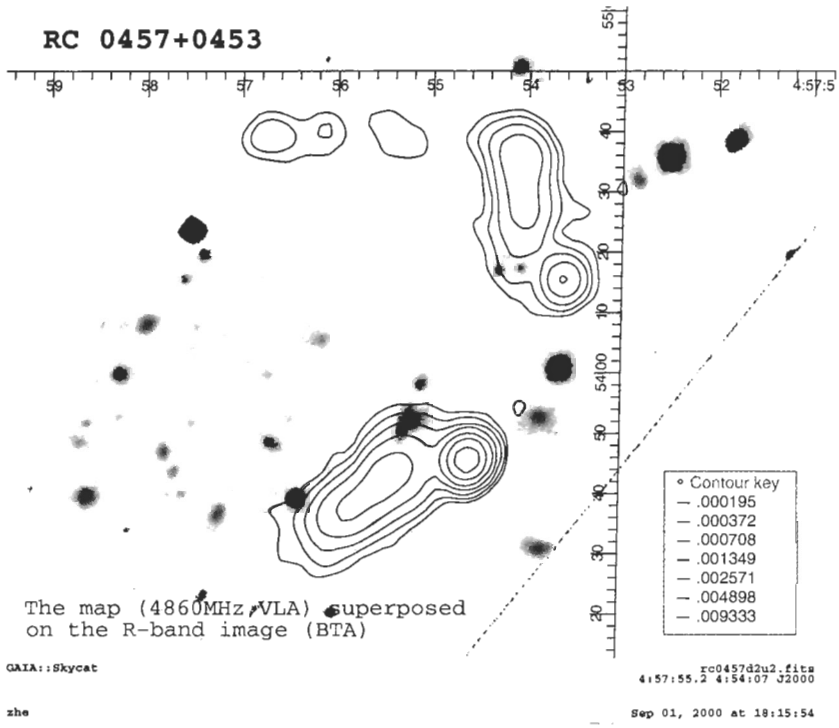
RC 0457+0453
The map (4860MHz, VLA) superposed
on the R-band image (BTA)
Contour key
.000195
.000372
.000708
.001349
.002571
.004898
.009333
GAIA::Skycat
zhe
Sep 01, 2000 at 18:15:54

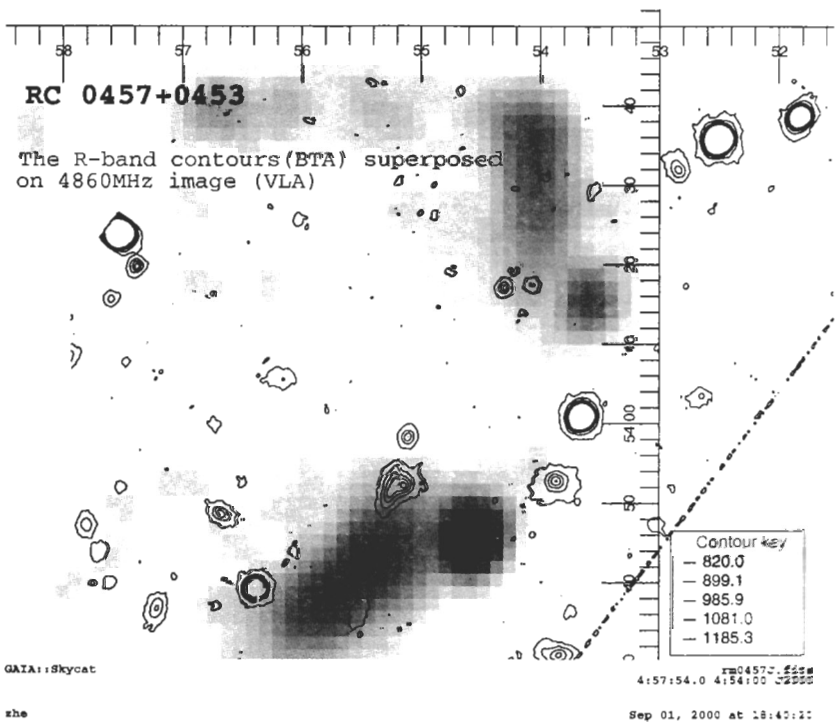
RC 0457+0453
The R-band contours(BTA) superposed
on 4860MHz image (VLA)
Contour key
820.0
899.1
985.9
1081.0
1185.3
GAIA::Skycat
zhe
Sep 01, 2000 at 18:43:11

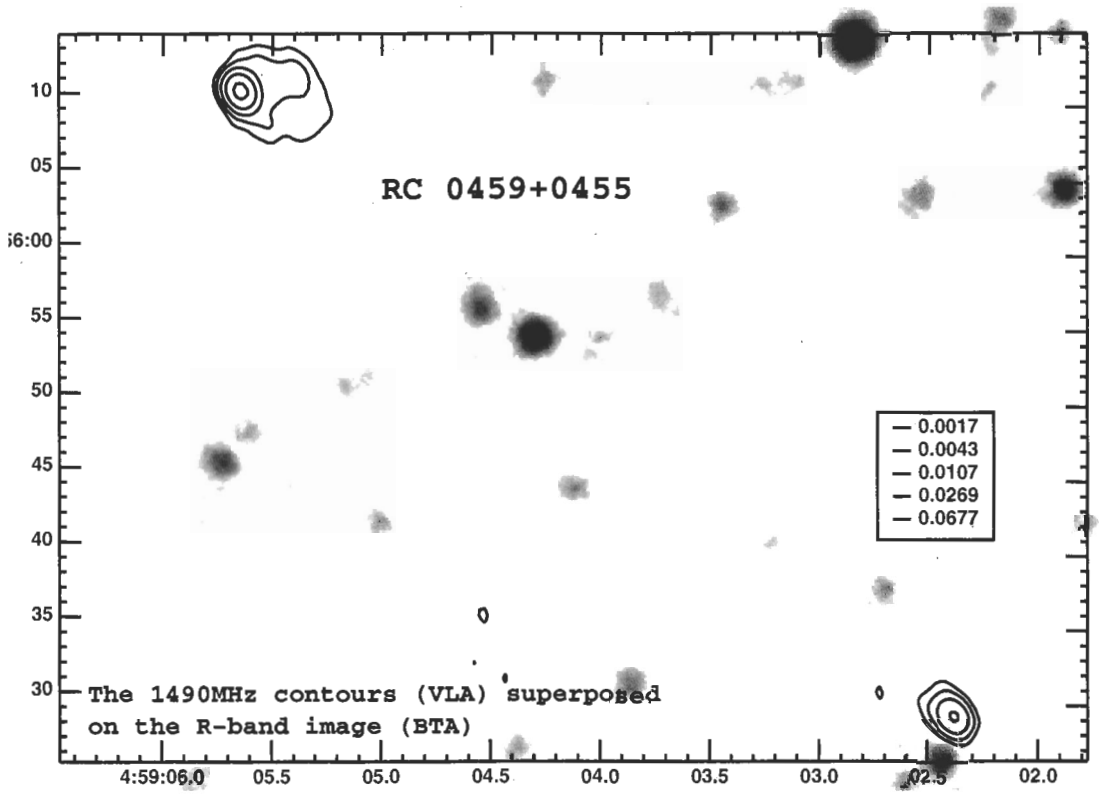
RC 0459+0455
— 0.0017
— 0.0043
— 0.0107
— 0.0269
— 0.0677
The 1490MHz contours (VLA) superposed
on the R-band image (BTA)
10
05
6:00
55
50
45
40
35
30
4:59:06.0
05.5
05.0
04.5
04.0
03.5
03.0
02.5
02.0

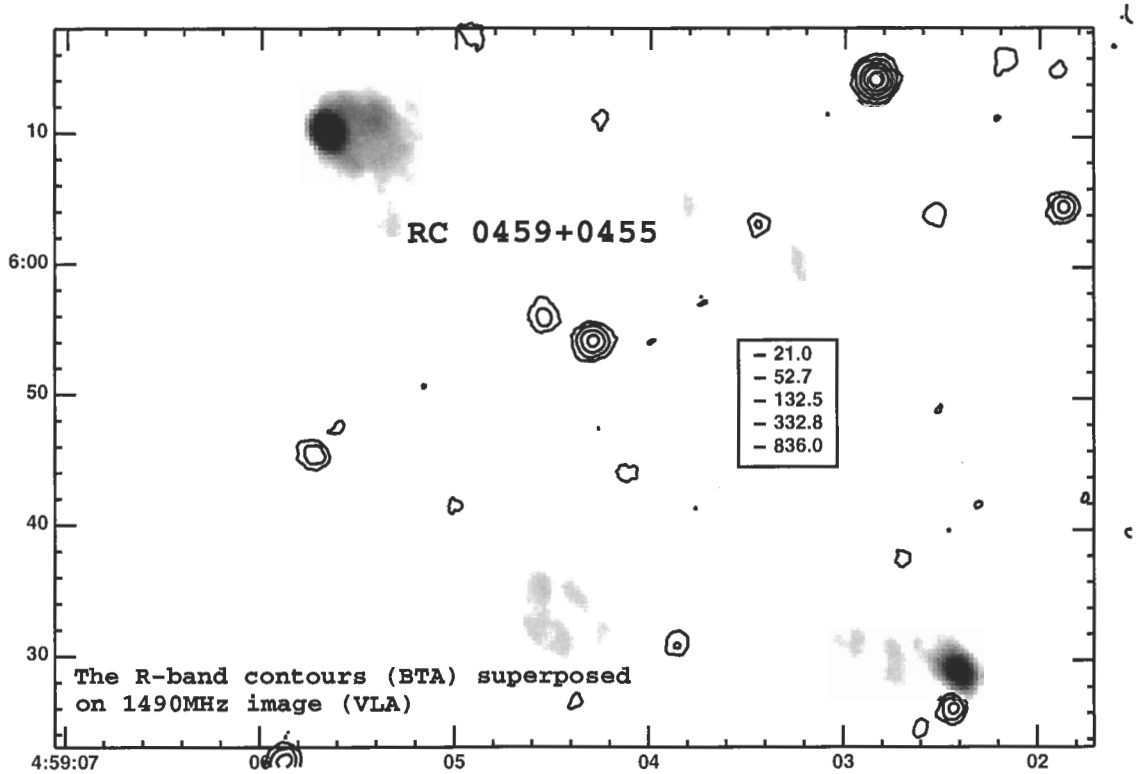
RC 0459+0455
— 21.0
— 52.7
— 132.5
— 332.8
— 836.0
The R-band contours (BTA) superposed
on 1490MHz image (VLA)
10
6:00
50
40
30
4:59:07
05
04
03
02

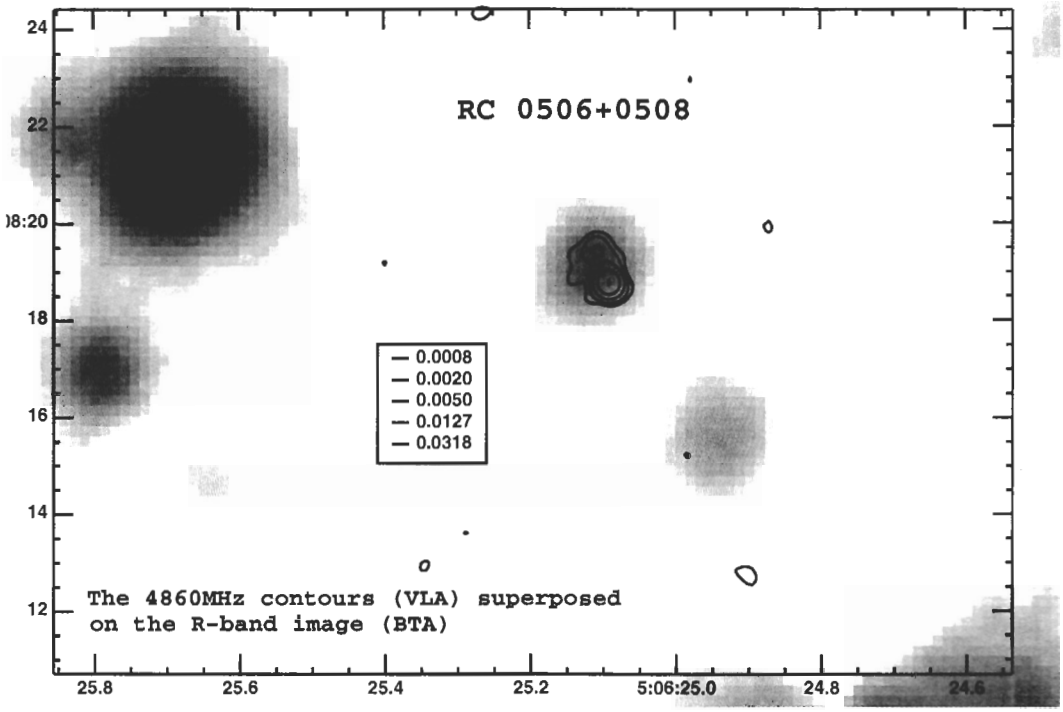
RC 0506+0508
— 0.0008
— 0.0020
— 0.0050
— 0.0127
— 0.0318
The 4860MHz contours (VLA) superposed
on the R-band image (BTA)
24
22
08:20
18
16
14
12
25.8
25.6
25.4
25.2
5:06:25.0
24.8
24.6

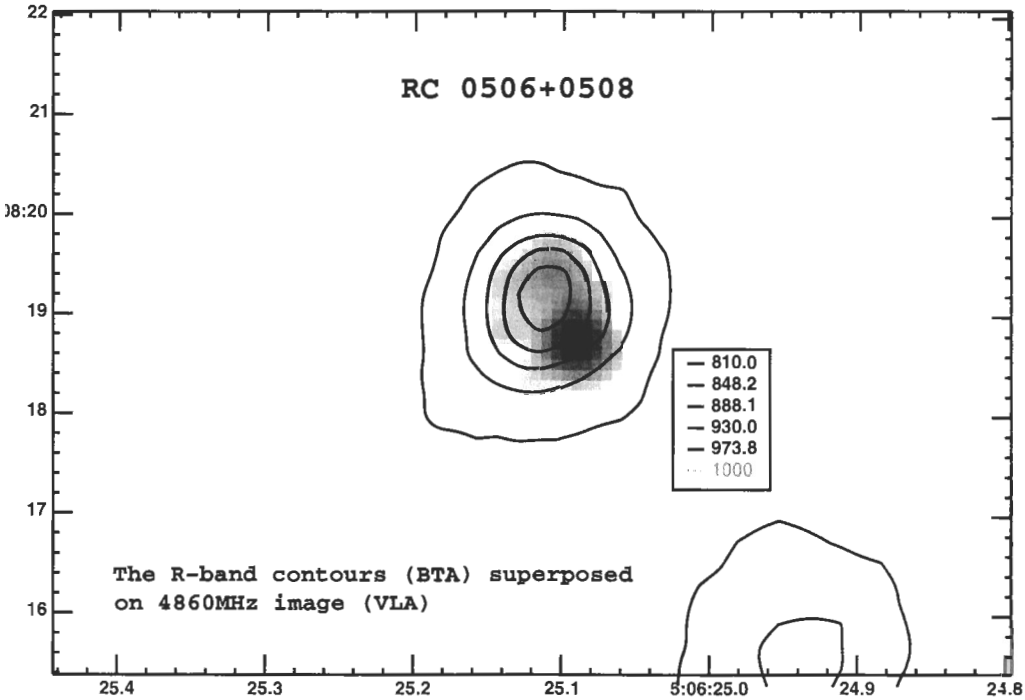
RC 0506+0508
— 810.0
— 848.2
— 888.1
— 930.0
— 973.8
1000
The R-band contours (BTA) superposed
on 4860MHz image (VLA)
22
21
08:20
19
18
17
16
25.4
25.3
25.2
25.1
5:06:25.0
24.9
24.8

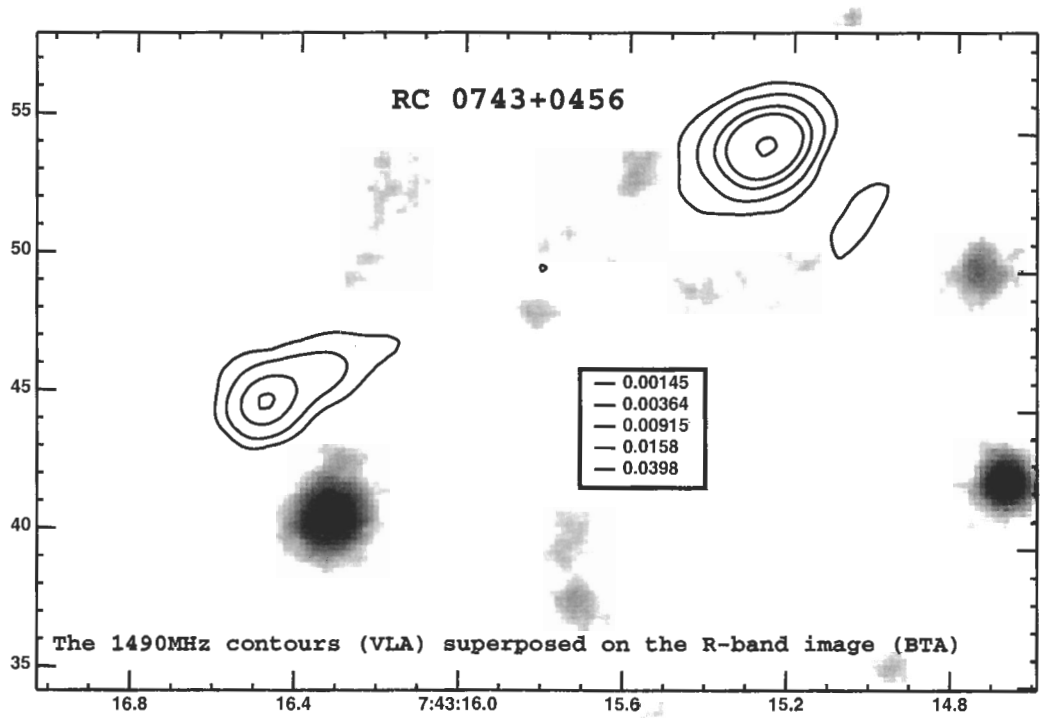
RC 0743+0456
0.00145
0.00364
0.00915
0.0158
0.0398
The 1490MHz contours (VLA) superposed on the R-band image (BTA)
55
50
45
40
35
16.8
16.4
7:43:16.0
15.6
15.2
14.8

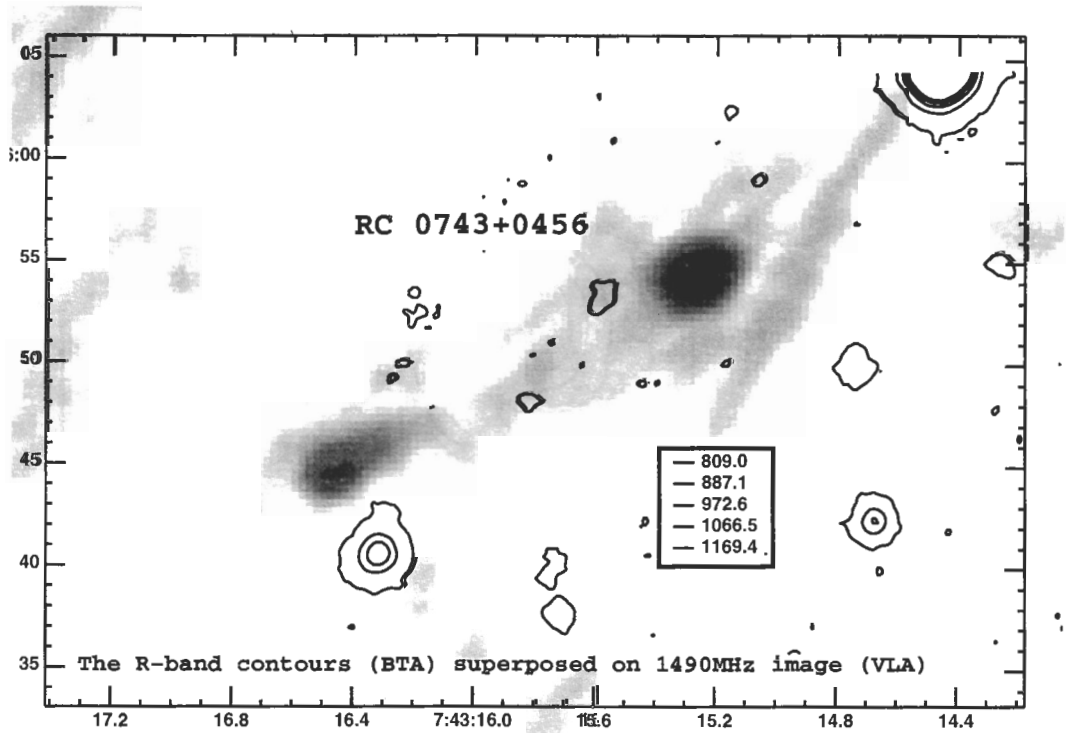
RC 0743+0456
809.0
887.1
972.6
1066.5
1169.4
The R-band contours (BTA) superposed on 1490MHz image (VLA)
55
50
45
40
35
17.2
16.8
16.4
7:43:16.0
15.2
14.8
14.4

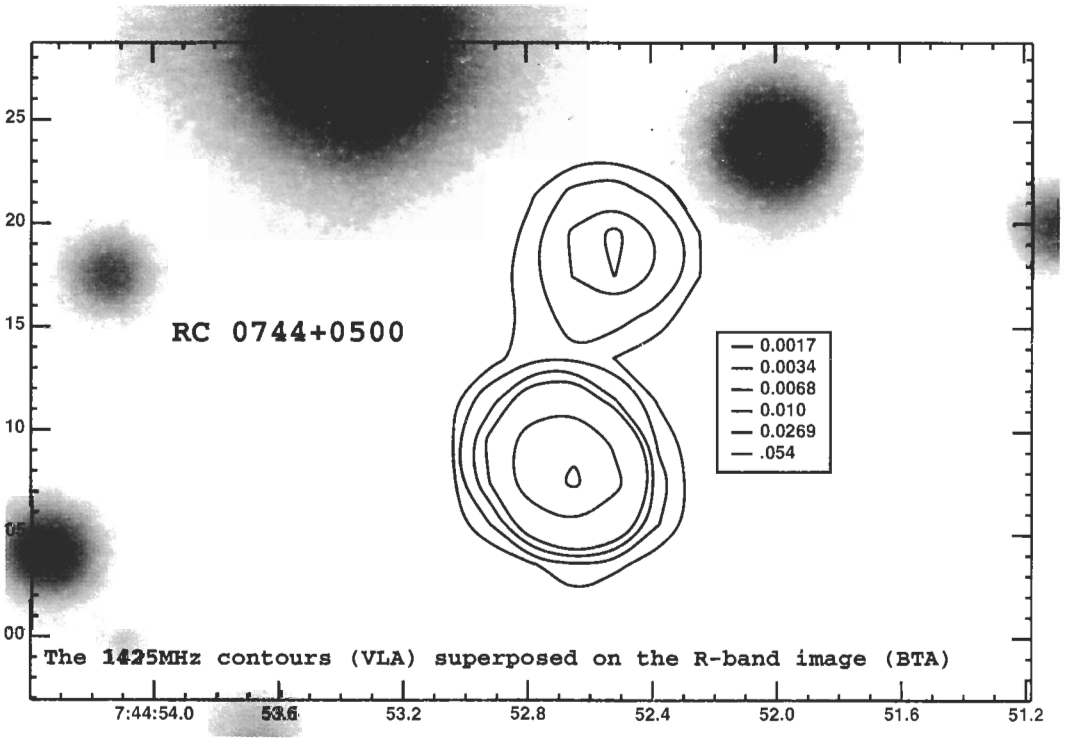
RC 0744+0500
0.0017
0.0034
0.0068
0.010
0.0269
.054
The 1425MHz contours (VLA) superposed on the R-band image (BTA)
25
20
15
10
00
7:44:54.0
53.6
53.2
52.8
52.4
52.0
51.6
51.2

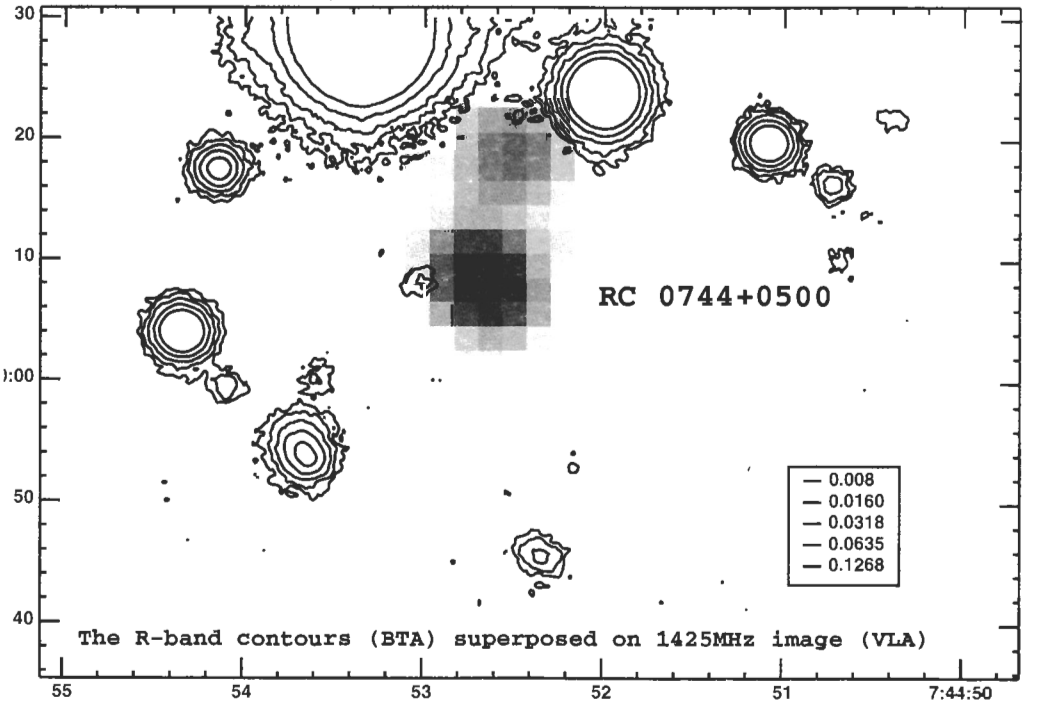
RC 0744+0500
0.008
0.0160
0.0318
0.0635
0.1268
The R-band contours (BTA) superposed on 1425MHz image (VLA)
30
20
10
50
40
55
54
53
52
51
7:44:50

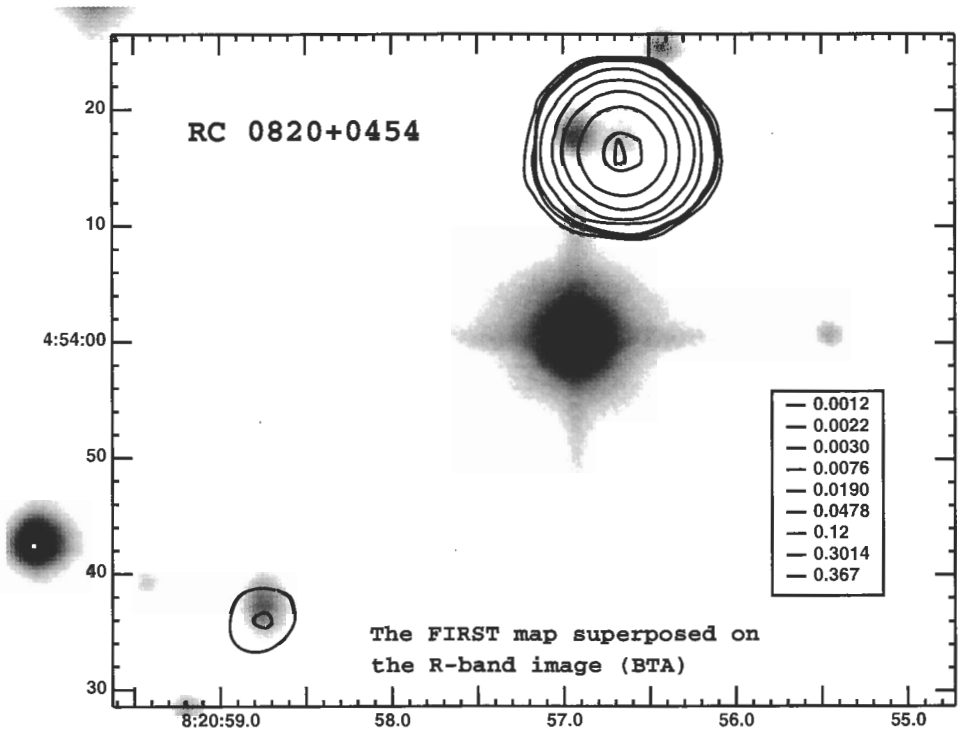
RC 0820+0454
0.0012
0.0022
0.0030
0.0076
0.0190
0.0478
0.12
0.3014
0.367
The FIRST map superposed on
the R-band image (BTA)
20
10
4:54:00
50
40
30
8:20:59.0
58.0
57.0
56.0
55.0

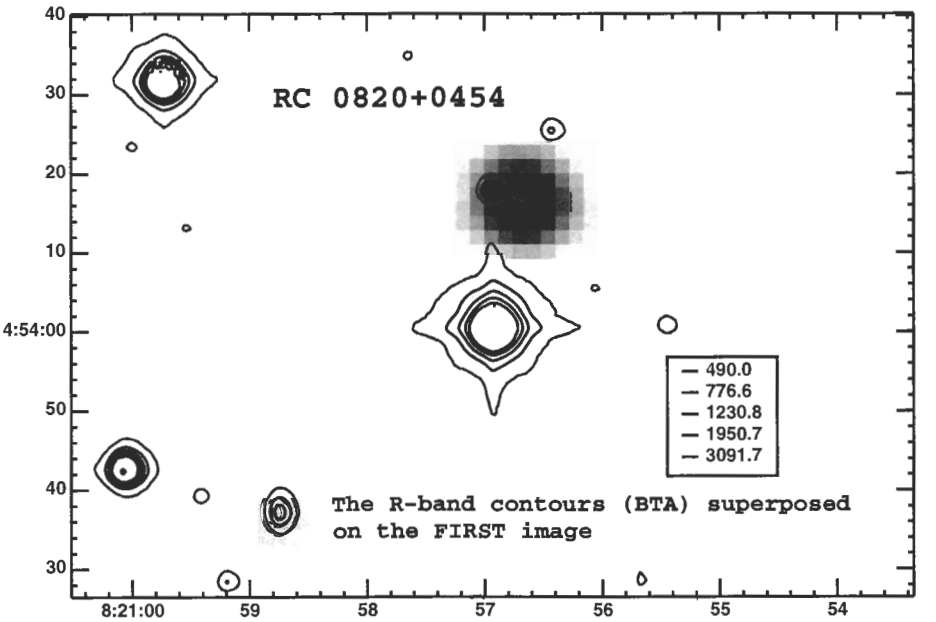
RC 0820+0454
490.0
776.6
1230.8
1950.7
3091.7
The R-band contours (BTA) superposed
on the FIRST image
40
30
20
10
4:54:00
50
40
30
8:21:00
59
58
57
56
55
54

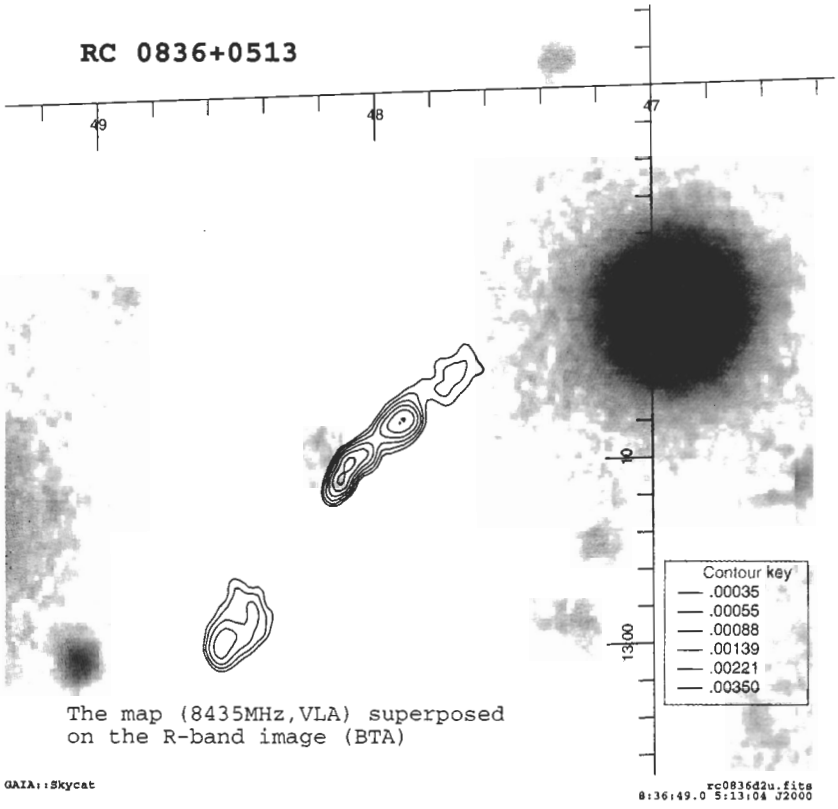
RC 0836+0513
49
48
47
10
13:00
Contour key
.00035
.00055
.00088
.00139
.00221
.00350
The map (8435MHz,VLA) superposed
on the R-band image (BTA)
GAIA::Skycat
rc0836d2u.fits
8:36:49.0 5:13:04 J2000
zhe
Jul 17, 1980 at 12:13:32

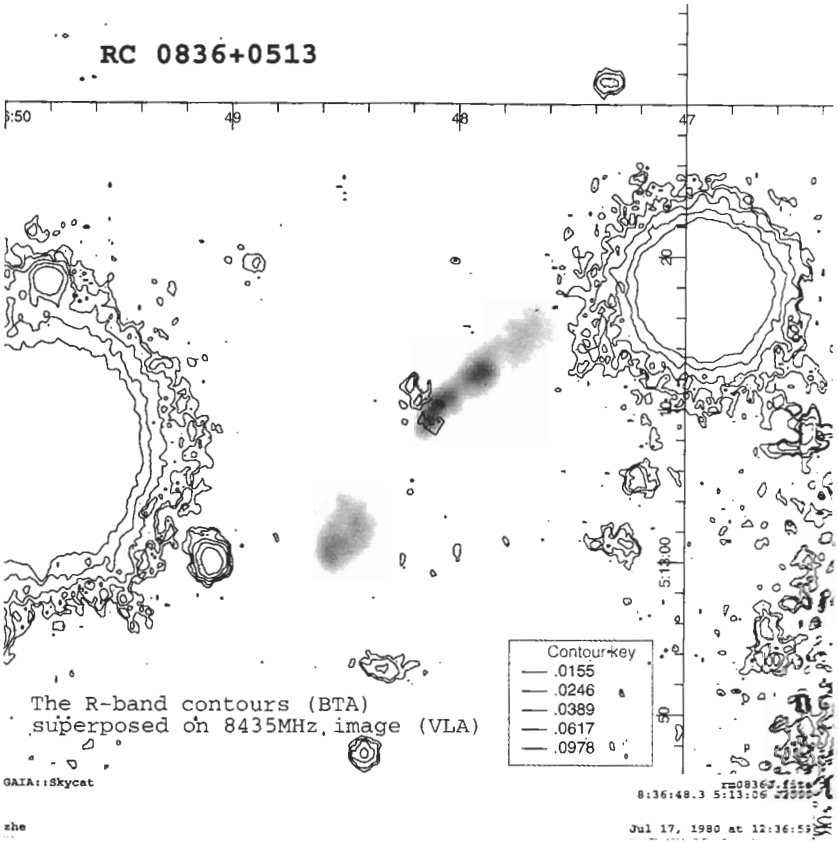
RC 0836+0513
:50
49
48
47
20
5:13:00
50
Contour key
.0155
.0246
.0389
.0617
.0978
The R-band contours (BTA)
superposed on 8435MHz image (VLA)
GAIA::Skycat
8:36:48.3 5:13:05
zhe
Jul 17, 1980 at 12:36:5

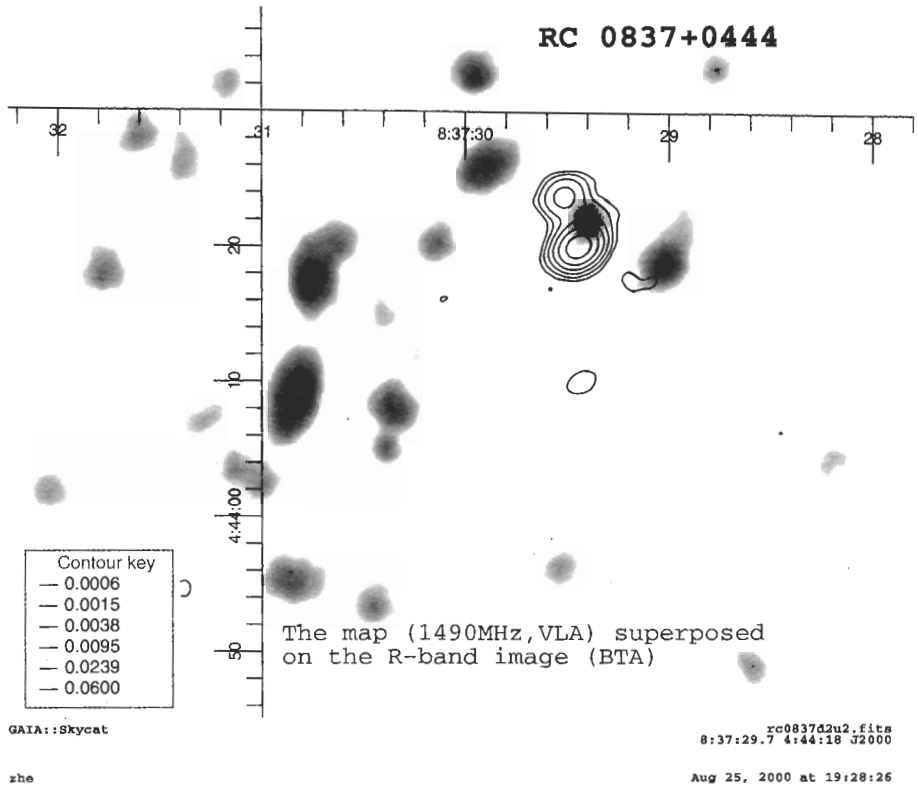
RC 0837+0444
32
31
8:37:30
29
28
20
10
4:44:00
50
Contour key
— 0.0006
— 0.0015
— 0.0038
— 0.0095
— 0.0239
— 0.0600
The map (1490MHz,VLA) superposed
on the R-band image (BTA)
GAIA::Skycat
rc0837d2u2.fits
8:37:29.7 4:44:18 J2000
zhe
Aug 25, 2000 at 19:28:26

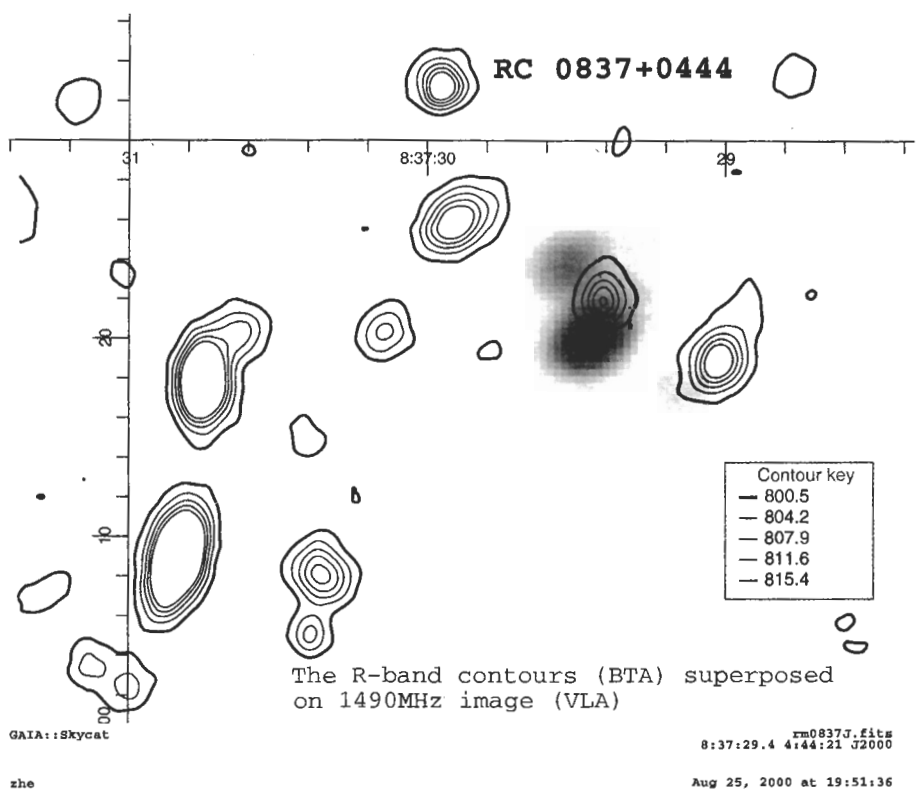
RC 0837+0444
31
8:37:30
29
20
10
00
Contour key
— 800.5
— 804.2
— 807.9
— 811.6
— 815.4
The R-band contours (BTA) superposed
on 1490MHz image (VLA)
GAIA::Skycat
rm0837J.fits
8:37:29.4 4:44:21 J2000
zhe
Aug 25, 2000 at 19:51:36

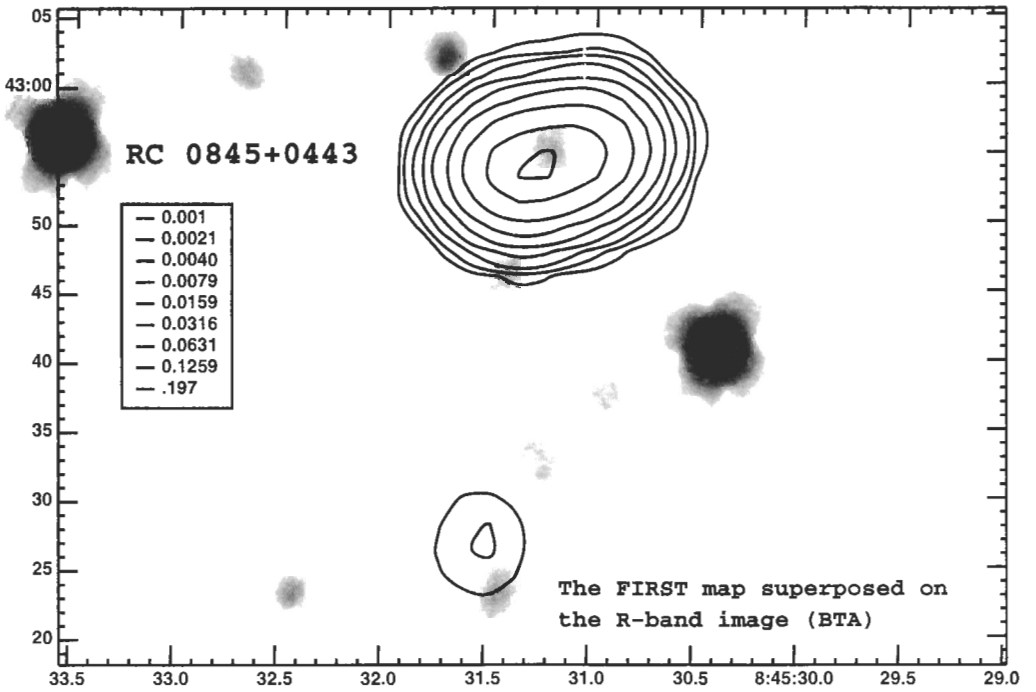
RC 0845+0443
0.001
0.0021
0.0040
0.0079
0.0159
0.0316
0.0631
0.1259
.197
The FIRST map superposed on
the R-band image (BTA)
05
43:00
50
45
40
35
30
25
20
33.5
33.0
32.5
32.0
31.5
31.0
30.5
8:45:30.0
29.5
29.0

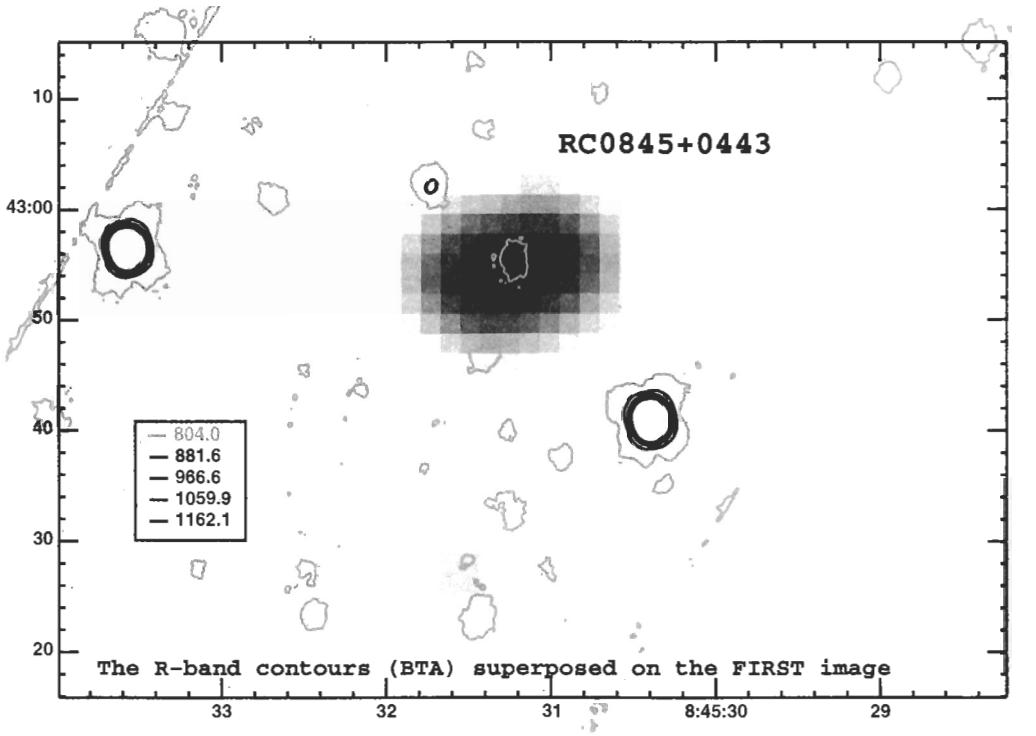
RC0845+0443
804.0
881.6
966.6
1059.9
1162.1
The R-band contours (BTA) superposed on the FIRST image
10
43:00
50
40
30
20
33
32
31
8:45:30
29

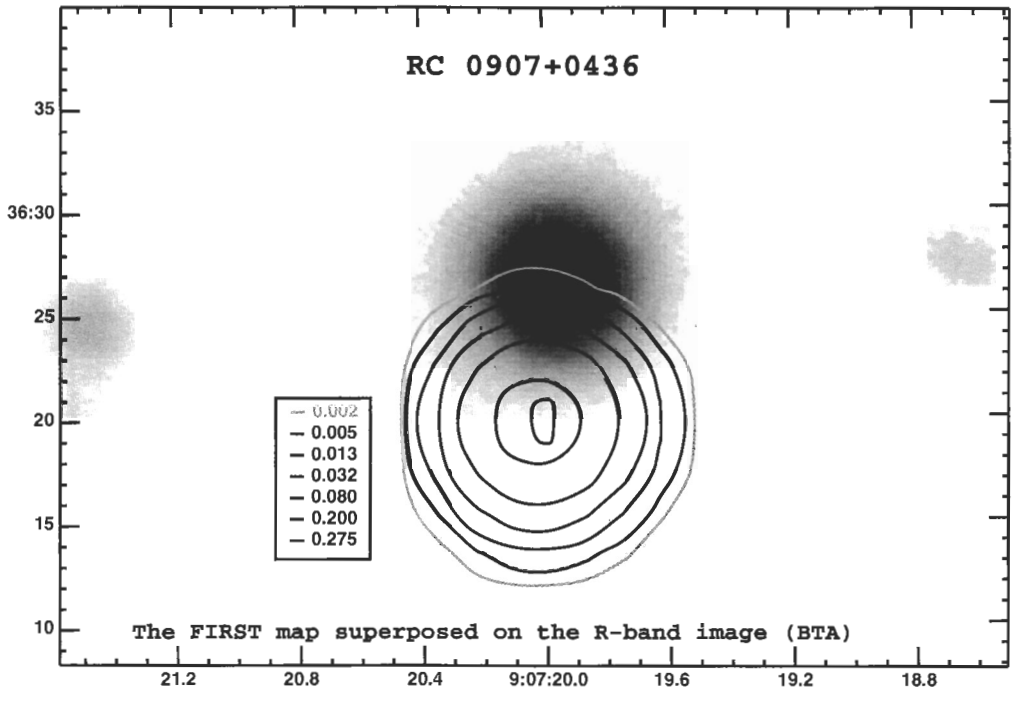
RC 0907+0436
35
36:30
25
20
15
10
0.002
0.005
0.013
0.032
0.080
0.200
0.275
The FIRST map superposed on the R-band image (BTA)
21.2
20.8
20.4
9:07:20.0
19.6
19.2
18.8

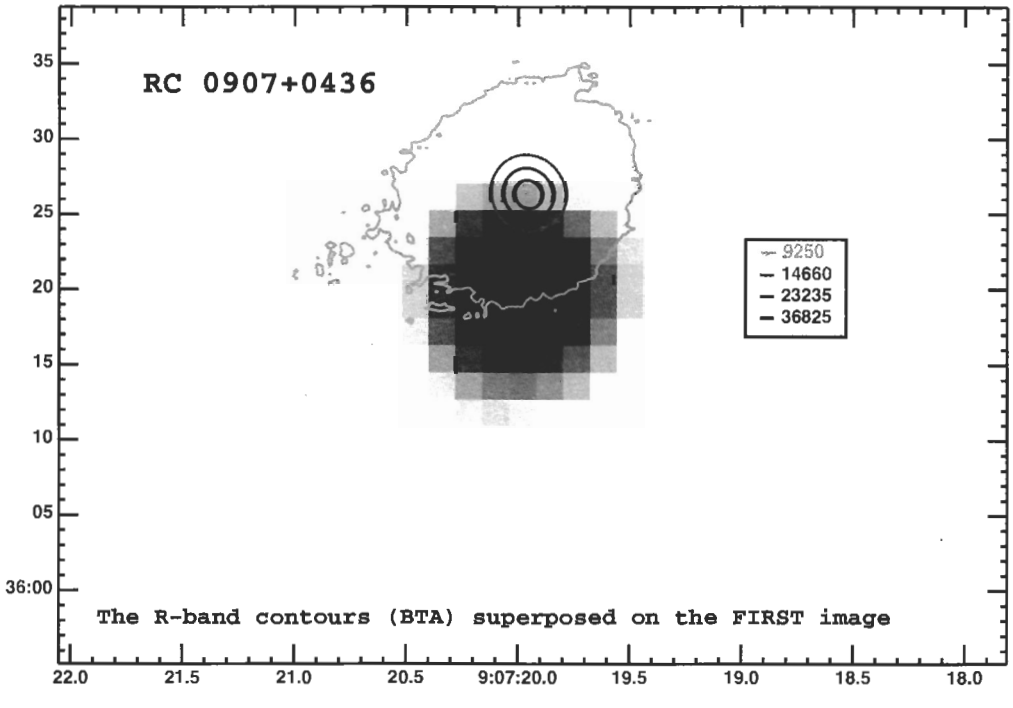
RC 0907+0436
35
30
25
20
15
10
05
36:00
9250
14660
23235
36825
The R-band contours (BTA) superposed on the FIRST image
22.0
21.5
21.0
20.5
9:07:20.0
19.5
19.0
18.5
18.0

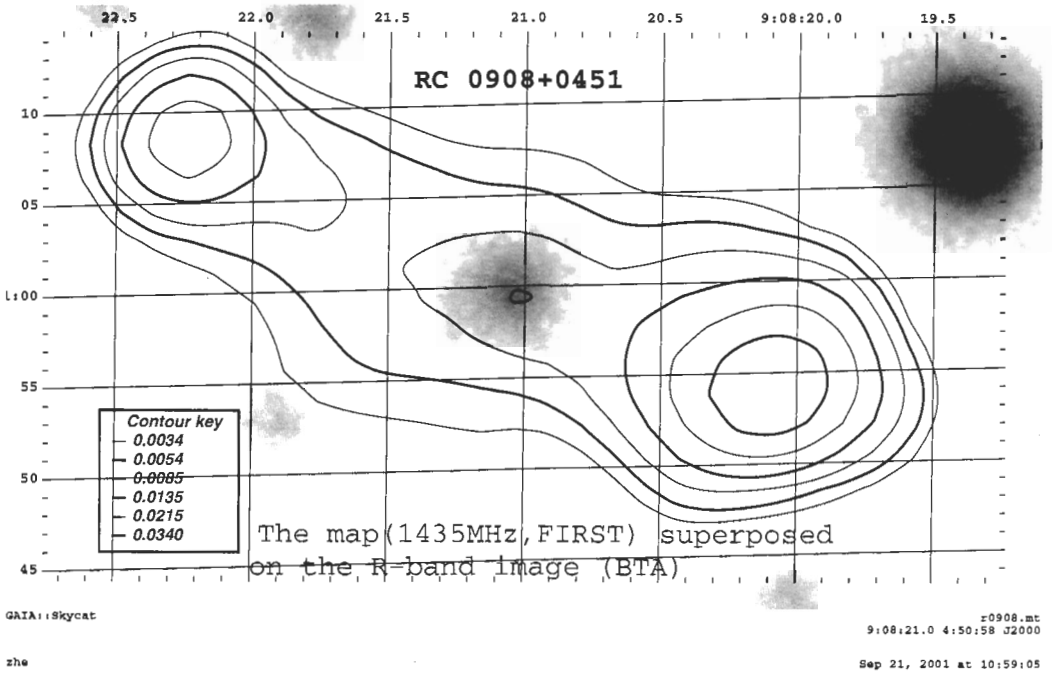
RC 0908+0451
22.5
22.0
21.5
21.0
20.5
9:08:20.0
19.5
10
05
1:00
55
50
45
Contour key
0.0034
0.0054
0.0085
0.0135
0.0215
0.0340
The map(1435MHz,FIRST) superposed
on the R-band image (BTA)
GAIA::Skycat
zhe
r0908.mt
9:08:21.0 4:50:58 J2000
Sep 21, 2001 at 10:59:05

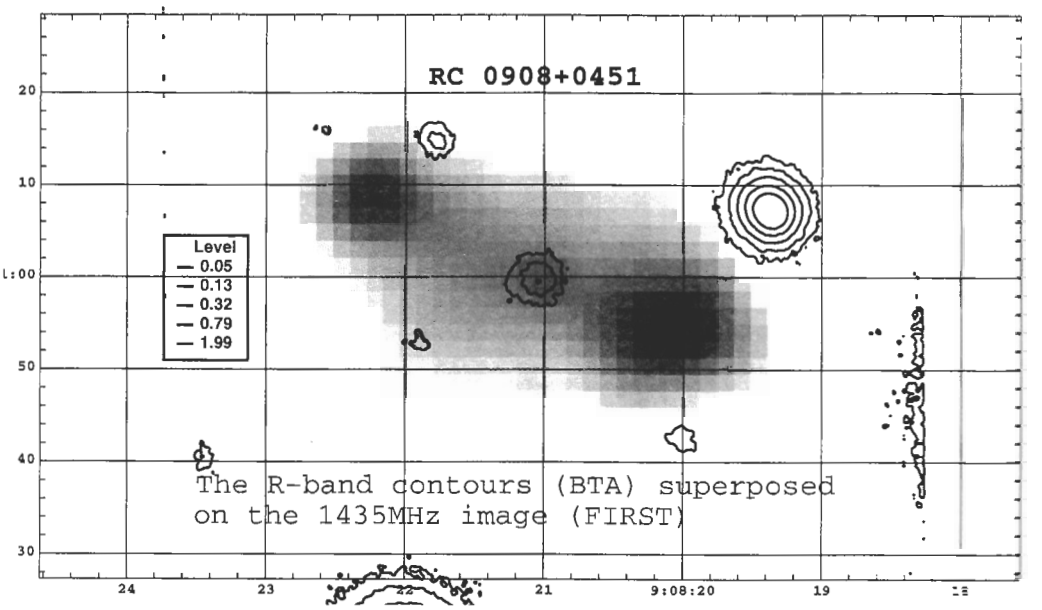
RC 0908+0451
20
10
1:00
50
40
30
Level
0.05
0.13
0.32
0.79
1.99
The R-band contours (BTA) superposed
on the 1435MHz image (FIRST)
24
23
22
21
9:08:20
19

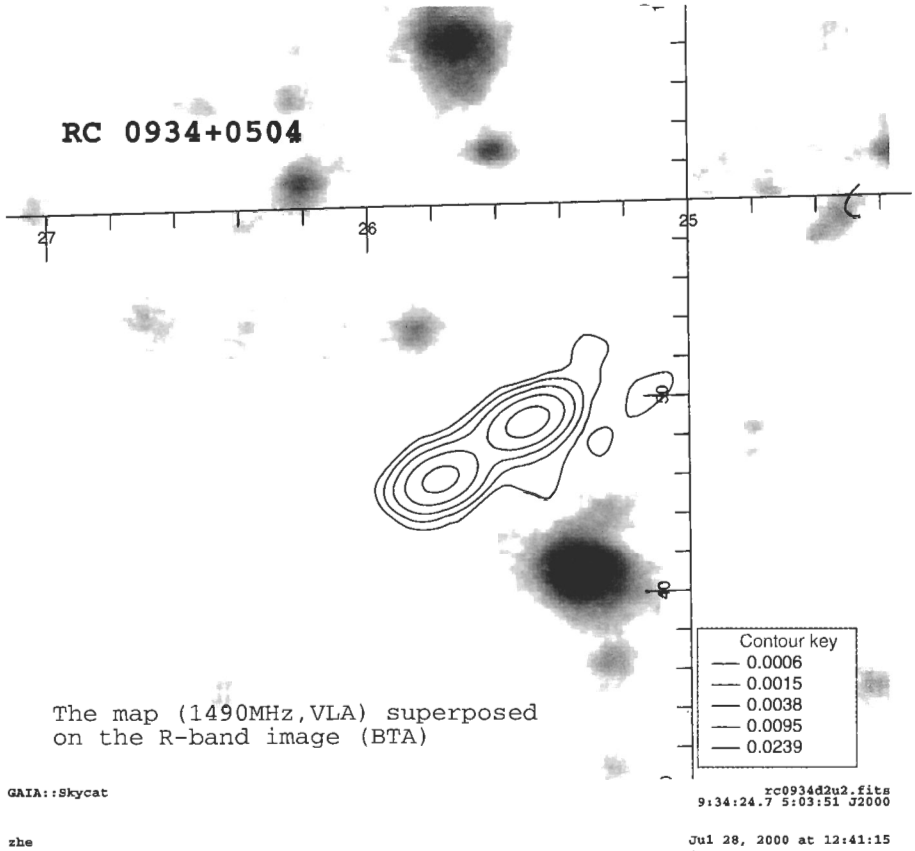

The map (1490MHz,VLA) superposed on the R-band image (BTA)

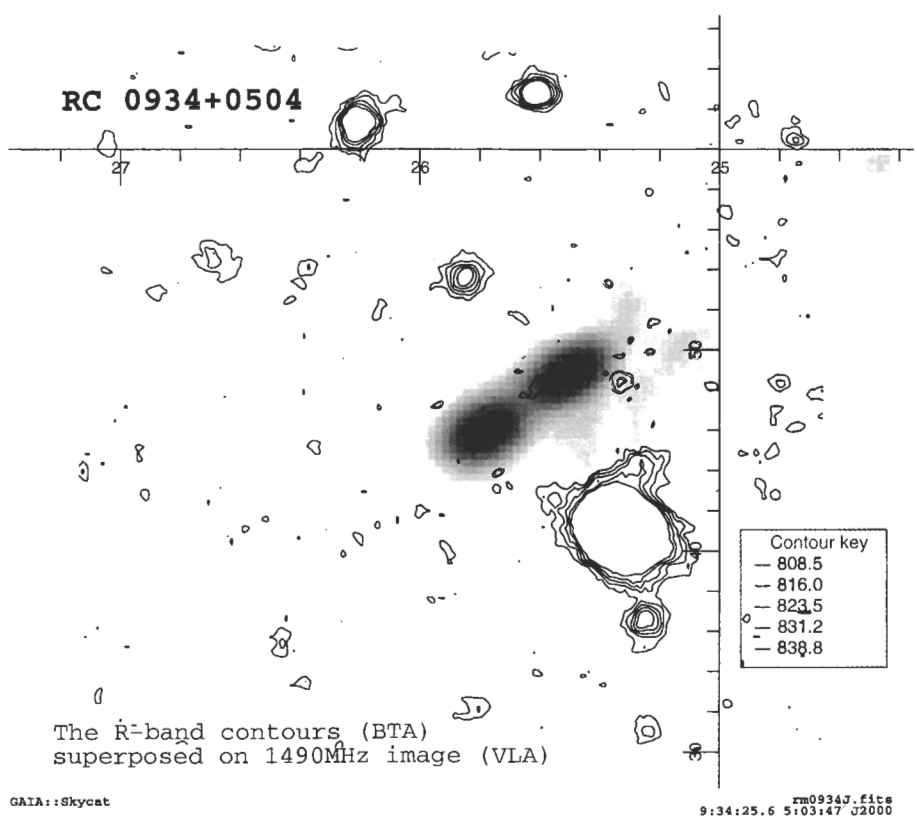

The R-band contours (BTA) superposed on 1490MHz image (VLA)

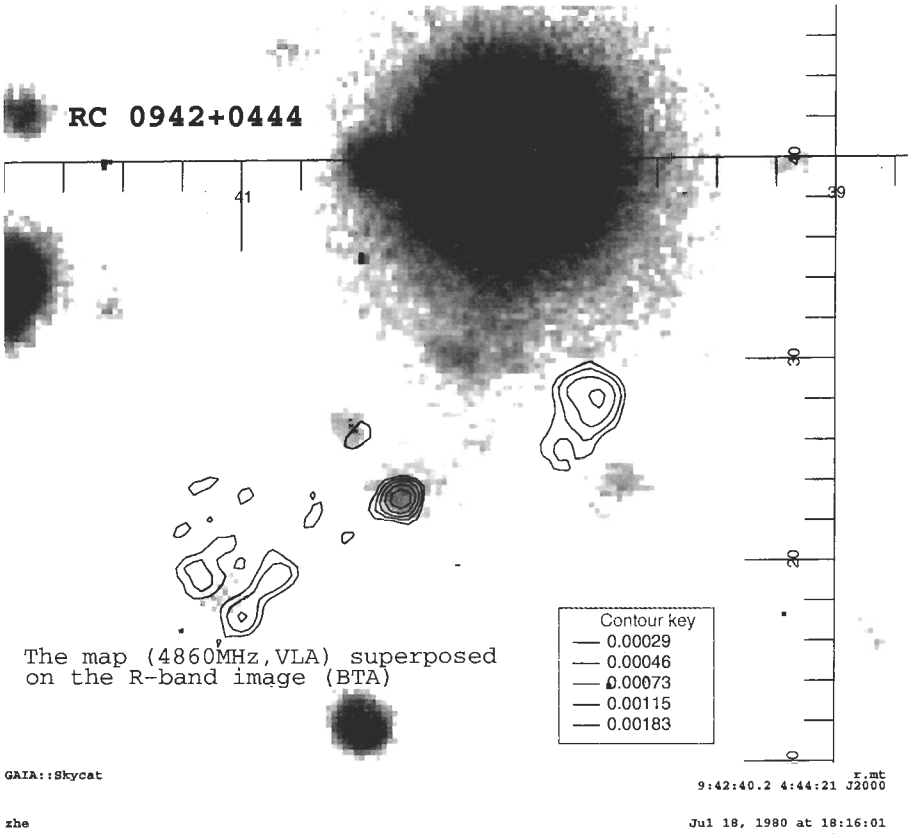

The map (4860MHz,VLA) superposed on the R-band image (BTA)

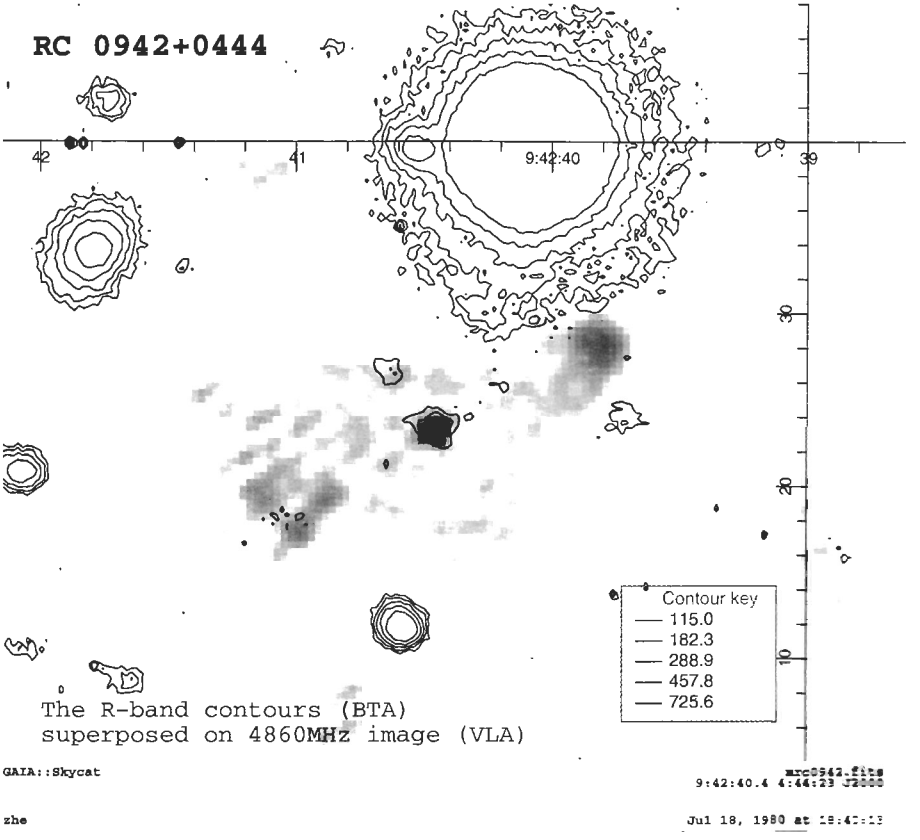

The R-band contours (BTA) superposed on 4860MHz image (VLA)

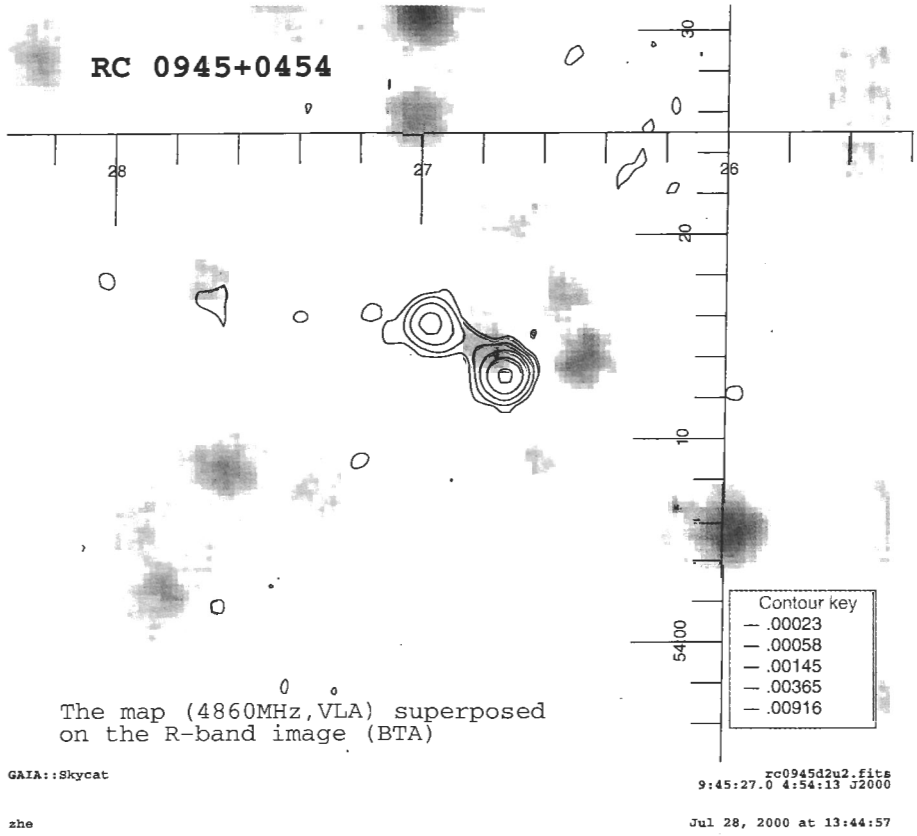

The map (4860MHz,VLA) superposed on the R-band image (BTA)

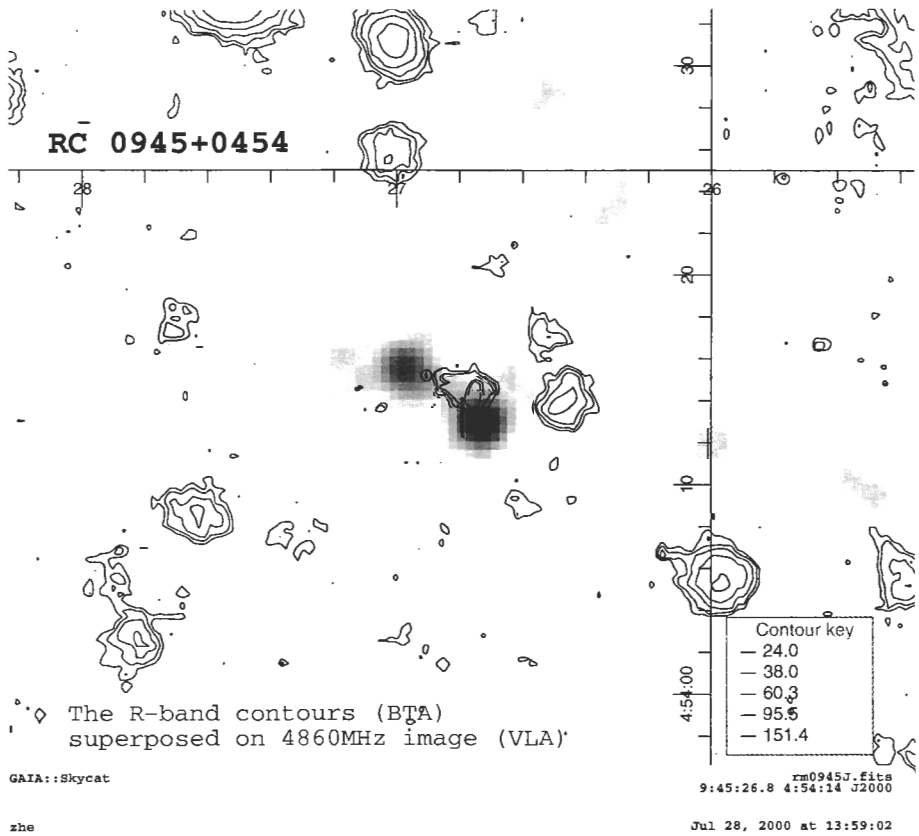

The R-band contours (BTA) superposed on 4860MHz image (VLA)

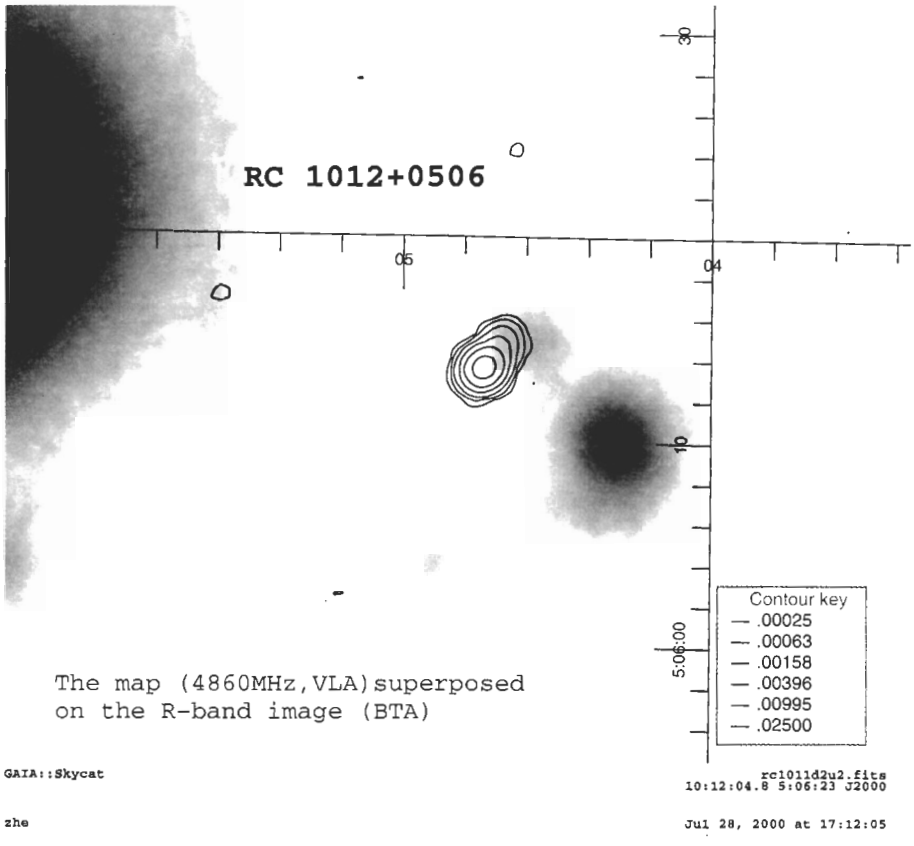

The map (4860MHz, VLA) superposed on the R-band image (BTA)

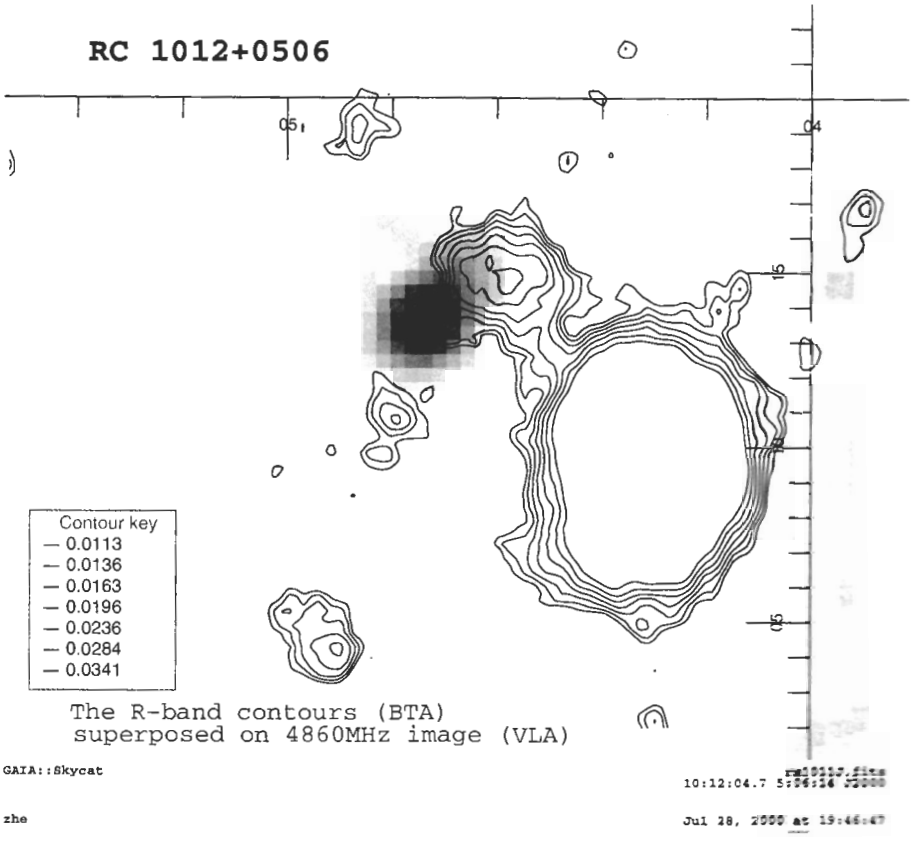

The R-band contours (BTA) superposed on 4860MHz image (VLA)

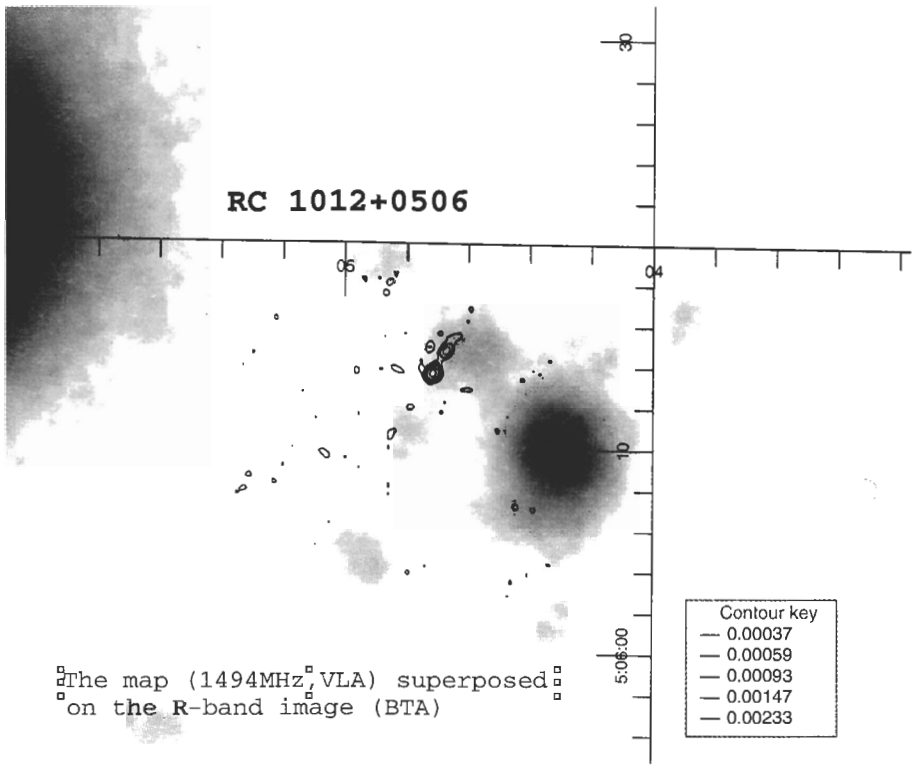

The map (1494MHz, VLA) superposed on the R-band image (BTA)

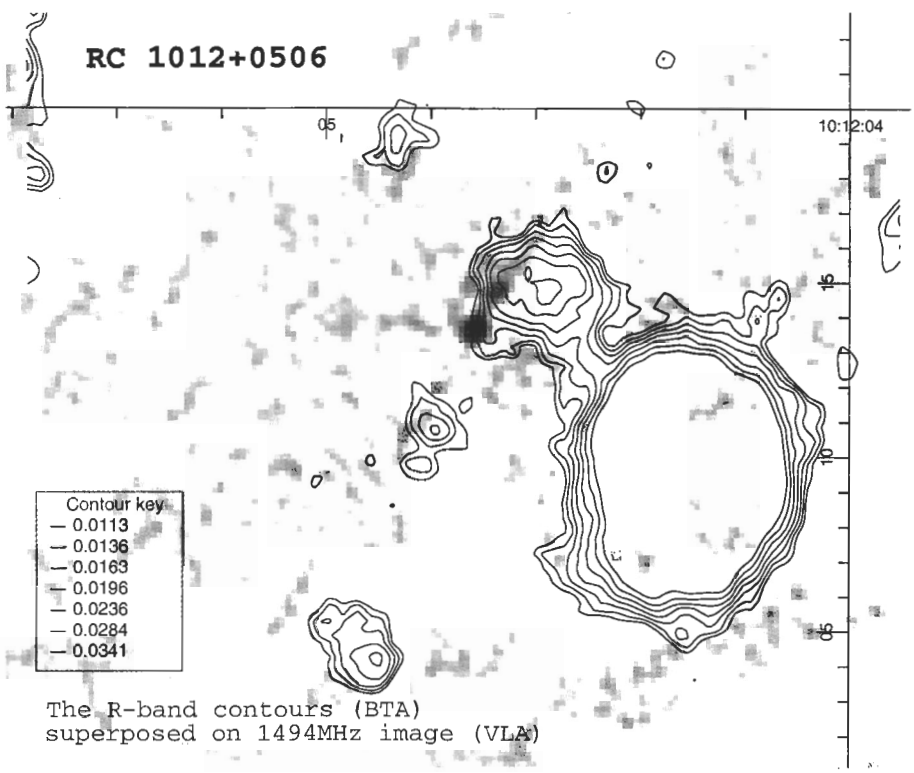

The R-band contours (BTA) superposed on 1494MHz image (VLA)

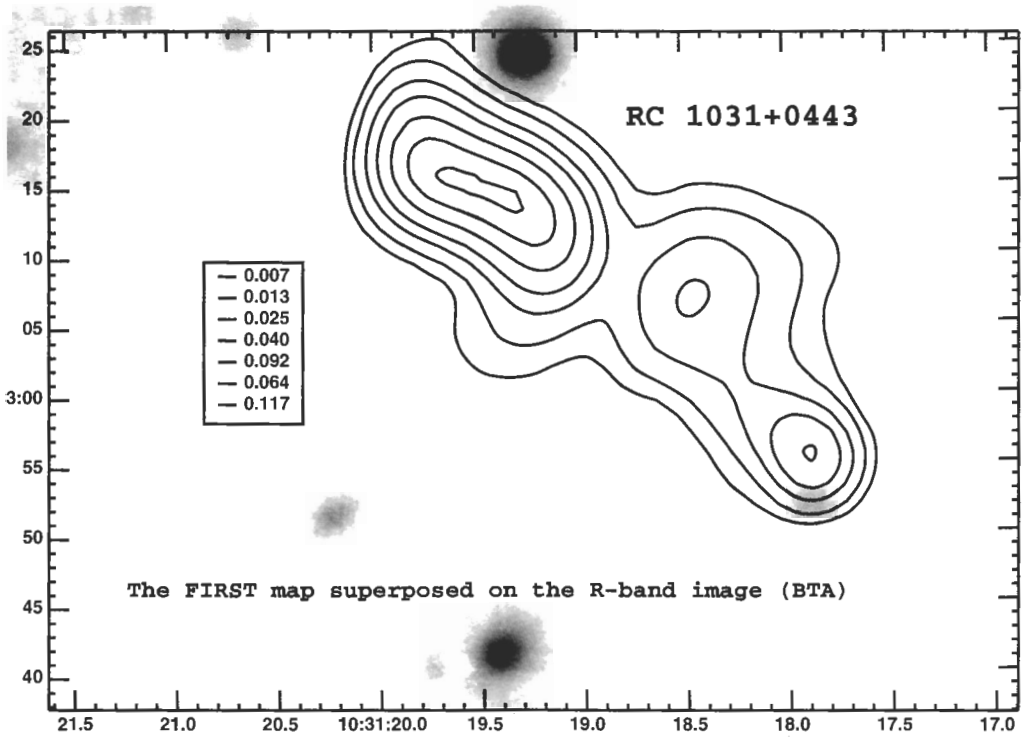

The FIRST map superposed on the R-band image (BTA)

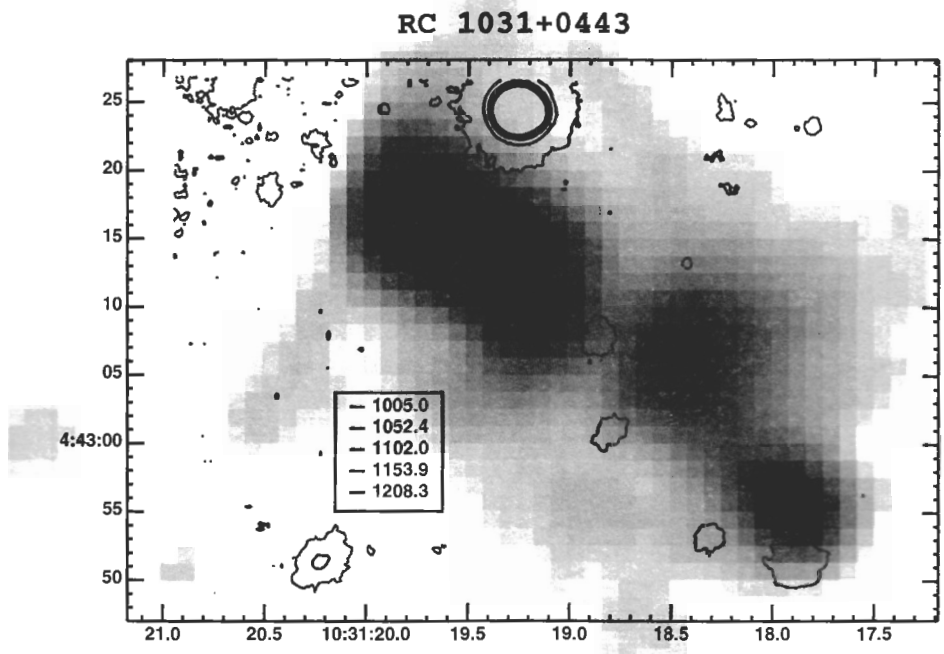

The R-band contours (BTA) superposed on the FIRST image

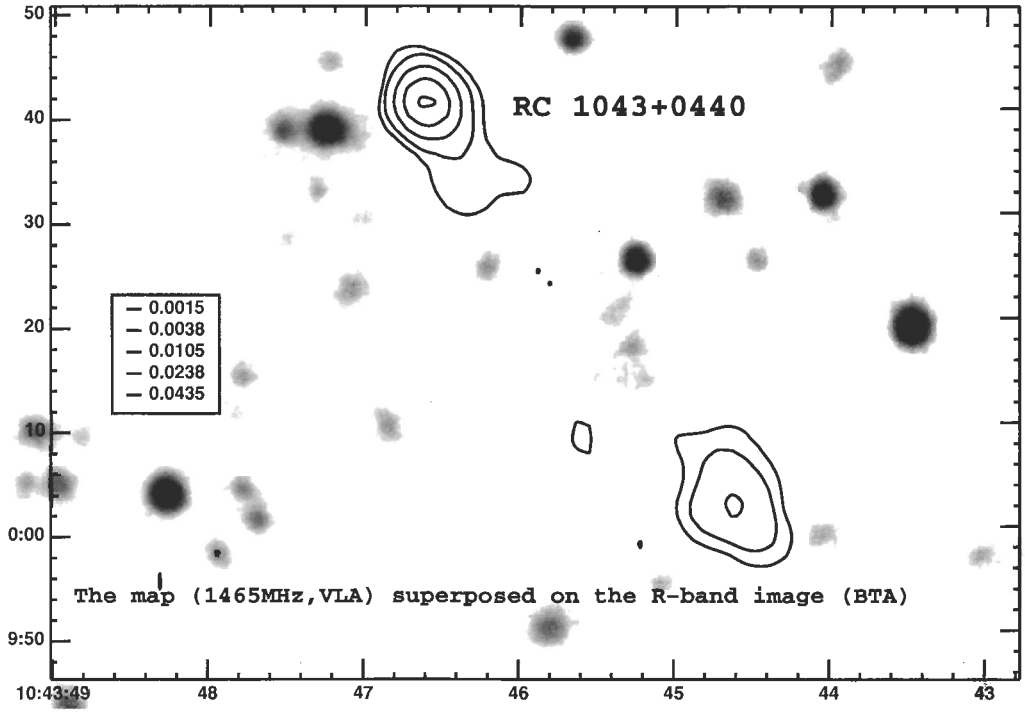

The map (1465MHz,VLA) superposed on the R-band image (BTA)

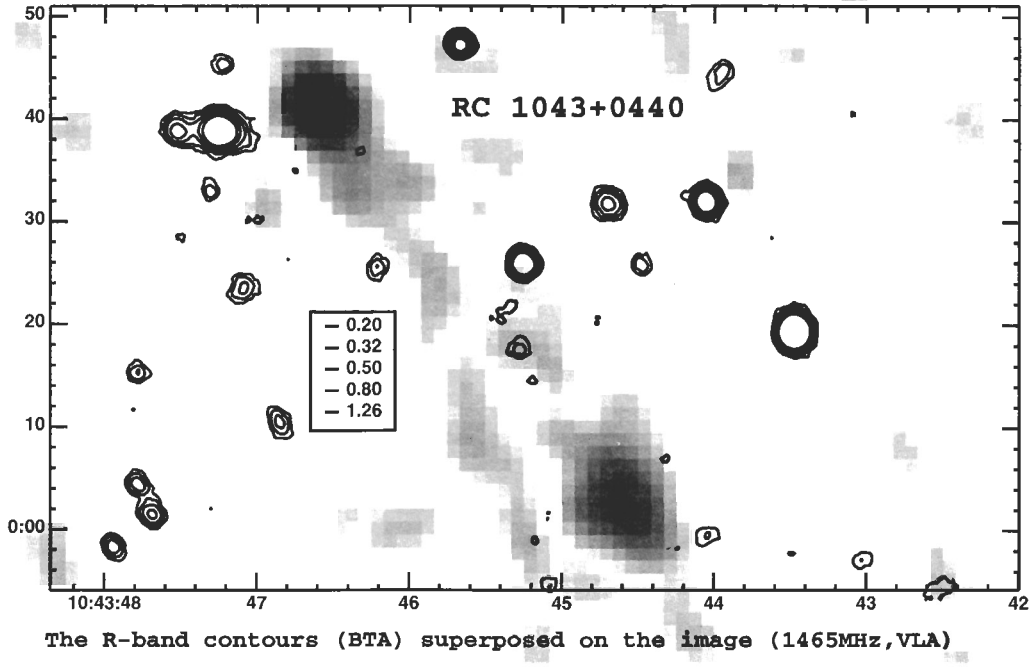

The R-band contours (BTA) superposed on the image (1465MHz,VLA)

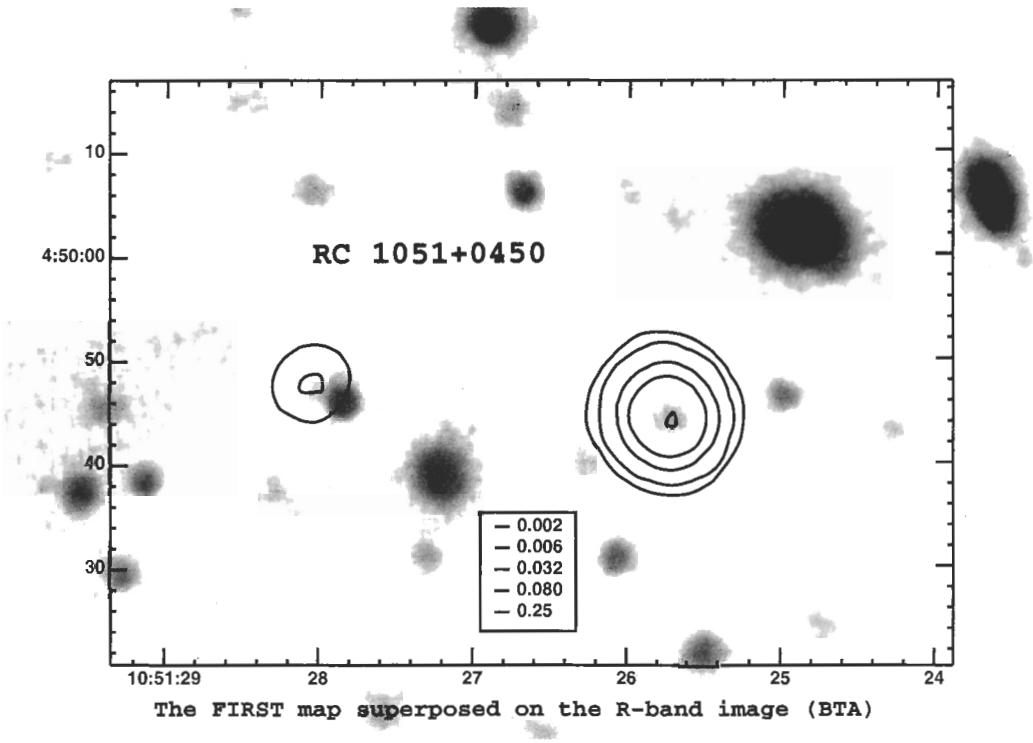

The FIRST map superposed on the R-band image (BTA)

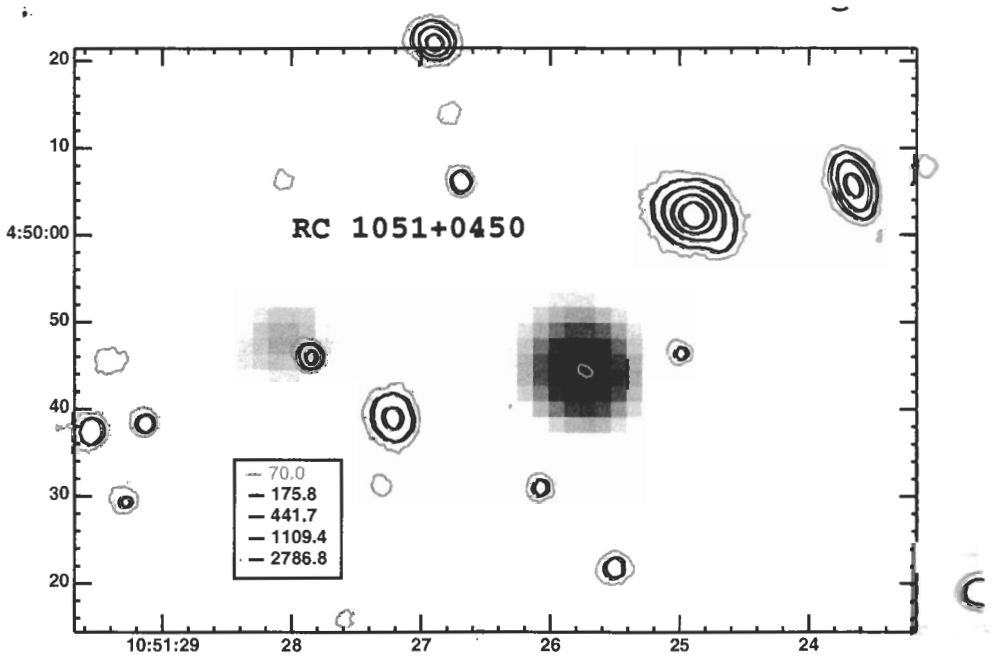

The R-band contours (BTA) superposed on the FIRST image

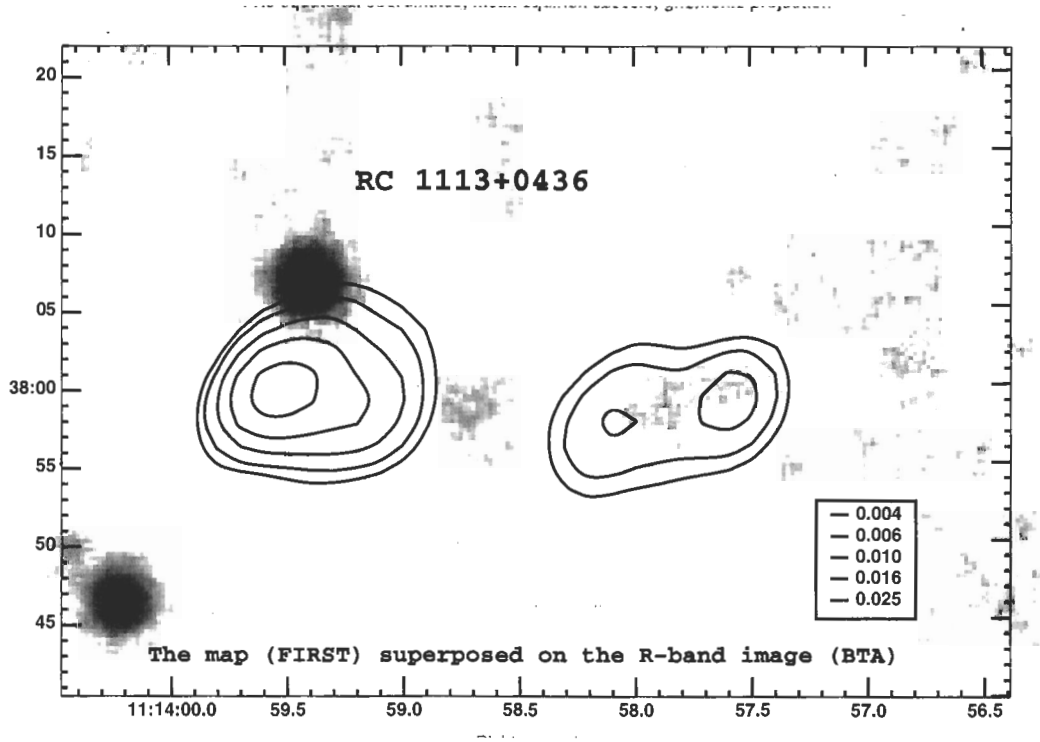
RC 1113+0436
0.004
0.006
0.010
0.016
0.025
The map (FIRST) superposed on the R-band image (BTA)
20
15
10
05
38:00
55
50
45
11:14:00.0
59.5
59.0
58.5
58.0
57.5
57.0
56.5

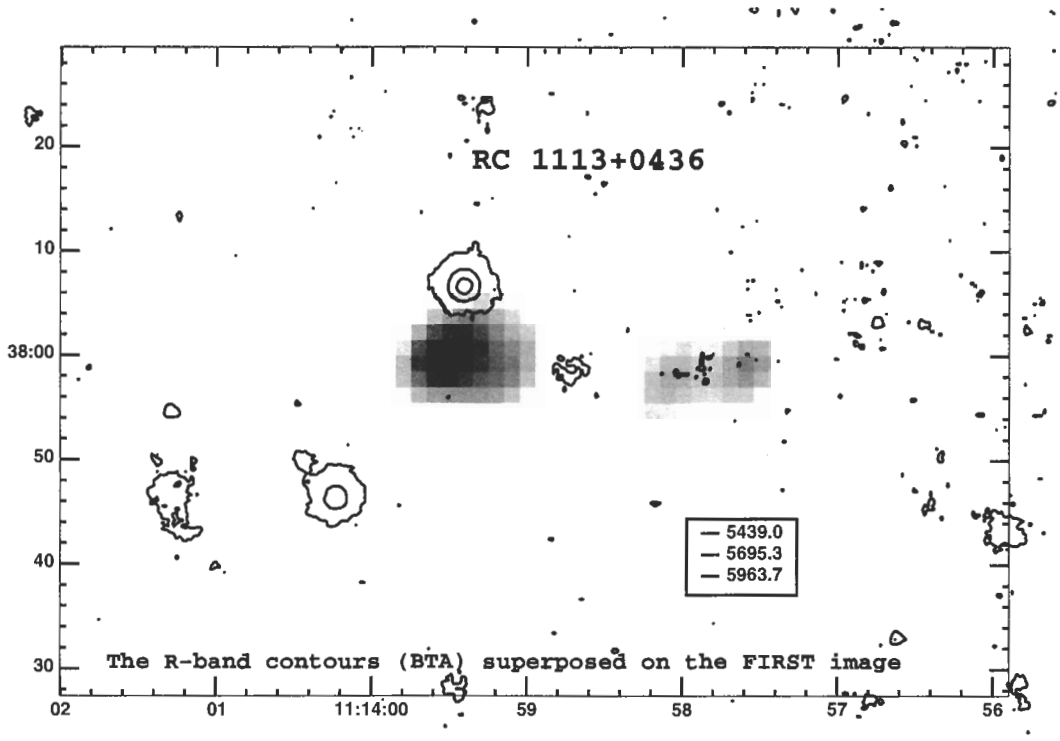
RC 1113+0436
5439.0
5695.3
5963.7
The R-band contours (BTA) superposed on the FIRST image
20
10
38:00
50
40
30
02
01
11:14:00
59
58
57
56

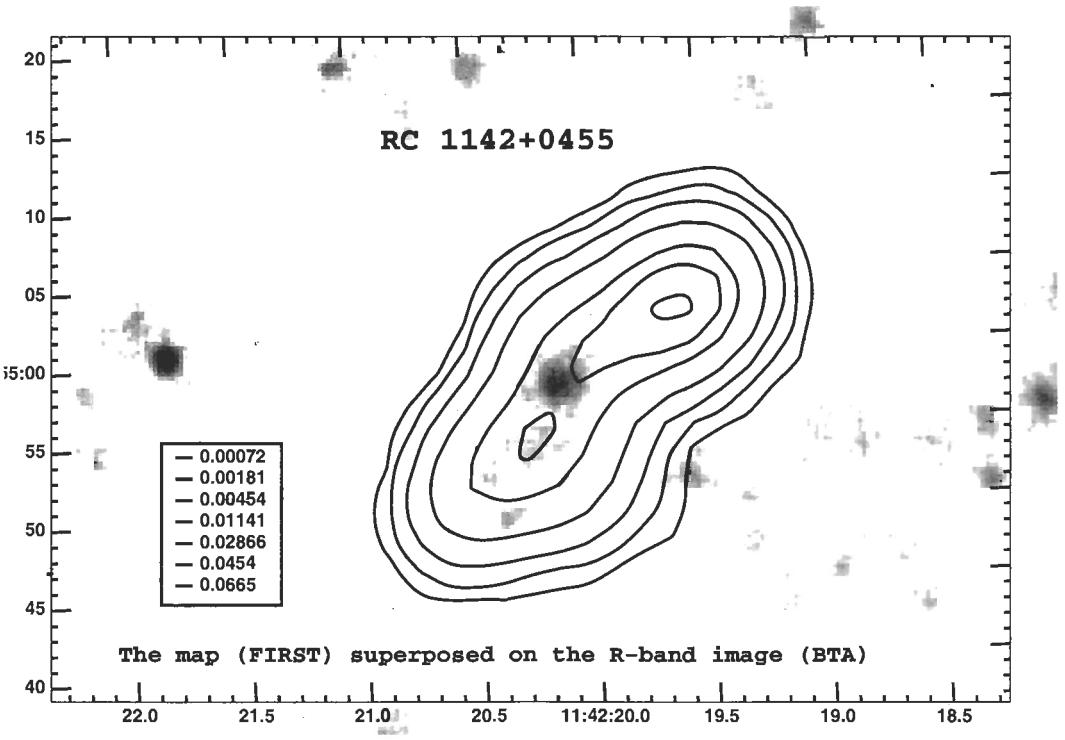
RC 1142+0455
0.00072
0.00181
0.00454
0.01141
0.02866
0.0454
0.0665
The map (FIRST) superposed on the R-band image (BTA)
20
15
10
05
55:00
55
50
45
40
22.0
21.5
21.0
20.5
11:42:20.0
19.5
19.0
18.5

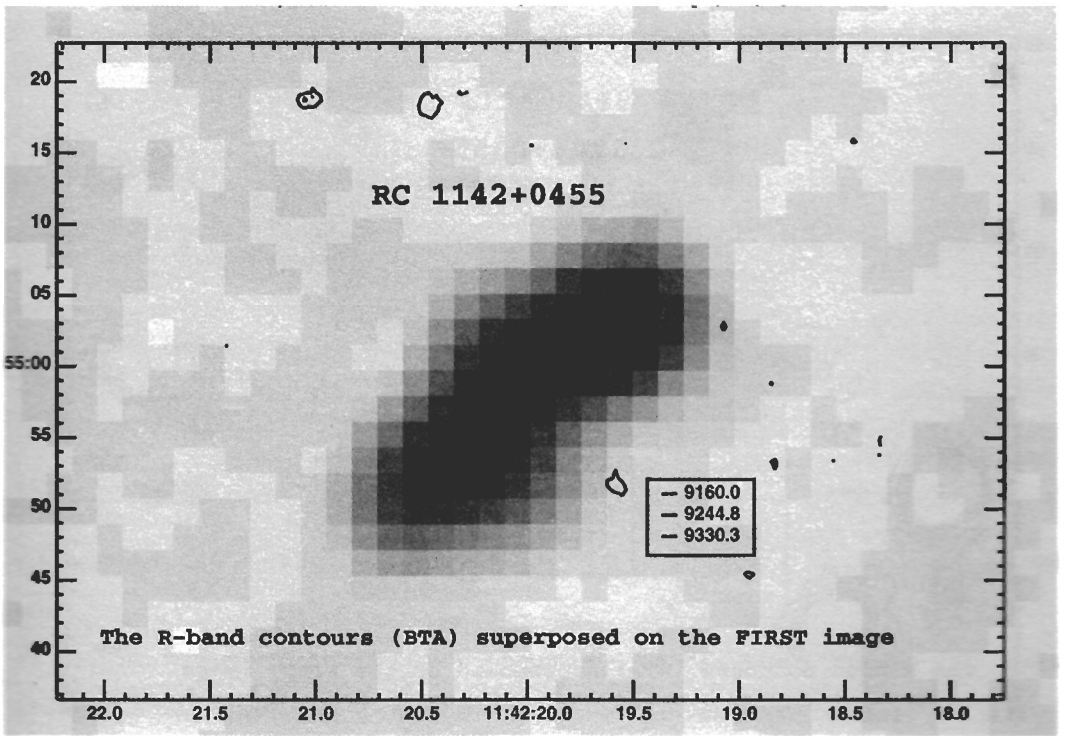
RC 1142+0455
9160.0
9244.8
9330.3
The R-band contours (BTA) superposed on the FIRST image
20
15
10
05
55:00
55
50
45
40
22.0
21.5
21.0
20.5
11:42:20.0
19.5
19.0
18.5
18.0

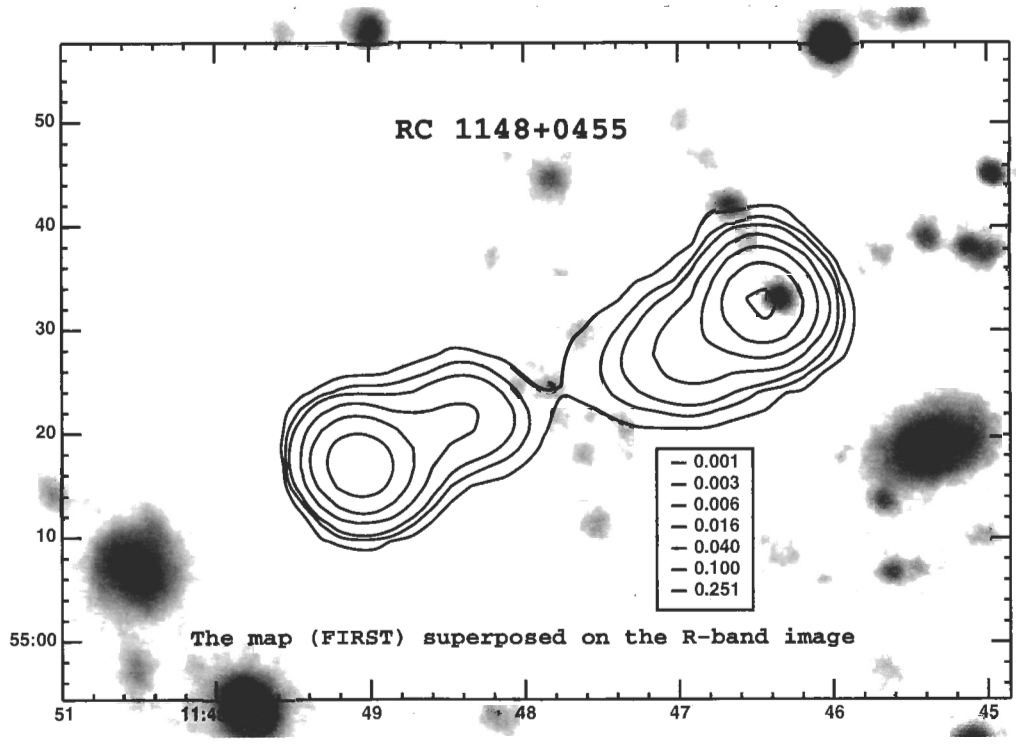
RC 1148+0455
— 0.001
— 0.003
— 0.006
— 0.016
— 0.040
— 0.100
— 0.251
The map (FIRST) superposed on the R-band image
50
40
30
20
10
55:00
51
49
48
47
46
45

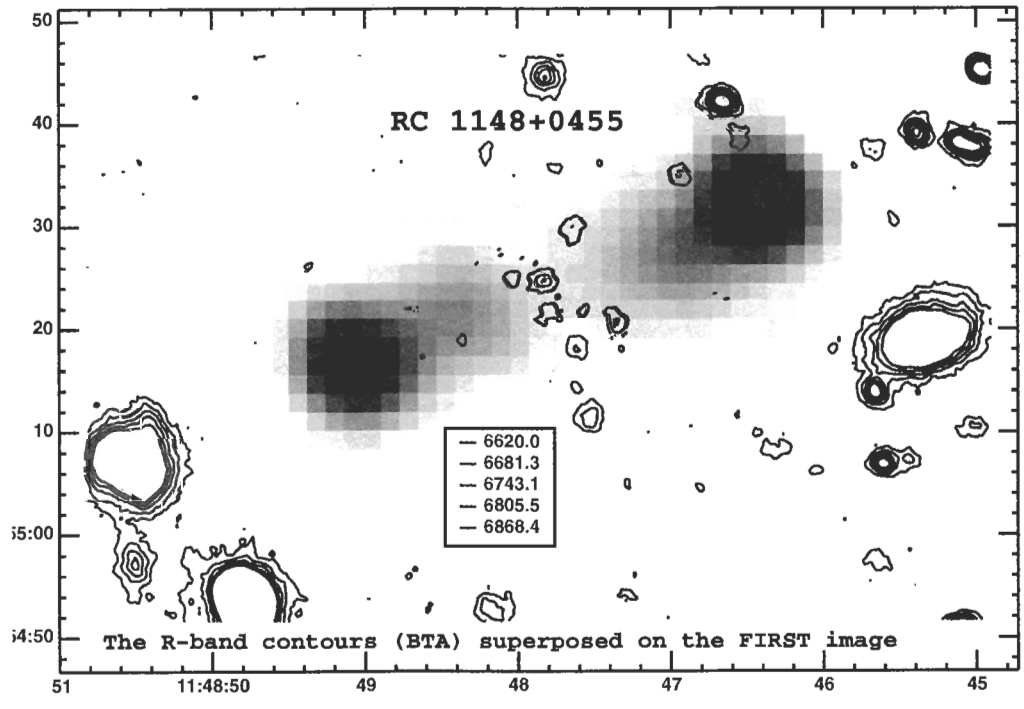
RC 1148+0455
— 6620.0
— 6681.3
— 6743.1
— 6805.5
— 6868.4
The R-band contours (BTA) superposed on the FIRST image
50
40
30
20
10
55:00
54:50
51
11:48:50
49
48
47
46
45

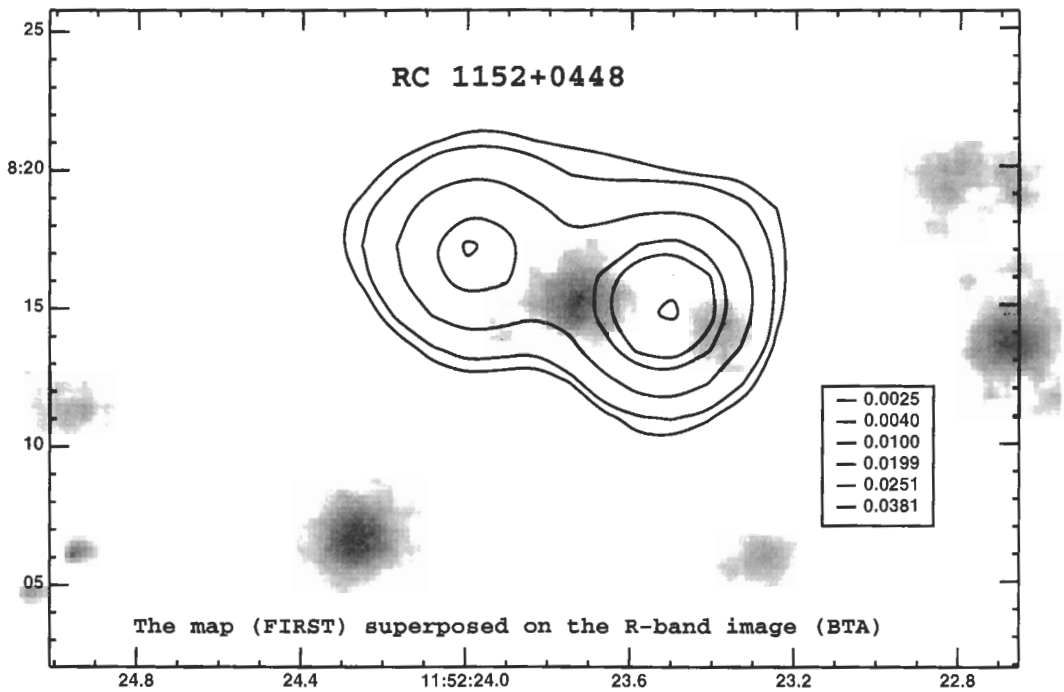
RC 1152+0448
— 0.0025
— 0.0040
— 0.0100
— 0.0199
— 0.0251
— 0.0381
The map (FIRST) superposed on the R-band image (BTA)
25
8:20
15
10
05
24.8
24.4
11:52:24.0
23.6
23.2
22.8

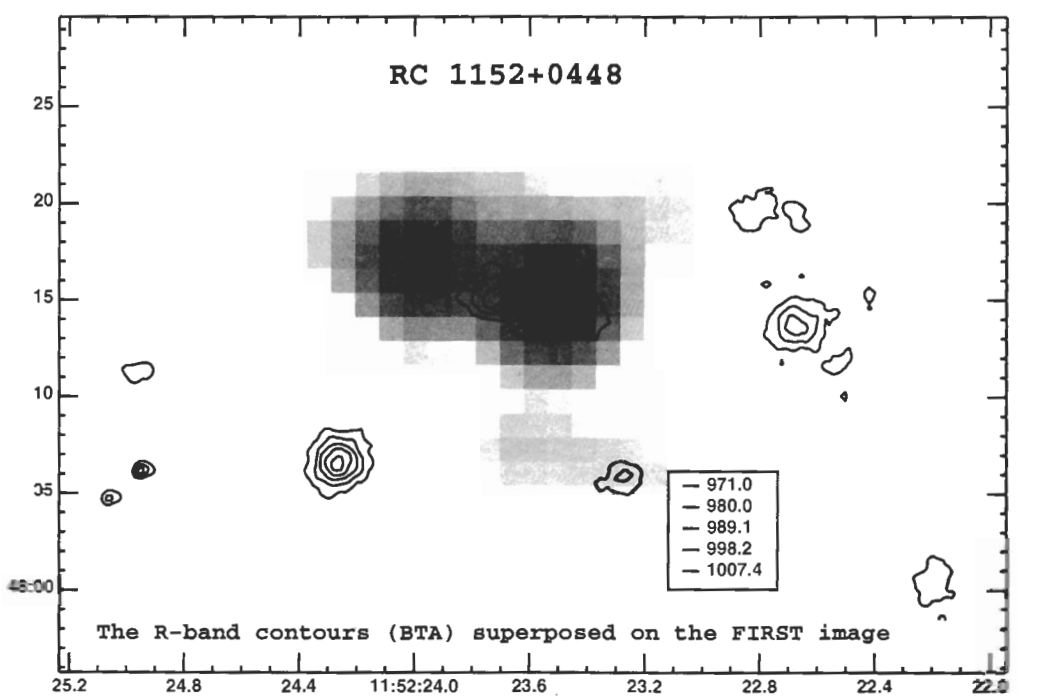
RC 1152+0448
— 971.0
— 980.0
— 989.1
— 998.2
— 1007.4
The R-band contours (BTA) superposed on the FIRST image
25
20
15
10
35
48:00
25.2
24.8
24.4
11:52:24.0
23.6
23.2
22.8
22.4
22.0

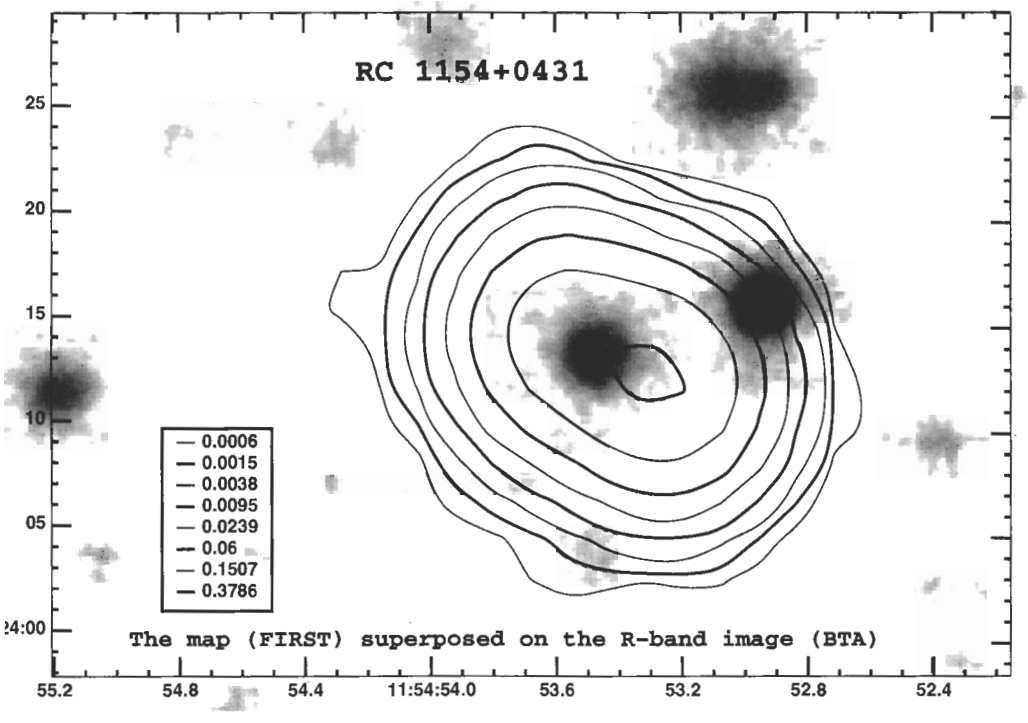
RC 1154+0431
0.0006
0.0015
0.0038
0.0095
0.0239
0.06
0.1507
0.3786
The map (FIRST) superposed on the R-band image (BTA)
25
20
15
10
05
24:00
55.2
54.8
54.4
11:54:54.0
53.6
53.2
52.8
52.4

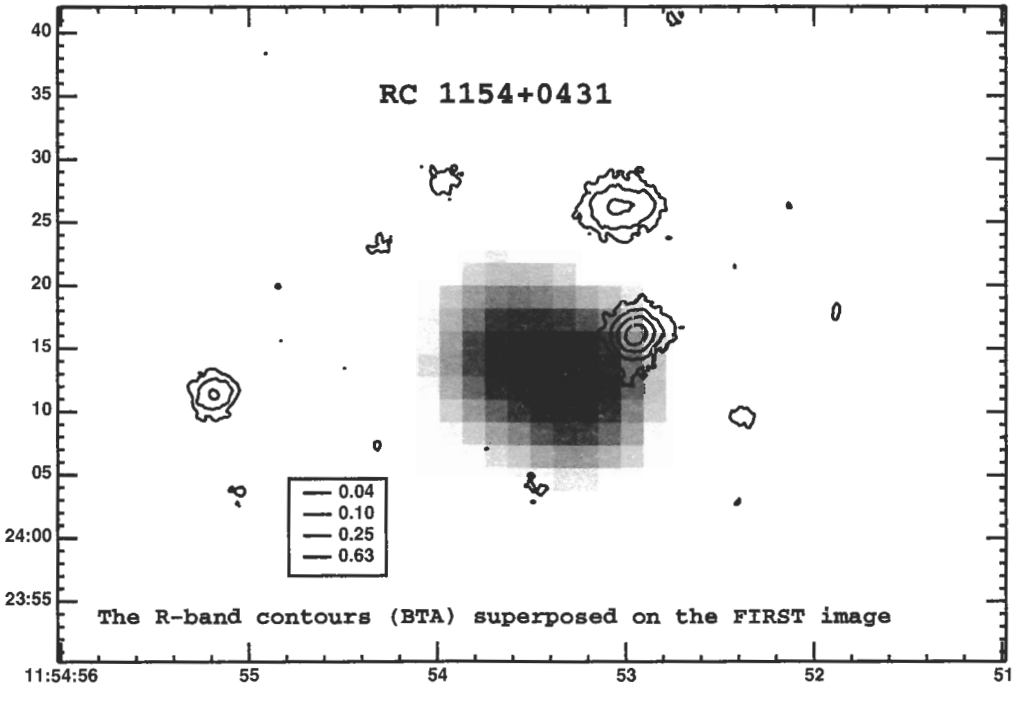
RC 1154+0431
0.04
0.10
0.25
0.63
The R-band contours (BTA) superposed on the FIRST image
40
35
30
25
20
15
10
05
24:00
23:55
11:54:56
55
54
53
52
51

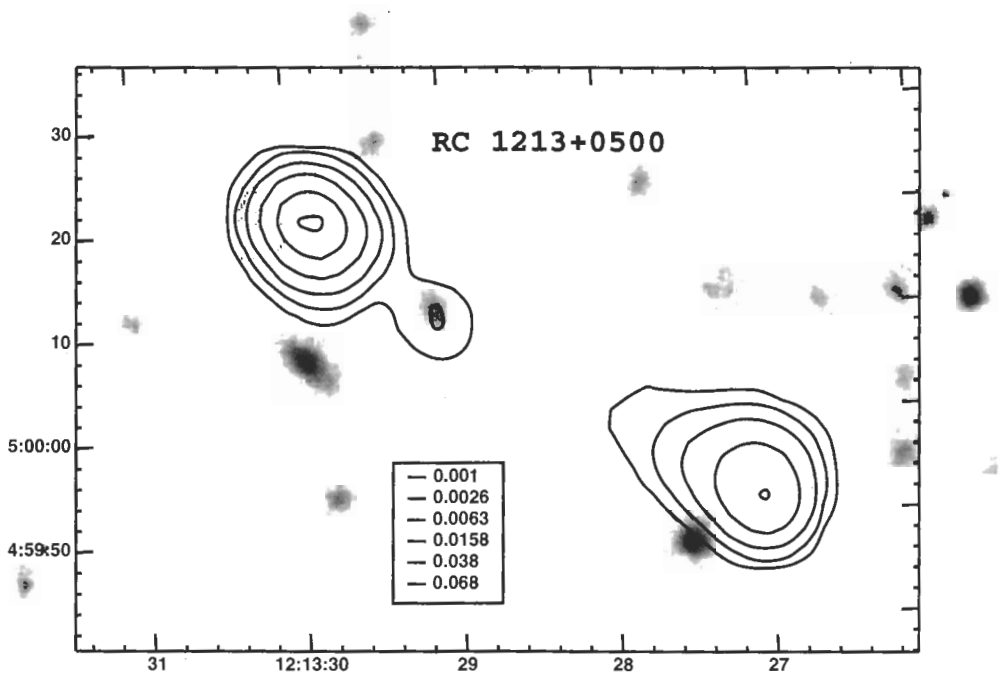

The FIRST map superposed on the R-band image (BTA)

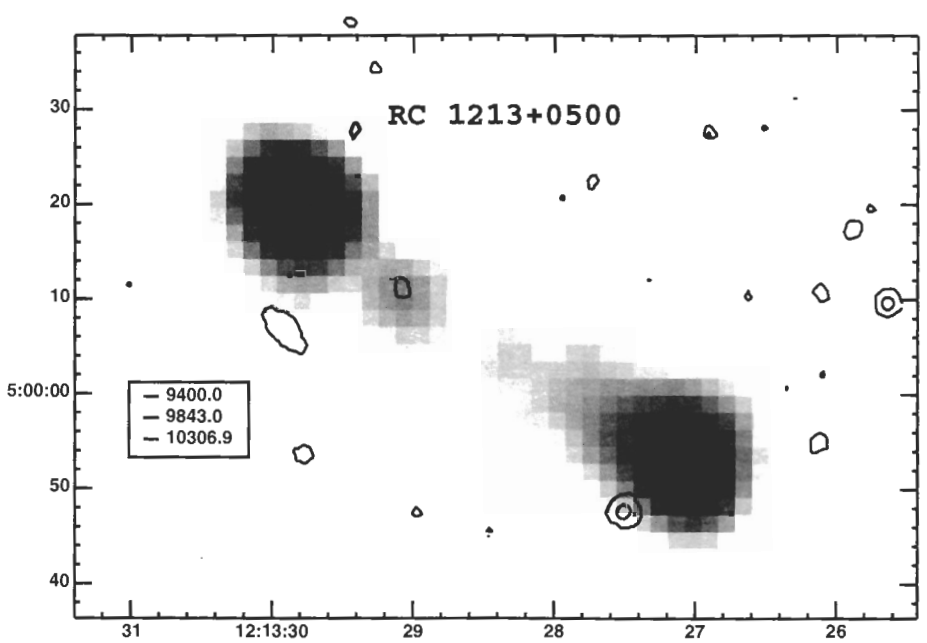

The R-band contours (BTA) superposed on the FIRST map

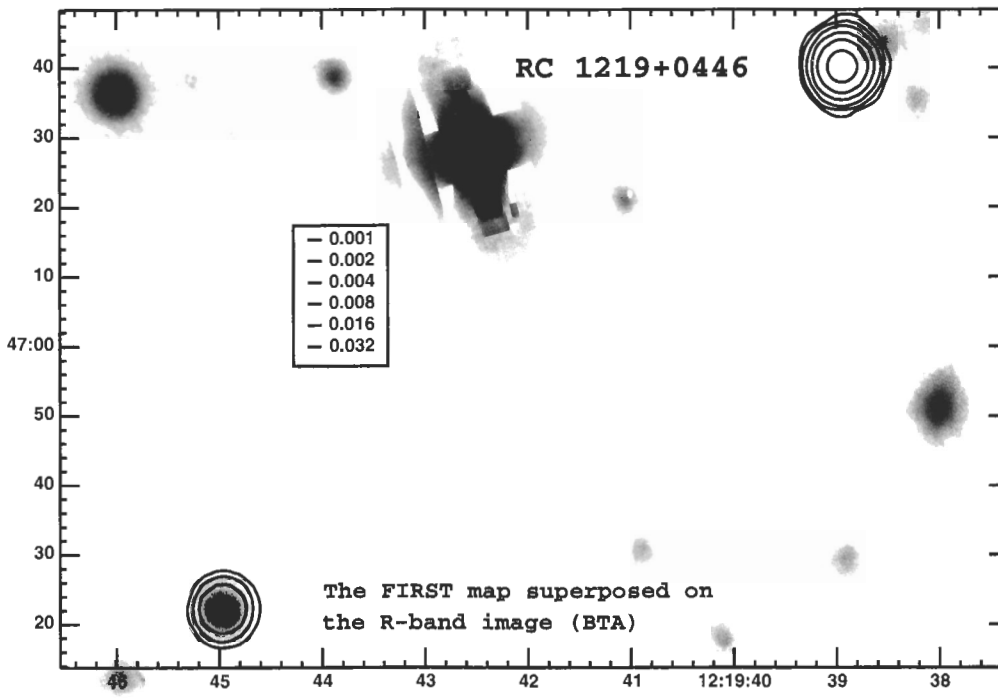

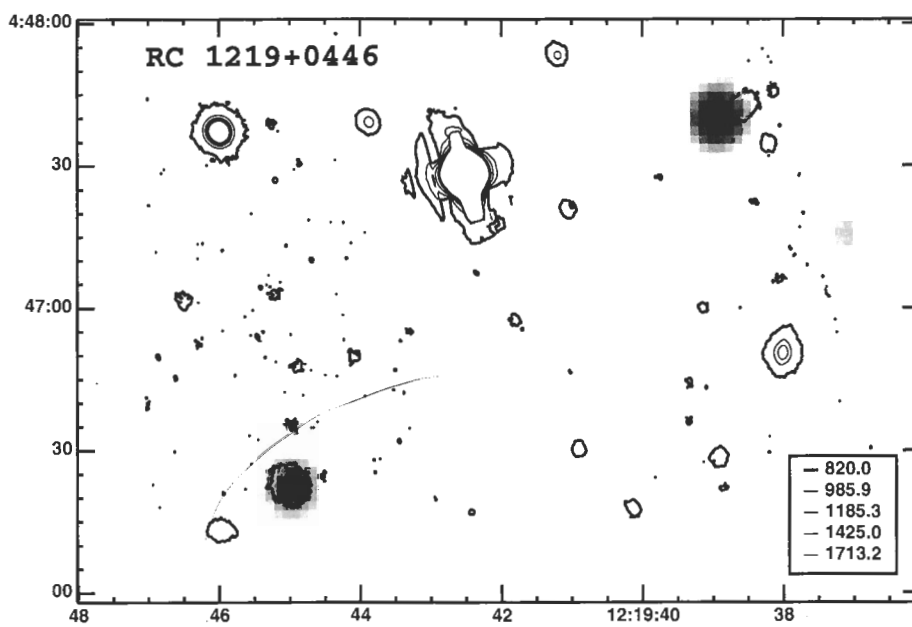

The R-band contours superposed on the FIRST image

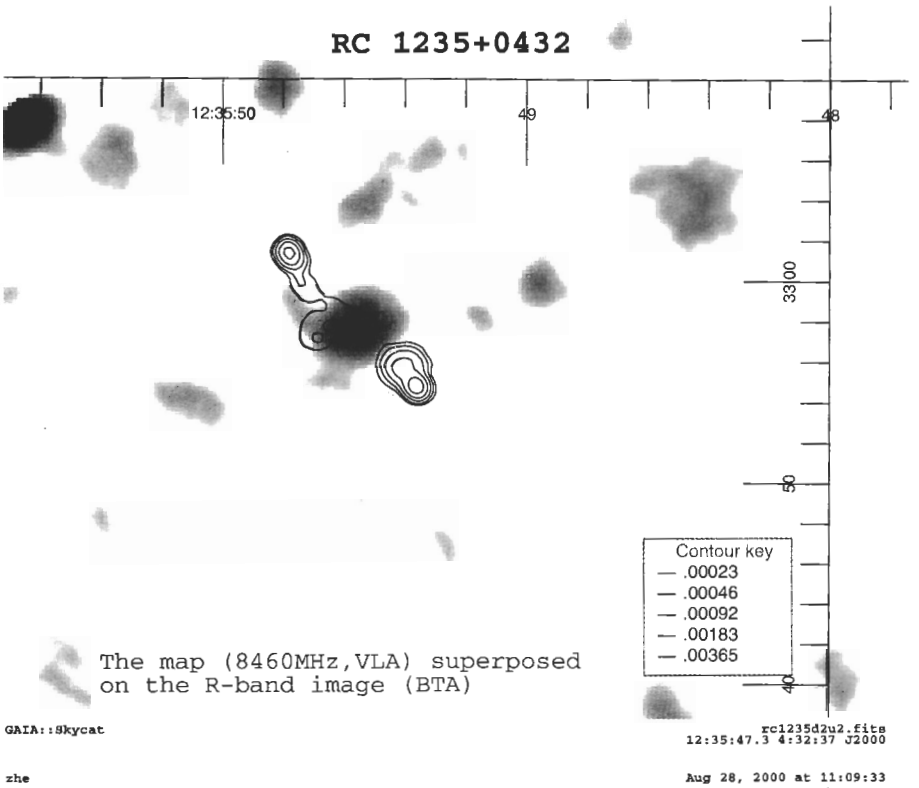
RC 1235+0432
12:35:50
49
48
33'00
50
40
Contour key
— .00023
— .00046
— .00092
— .00183
— .00365
The map (8460MHz,VLA) superposed
on the R-band image (BTA)
GAIA::Skycat
rc1235d2u2.fits
12:35:47.3 4:32:37 J2000
zhe
Aug 28, 2000 at 11:09:33

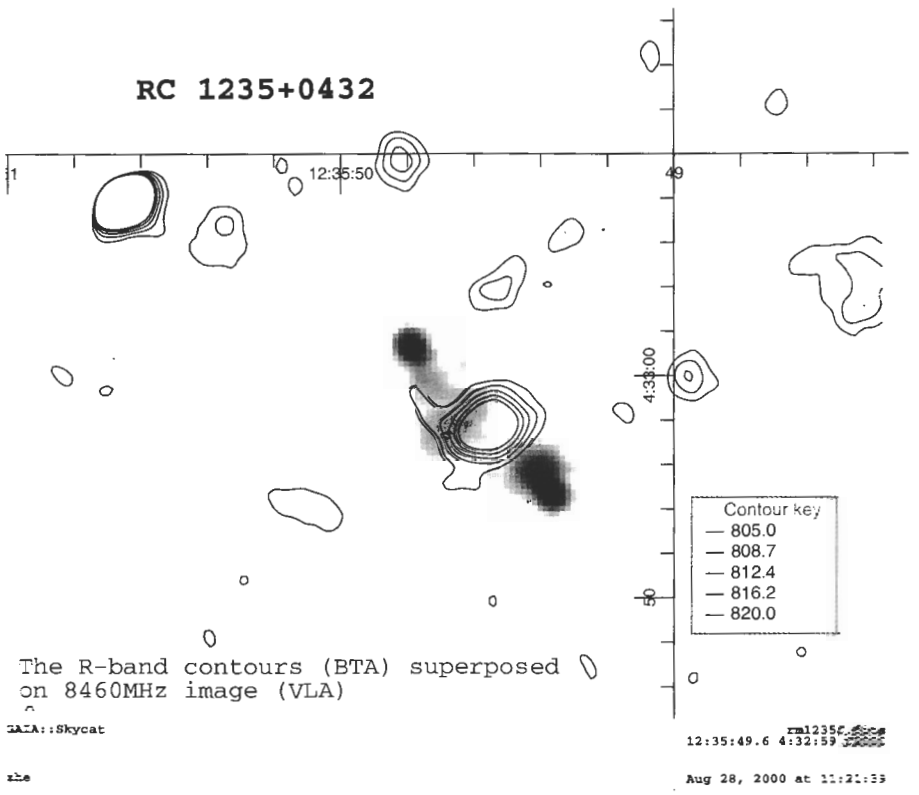
RC 1235+0432
11
12:35:50
49
4:33:00
50
Contour key
— 805.0
— 808.7
— 812.4
— 816.2
— 820.0
The R-band contours (BTA) superposed
on 8460MHz image (VLA)
GAIA::Skycat
12:35:49.6 4:32:59
zhe
Aug 28, 2000 at 11:21:33

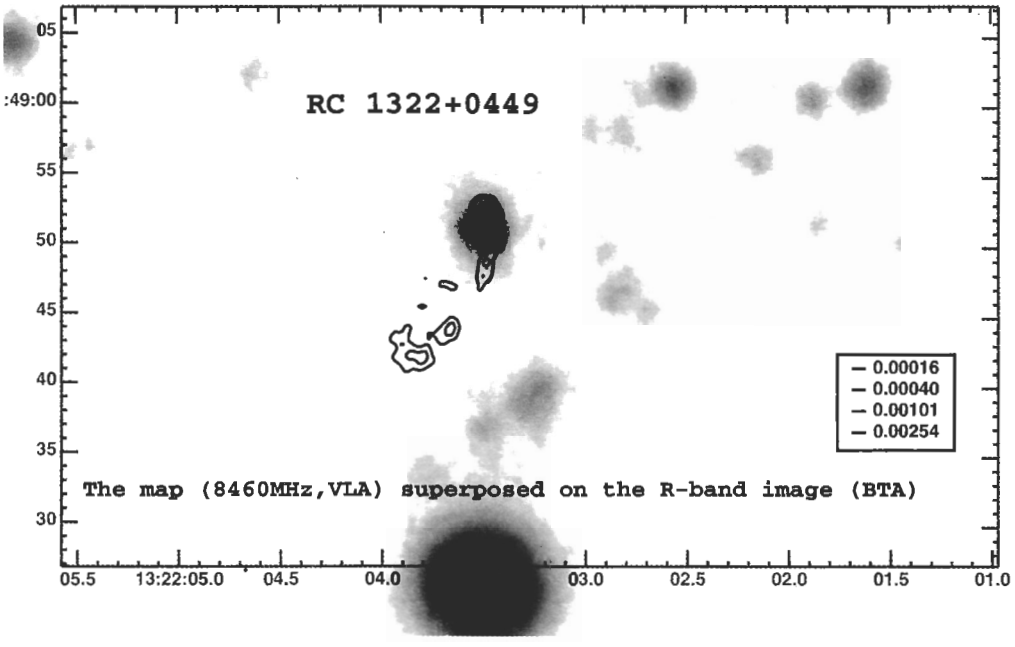
RC 1322+0449
— 0.00016
— 0.00040
— 0.00101
— 0.00254
The map (8460MHz,VLA) superposed on the R-band image (BTA)
05
:49:00
55
50
45
40
35
30
05.5
13:22:05.0
04.5
04.0
03.0
02.5
02.0
01.5
01.0

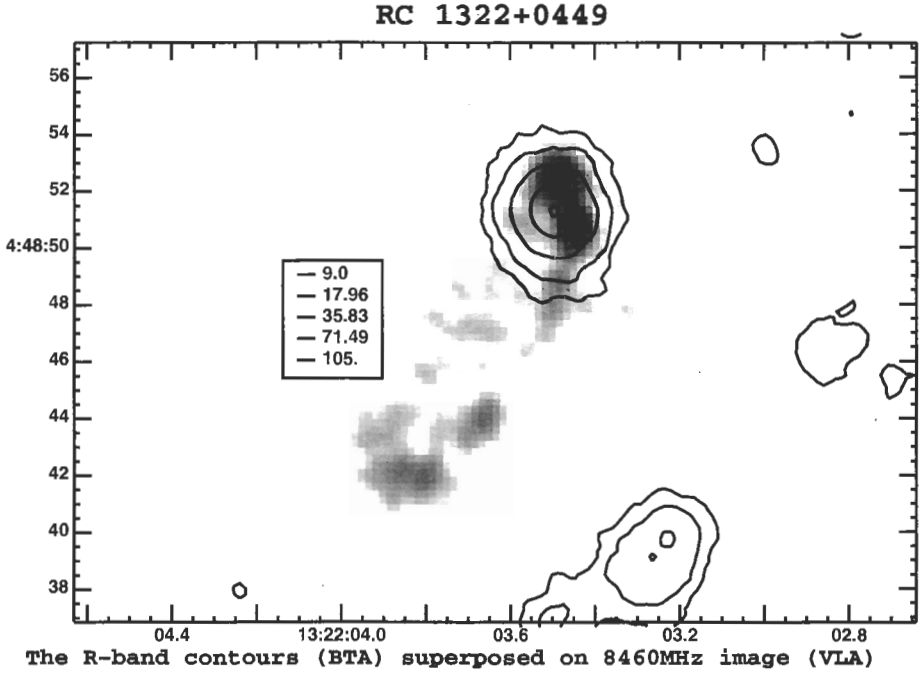
RC 1322+0449
— 9.0
— 17.96
— 35.83
— 71.49
— 105.
The R-band contours (BTA) superposed on 8460MHz image (VLA)
56
54
52
4:48:50
48
46
44
42
40
38
04.4
13:22:04.0
03.6
03.2
02.8

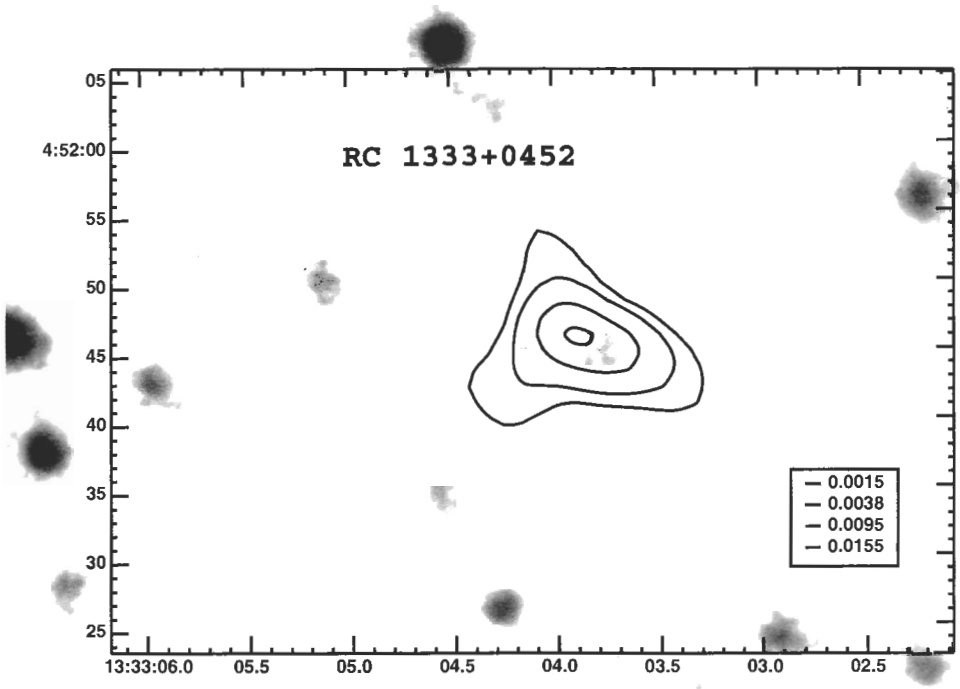

The map (1465MHz,VLA) superposed on the R-band image (BTA)

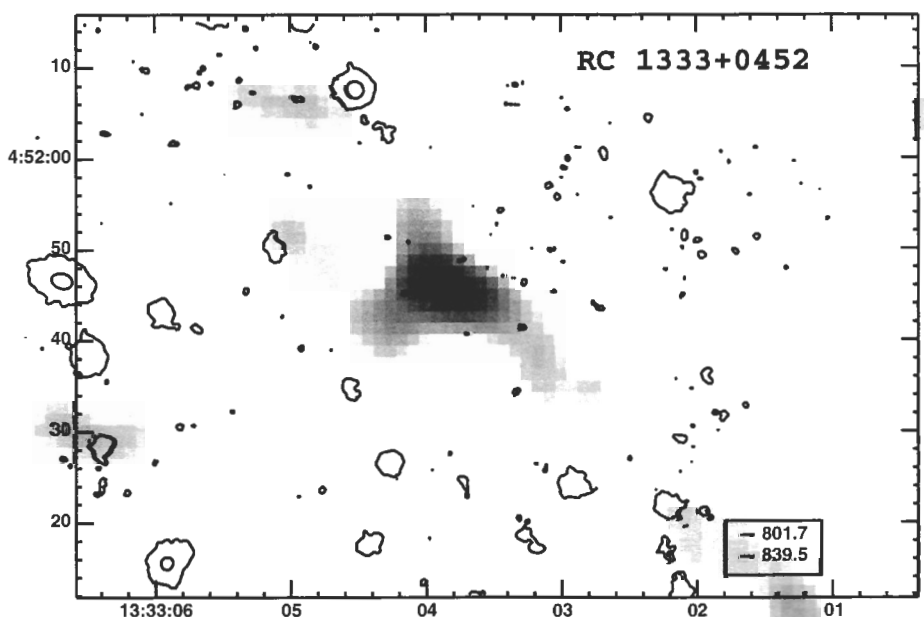

The R-band contours (BTA) superposed on 1465MHz image (BTA)

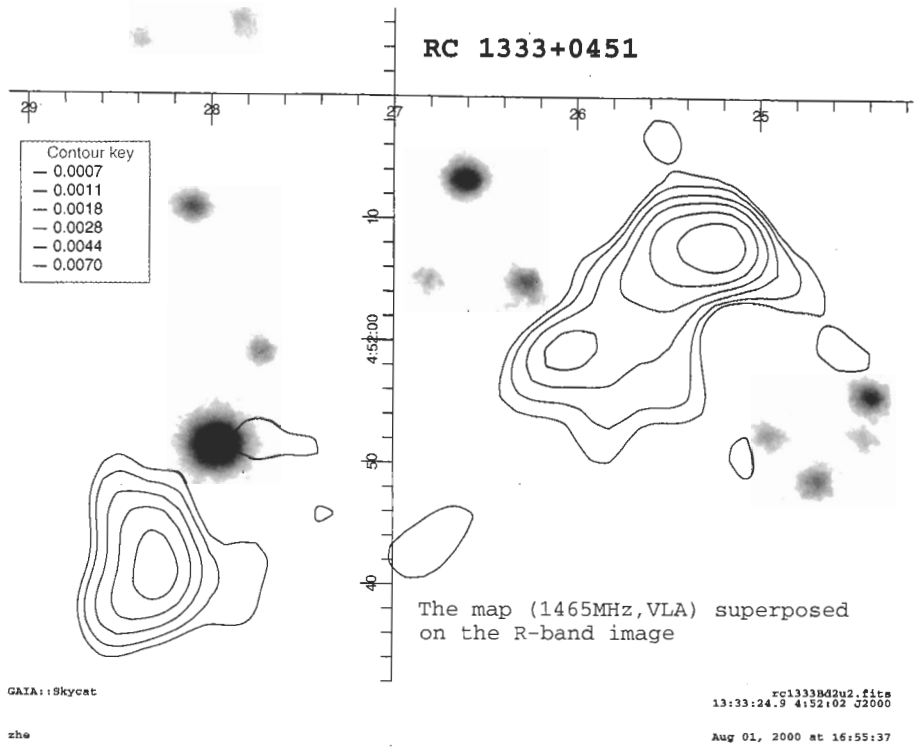
RC 1333+0451
Contour key
— 0.0007
— 0.0011
— 0.0018
— 0.0028
— 0.0044
— 0.0070
The map (1465MHz,VLA) superposed
on the R-band image
GAIA::Skycat
zhe
rc1333Bd2u2.fits
13:33:24.9 4:52:02 J2000
Aug 01, 2000 at 16:55:37

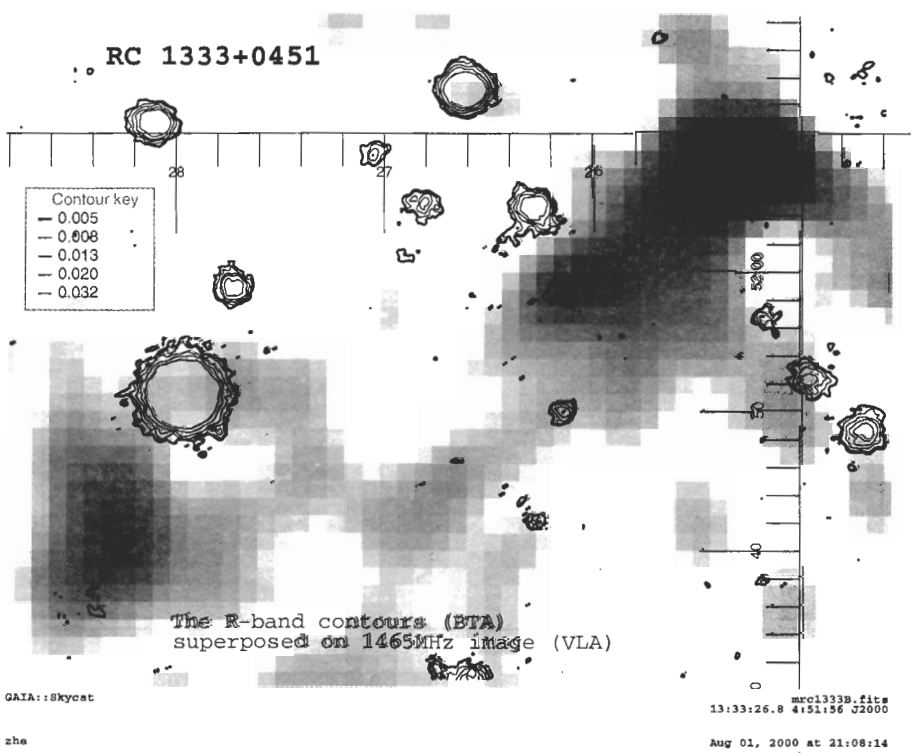
RC 1333+0451
Contour key
— 0.005
— 0.008
— 0.013
— 0.020
— 0.032
The R-band contours (BTA)
superposed on 1465MHz image (VLA)
GAIA::Skycat
zhe
mrc1333B.fits
13:33:26.8 4:51:56 J2000
Aug 01, 2000 at 21:08:14

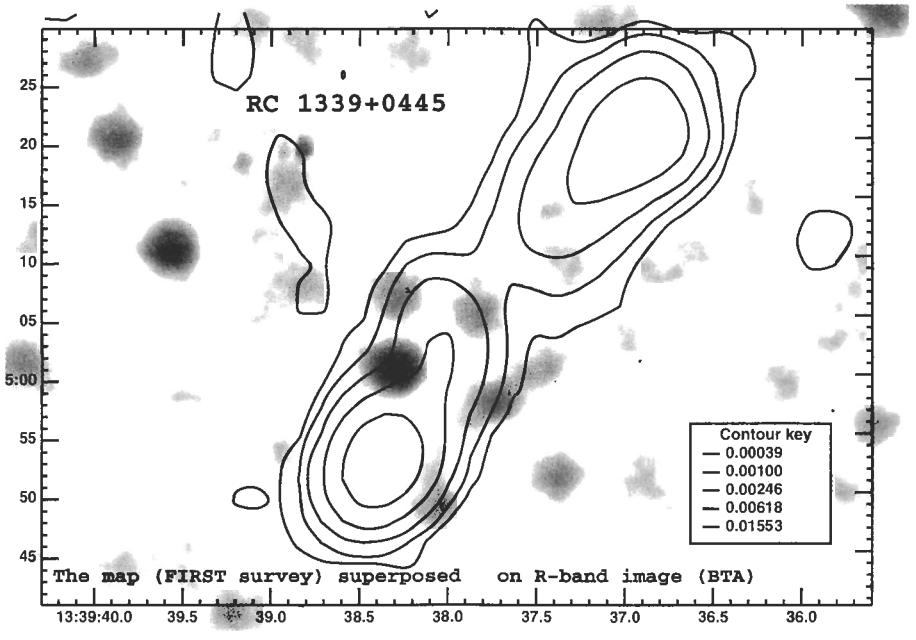
RC 1339+0445
Contour key
0.00039
0.00100
0.00246
0.00618
0.01553
The map (FIRST survey) superposed on R-band image (BTA)
25
20
15
10
05
5:00
55
50
45
13:39:40.0
39.5
39.0
38.5
38.0
37.5
37.0
36.5
36.0

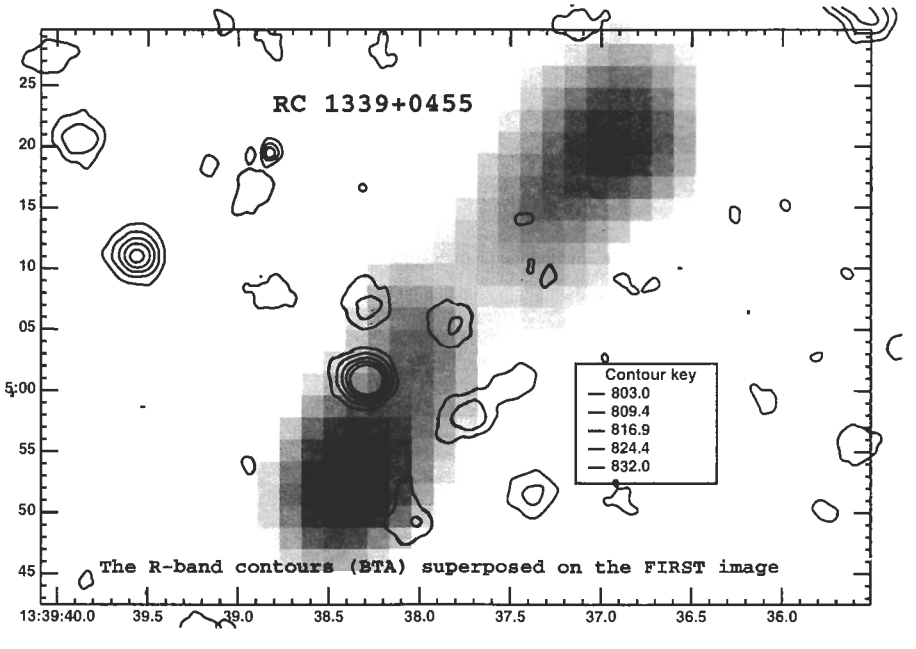
RC 1339+0455
Contour key
803.0
809.4
816.9
824.4
832.0
The R-band contours (BTA) superposed on the FIRST image
25
20
15
10
05
5:00
55
50
45
13:39:40.0
39.5
39.0
38.5
38.0
37.5
37.0
36.5
36.0

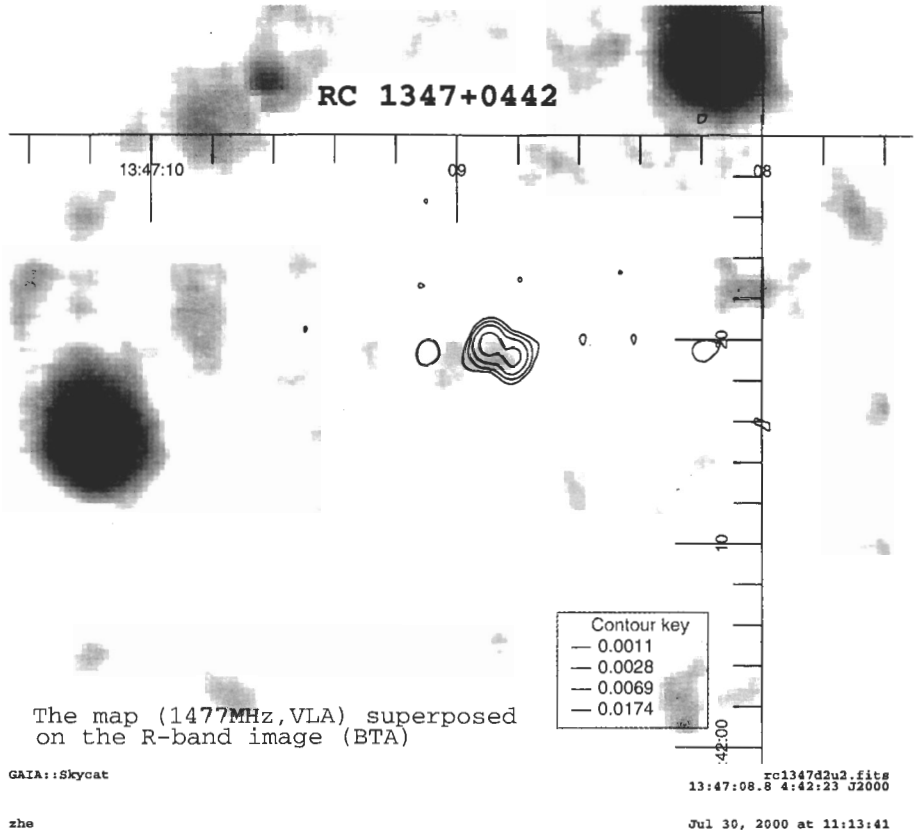

The map (1477MHz,VLA) superposed on the R-band image (BTA)

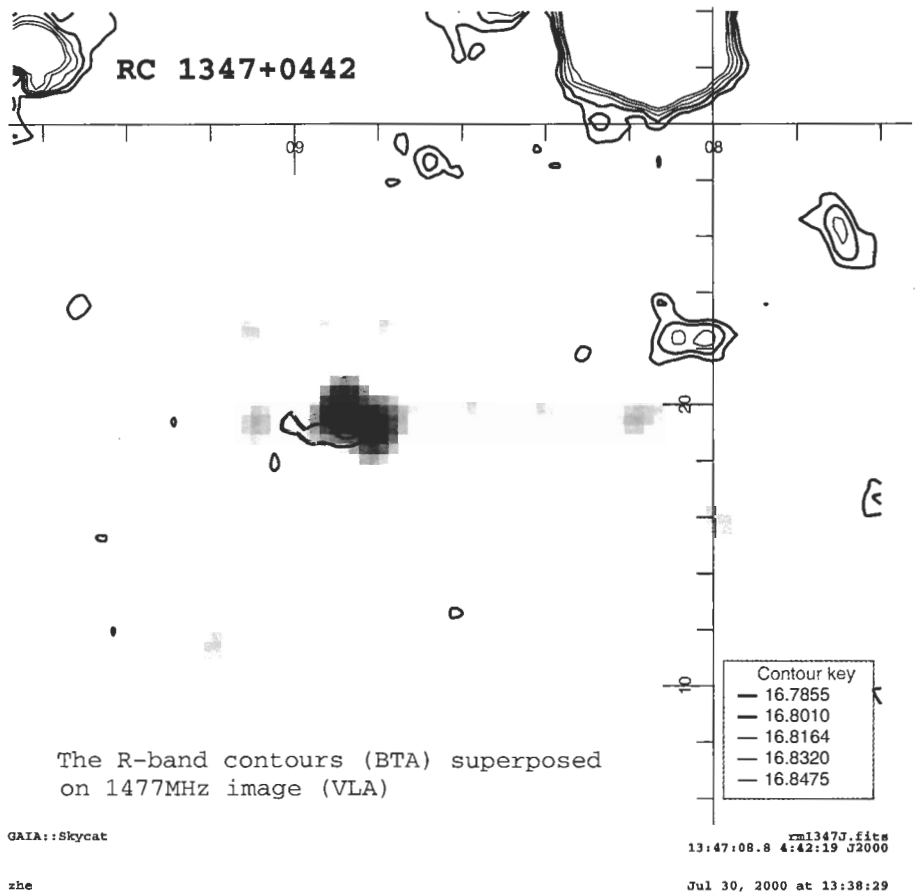

The R-band contours (BTA) superposed on 1477MHz image (VLA)

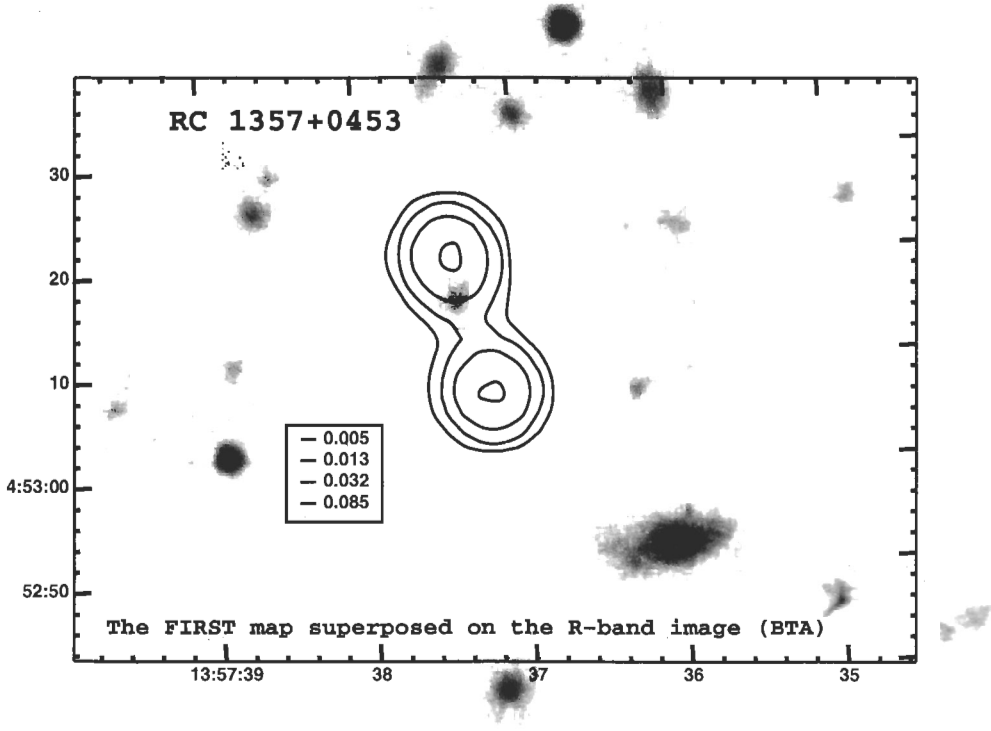

The FIRST map superposed on the R-band image (BTA)

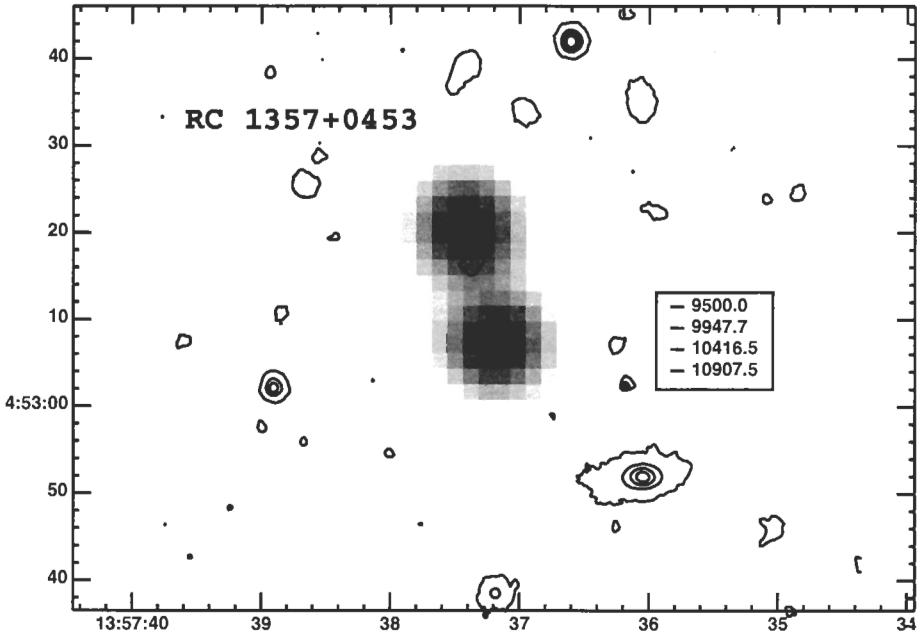

The FIRST map superposed on the R-band image (BTA)

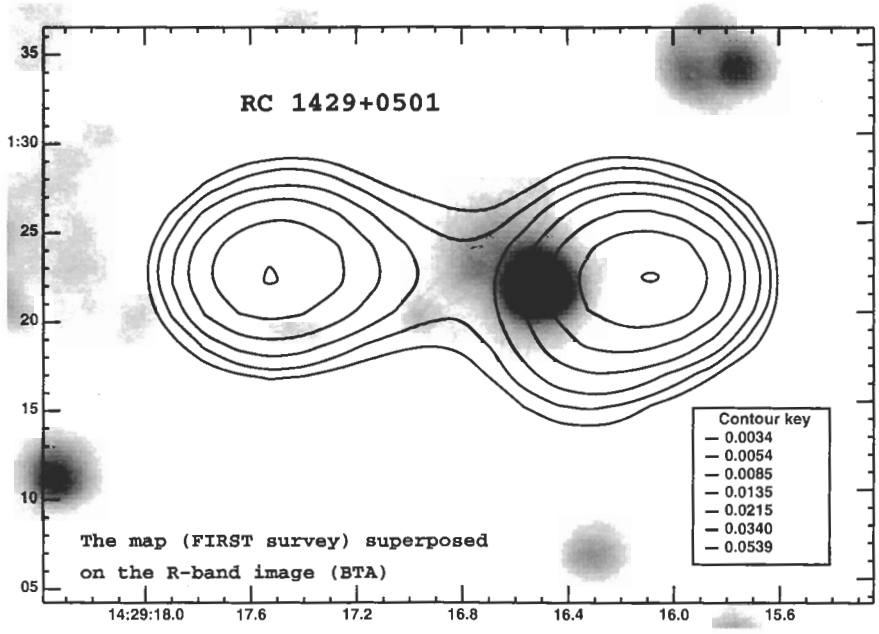
RC 1429+0501
Contour key
0.0034
0.0054
0.0085
0.0135
0.0215
0.0340
0.0539
The map (FIRST survey) superposed
on the R-band image (BTA)
35
1:30
25
20
15
10
05
14:29:18.0
17.6
17.2
16.8
16.4
16.0
15.6

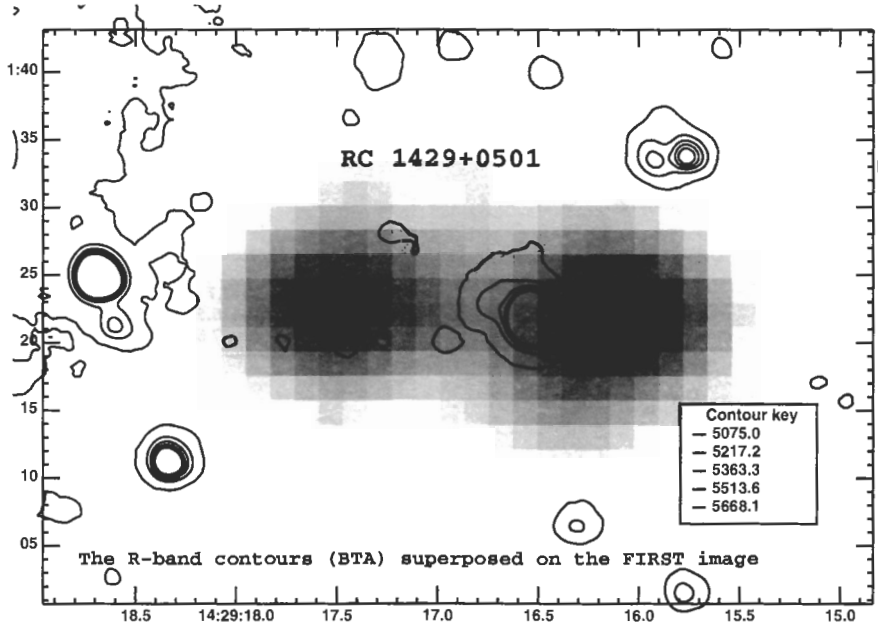
RC 1429+0501
Contour key
5075.0
5217.2
5363.3
5513.6
5668.1
The R-band contours (BTA) superposed on the FIRST image
1:40
35
30
25
20
15
10
05
18.5
14:29:18.0
17.5
17.0
16.5
16.0
15.5
15.0

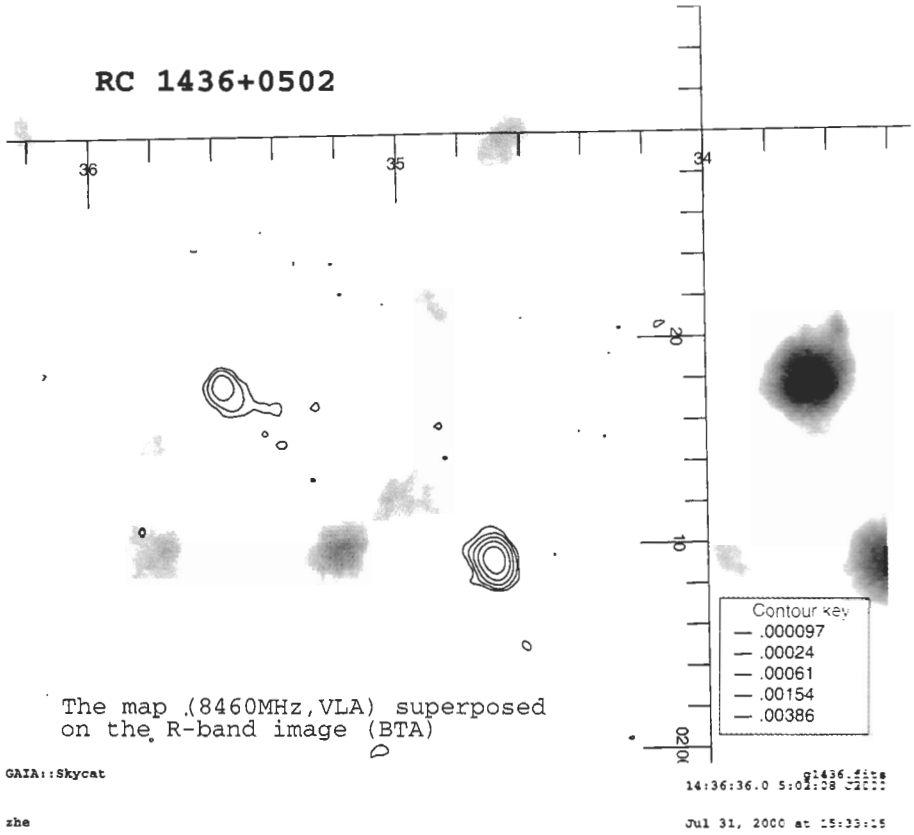
RC 1436+0502
36
35
34
20
10
02'00"
Contour key
— .000097
— .00024
— .00061
— .00154
— .00386
The map (8460MHz,VLA) superposed
on the R-band image (BTA)
GAIA::Skycat
zhe
Jul 31, 2000 at 15:33:15

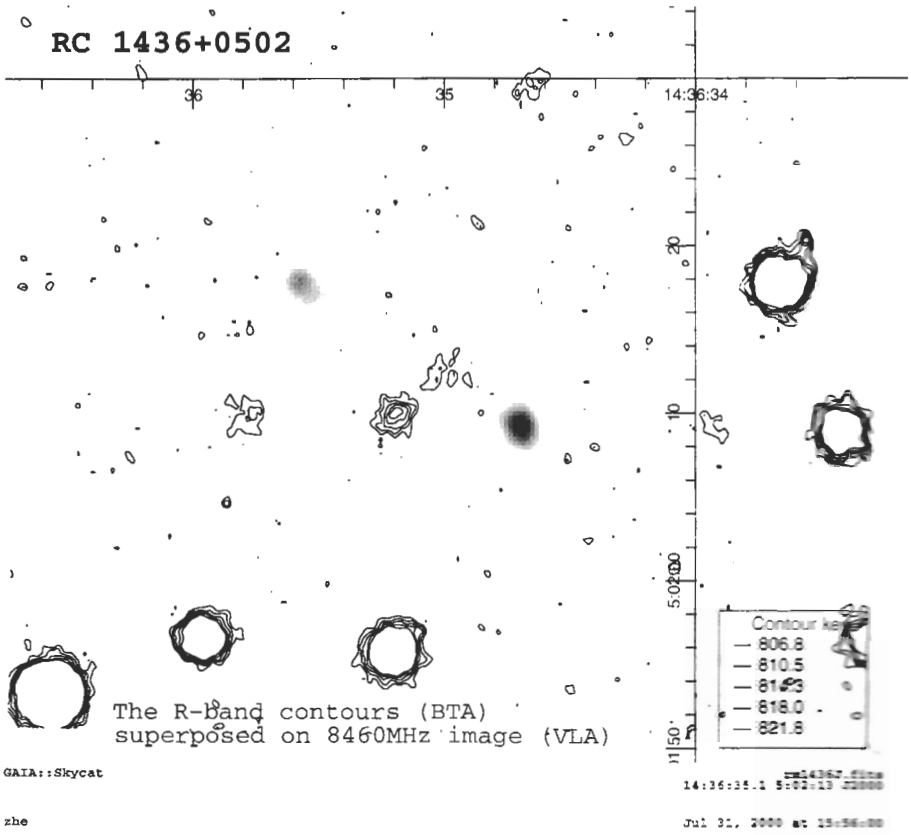
RC 1436+0502
36
35
14:36:34
20
10
5:02'00"
50
Contour ke
— 806.8
— 810.5
— 814.3
— 818.0
— 821.8
The R-band contours (BTA)
superposed on 8460MHz image (VLA)
GAIA::Skycat
zhe
Jul 31, 2000 at

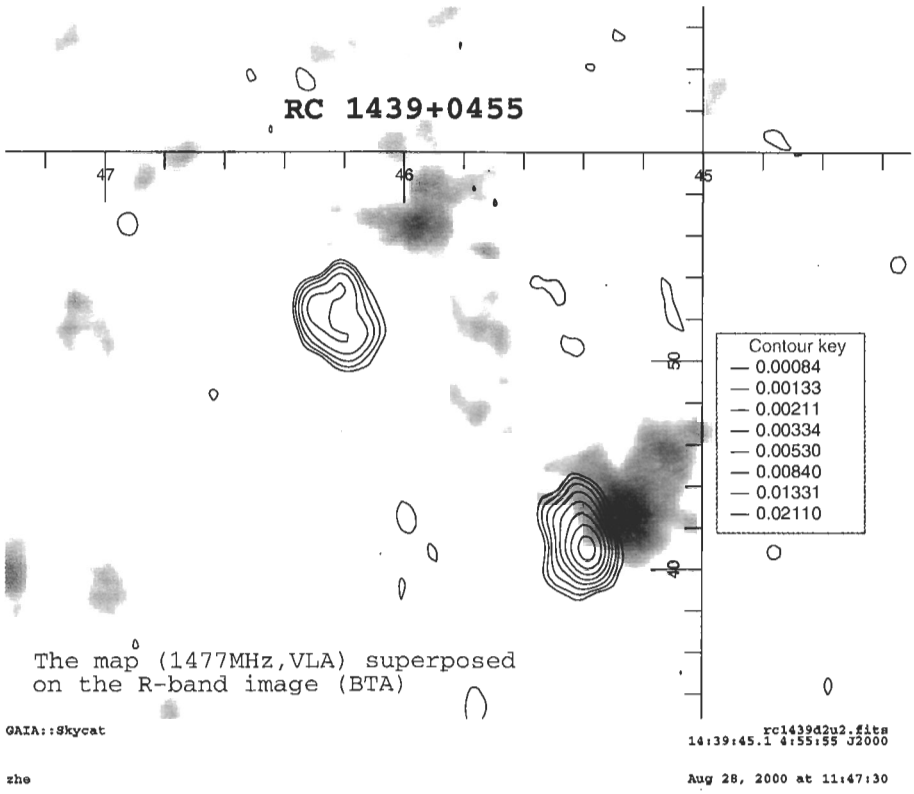

The map (1477MHz,VLA) superposed on the R-band image (BTA)

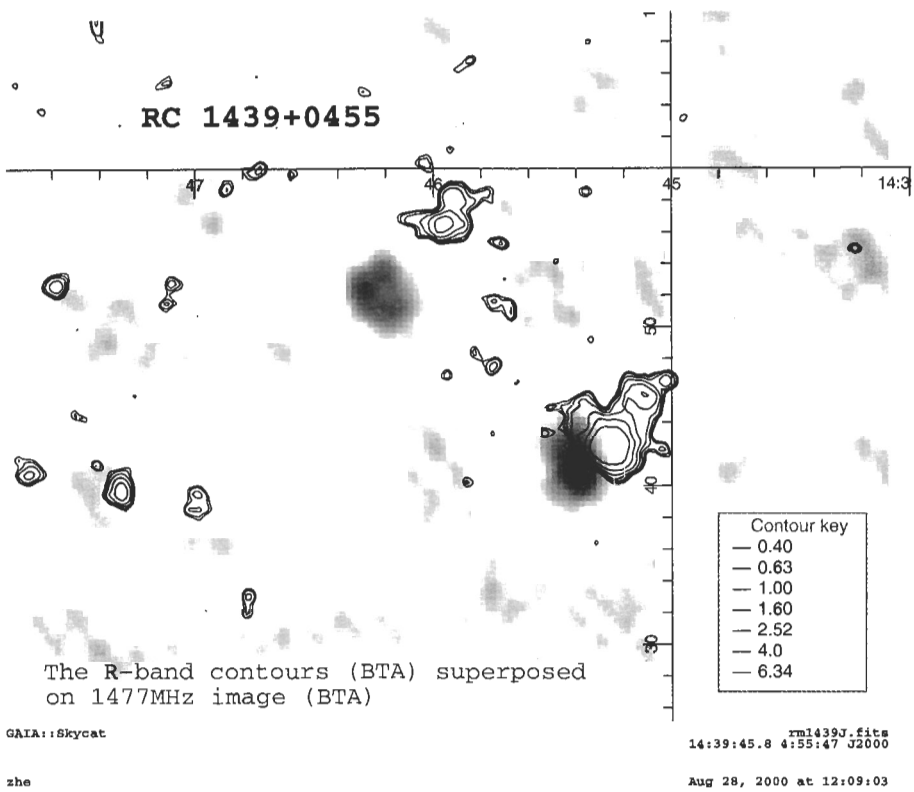

The R-band contours (BTA) superposed on 1477MHz image (BTA)

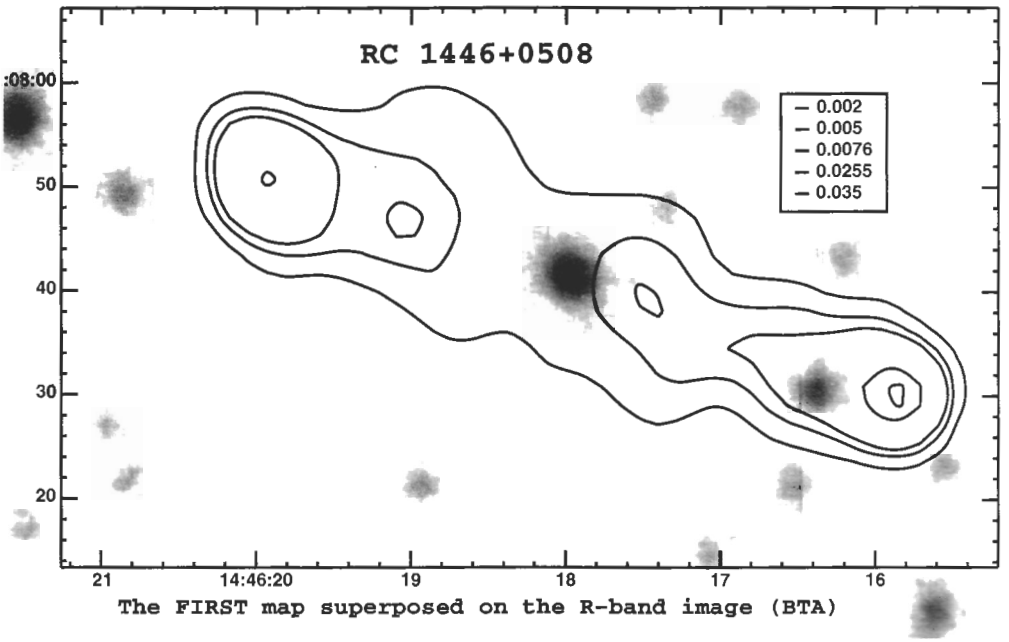

The FIRST map superposed on the R-band image (BTA)

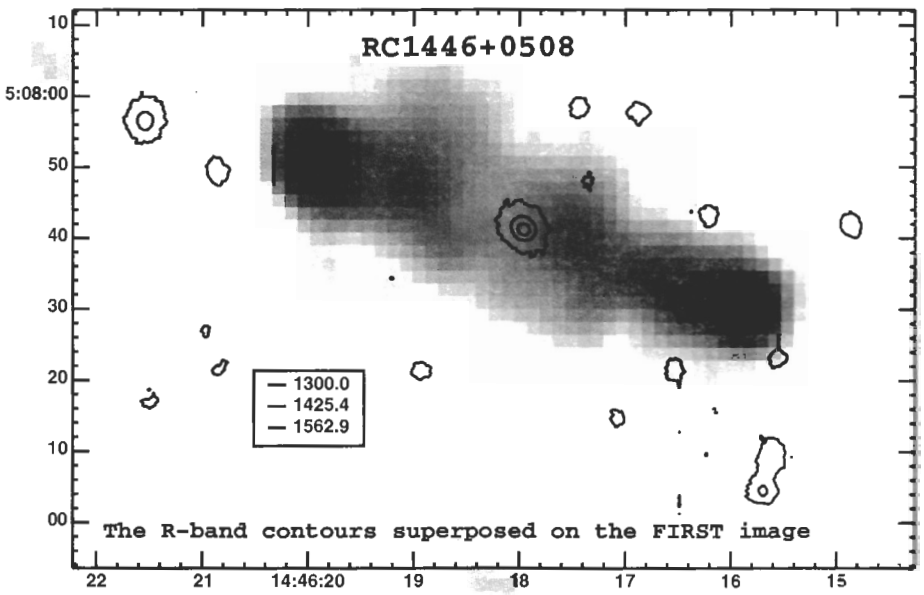

The R-band contours superposed on the FIRST image

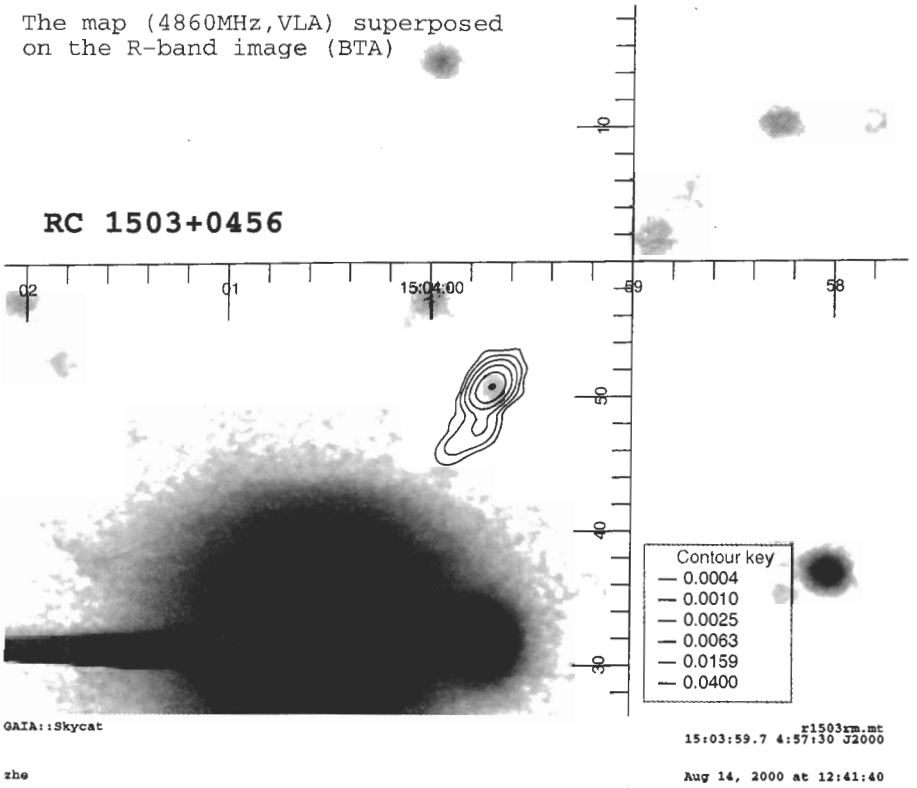
The map (4860MHz,VLA) superposed
on the R-band image (BTA)
RC 1503+0456
02
01
15:04:00
59
58
10
50
40
30
Contour key
0.0004
0.0010
0.0025
0.0063
0.0159
0.0400
GAIA::Skycat
r1503rm.mt
15:03:59.7 4:57:30 J2000
zhe
Aug 14, 2000 at 12:41:40

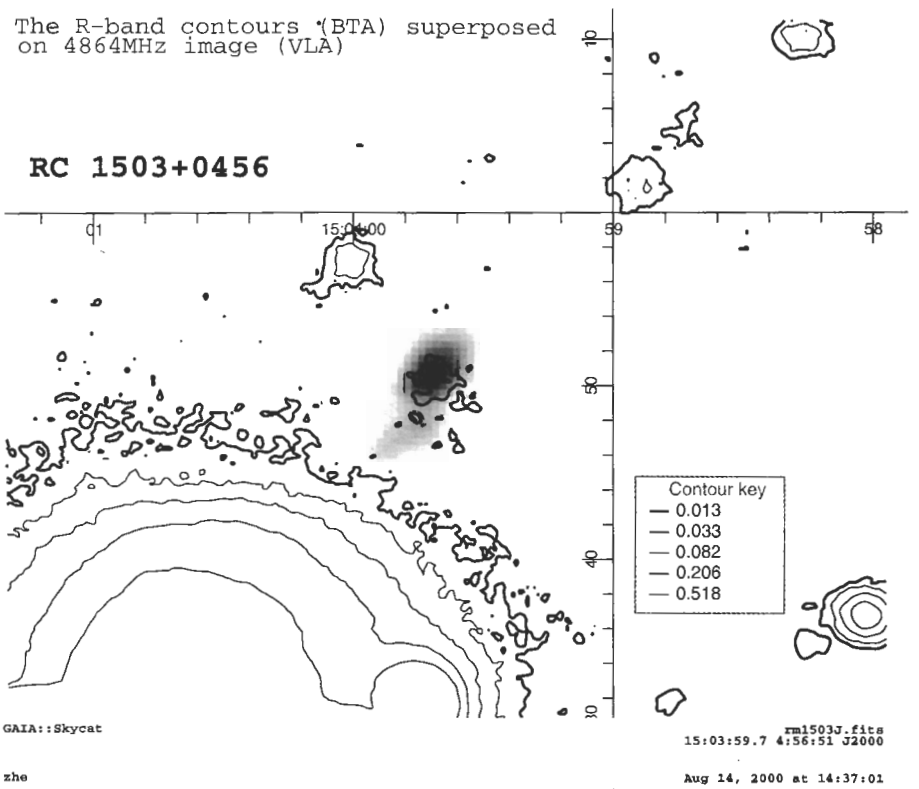
The R-band contours (BTA) superposed
on 4864MHz image (VLA)
RC 1503+0456
01
15:04:00
59
58
10
50
40
30
Contour key
0.013
0.033
0.082
0.206
0.518
GAIA::Skycat
rm1503J.fits
15:03:59.7 4:56:51 J2000
zhe
Aug 14, 2000 at 14:37:01

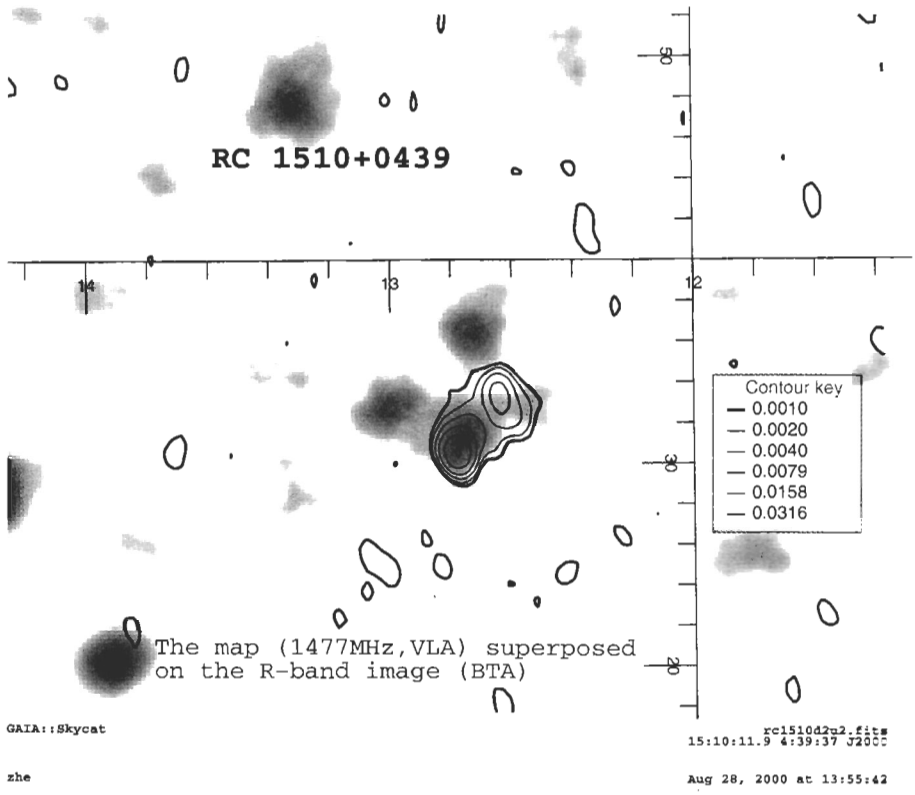

The map (1477MHz,VLA) superposed on the R-band image (BTA)

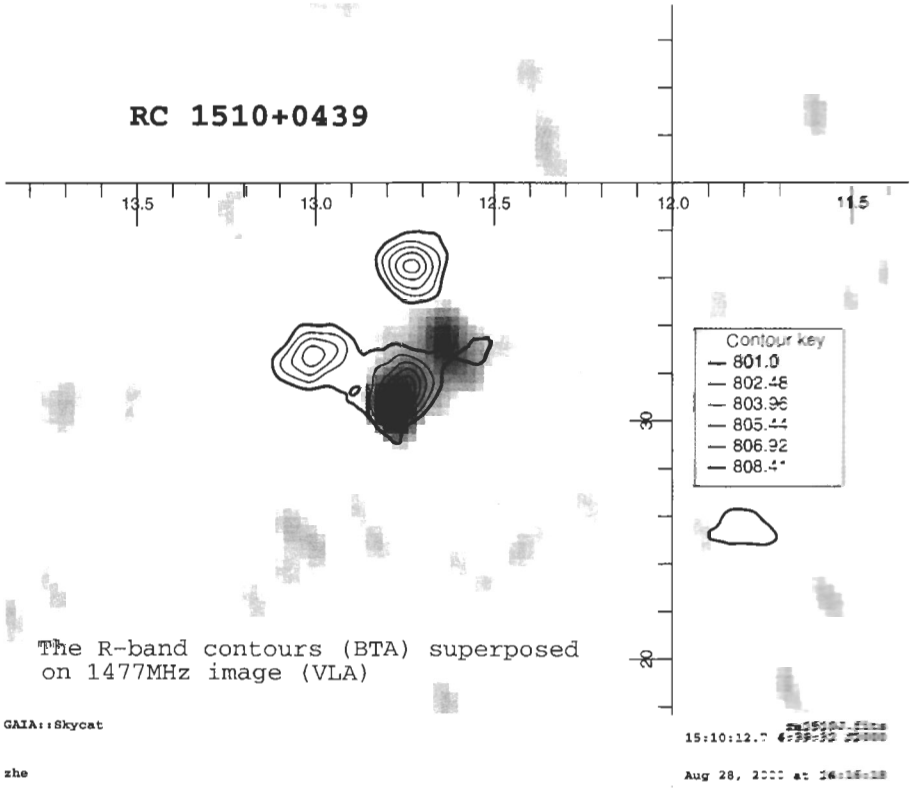

The R-band contours (BTA) superposed on 1477MHz image (VLA)

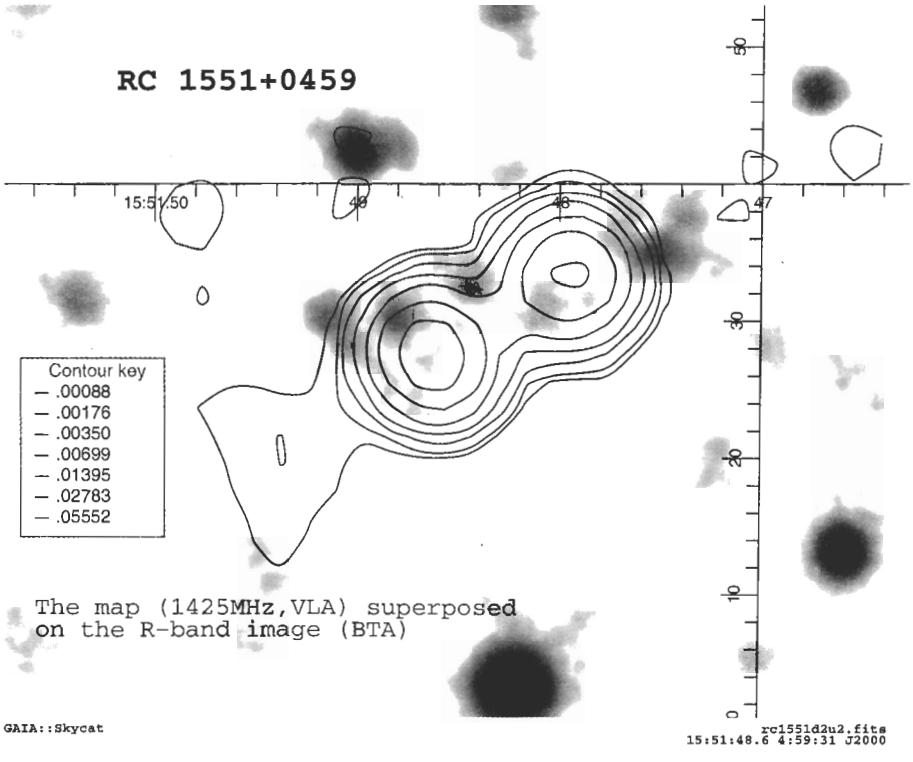
RC 1551+0459
15:51:50
49
48
47
50
30
20
10
1
0
Contour key
— .00088
— .00176
— .00350
— .00699
— .01395
— .02783
— .05552
The map (1425MHz,VLA) superposed
on the R-band image (BTA)
GAIA::Skycat
zhe
rc1551d2u2.fits
15:51:48.6 4:59:31 J2000
Aug 23, 1998 at 12:08:09

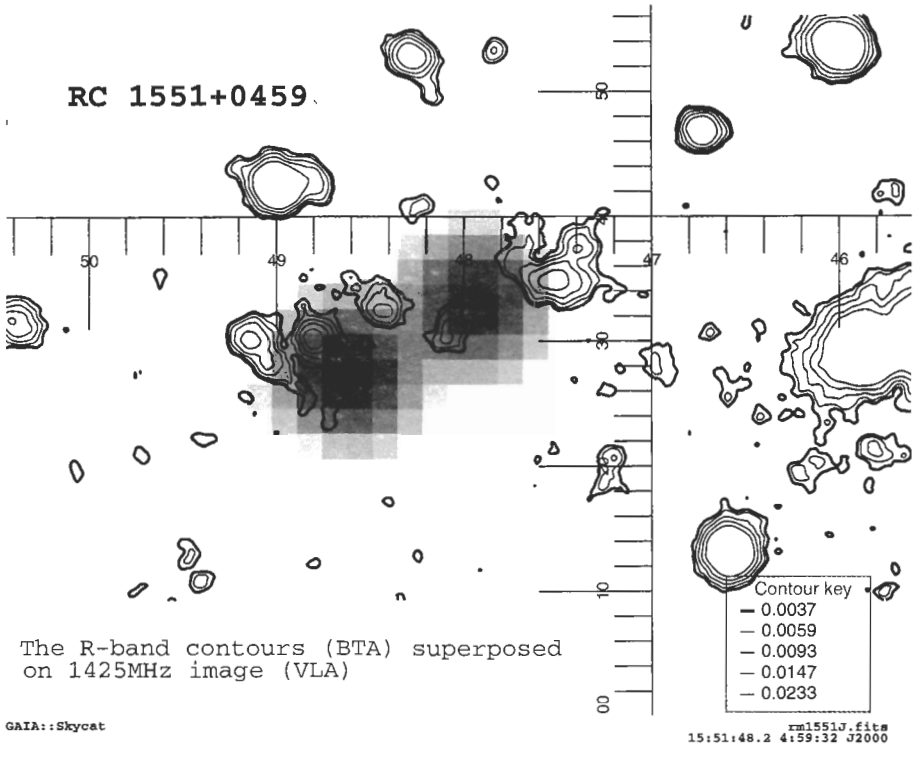
RC 1551+0459
50
49
48
47
46
50
30
10
00
Contour key
— 0.0037
— 0.0059
— 0.0093
— 0.0147
— 0.0233
The R-band contours (BTA) superposed
on 1425MHz image (VLA)
GAIA::Skycat
zhe
rm1551J.fits
15:51:48.2 4:59:32 J2000
Aug 23, 1998 at 12:38:20

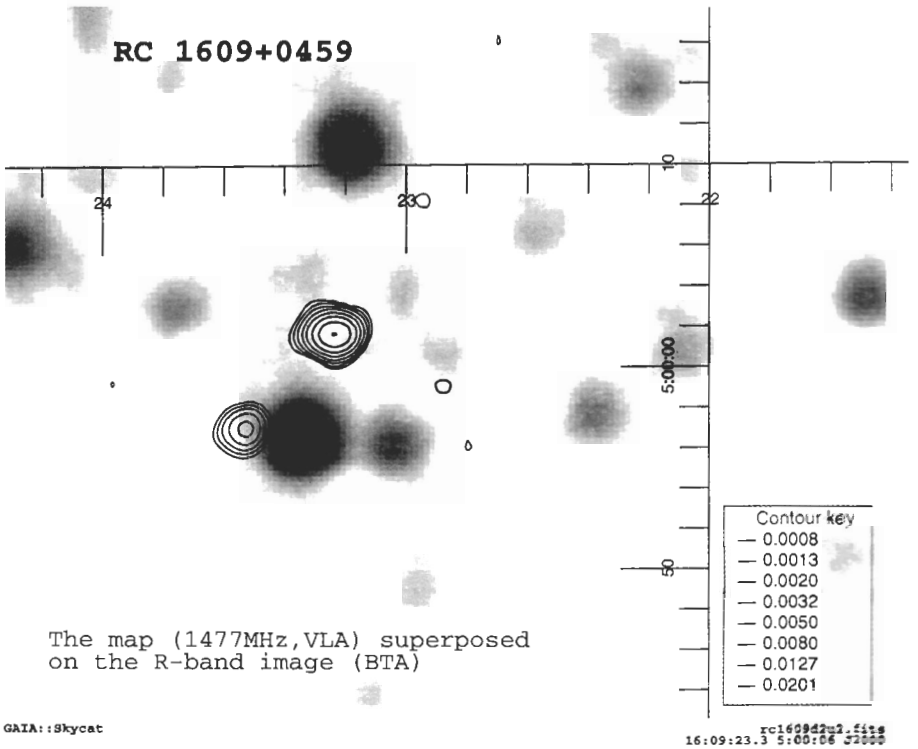

The map (1477MHz,VLA) superposed on the R-band image (BTA)

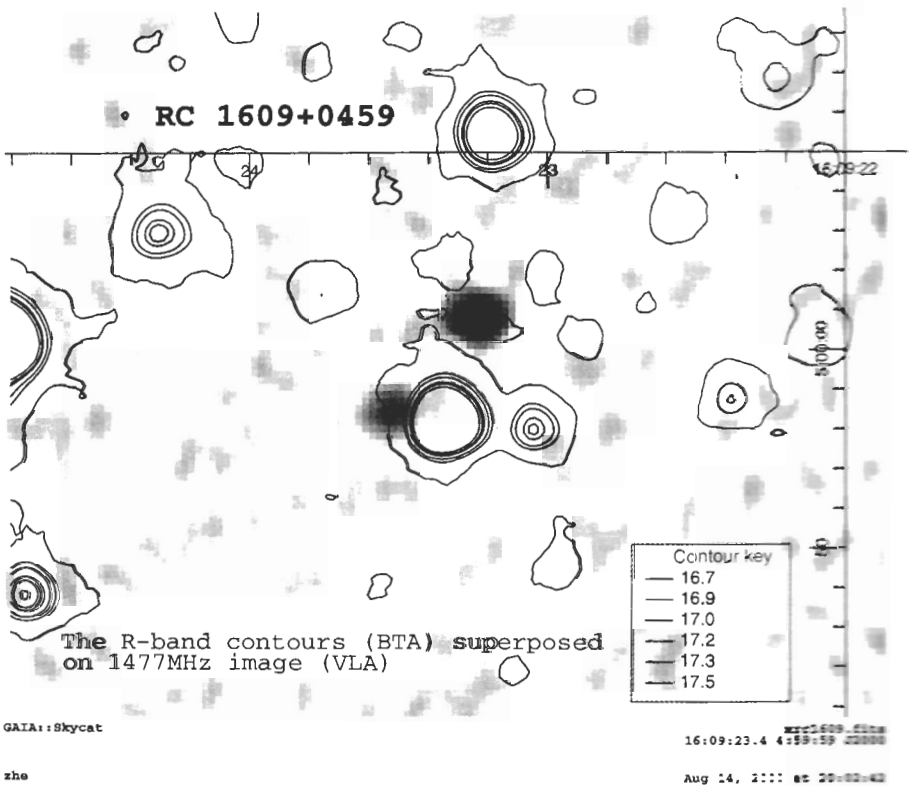

The R-band contours (BTA) superposed on 1477MHz image (VLA)

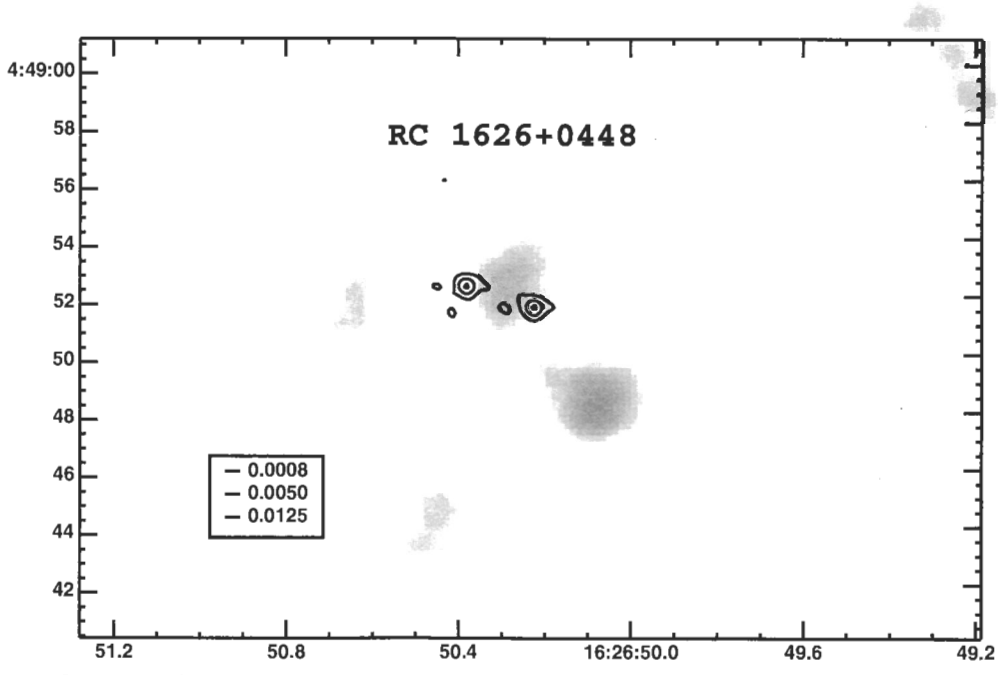

The map (4860MHz,VLA) superposed on the R-band image (BTA)

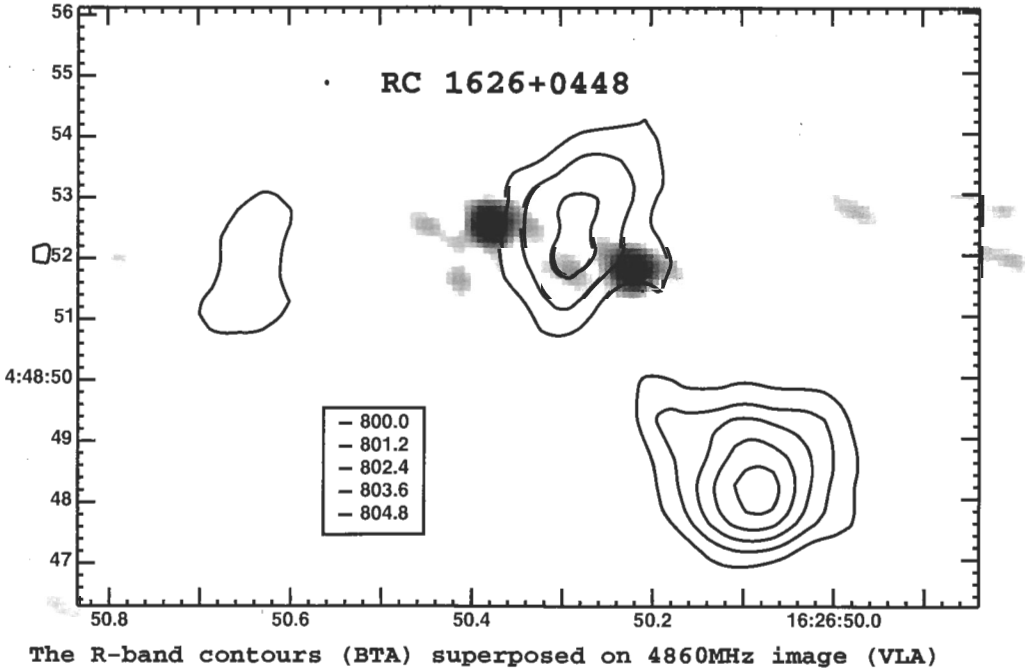

The R-band contours (BTA) superposed on 4860MHz image (VLA)

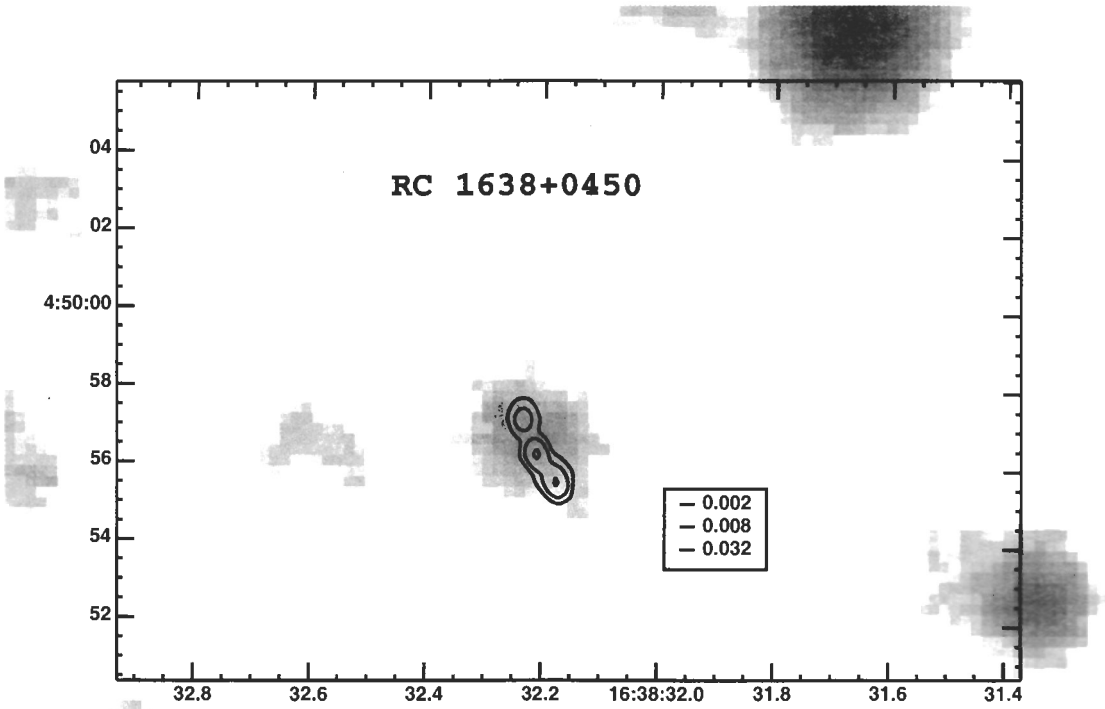

The map (4860MHz,VLA) superposed on the R-band image (BTA)

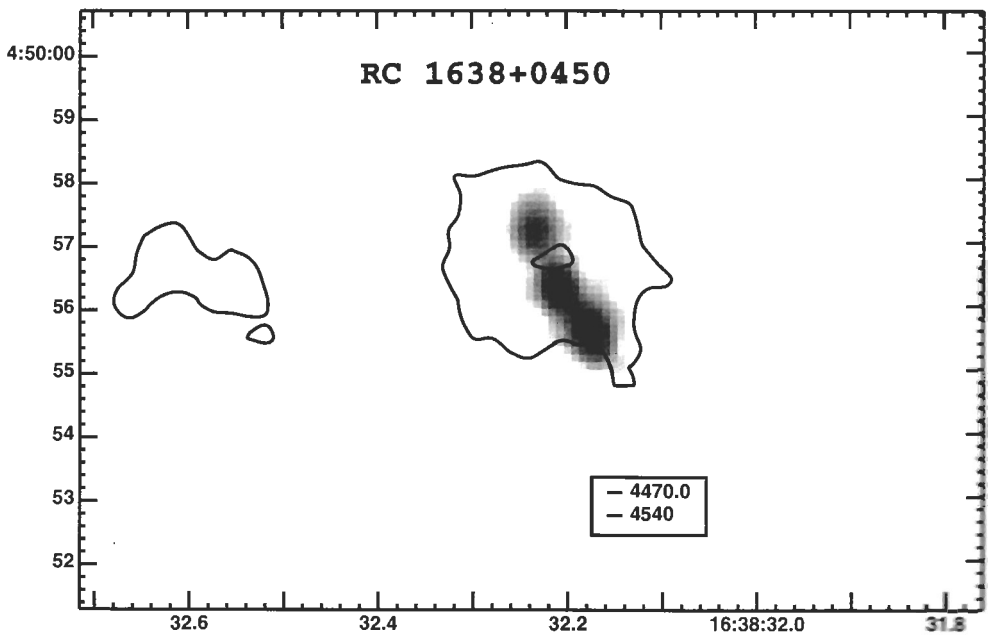

The R-band contours (BTA) superposed on 4860MHz image (VLA)

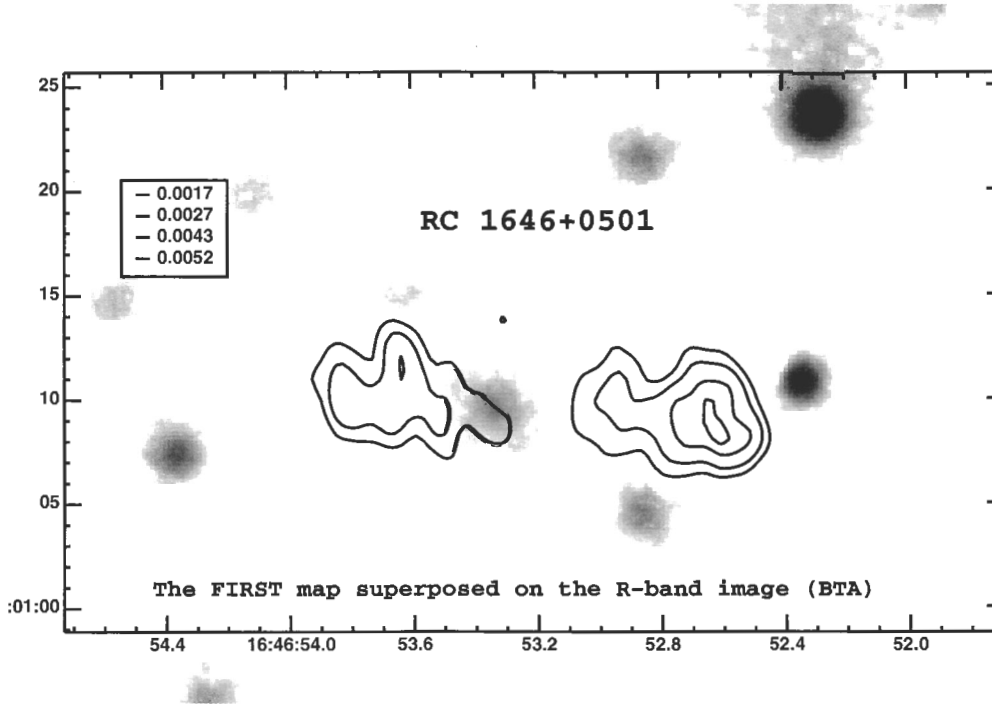

The FIRST map superposed on the R-band image (BTA)

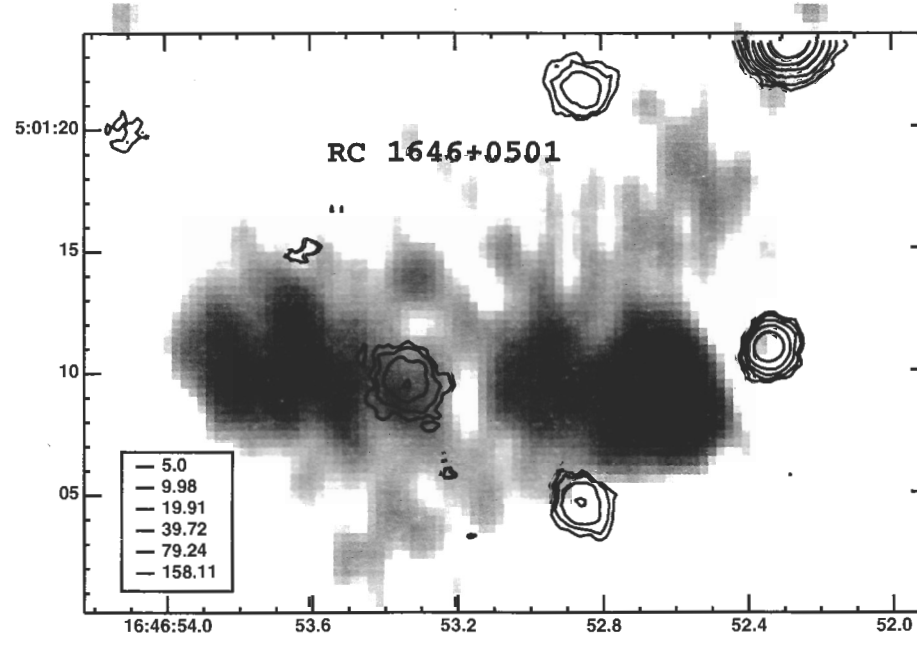

The R-band image (BTA) superposed on 1477MHz image (VLA)

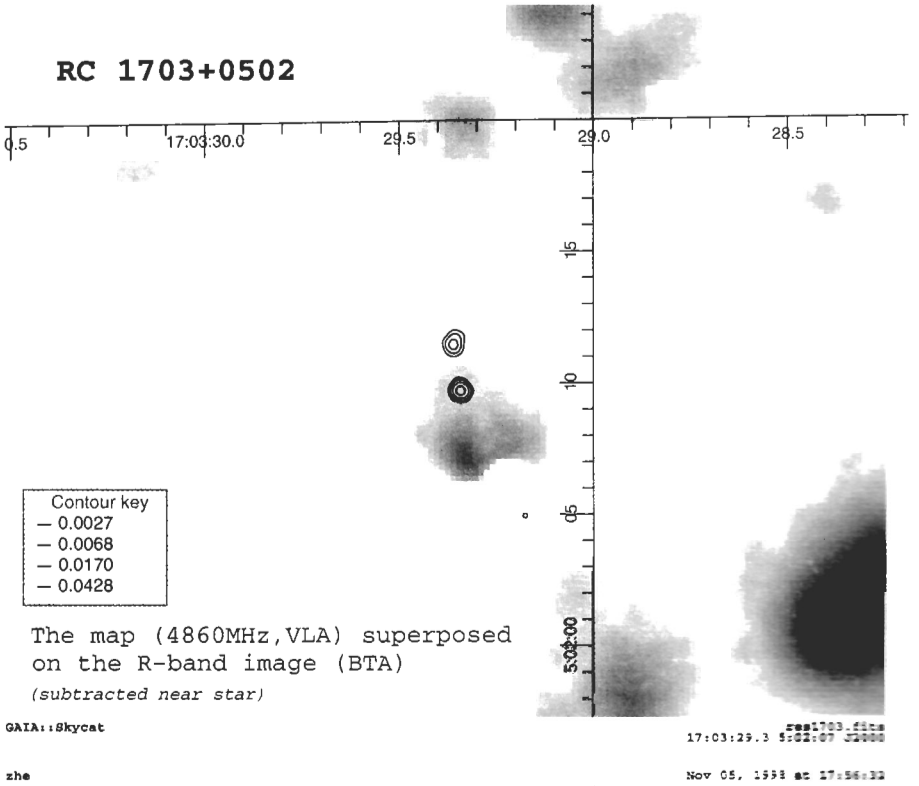
RC 1703+0502
0.5
17:03:30.0
29.5
29.0
28.5
15
10
05
5:02:00
Contour key
— 0.0027
— 0.0068
— 0.0170
— 0.0428
The map (4860MHz,VLA) superposed
on the R-band image (BTA)
(subtracted near star)
GAIA::Skycat
zhe
Nov 05, 1998 at 17:56:32

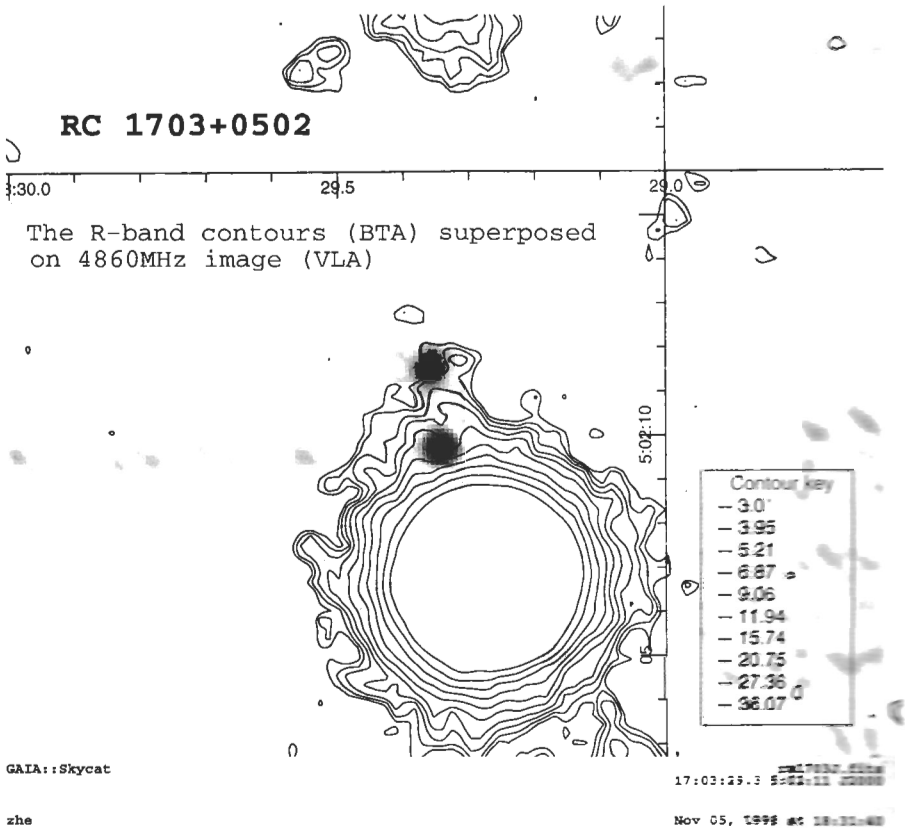
RC 1703+0502
:30.0
29.5
29.0
The R-band contours (BTA) superposed
on 4860MHz image (VLA)
5:02:10
05
Contour key
— 3.0
— 3.95
— 5.21
— 6.87
— 9.06
— 11.94
— 15.74
— 20.75
— 27.36
— 36.07
GAIA::Skycat
zhe

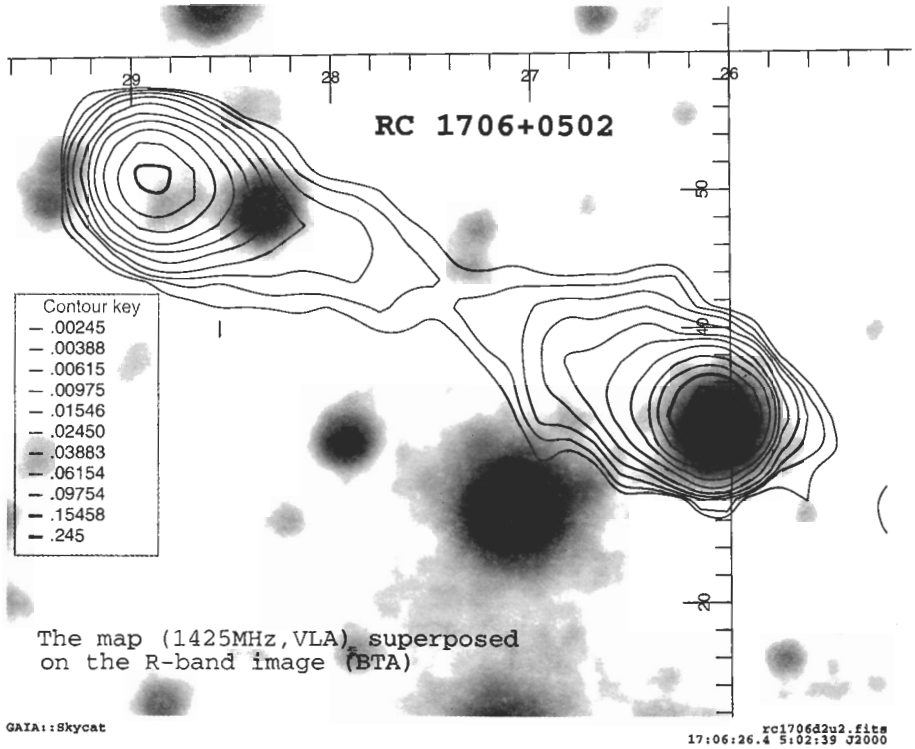
RC 1706+0502
Contour key
.00245
.00388
.00615
.00975
.01546
.02450
.03883
.06154
.09754
.15458
.245
The map (1425MHz,VLA) superposed
on the R-band image (BTA)
GAIA::Skycat
rc1706d2u2.fits
17:06:26.4 5:02:39 J2000
zhe
Aug 23, 1998 at 14:31:31

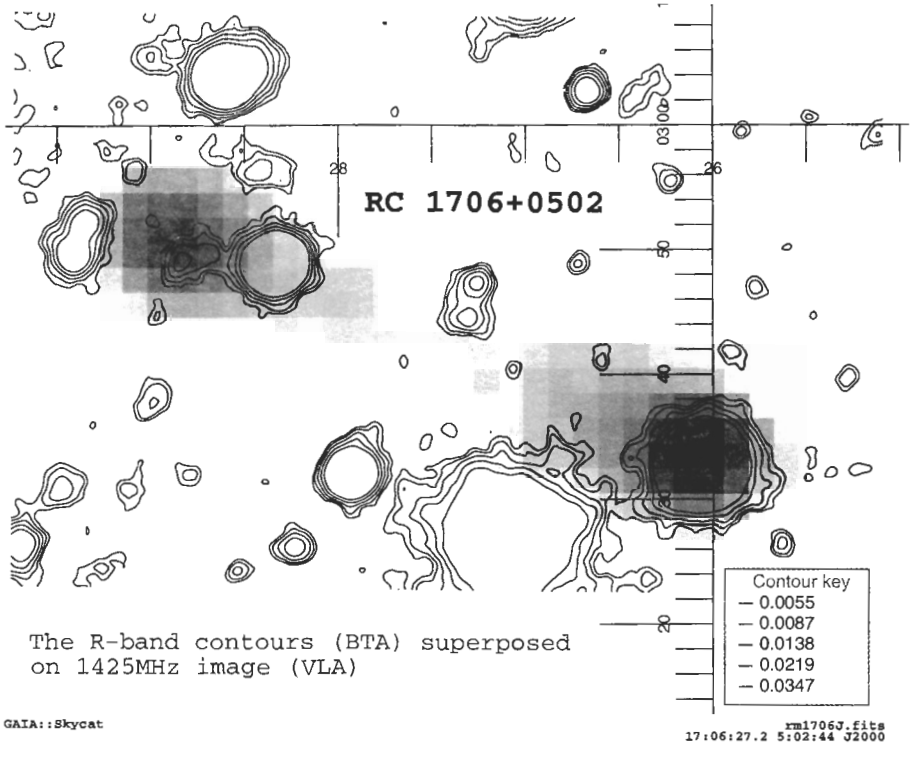
RC 1706+0502
Contour key
0.0055
0.0087
0.0138
0.0219
0.0347
The R-band contours (BTA) superposed
on 1425MHz image (VLA)
GAIA::Skycat
rm1706J.fits
17:06:27.2 5:02:44 J2000
zhe
Aug 23, 1998 at 15:37:48

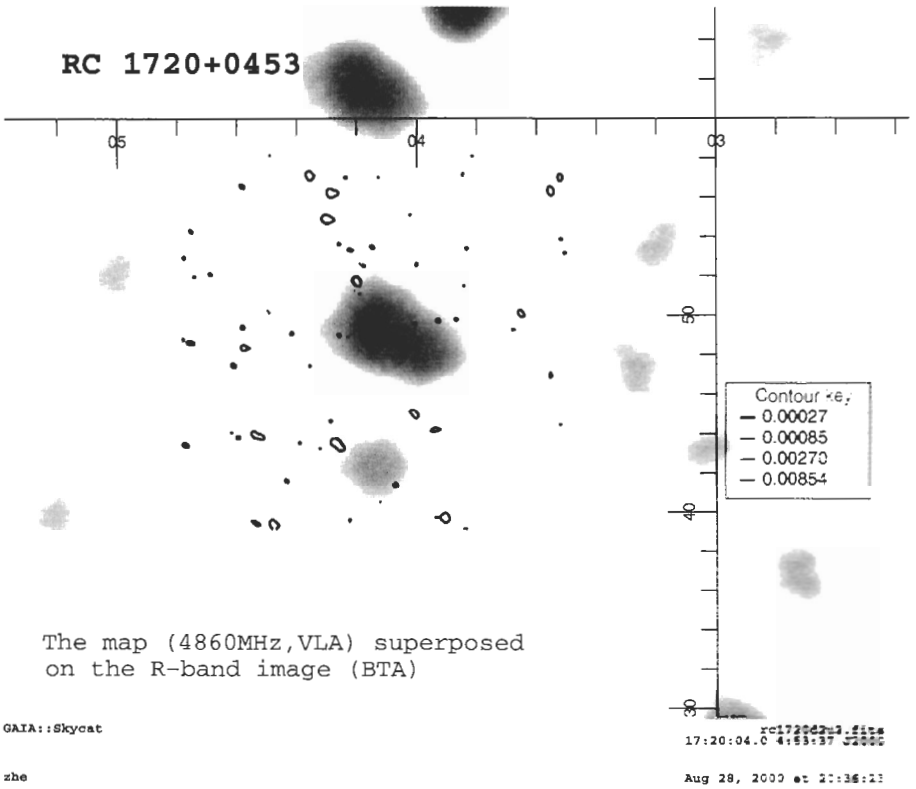

The map (4860MHz,VLA) superposed on the R-band image (BTA)

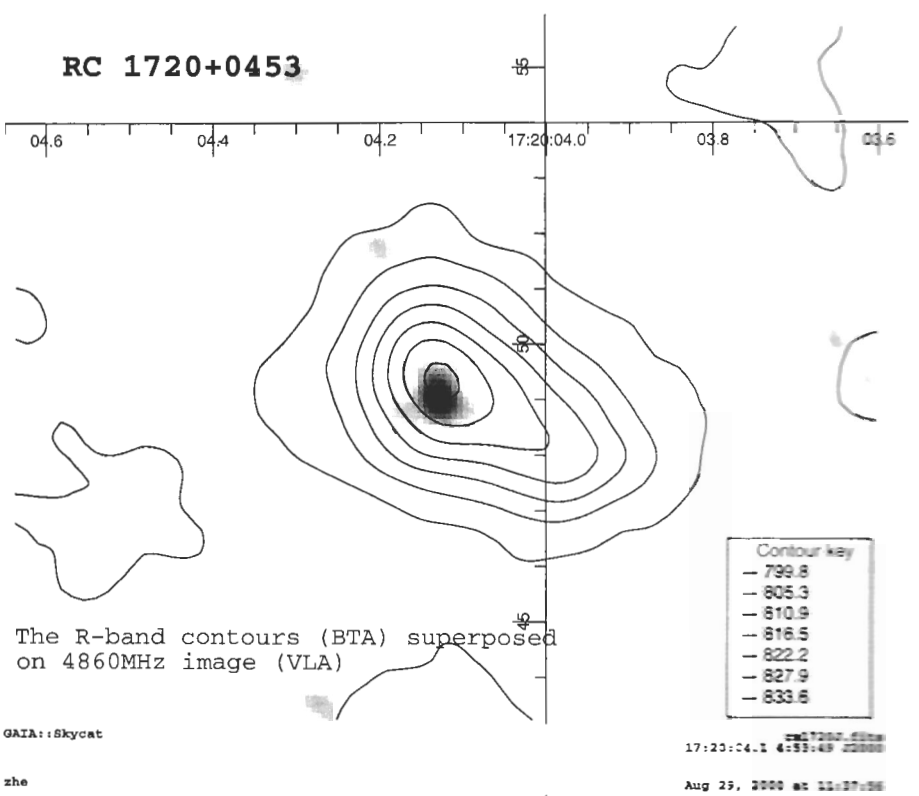

The R-band contours (BTA) superposed on 4860MHz image (VLA)

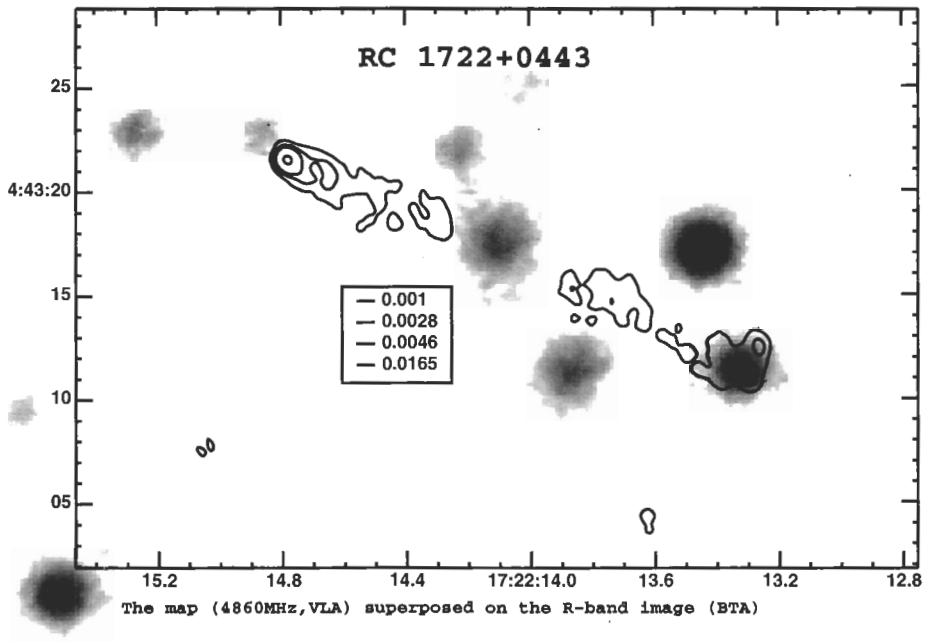

The map (4860MHz,VLA) superposed on the R-band image (BTA)

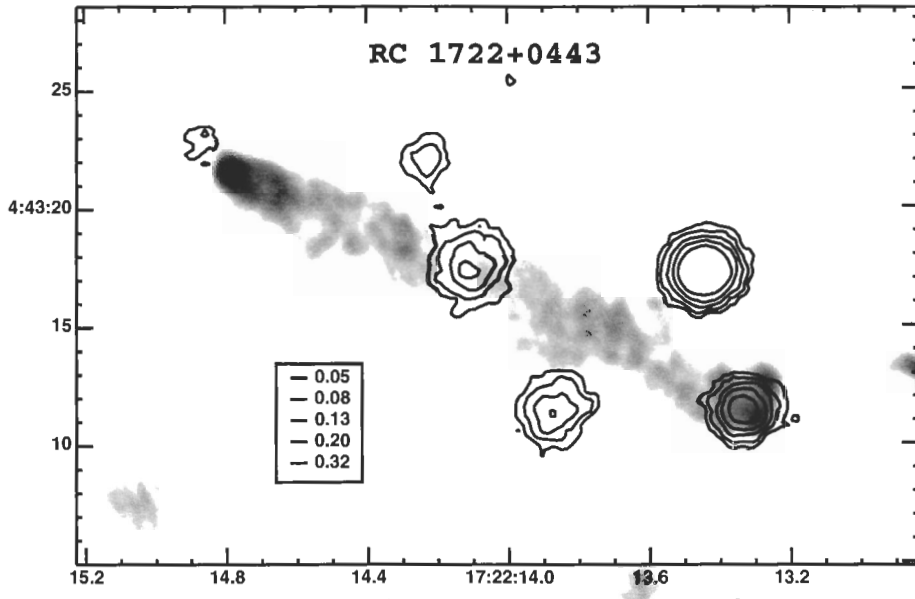

The R-band contours (BTA) superposed on 4860MHz image (VLA)

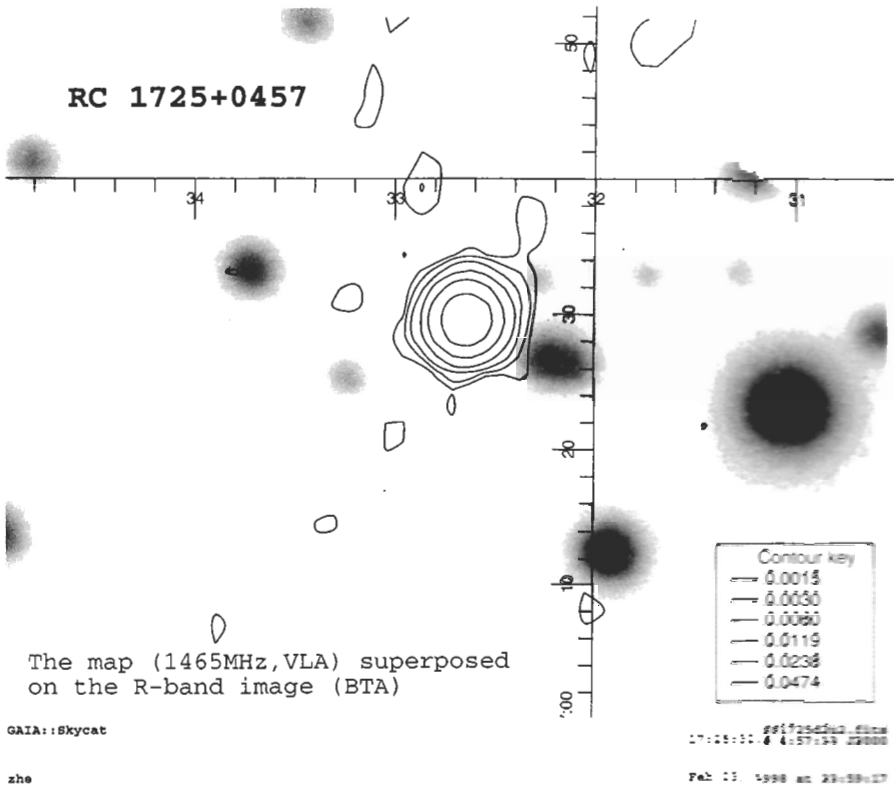

The map (1465MHz,VLA) superposed on the R-band image (BTA)

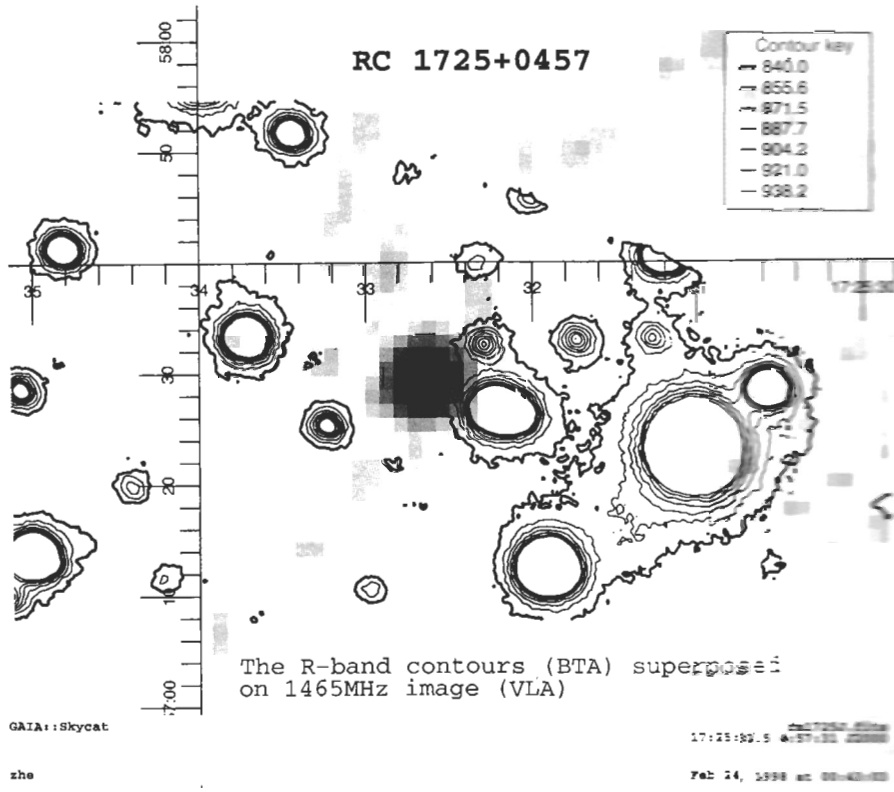

The R-band contours (BTA) superposed on 1465MHz image (VLA)

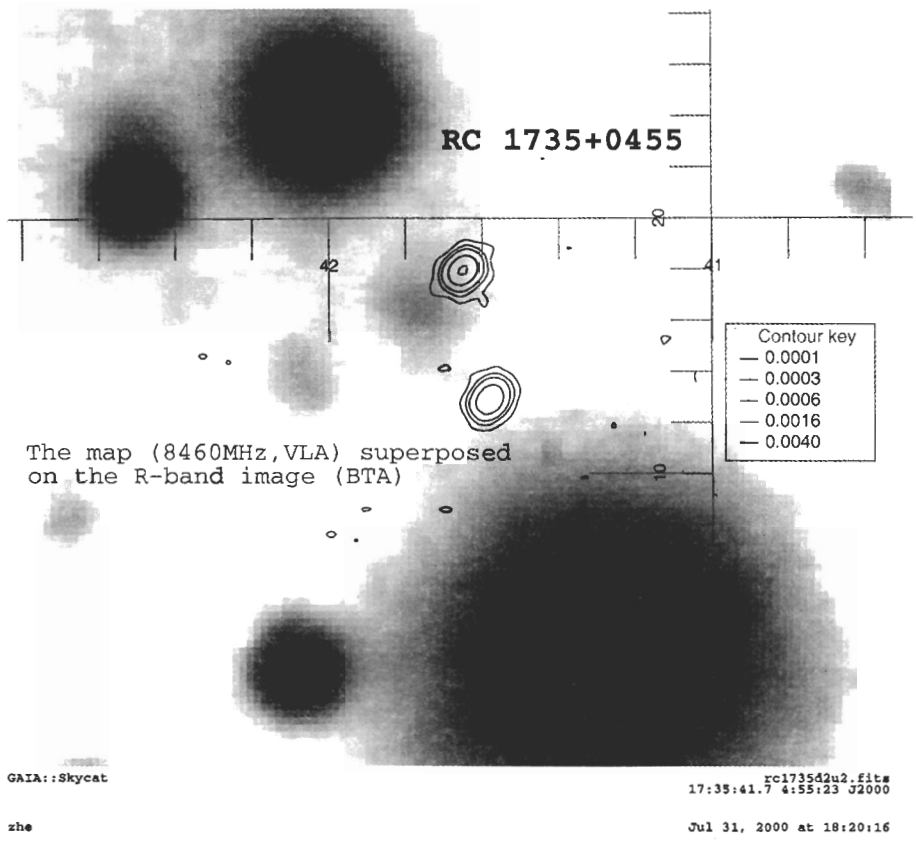
RC 1735+0455
Contour key
— 0.0001
— 0.0003
— 0.0006
— 0.0016
— 0.0040
The map (8460MHz,VLA) superposed
on the R-band image (BTA)
GAIA::Skycat
rc1735d2u2.fits
17:35:41.7 4:55:23 J2000
zhe
Jul 31, 2000 at 18:20:16

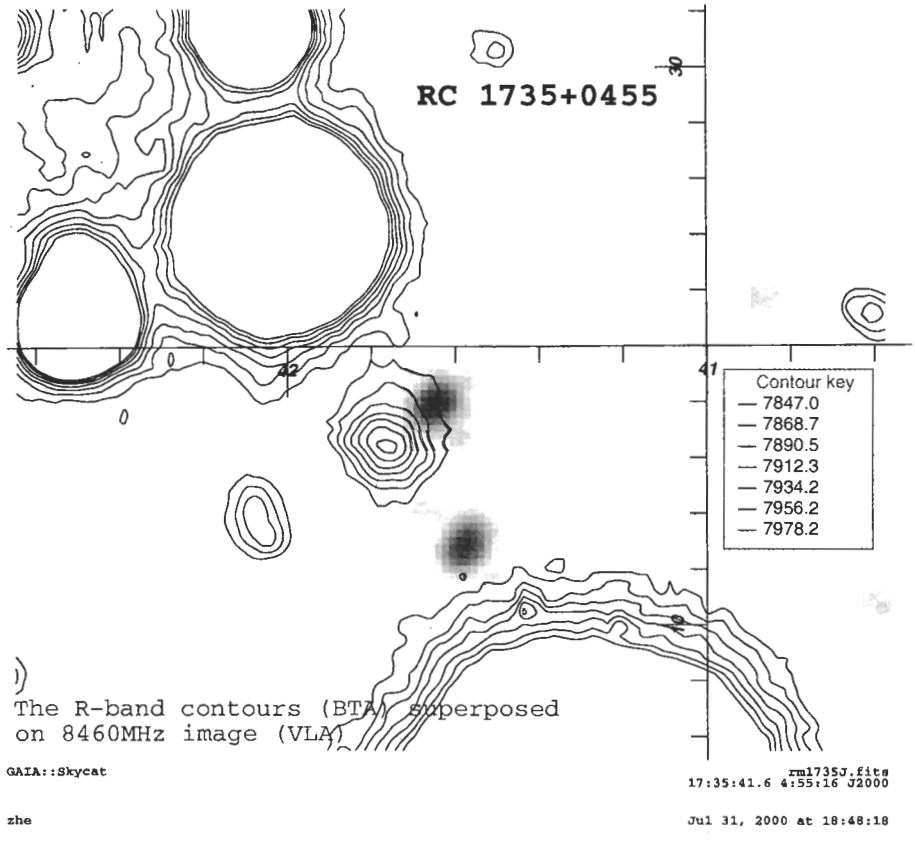
RC 1735+0455
Contour key
— 7847.0
— 7868.7
— 7890.5
— 7912.3
— 7934.2
— 7956.2
— 7978.2
The R-band contours (BTA) superposed
on 8460MHz image (VLA)
GAIA::Skycat
rm1735J.fits
17:35:41.6 4:55:16 J2000
zhe
Jul 31, 2000 at 18:48:18

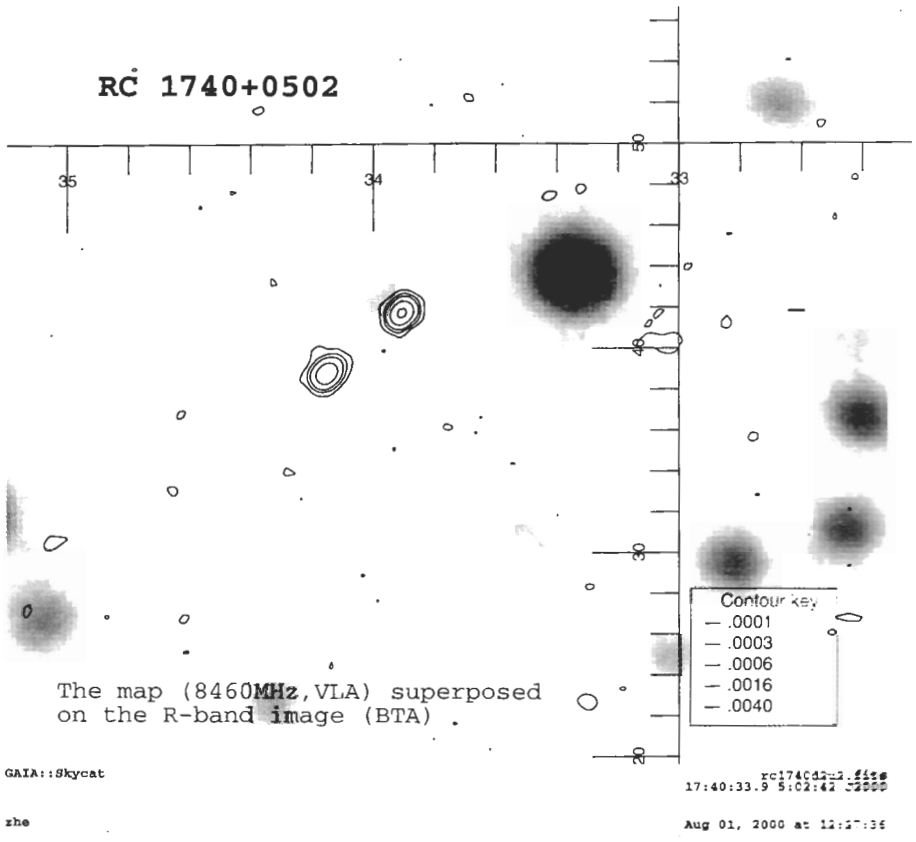

The map (8460MHz,VLA) superposed on the R-band image (BTA) .

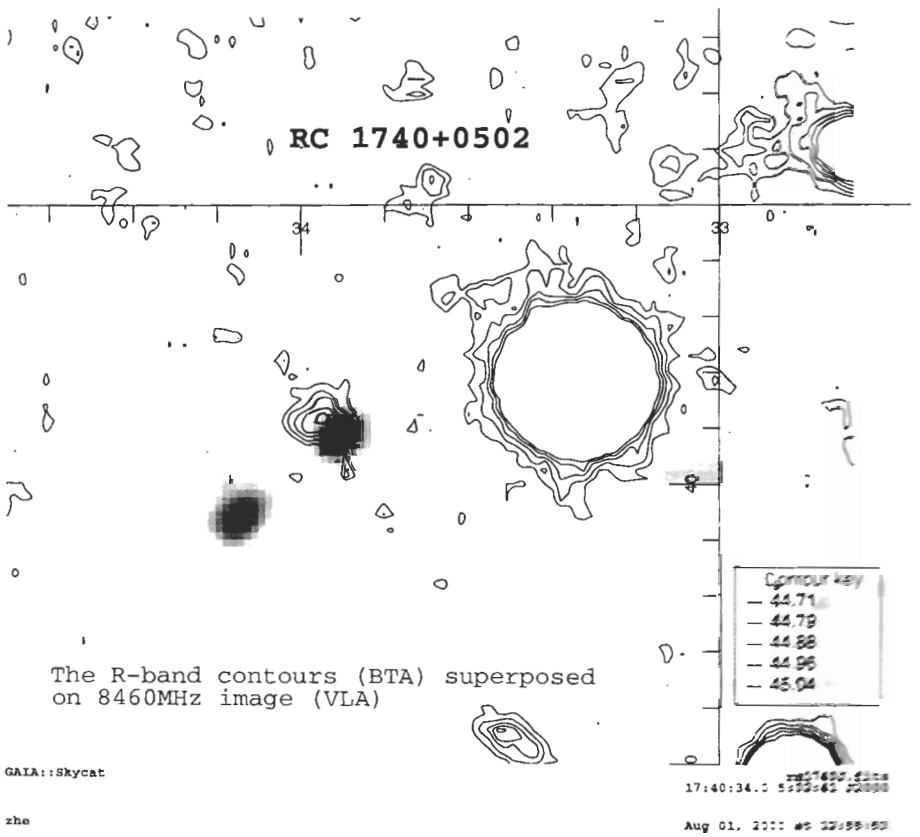

The R-band contours (BTA) superposed on 8460MHz image (VLA)

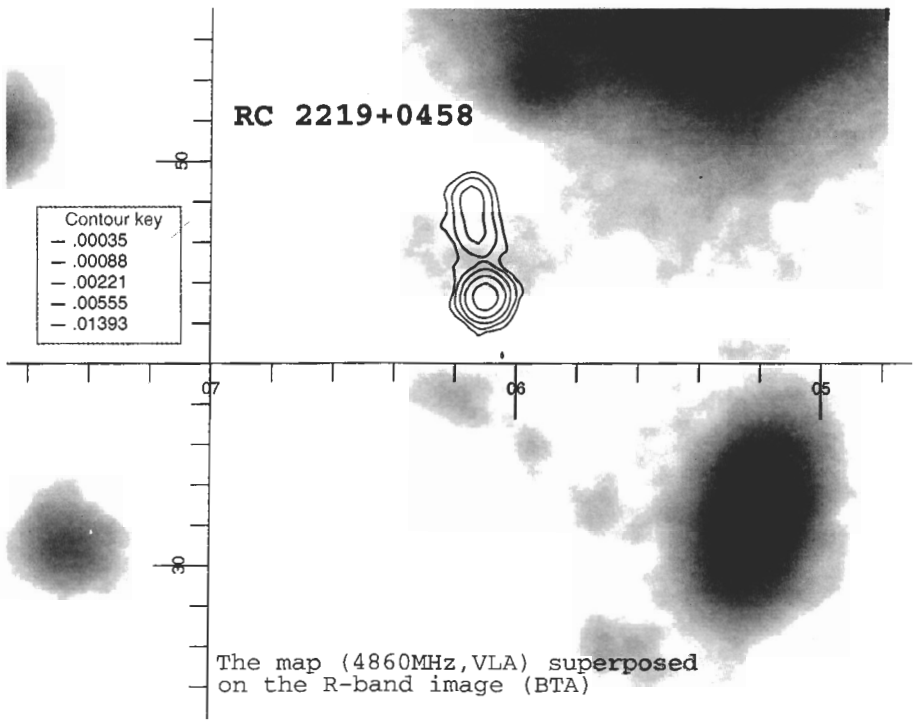
RC 2219+0458
Contour key
.00035
.00088
.00221
.00555
.01393
50
07
06
05
30
The map (4860MHz,VLA) superposed
on the R-band image (BTA)
GAIA::Skycat
rc2219d2u2.fits
22:19:04.9 4:58:36 J2000
zhe
Aug 23, 1998 at 17:09:14

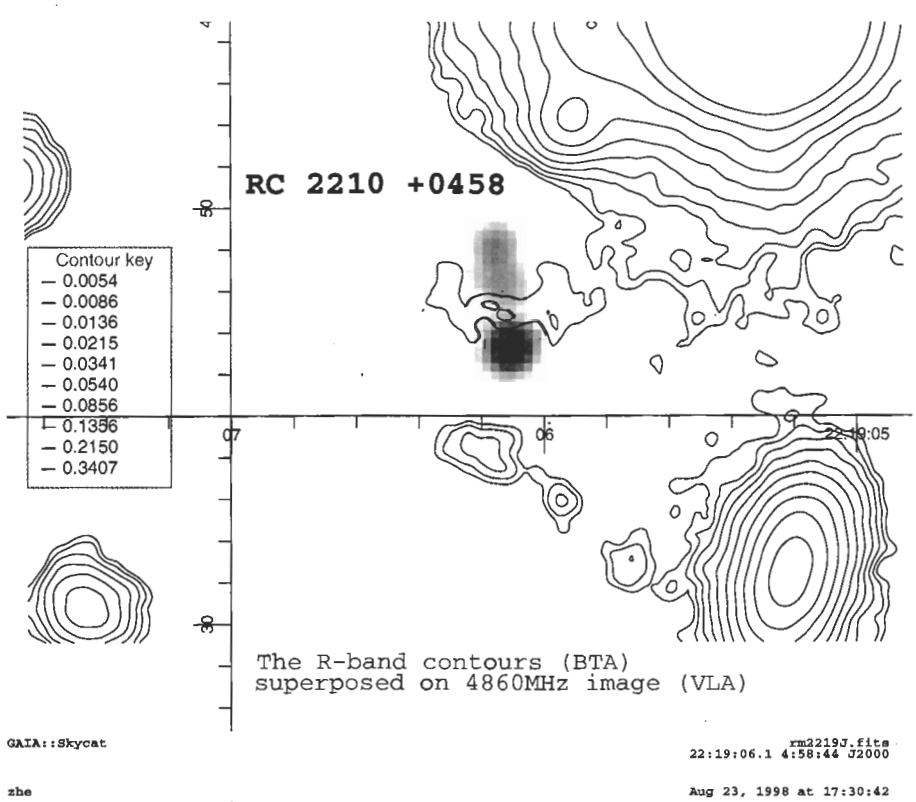
RC 2210 +0458
Contour key
0.0054
0.0086
0.0136
0.0215
0.0341
0.0540
0.0856
0.1356
0.2150
0.3407
50
07
06
22:19:05
30
The R-band contours (BTA)
superposed on 4860MHz image (VLA)
GAIA::Skycat
rm2219J.fits
22:19:06.1 4:58:44 J2000
zhe
Aug 23, 1998 at 17:30:42

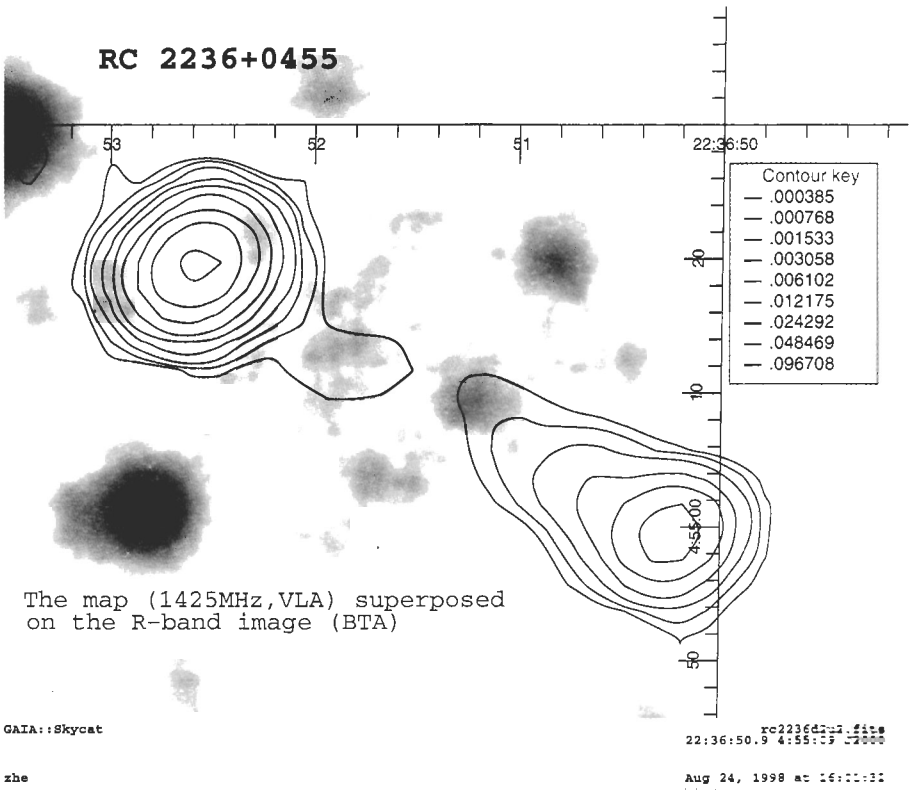

The map (1425MHz,VLA) superposed on the R-band image (BTA)

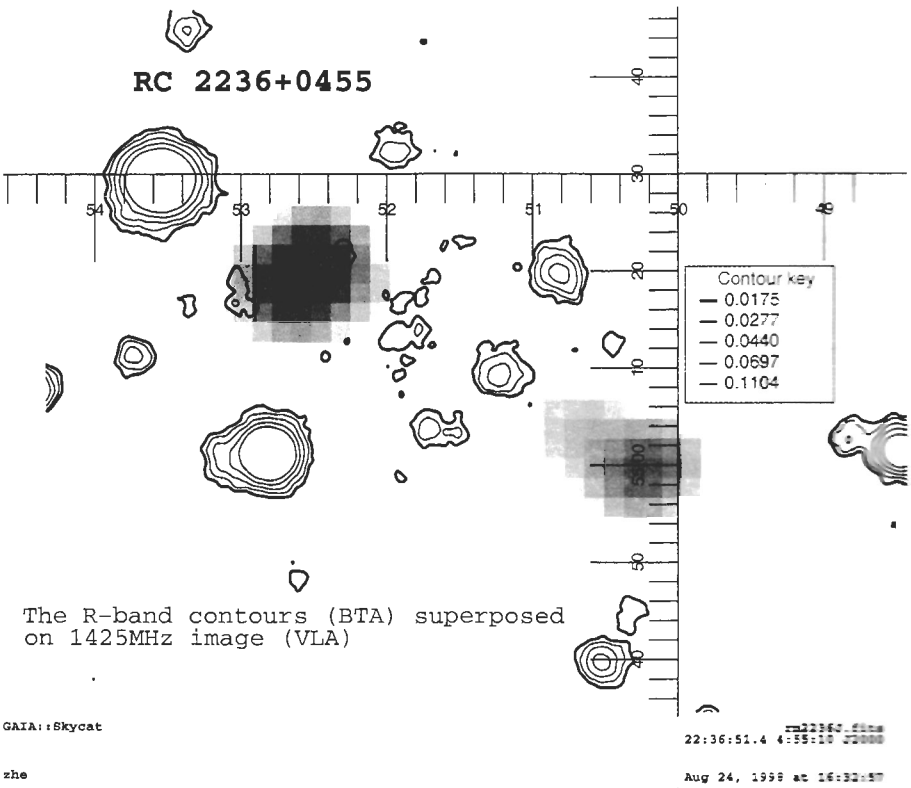

The R-band contours (BTA) superposed on 1425MHz image (VLA)

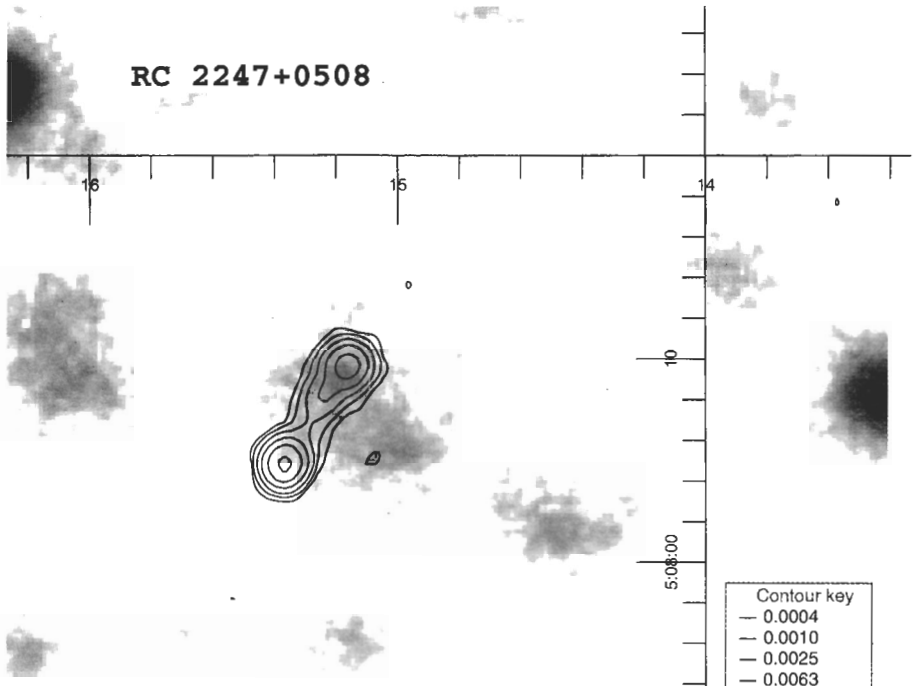

The map (4860MHz,VLA) superposed on the R-band image (BTA)

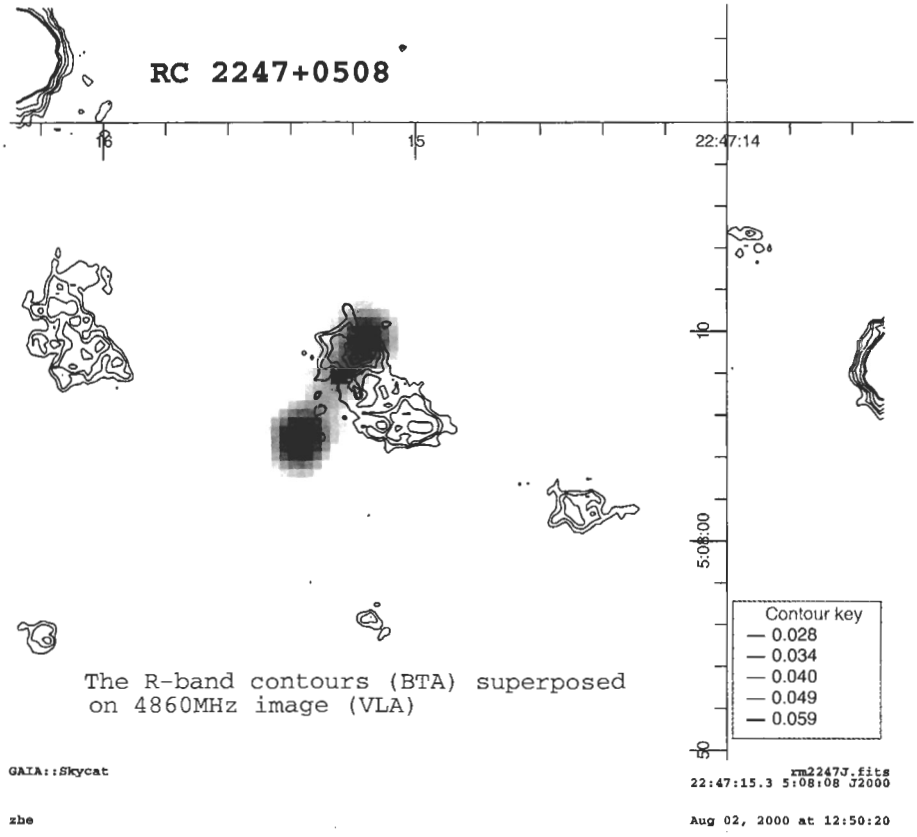

The R-band contours (BTA) superposed on 4860MHz image (VLA)

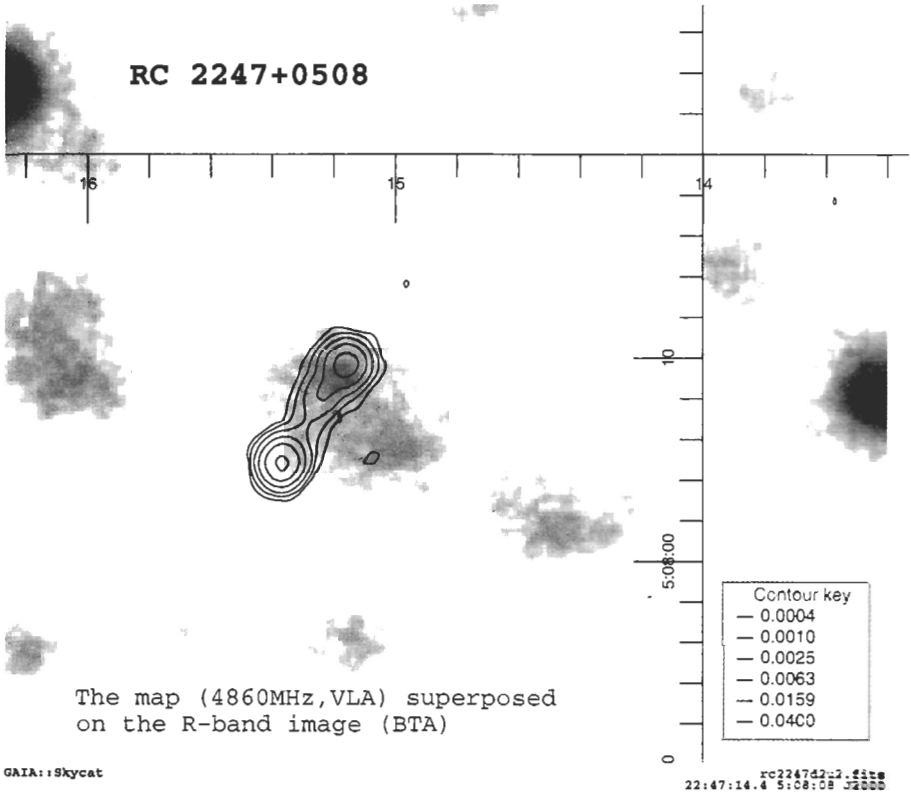

The map (4860MHz,VLA) superposed on the R-band image (BTA)

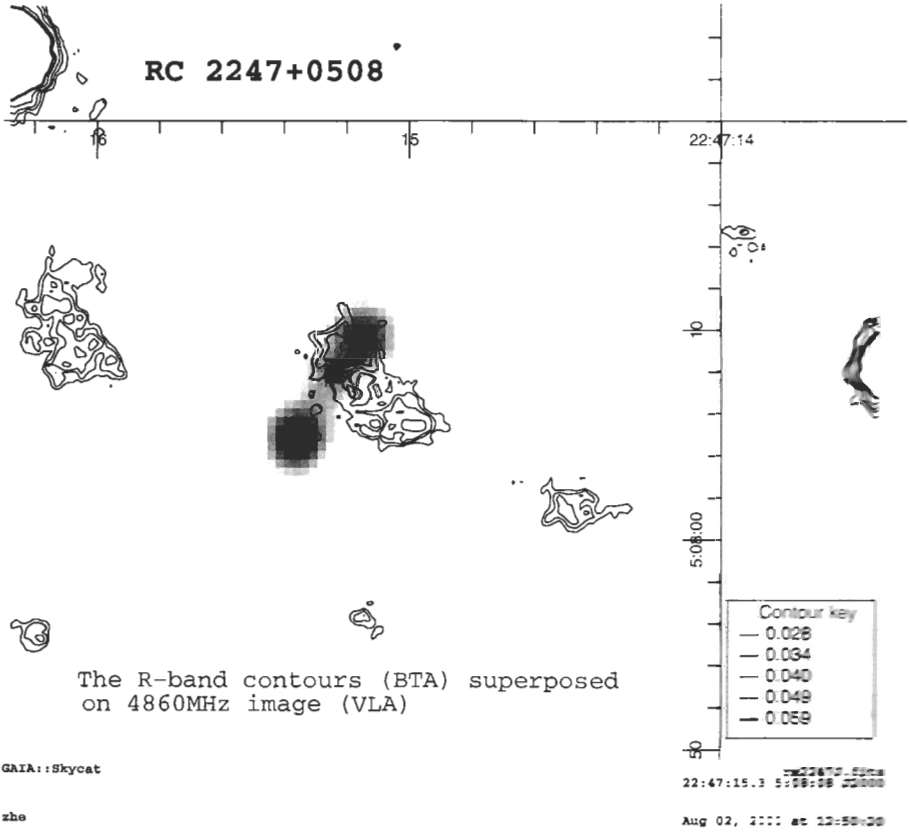

The R-band contours (BTA) superposed on 4860MHz image (VLA)

Fig. 6. Fitted SED models and corresponding probability functions for RC objects.

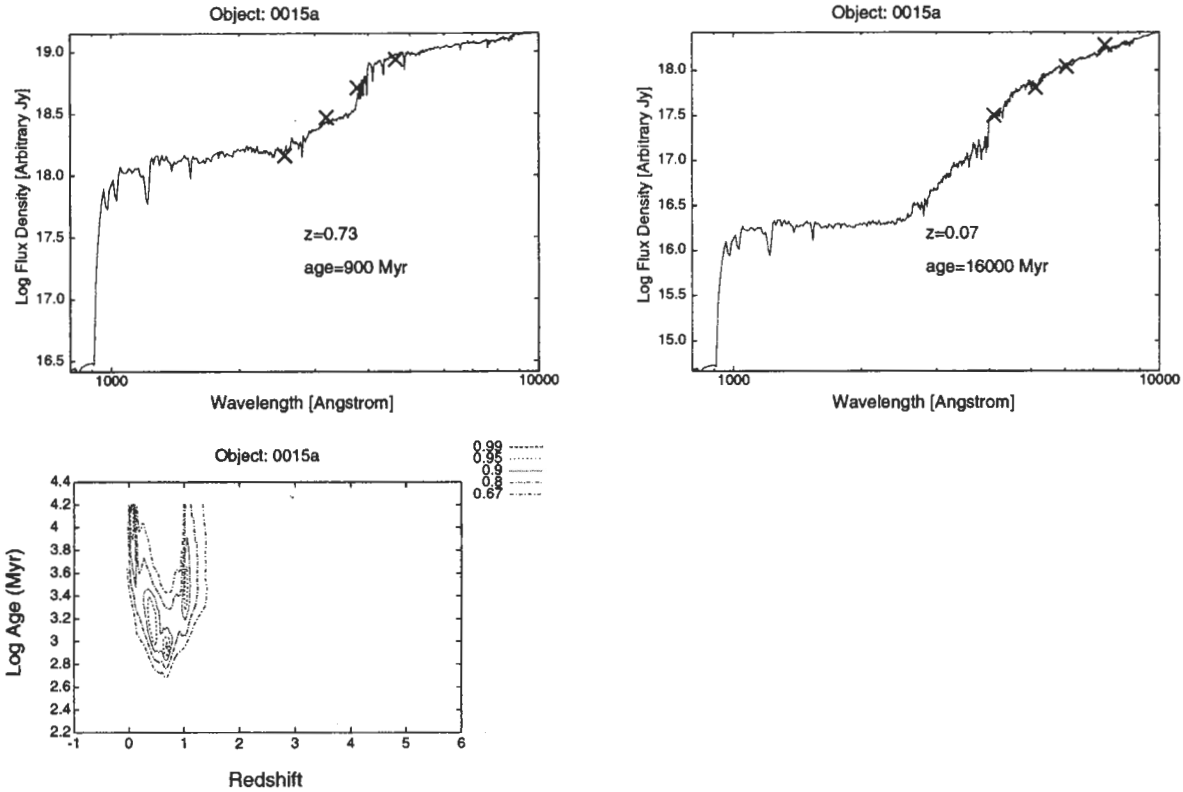

PEGASE models for RC J0015+0503a: SEDs and probability function

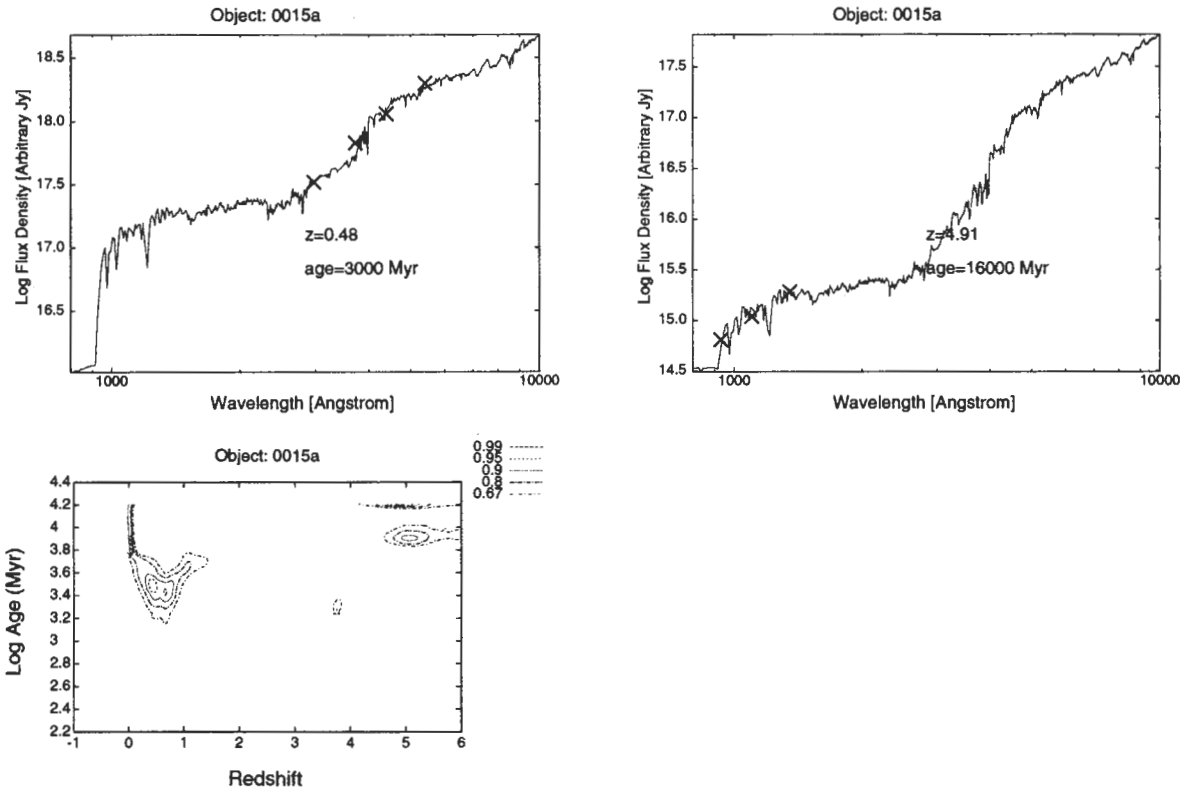

GISSEL models for RC J0015+0503a: SEDs and probability function

PEGASE models for RC J0015+0501

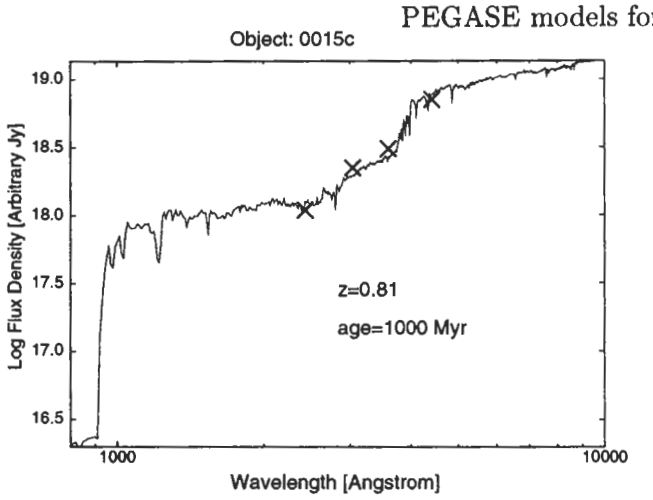

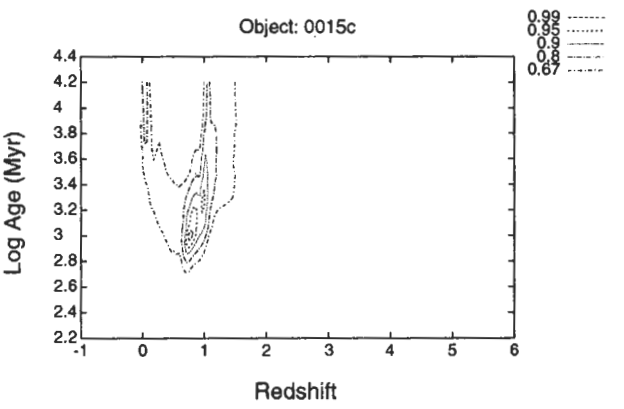

GISSEL models for RC J0015+0501

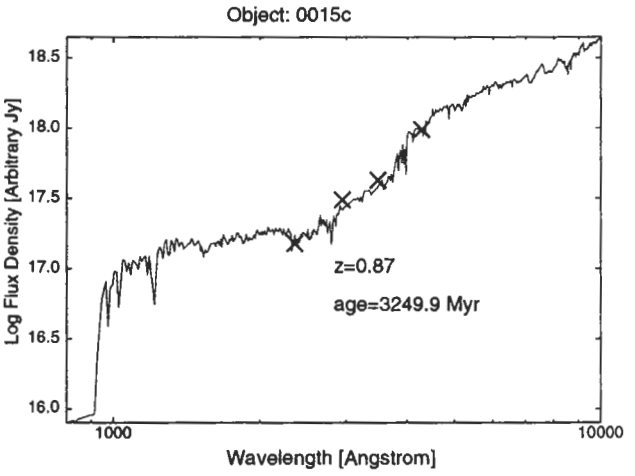

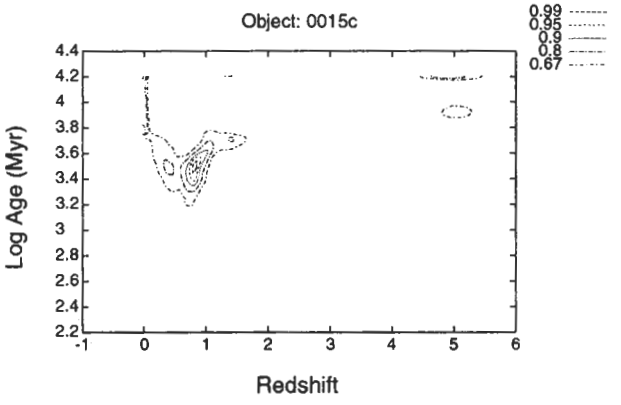

PEGASE models for RC J0034+0513

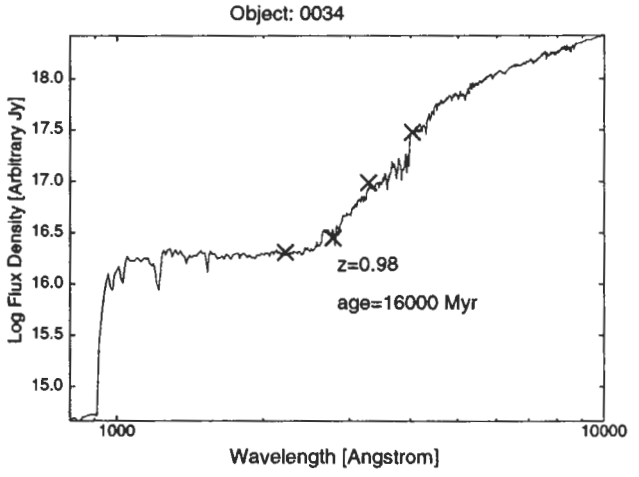

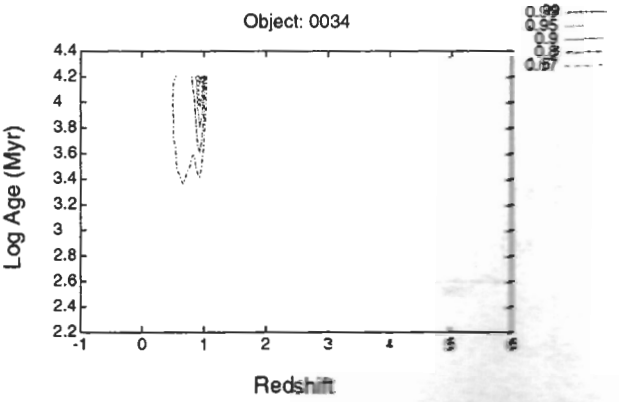

GISSEL models for RC J0034+0513

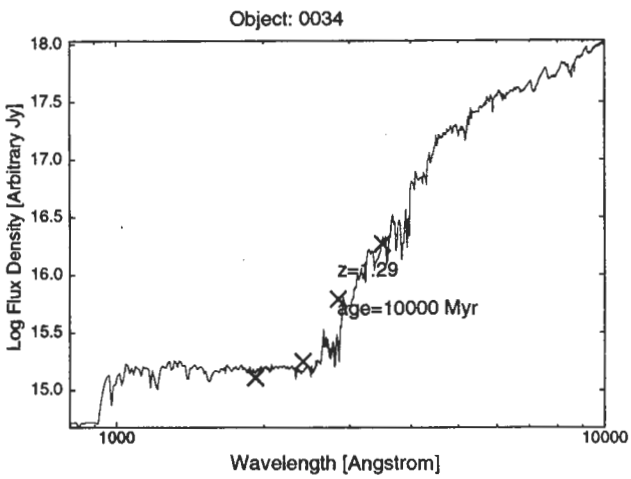

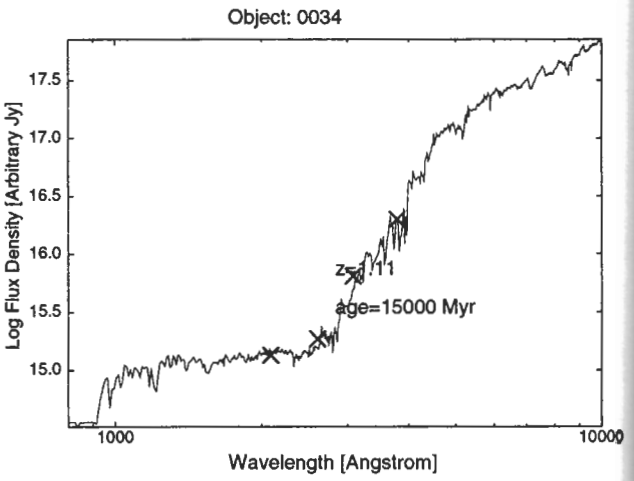

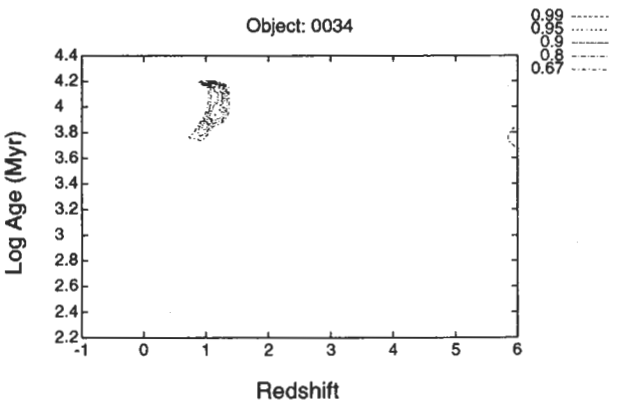

PEGASE models for RC J0039+0454

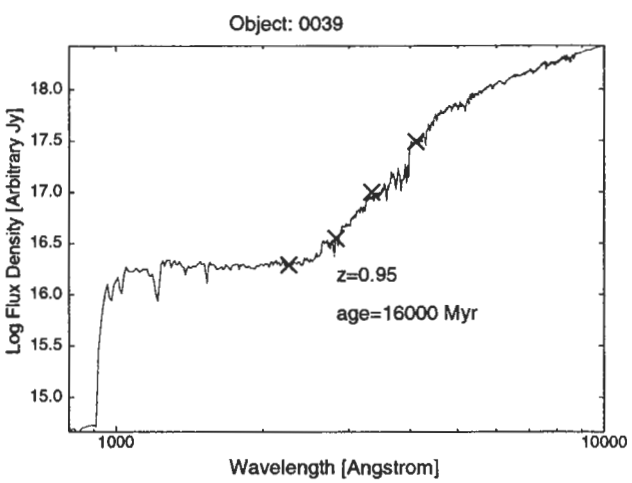

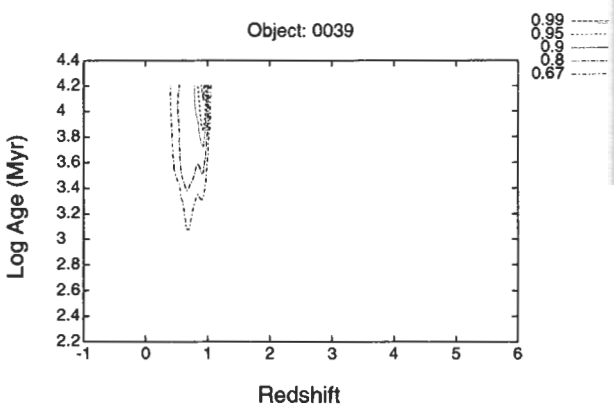

GISSEL models for RC J0039+0454

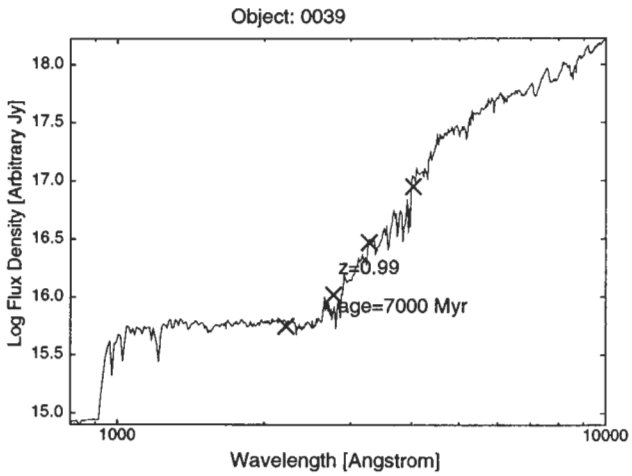

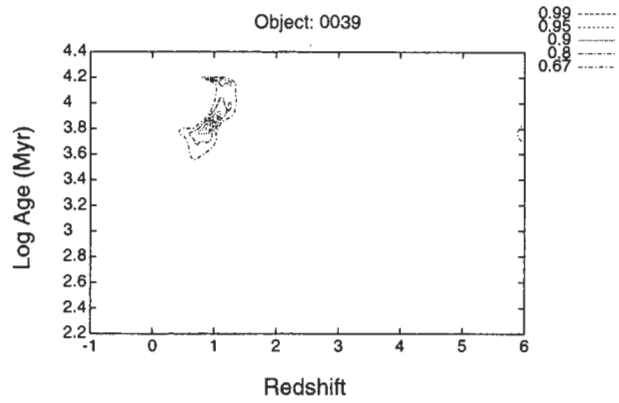

PEGASE for RC J0105+0501

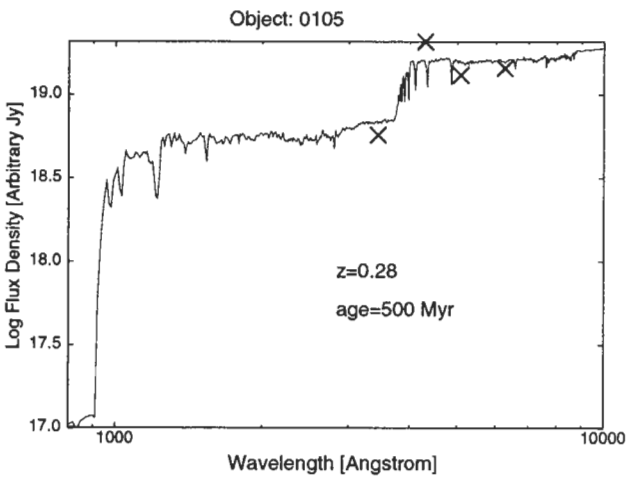

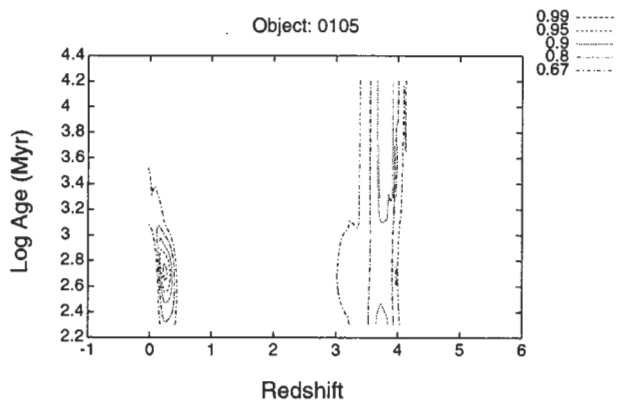

GISSEL models for RC J0105+0501

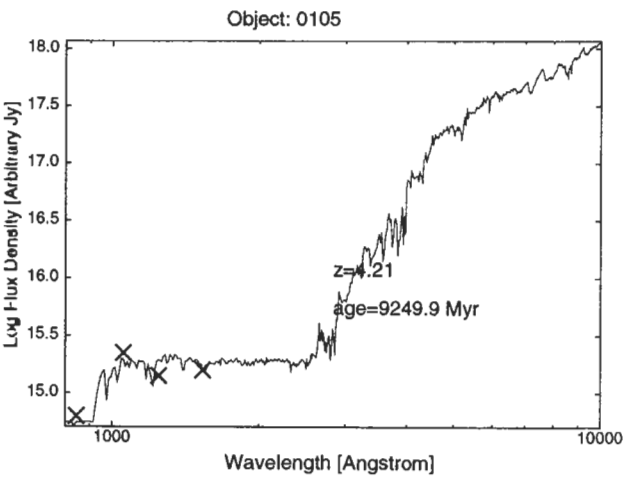

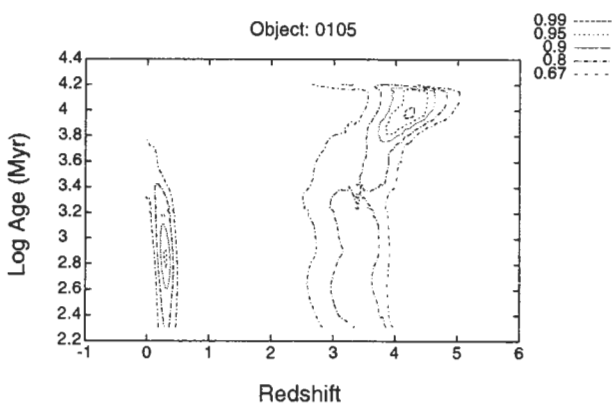

PEGASE for RC J0135+0450

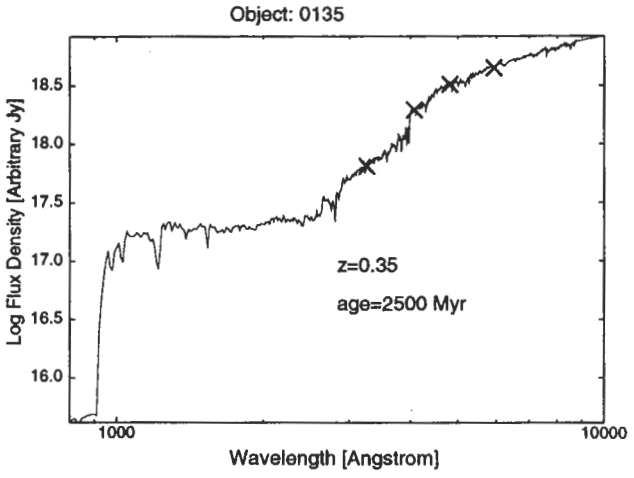

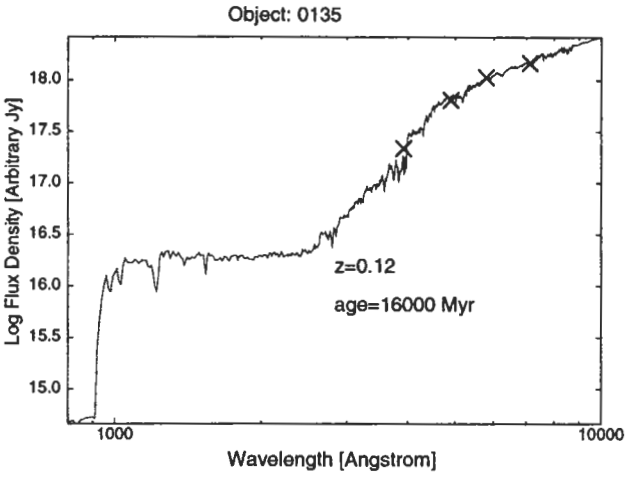

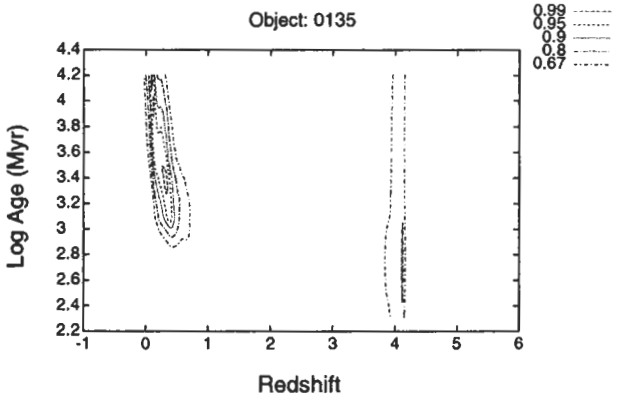

GISSEL for RC J0135+0450

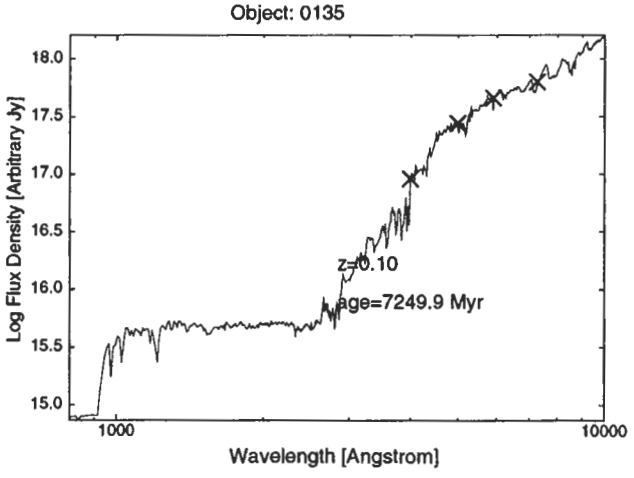

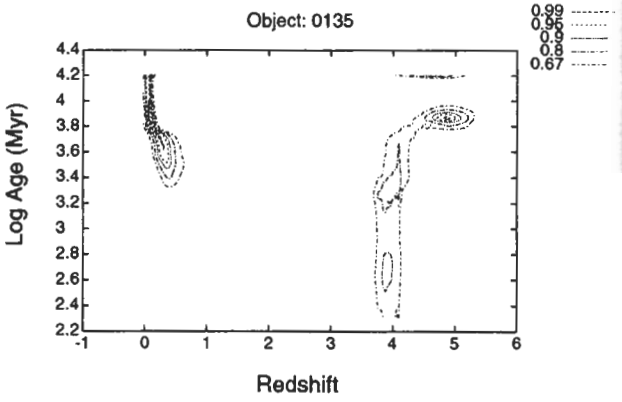

PEGASE models for RC 0152+0453

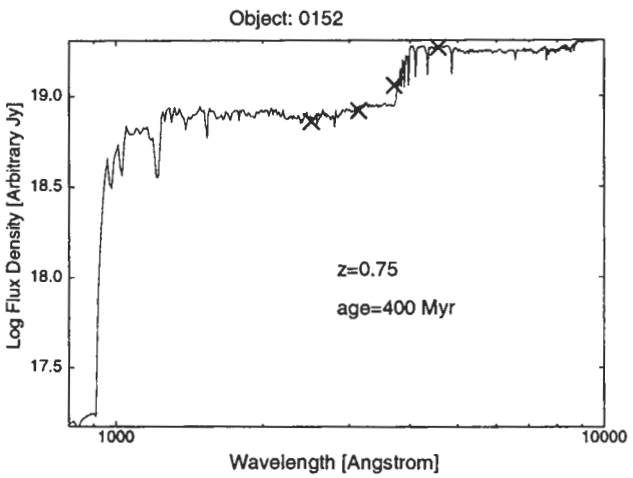

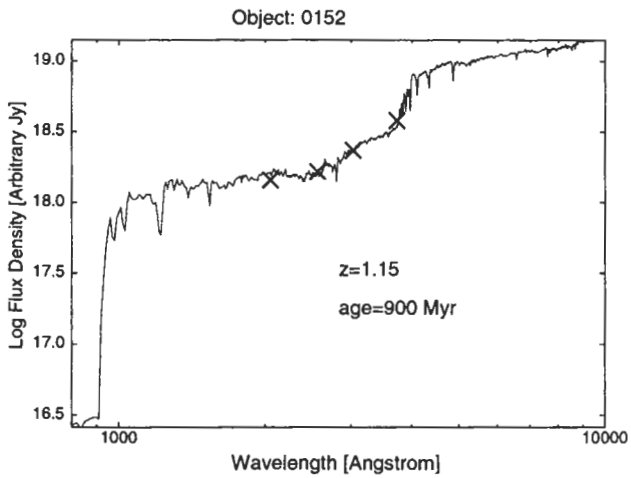

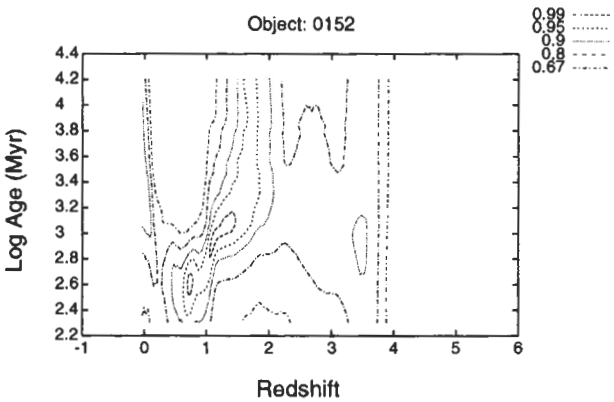

GISSEL models for RC 0152+0453

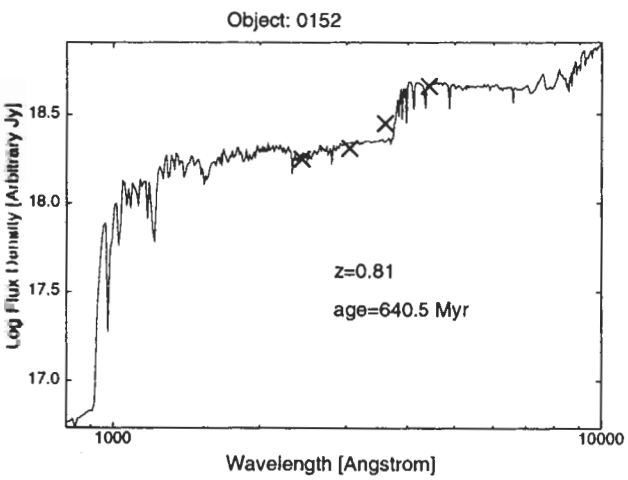

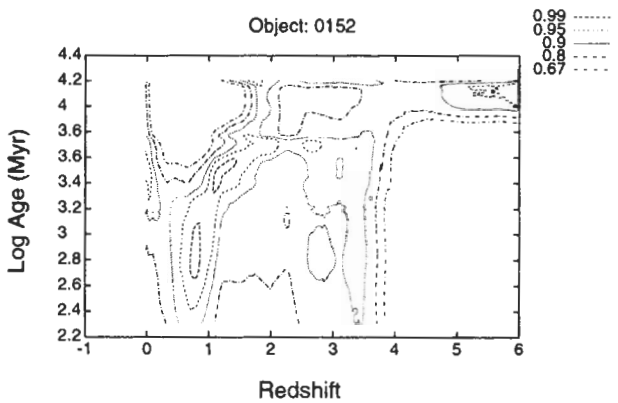

PEGASE models for RC J0159+0448

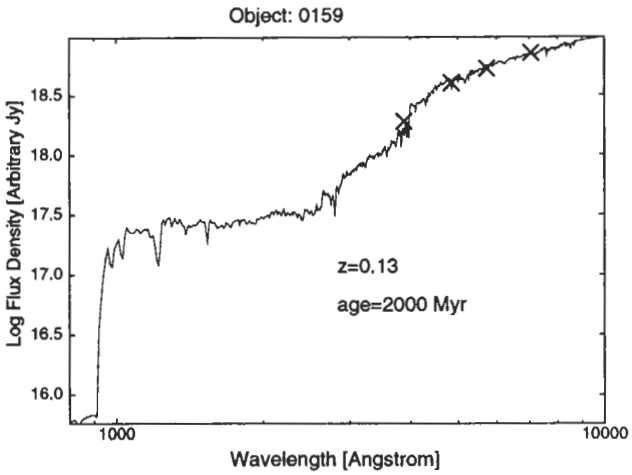

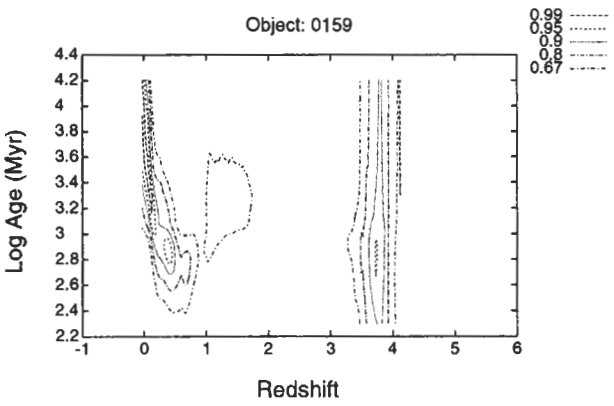

GISSEL models for RC J0159+0448

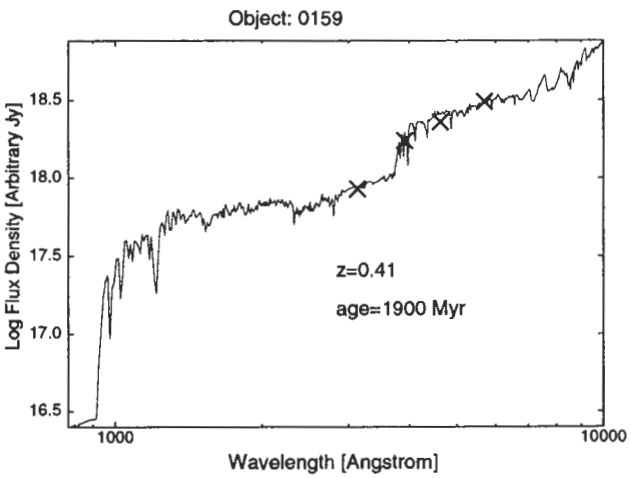

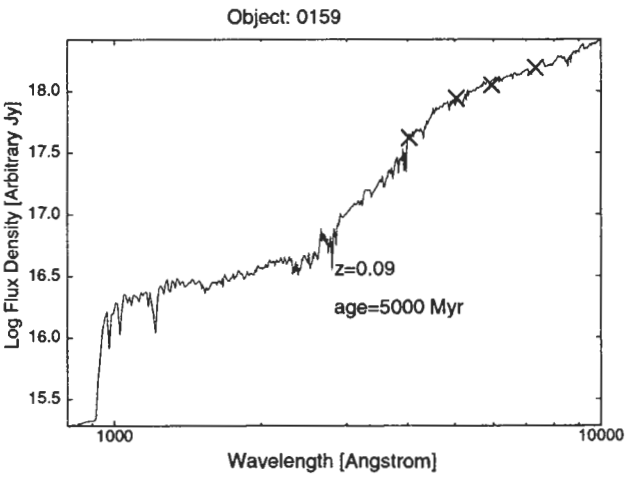

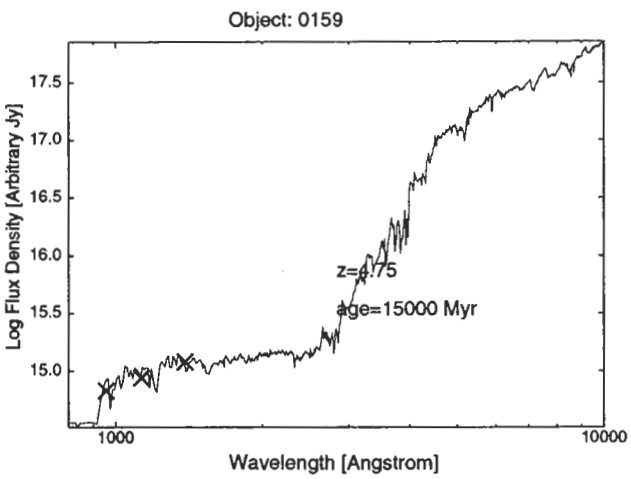

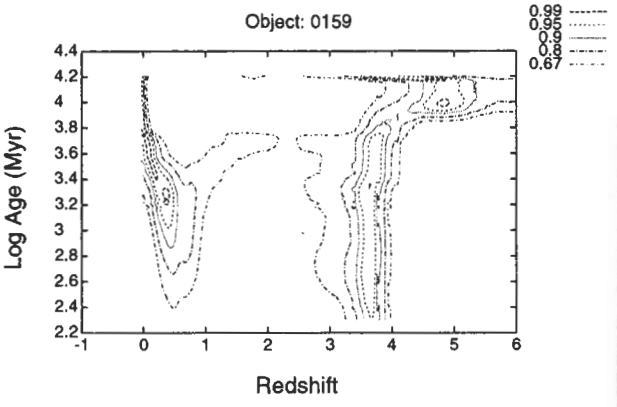

PEGASE models for RC J0209+0501a

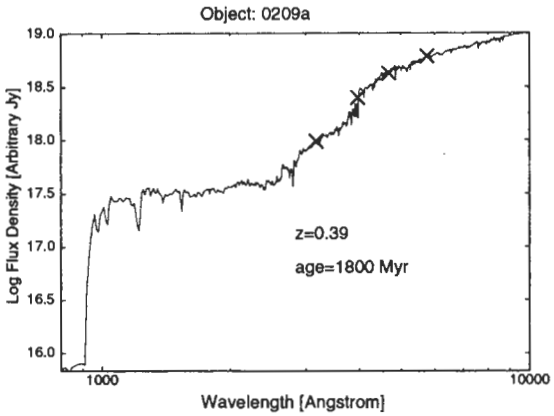

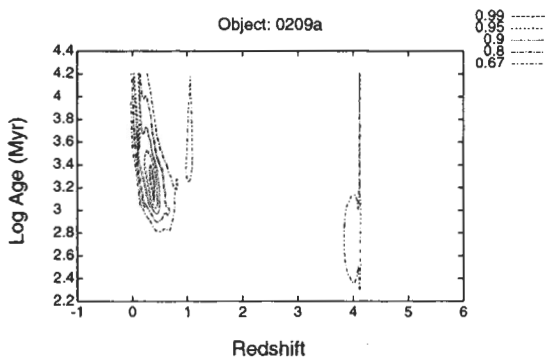

GISSEL models for RC J0209+0501a: SEDs and probability function

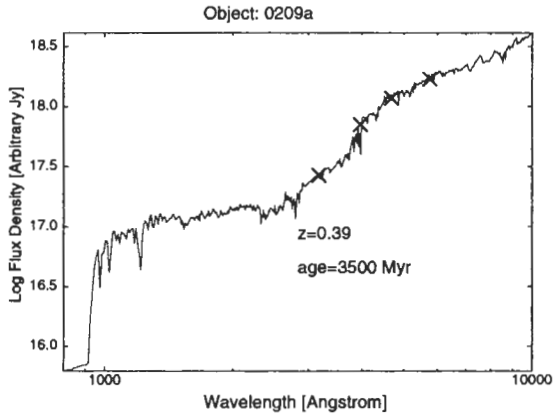

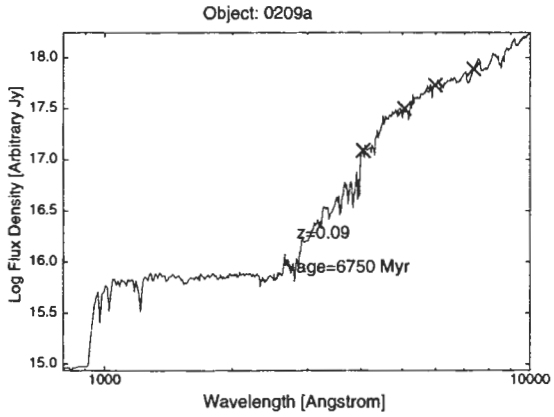

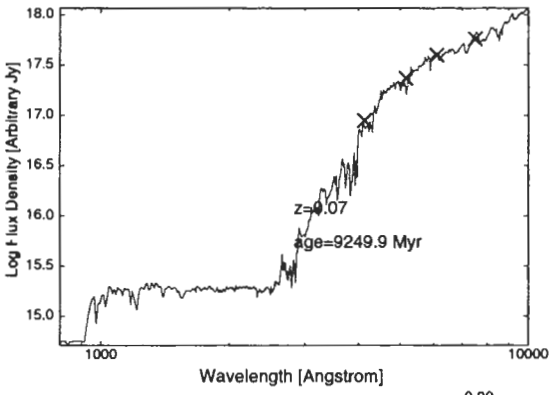

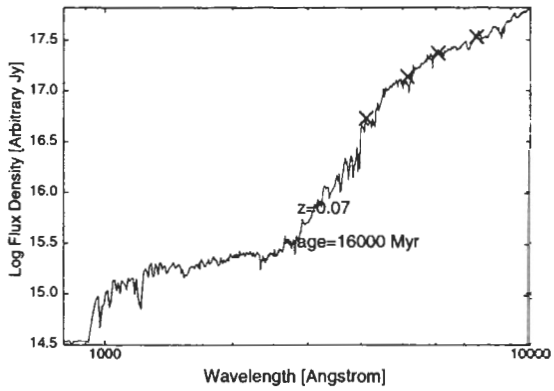

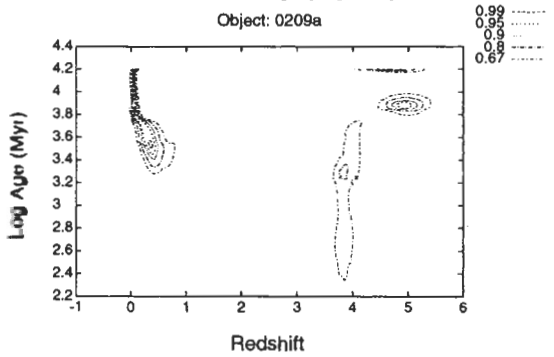

PEGASE models for RC J0209+0501b: SEDs and probability function

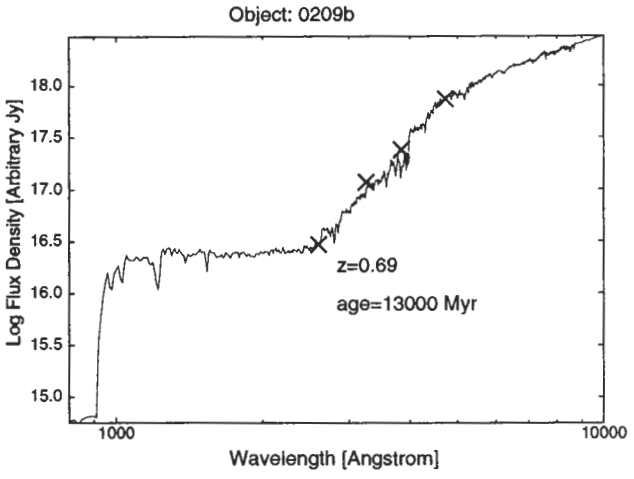

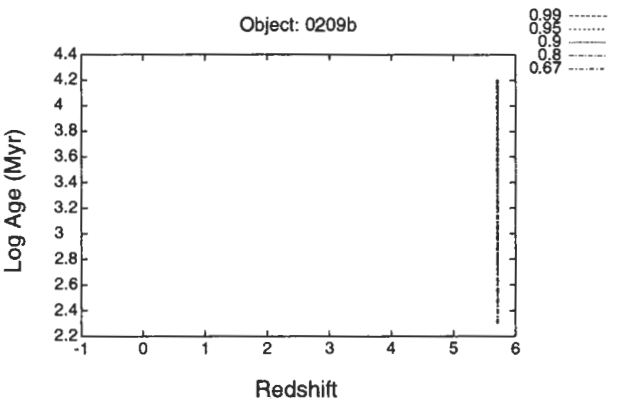

GISSEL models for RC J0209+0501b

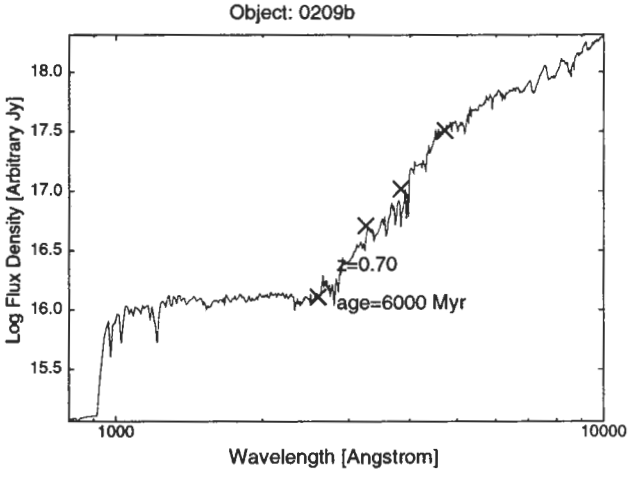

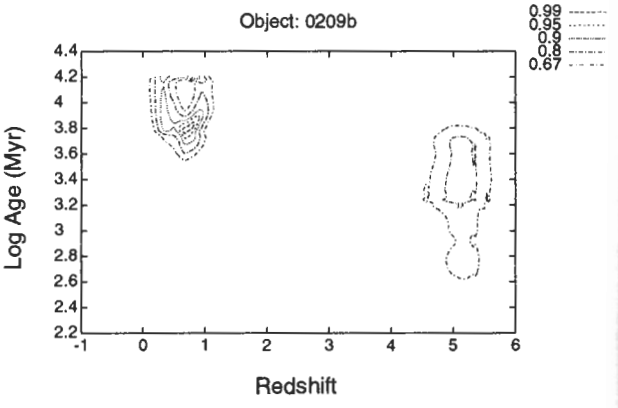

PEGASE models for RC J0318+0456

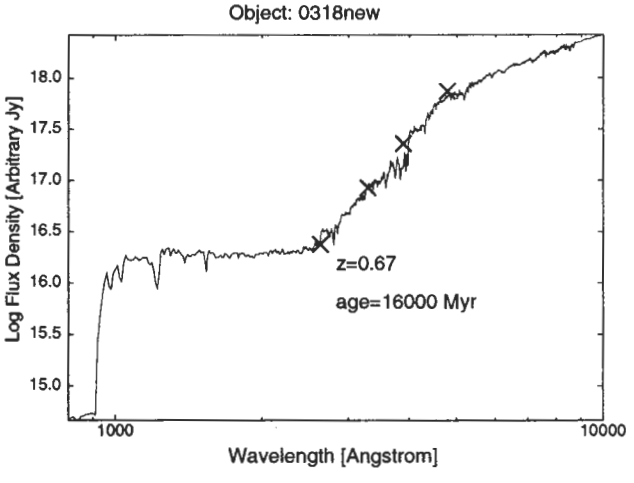

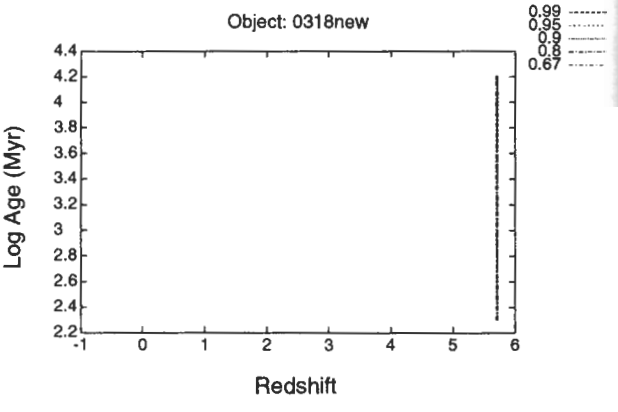

GISSEL models for RC J0318+0456

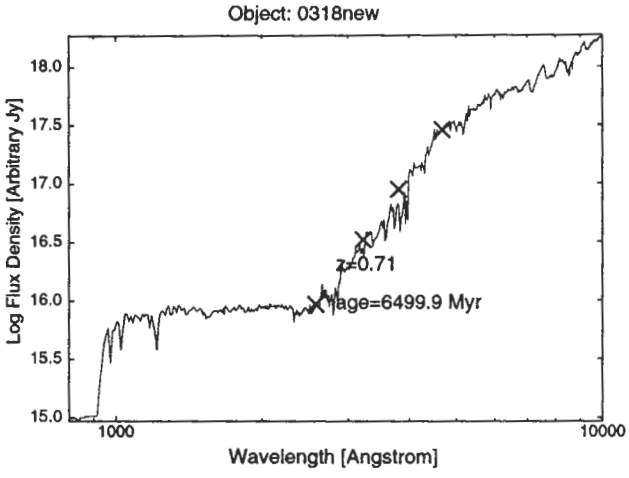

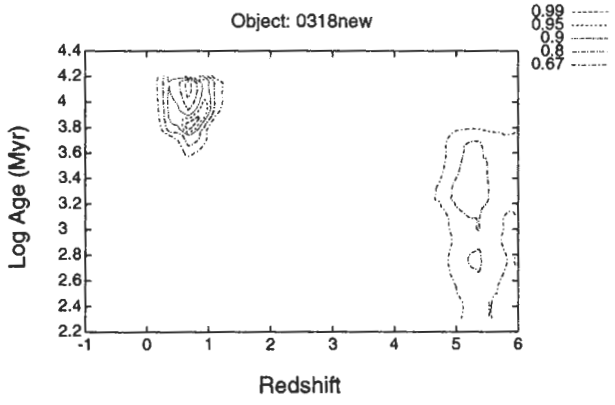

PEGASE models for RC J0444+0501

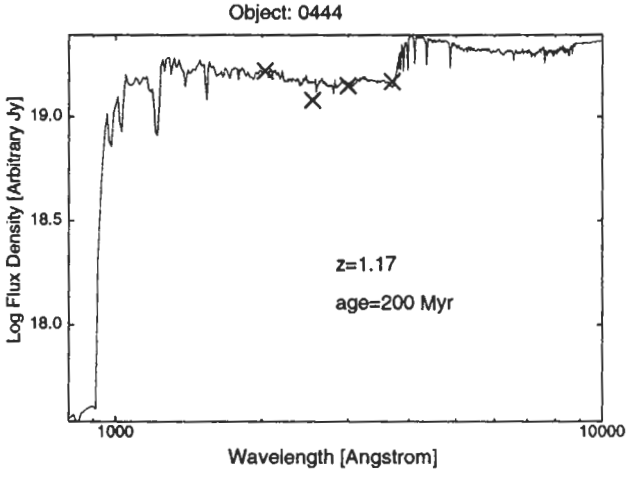

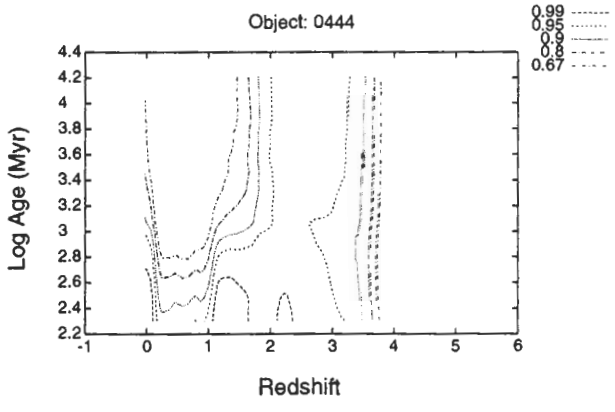

GISSEL models for RC J0444+0501

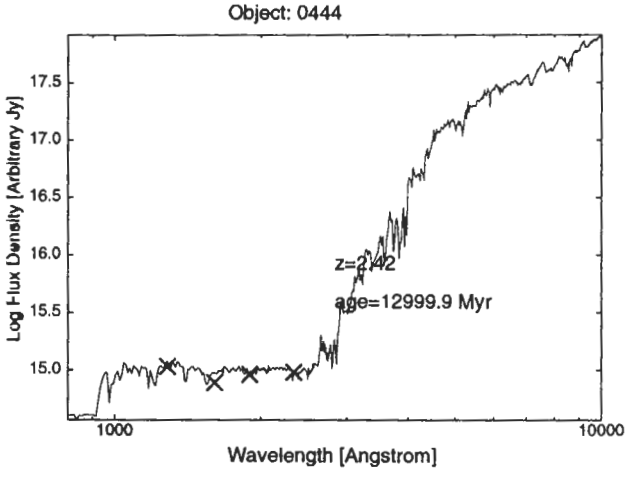

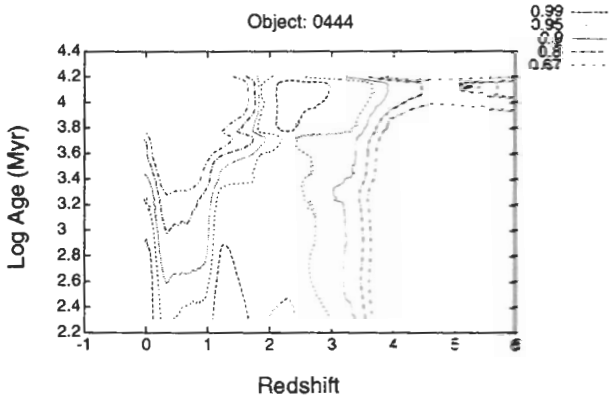

PEGASE models for RC J0457+0452

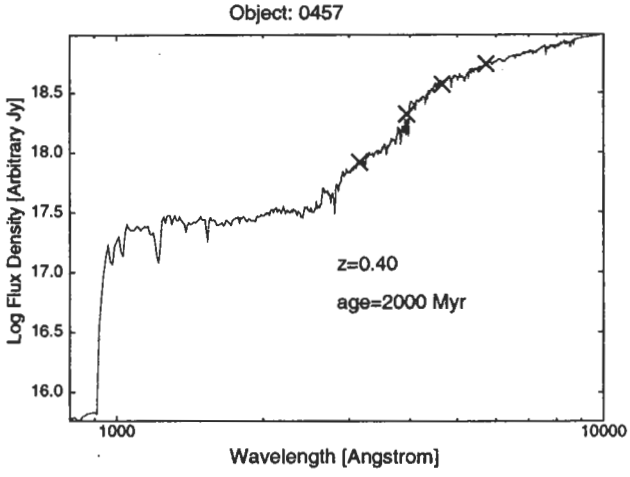

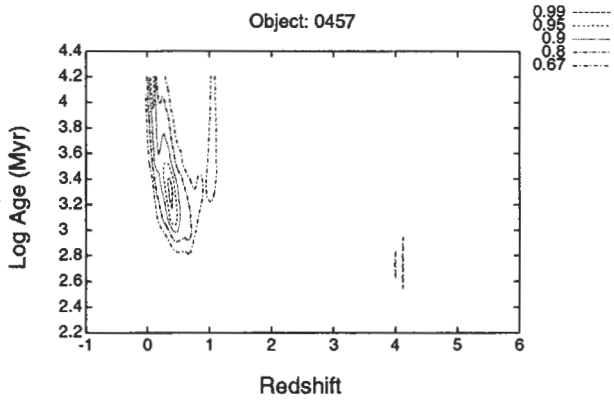

GISSEL models for RC J0457+0452

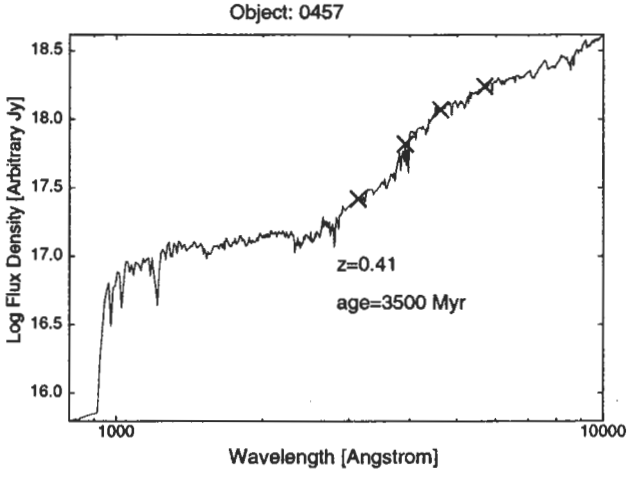

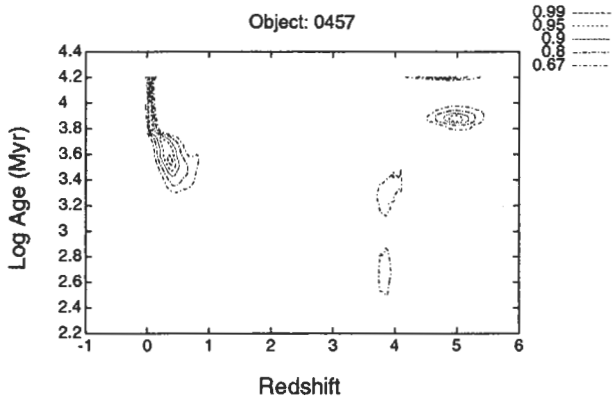

PEGASE models for RC J0836+0511

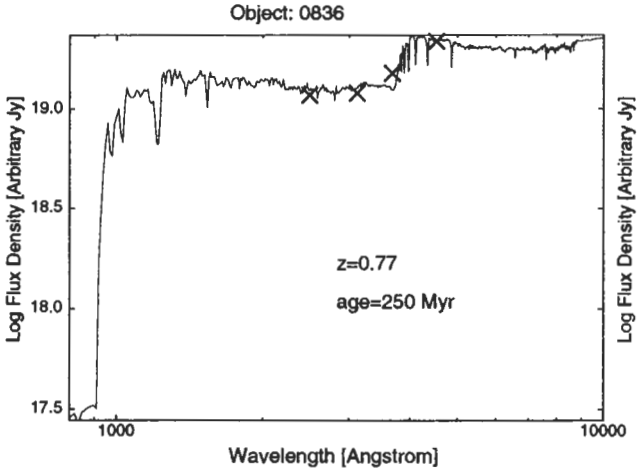

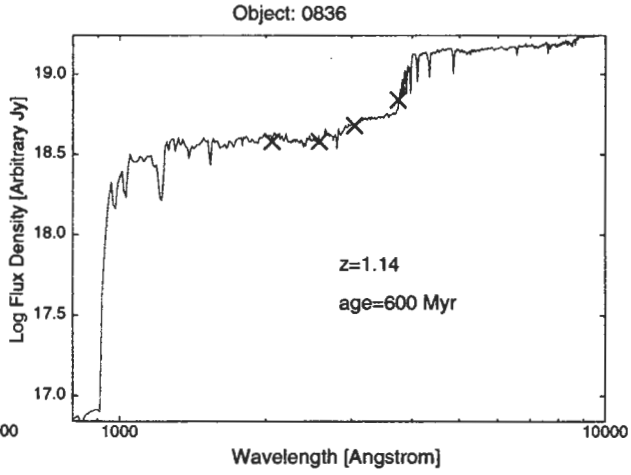

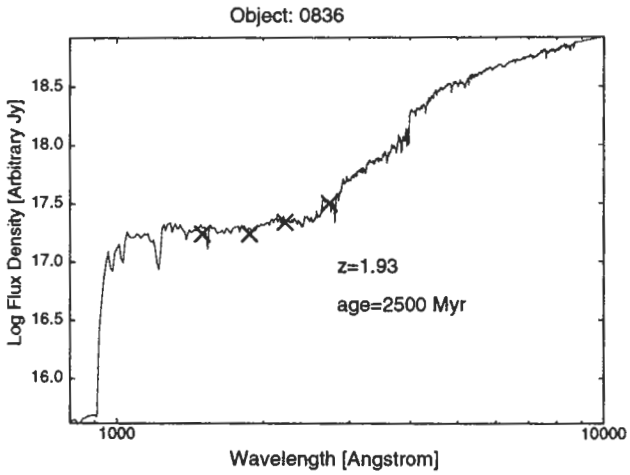

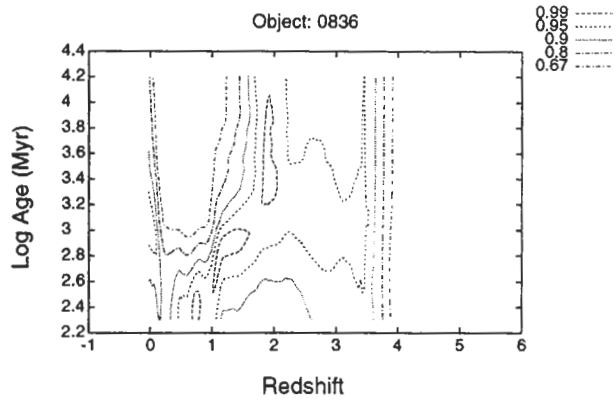

GISSEL models for RC J0836+0511

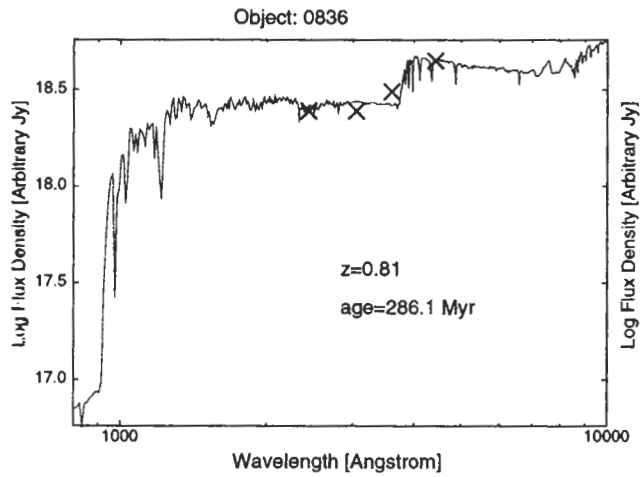

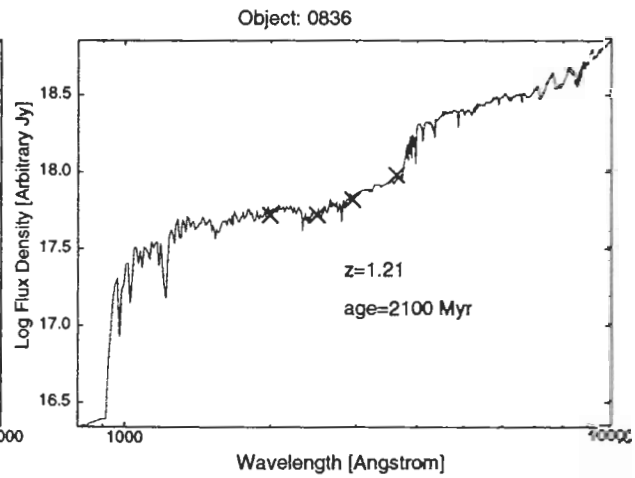

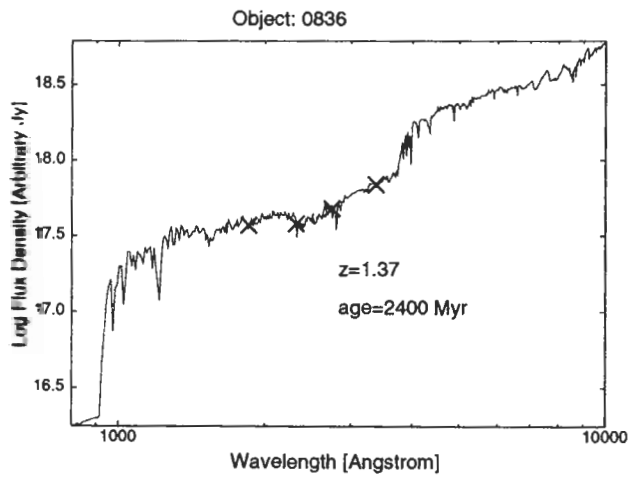

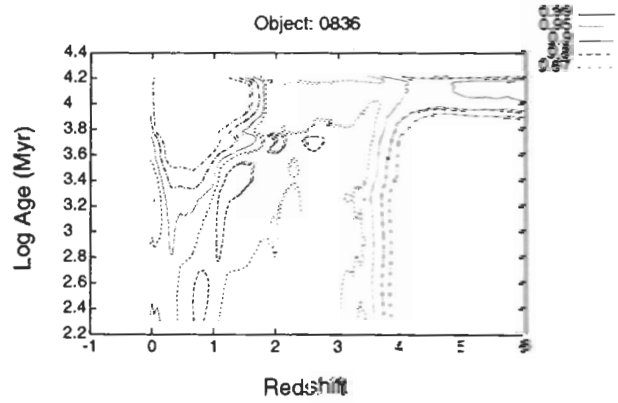

PEGASE models for RC J0837+0446

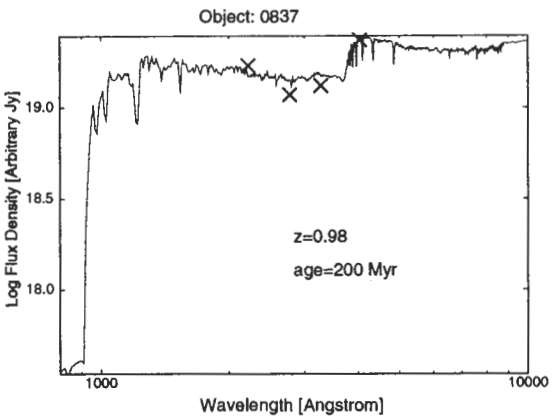

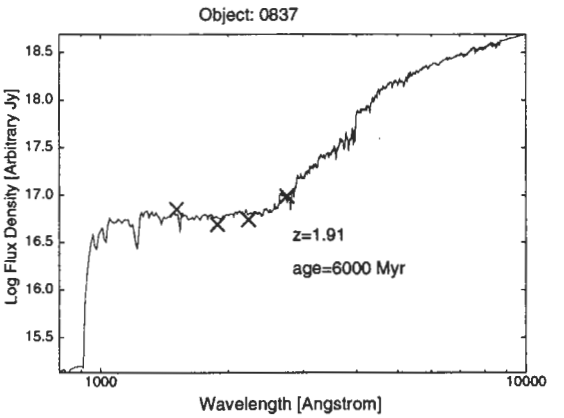

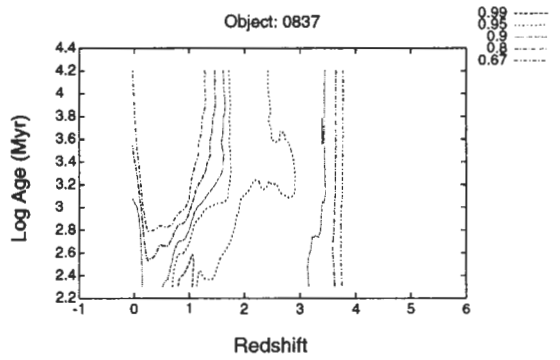

GISSEL models for RC J0837+0446

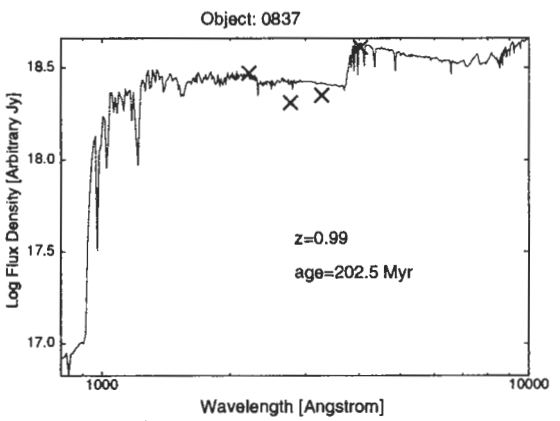

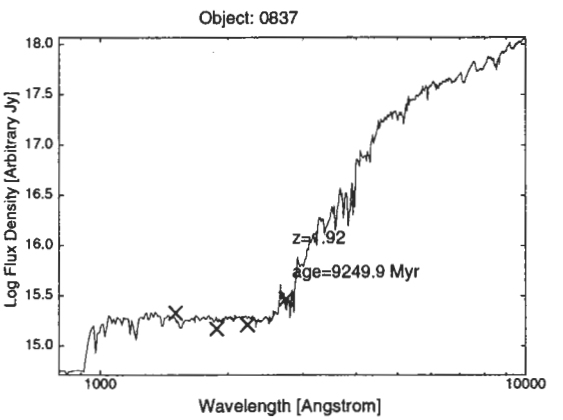

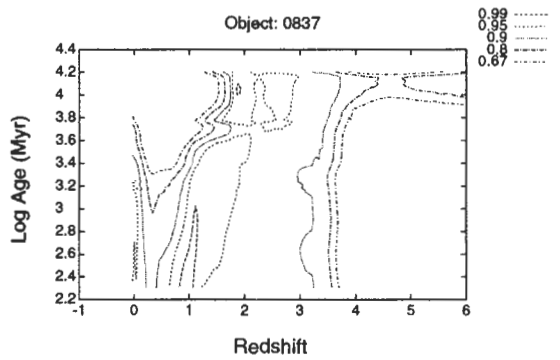

PEGASE models for RC J0845+0444

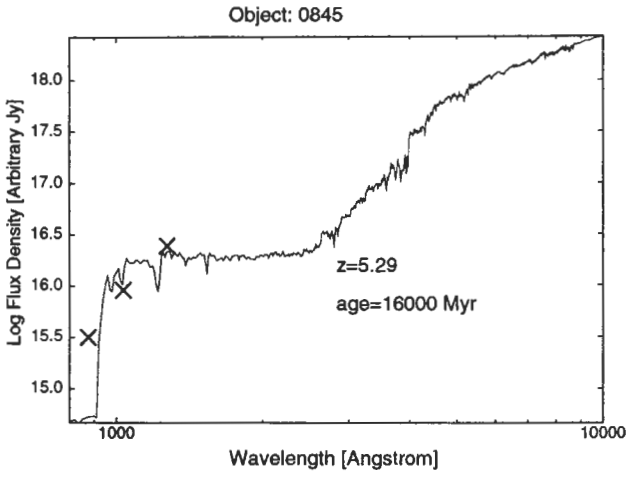

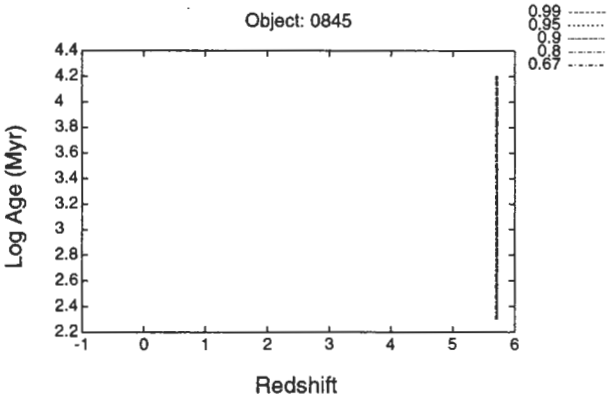

GISSEL models for RC J0845+0444

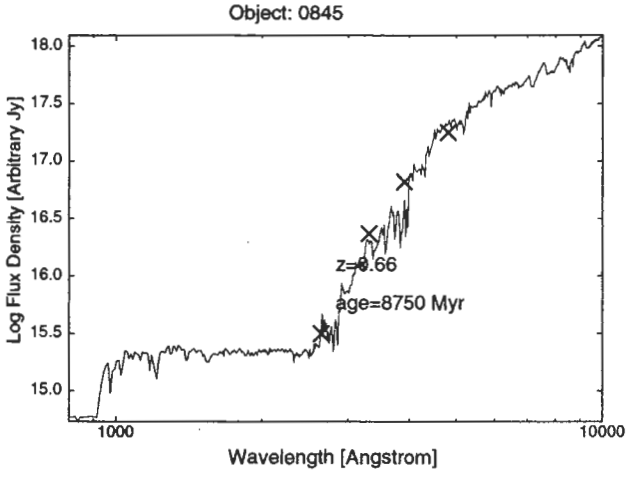

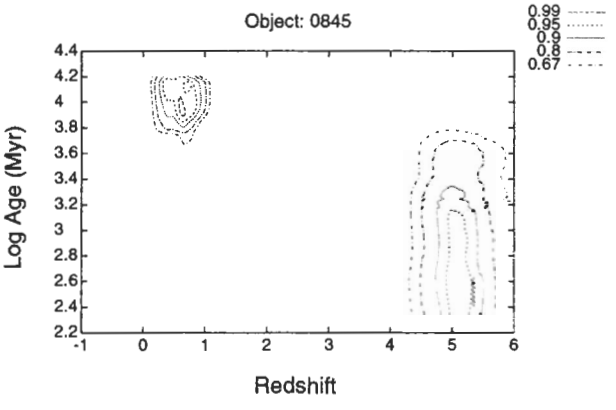

PEGASE models for RC J0908+0451

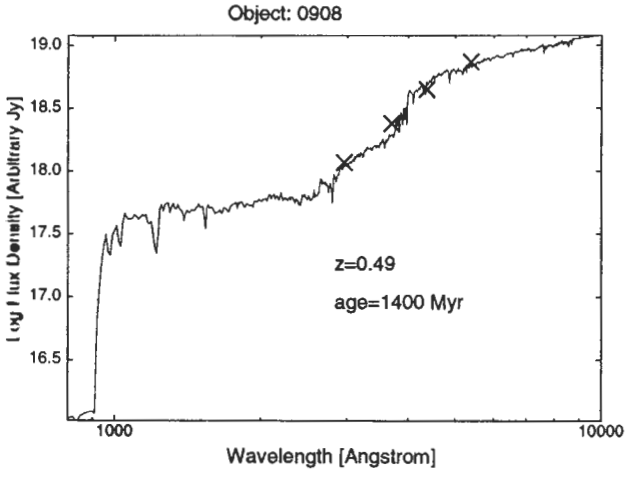

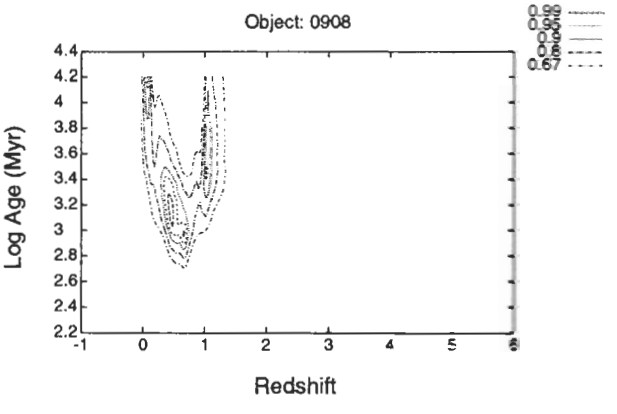

GISSEL models for RC J0908+0451

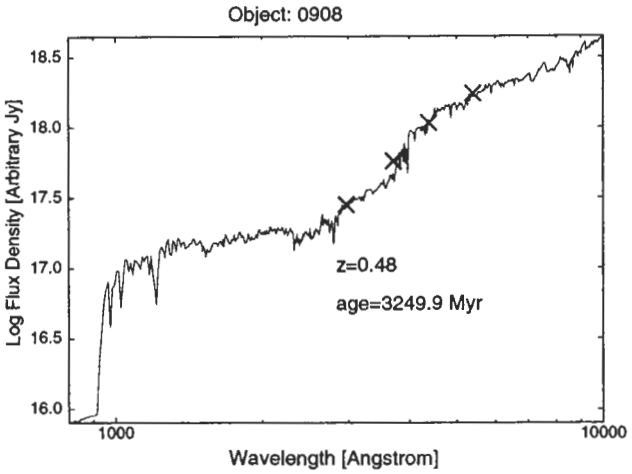

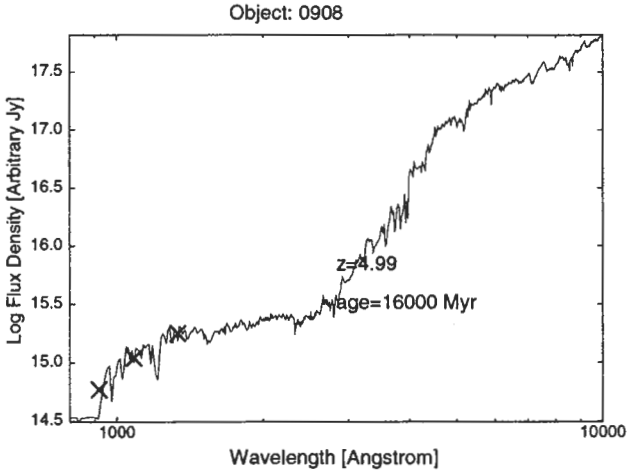

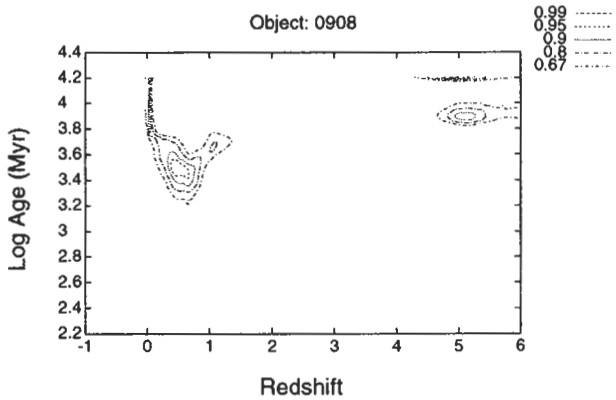

PEGASE models for RC J0909+0445

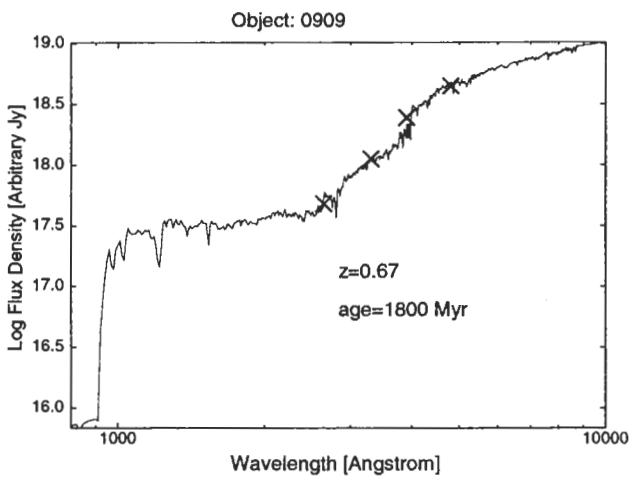

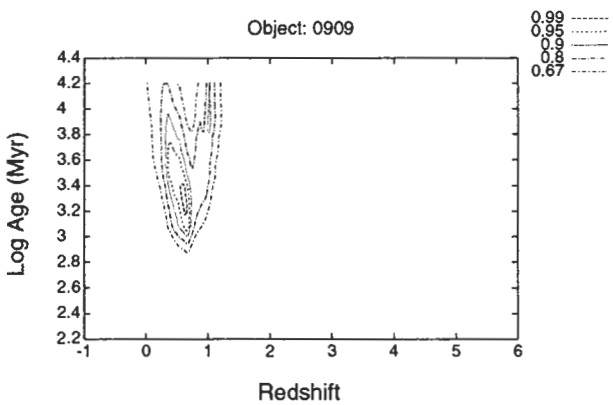

GISSEL models for RC J0909+0445

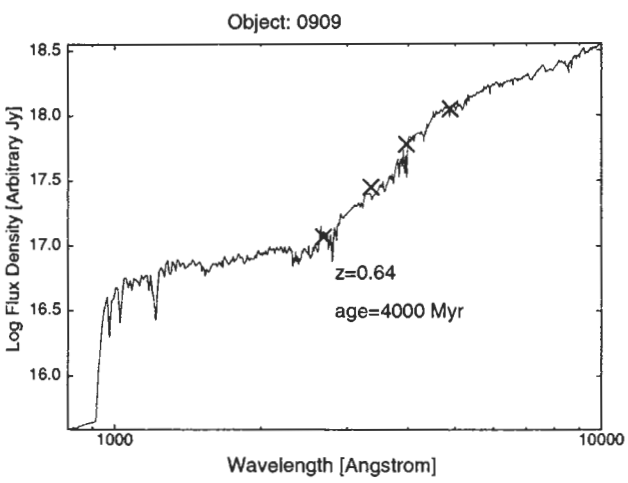

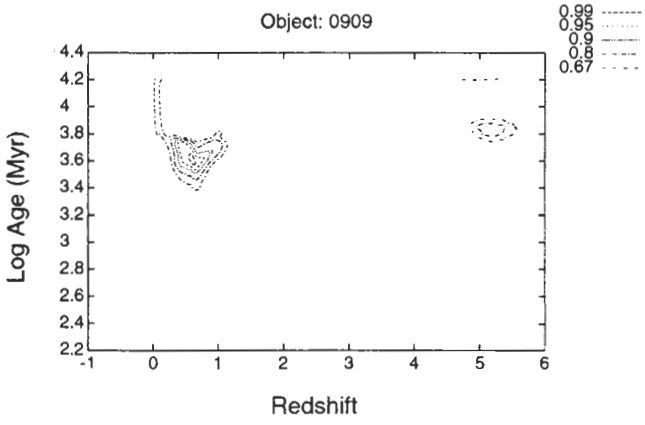

PEGASE models for RC J0934+0505

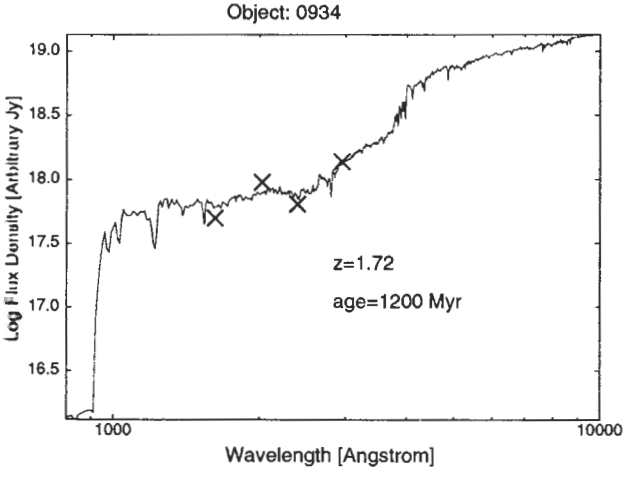

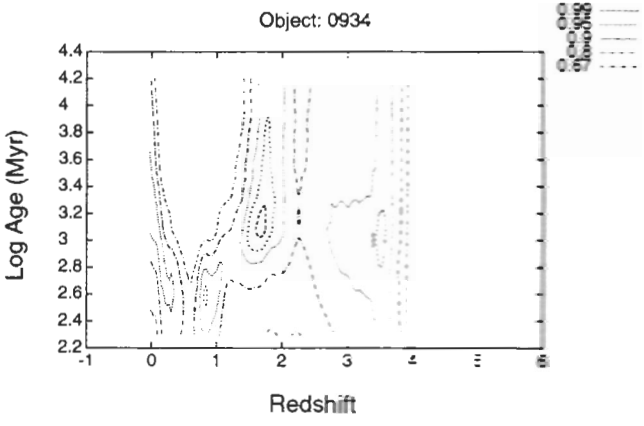

GISSEL models for RC J0934+0505

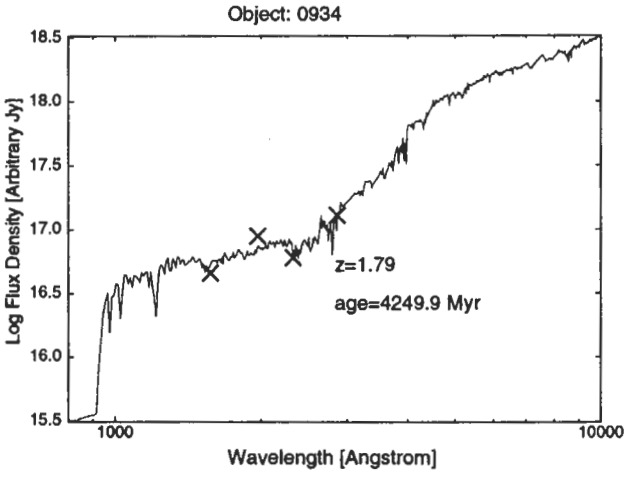

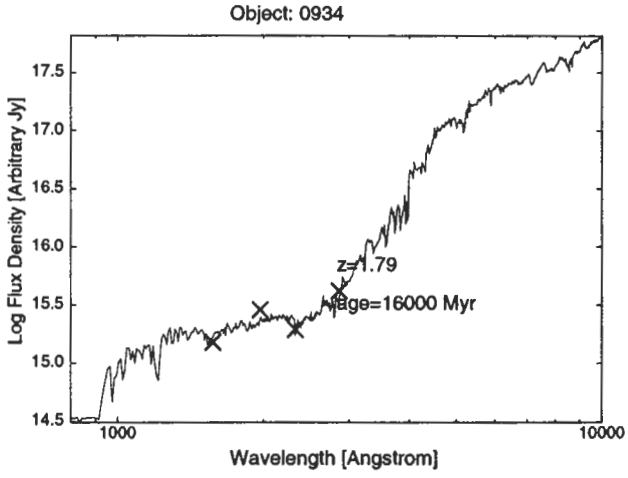

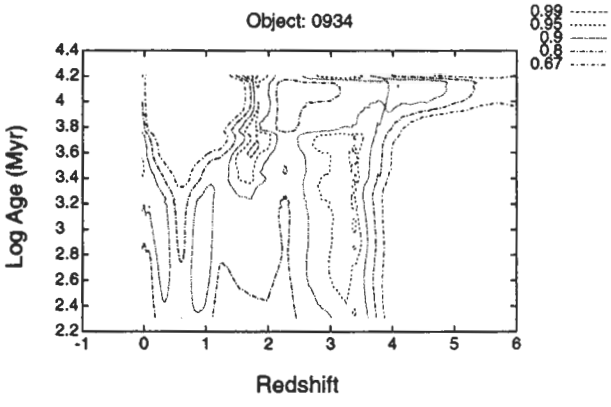

PEGASE models for RC J1011+0502

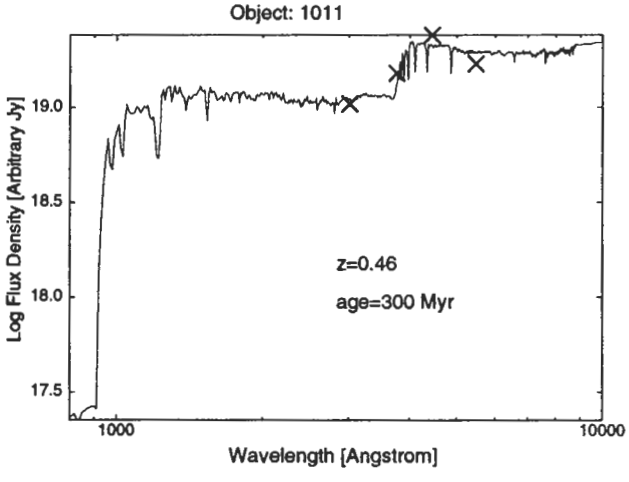

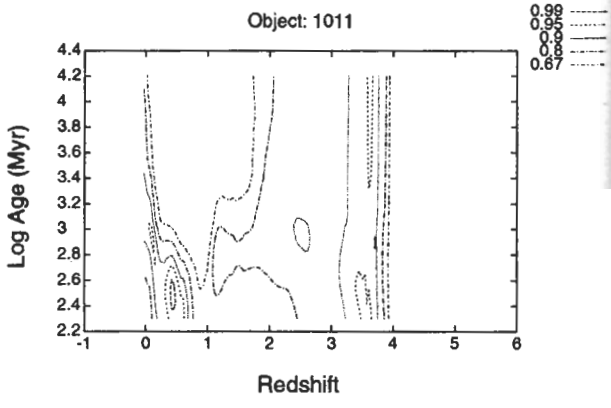

GISSEL models for RC J1011+0502

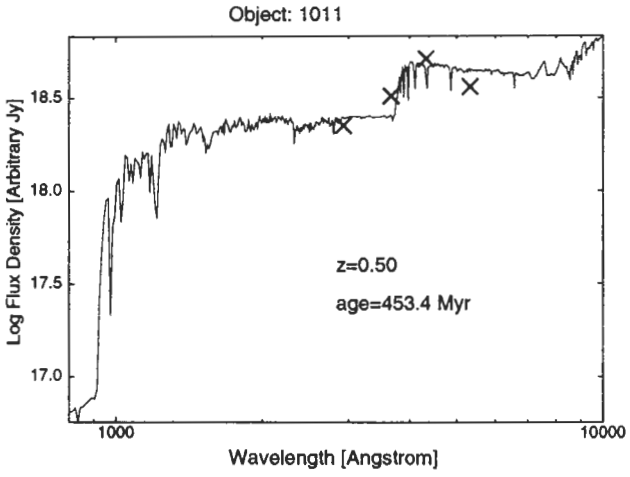

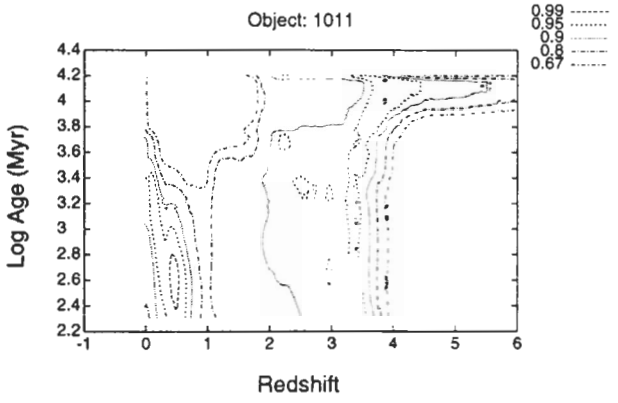

PEGASE models for RC J1031+0443

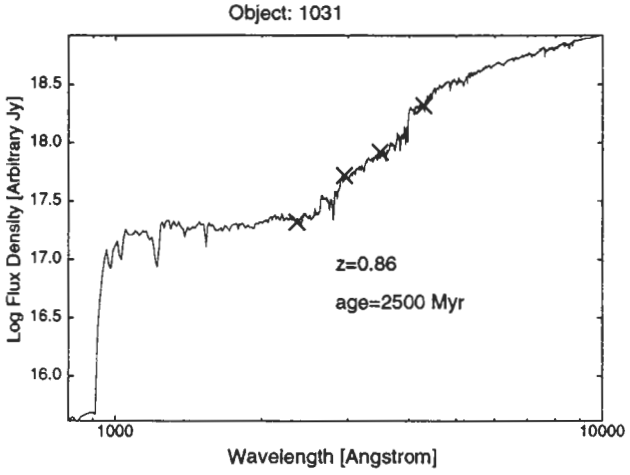

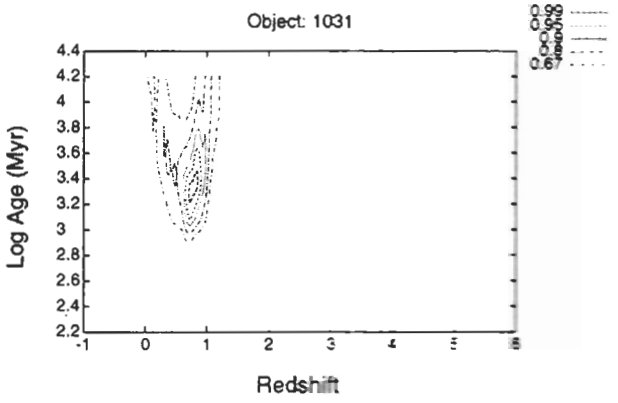

GISSEL models for RC J1031+0443

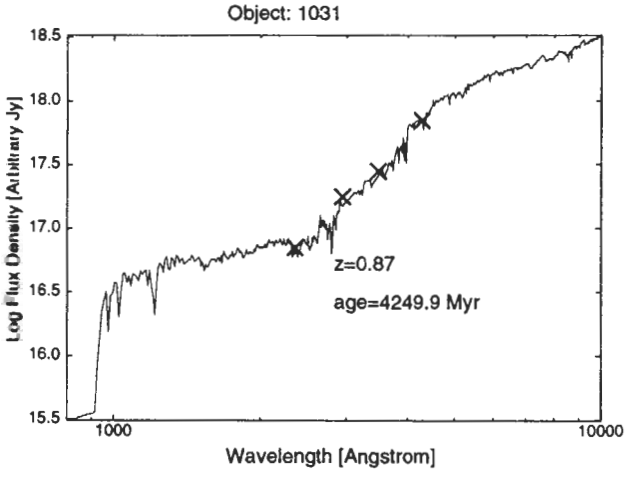

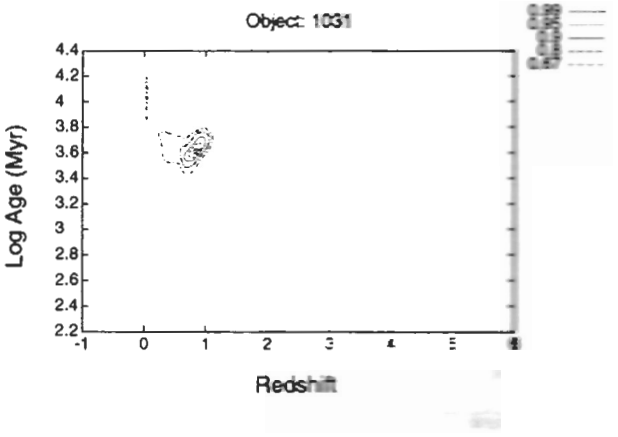

PEGASE models for RC J1043+0443

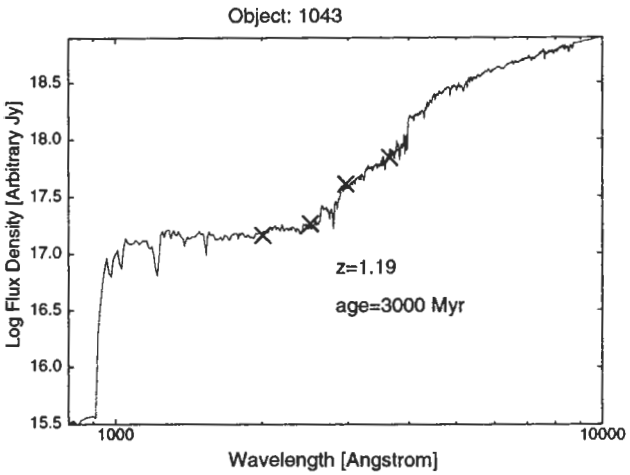

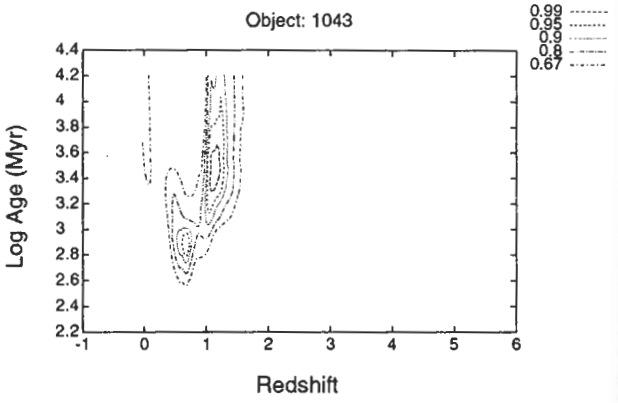

GISSEL models for RC J1043+0443

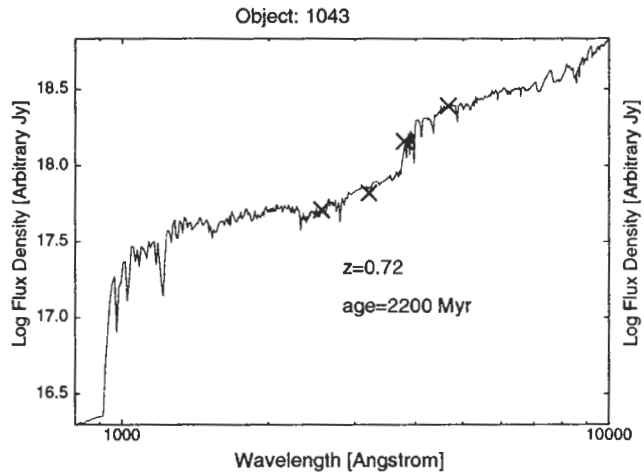

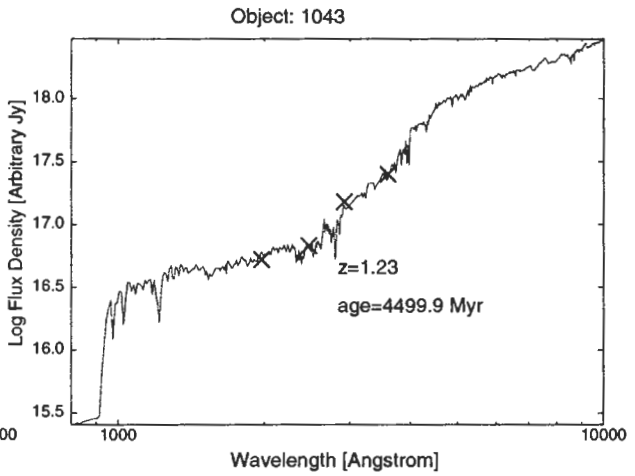

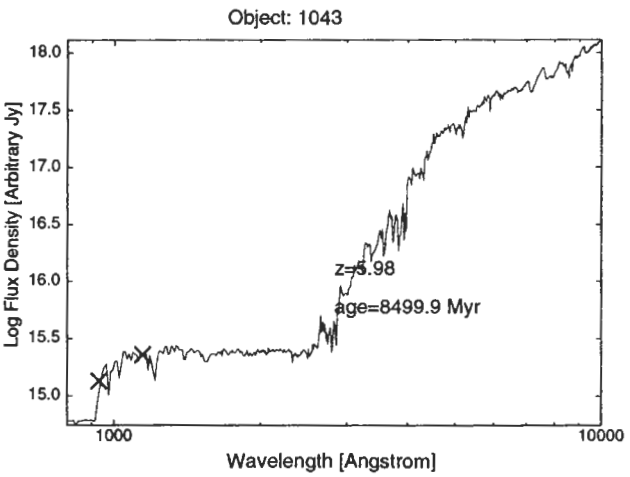

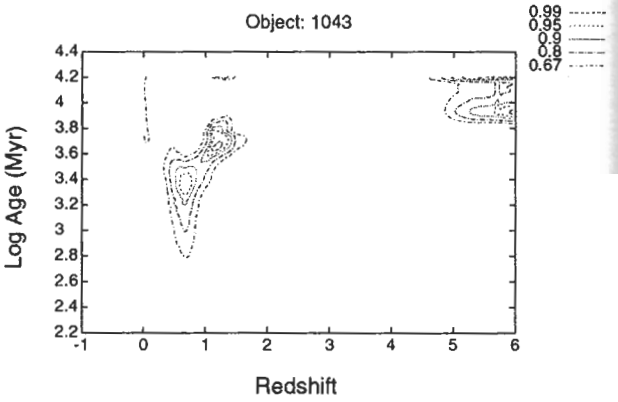

PEGASE models for RC J1124+0456

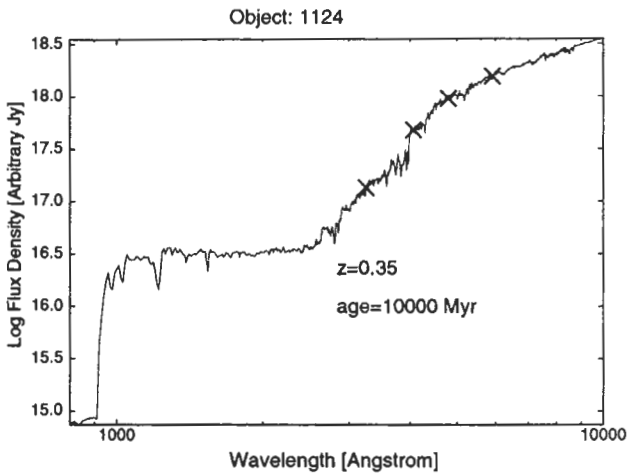

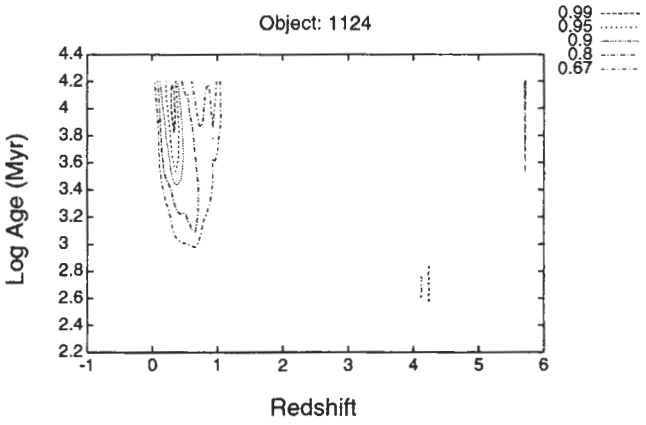

GISSEL models for RC J1124+0456

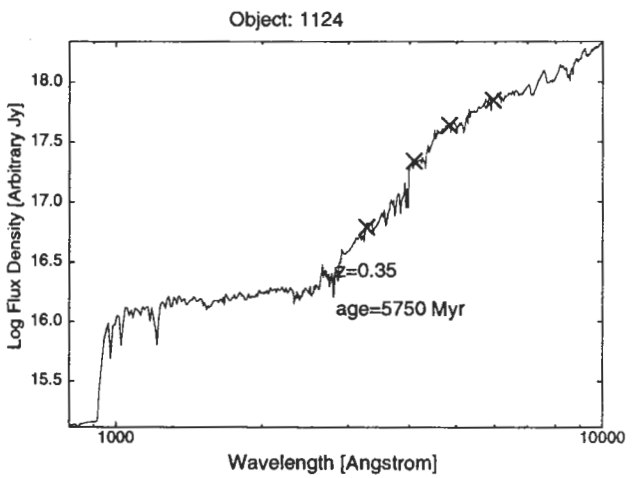

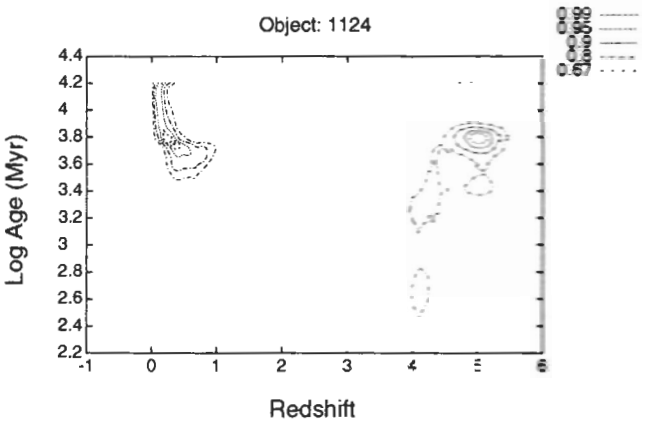

PEGASE models for RC J1142+0455

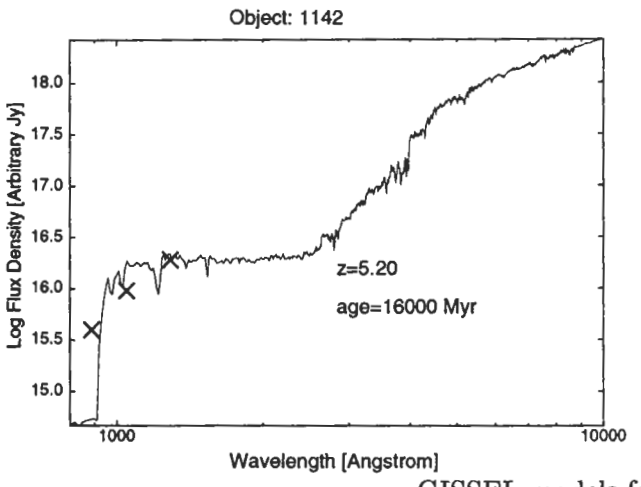

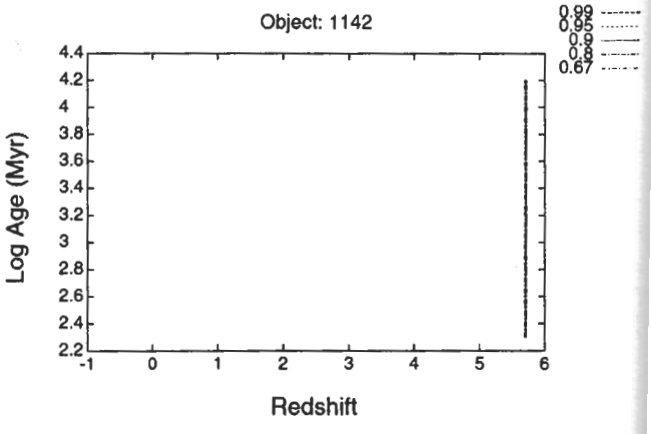

GISSEL models for RC J1142+0455

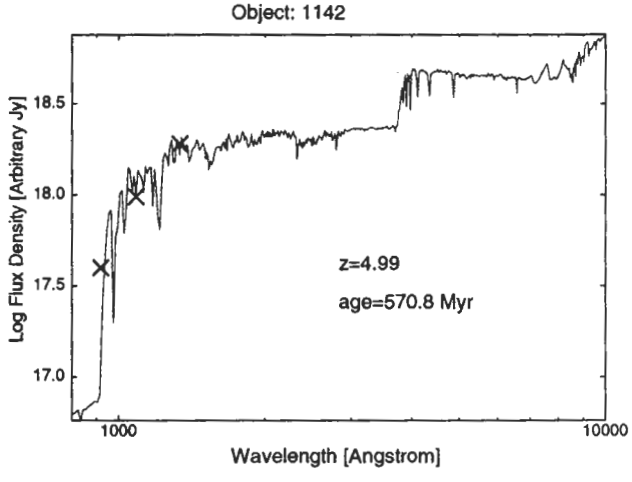

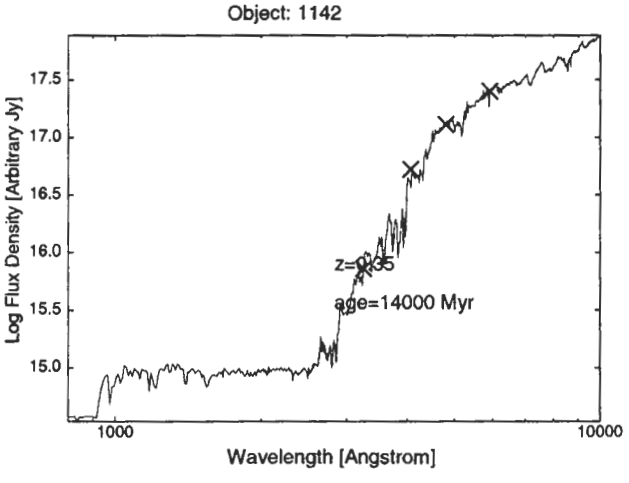

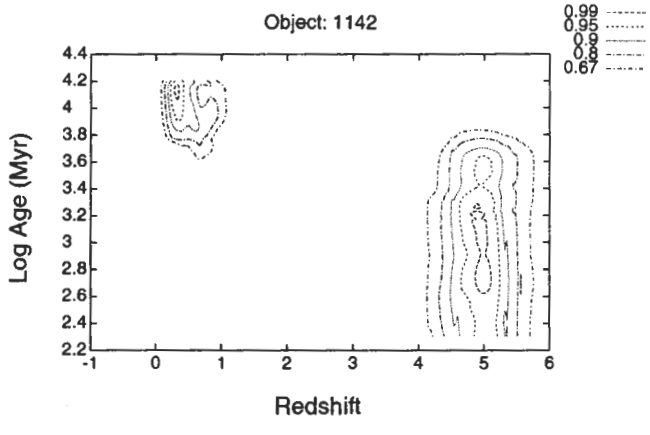

PEGASE models for RC J1152+0449

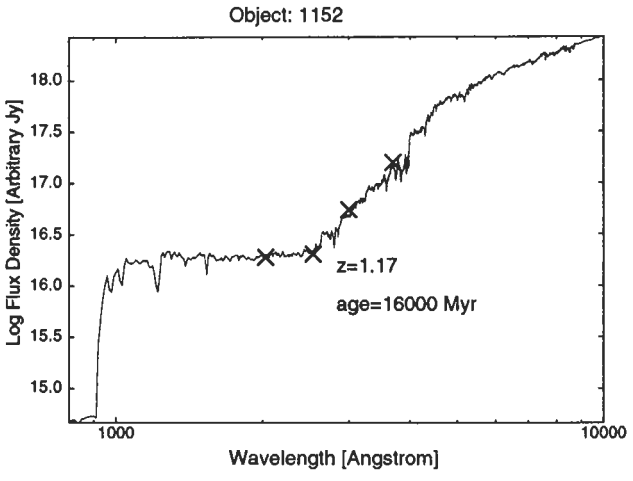

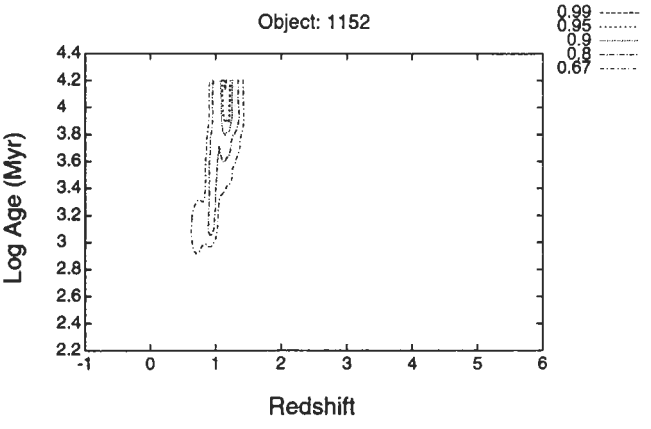

GISSEL models for RC J1152+0449

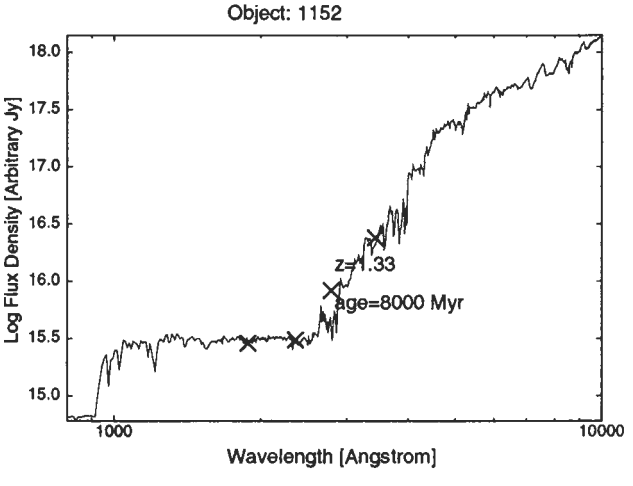

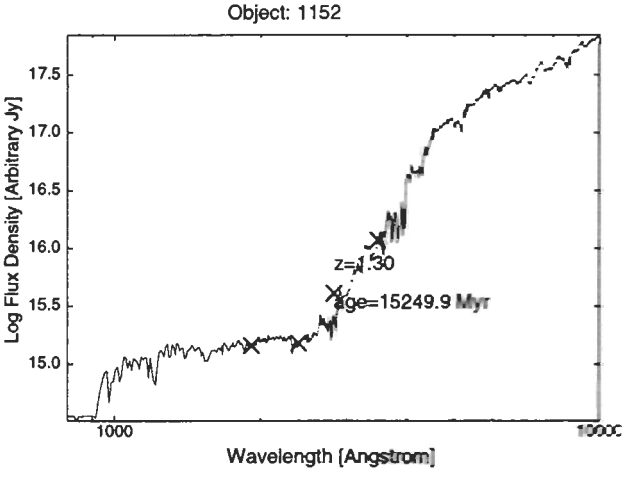

PEGASE models for RC J1155+0444

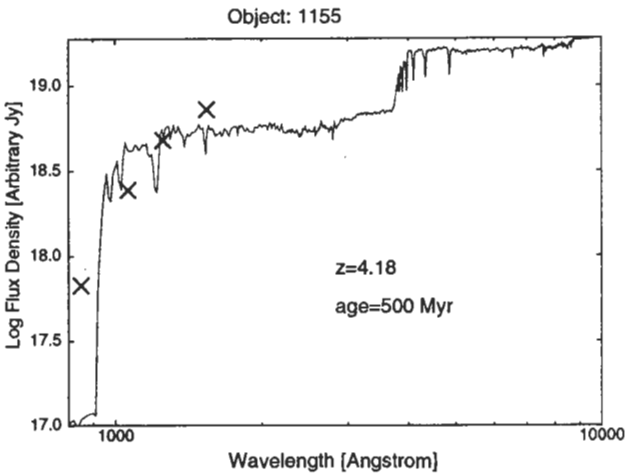

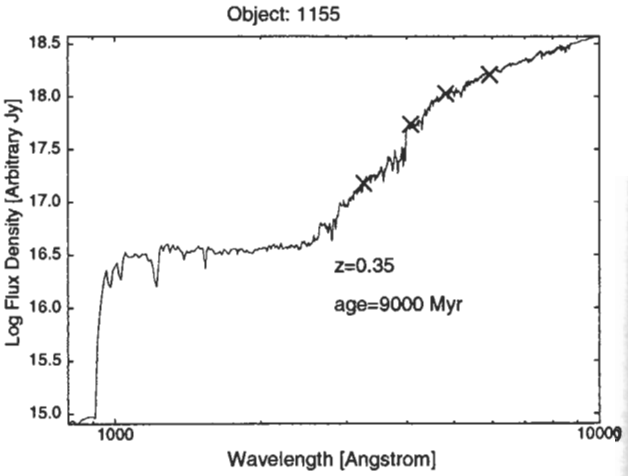

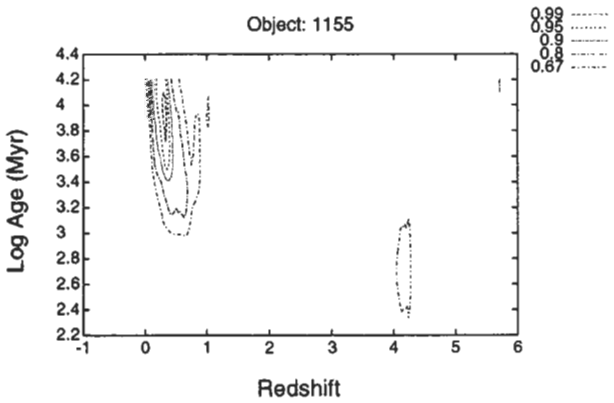

GISSEL models for RC J1155+0444

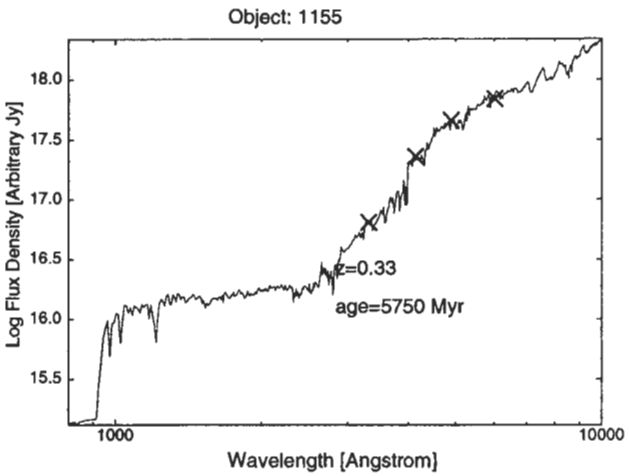

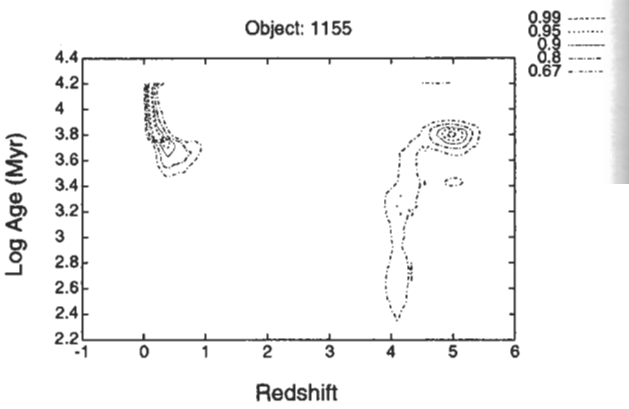

PEGASE models for RC J1213+0500

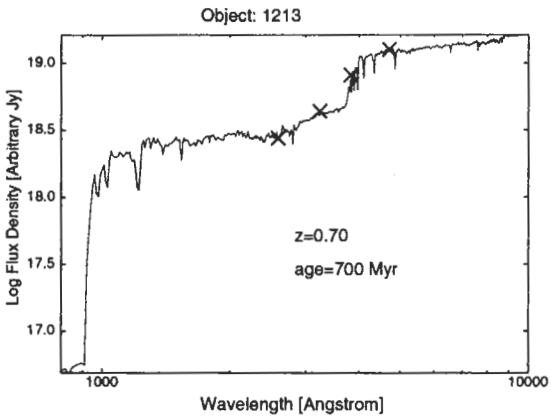

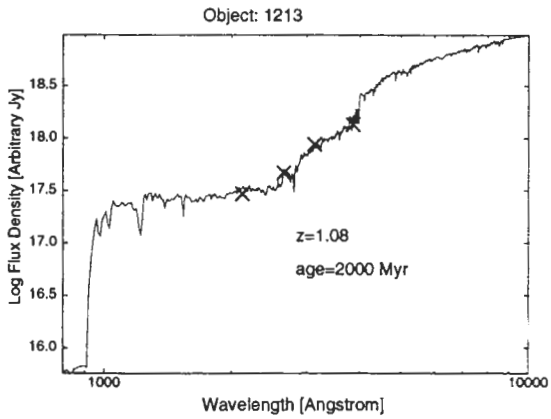

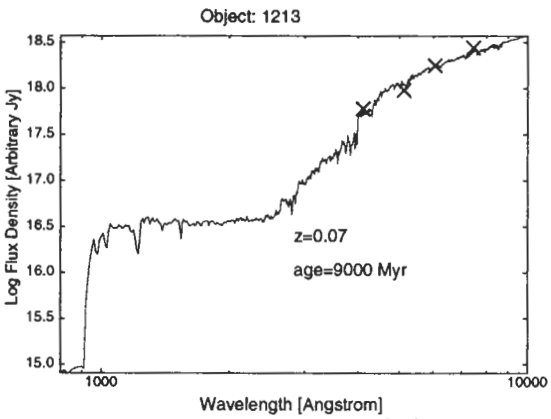

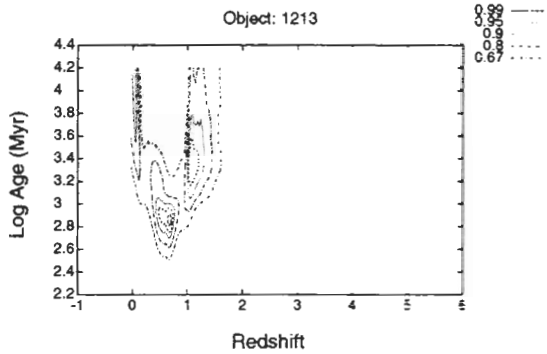

GISSEL models for RC J1213+0500

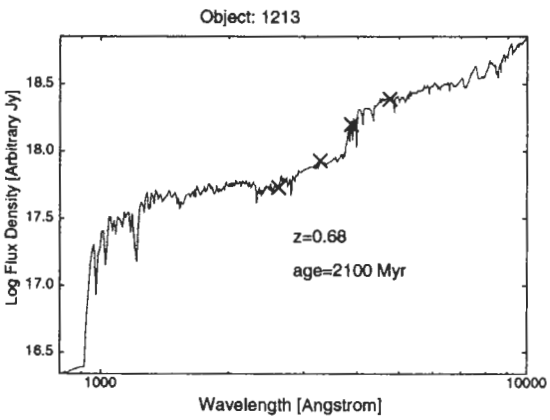

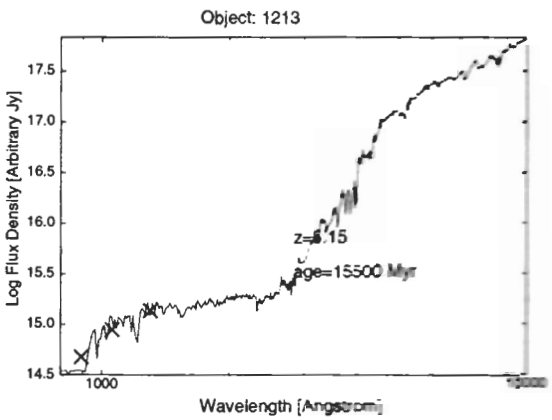

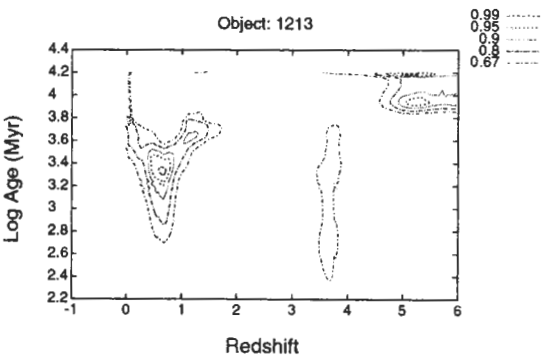

PEGASE models for RC J1235+0435b

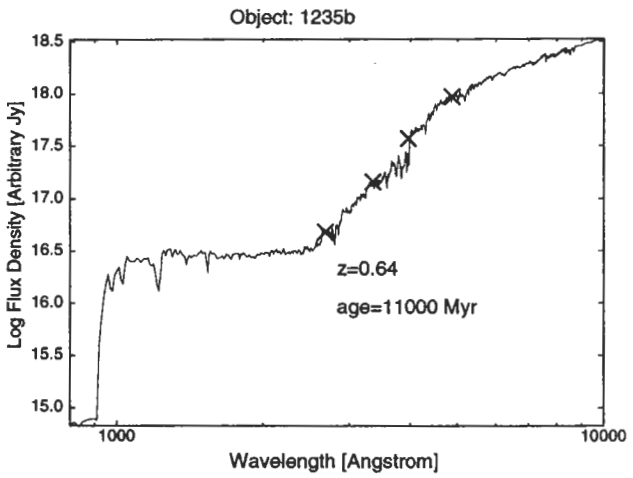

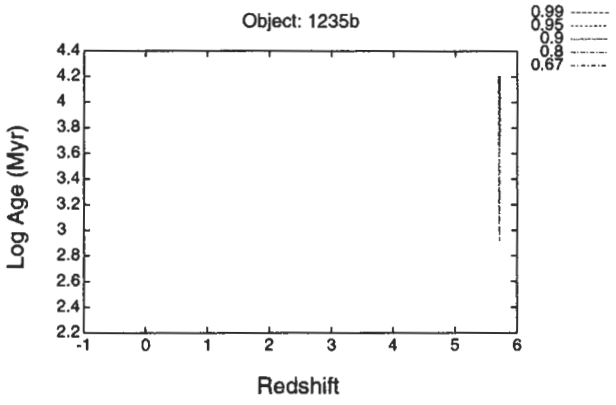

GISSEL models for RC J1235+0435b

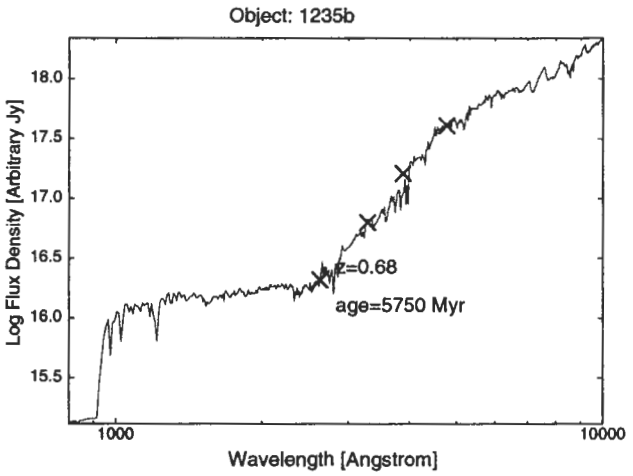

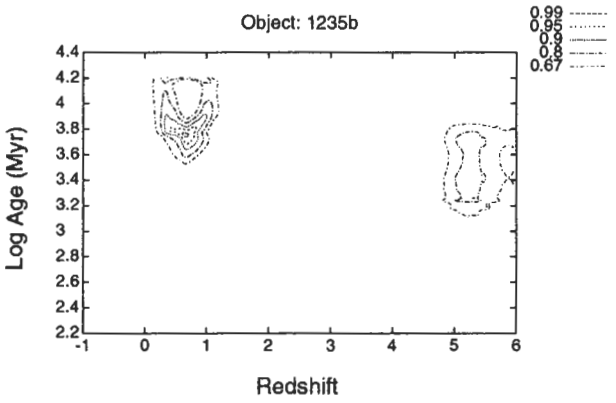

PEGASE models for RC J1322+0449

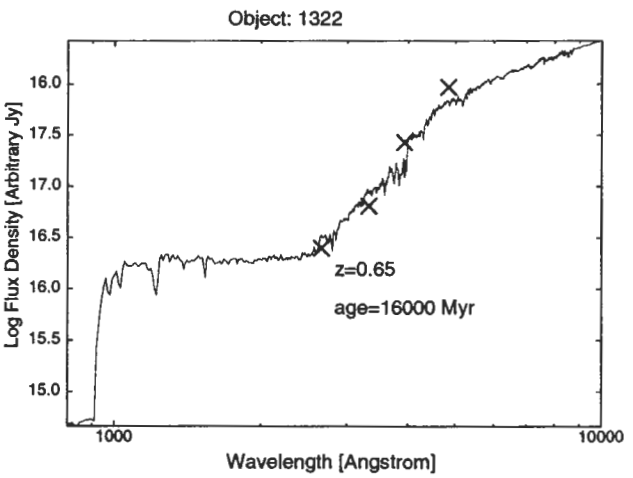

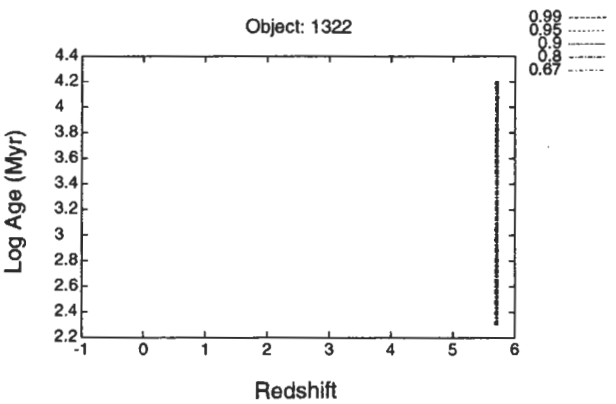

GISSEL models for RC J1322+0449

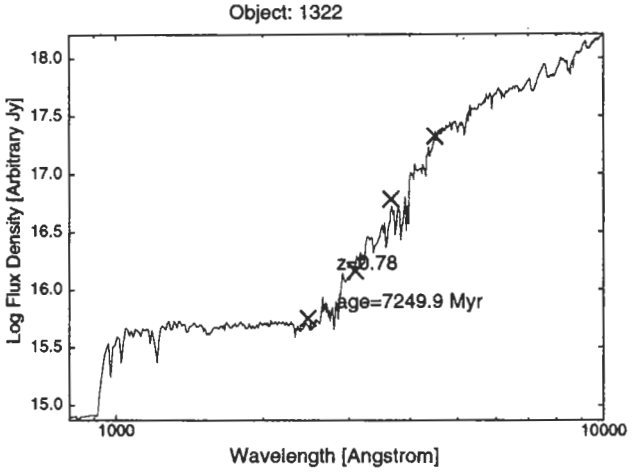

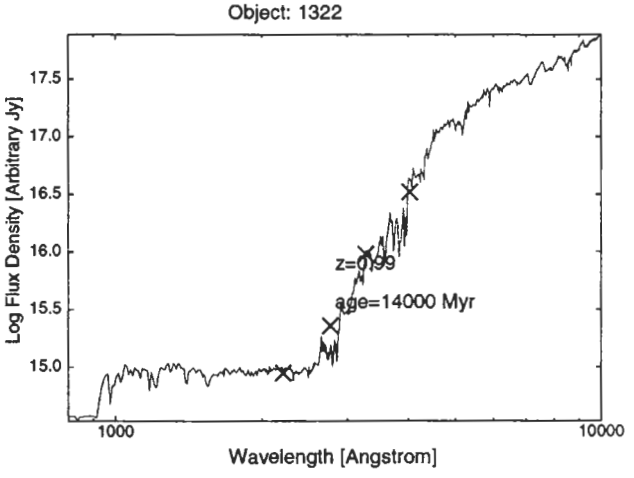

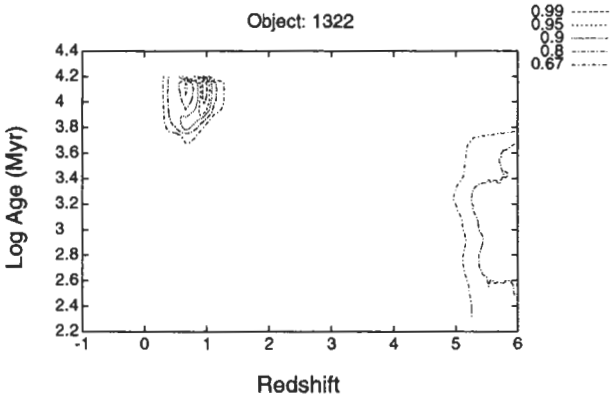

PEGASE models for RC J1333+0452

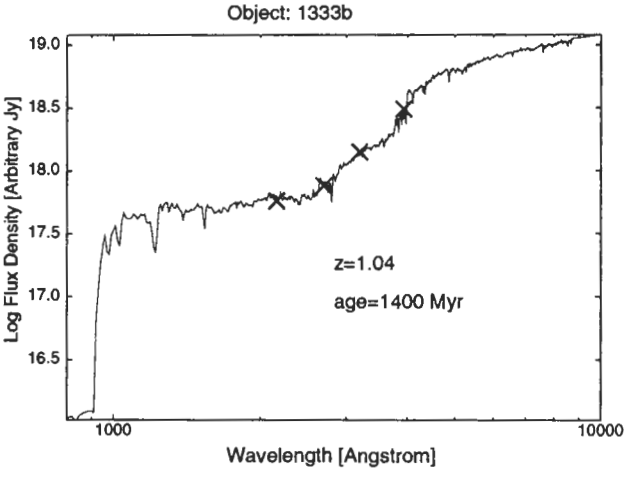

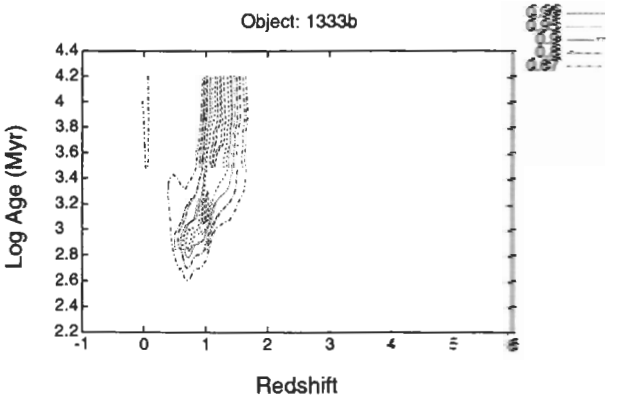

GISSEL models for RC J1333+0452

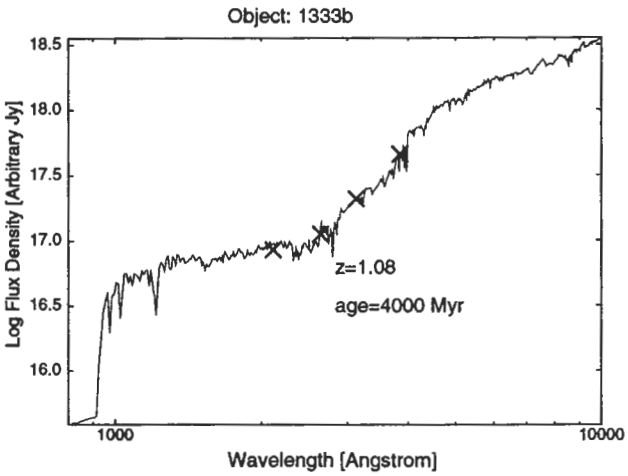

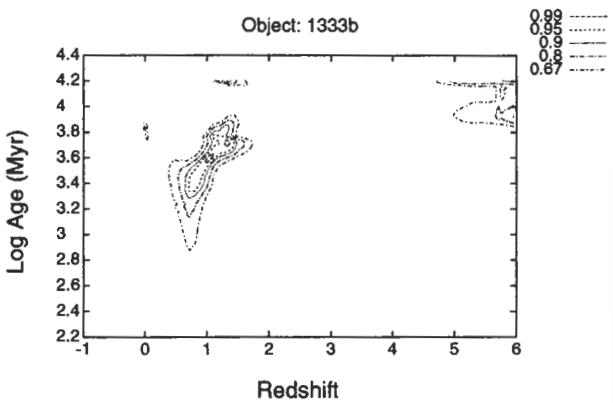

PEGASE models for RC J1339+0445

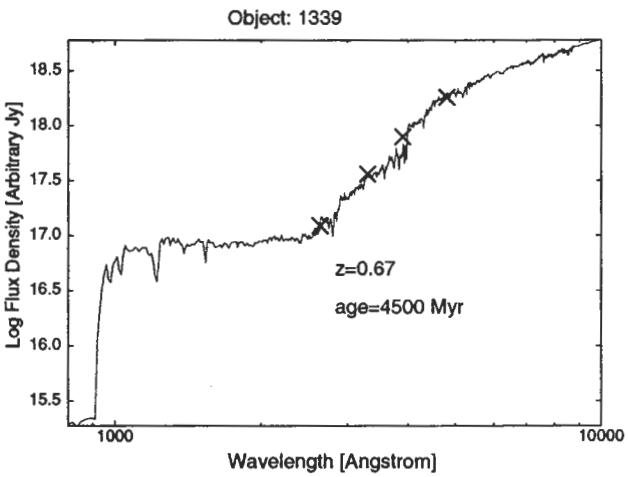

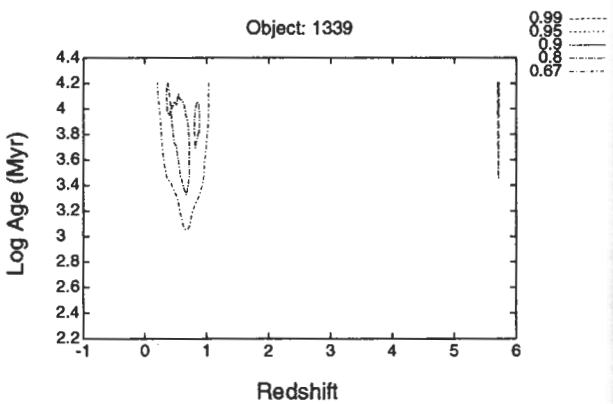

GISSEL models for RC J1339+0445

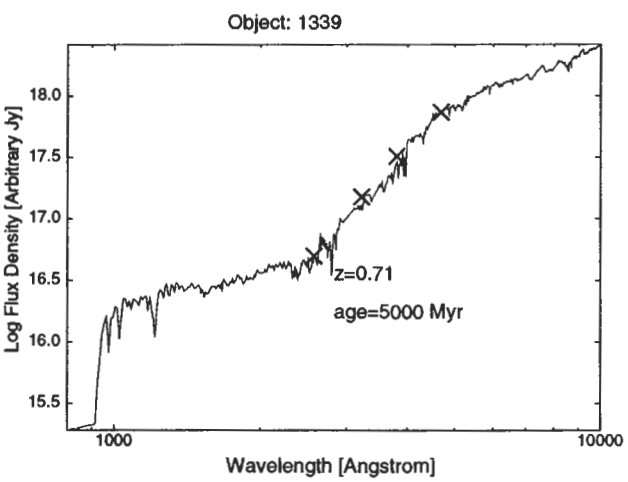

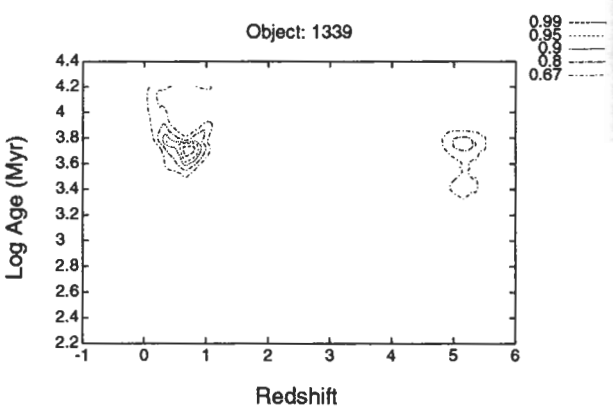

PEGASE models for RC J1357+0453

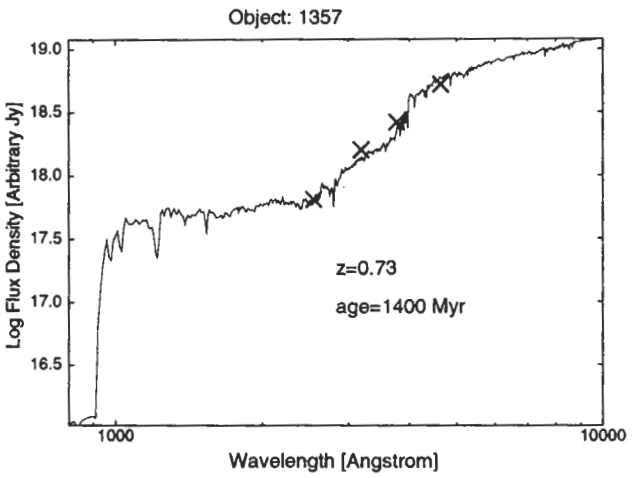

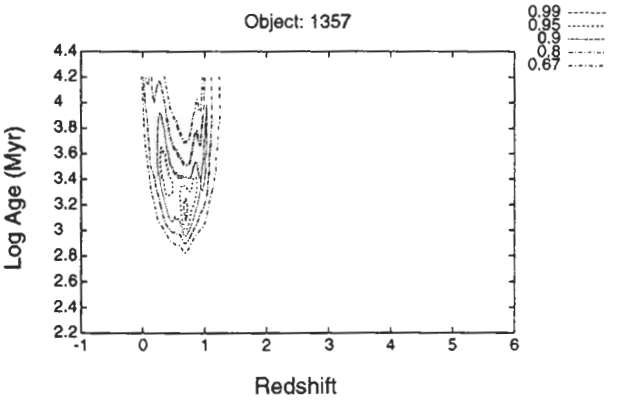

GISSEL models for RC J1357+0453

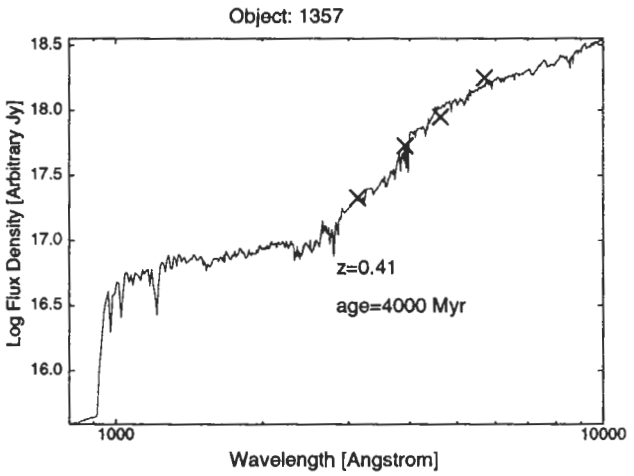

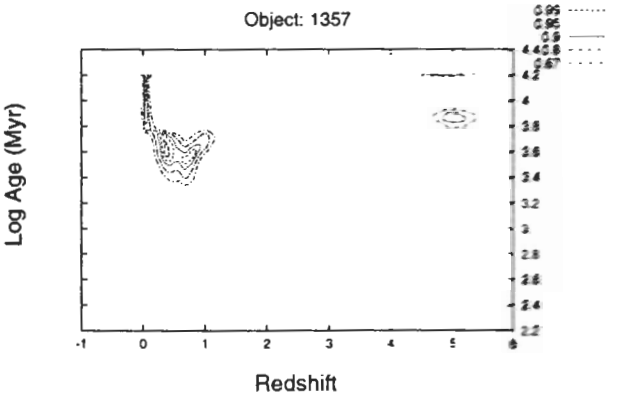

PEGASE models for RC J1429+0501

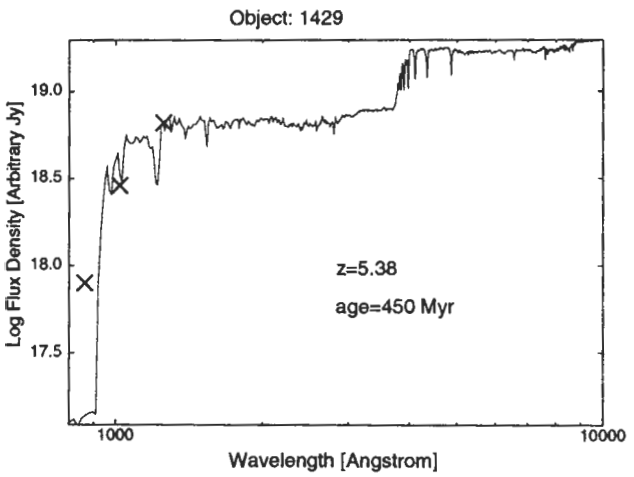

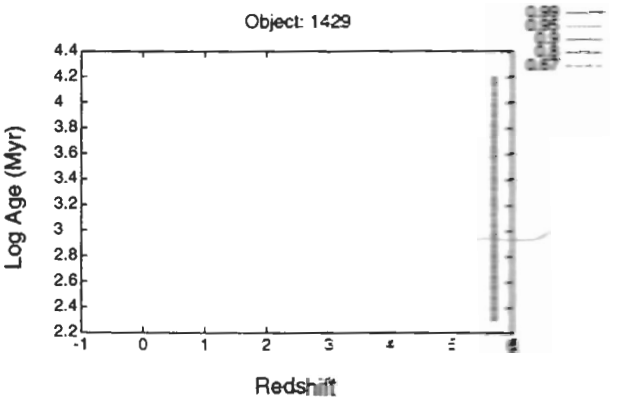

GISSEL models for RC J1429+0501

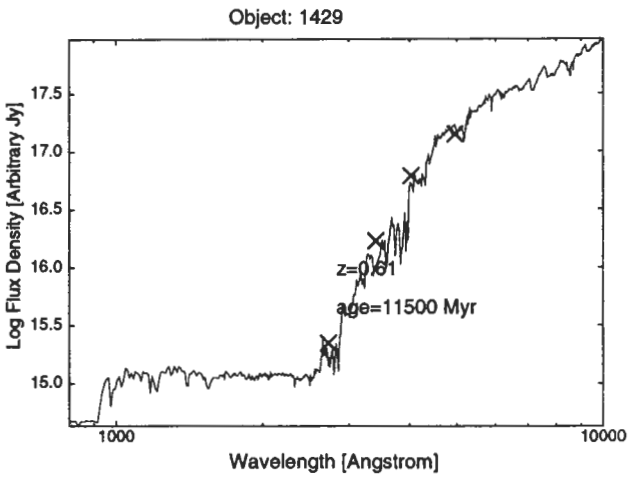

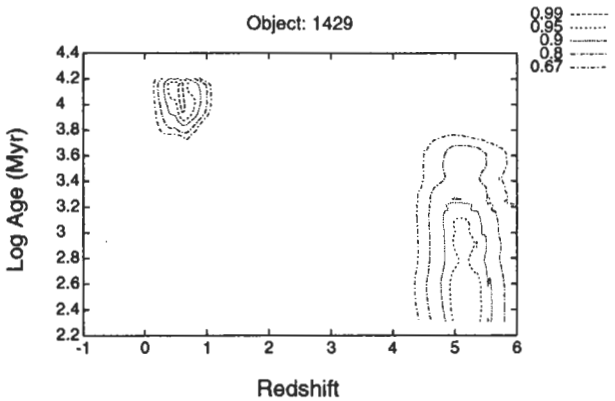

PEGASE models for RC J1436+0501

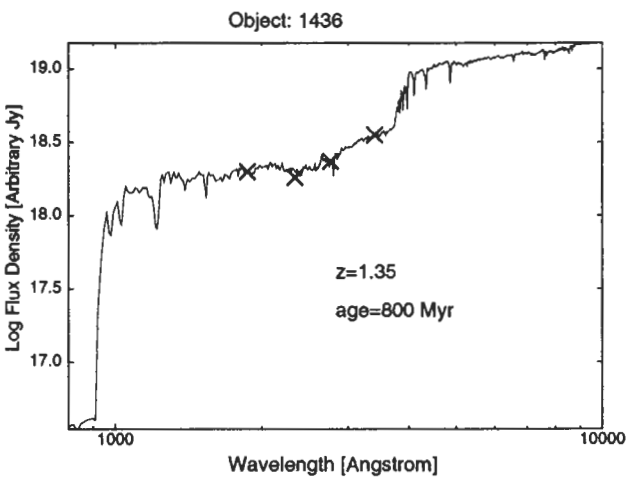

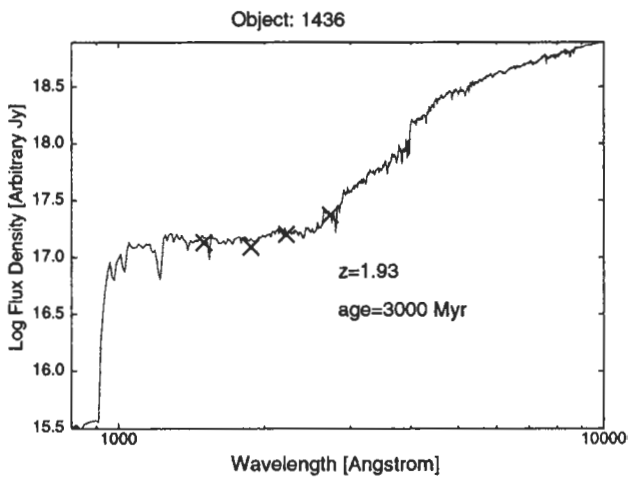

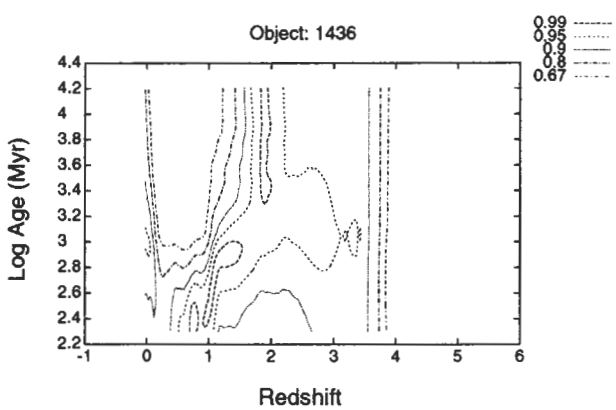

GISSEL models for RC J1436+0501

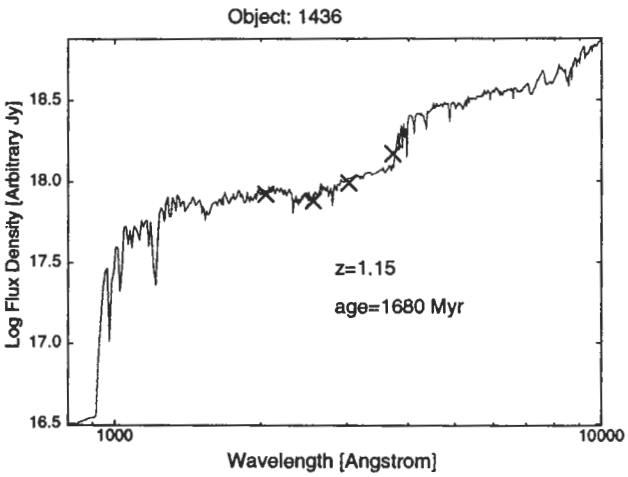

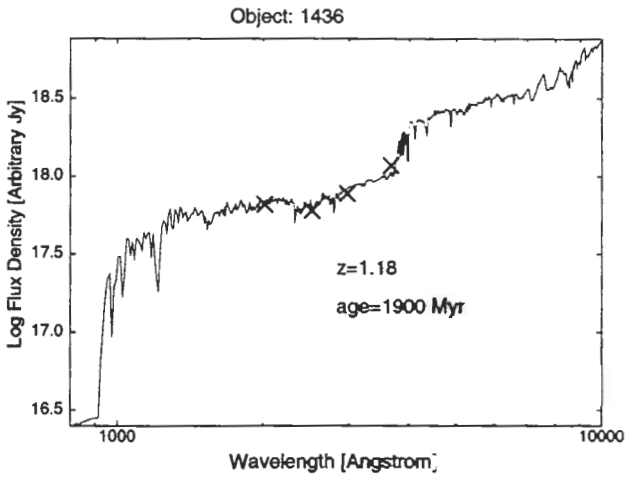

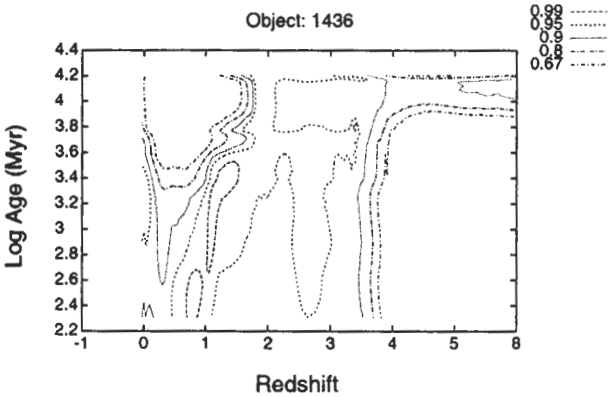

PEGASE models for RC J1446+0507

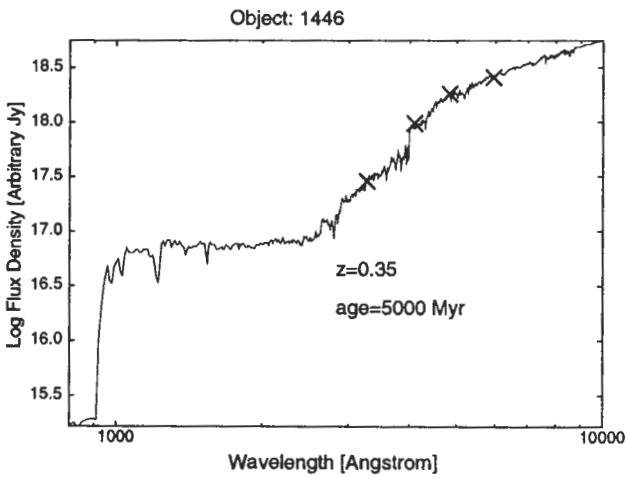

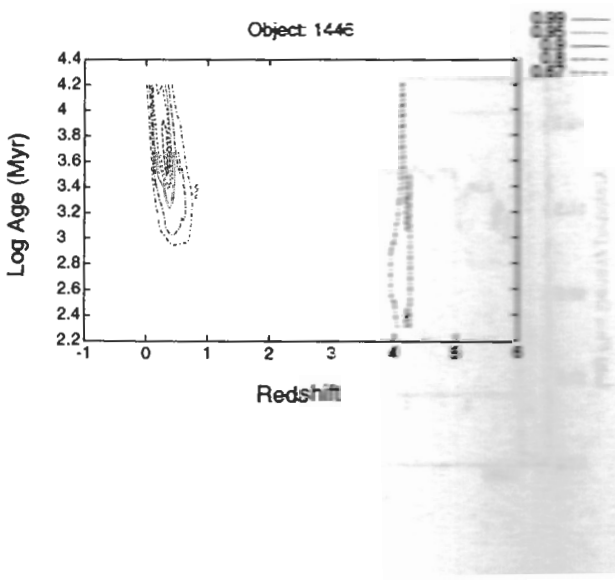

GISSEL models for RC J1446+0507

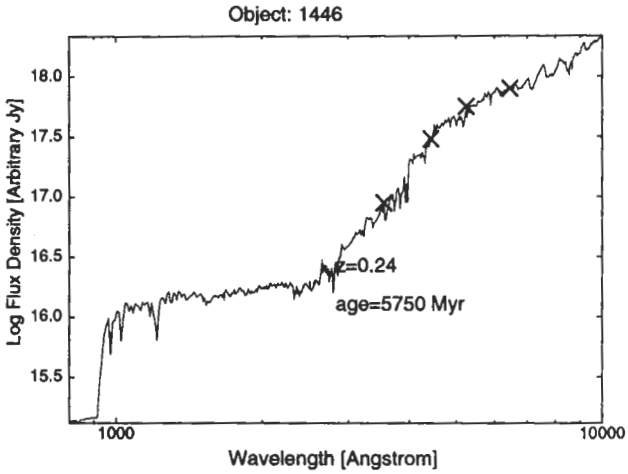

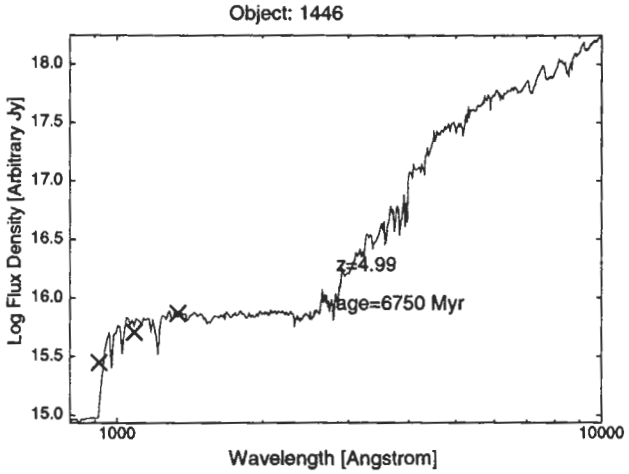

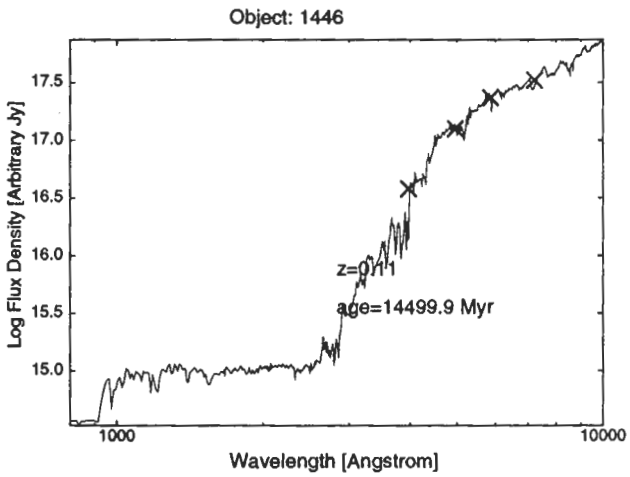

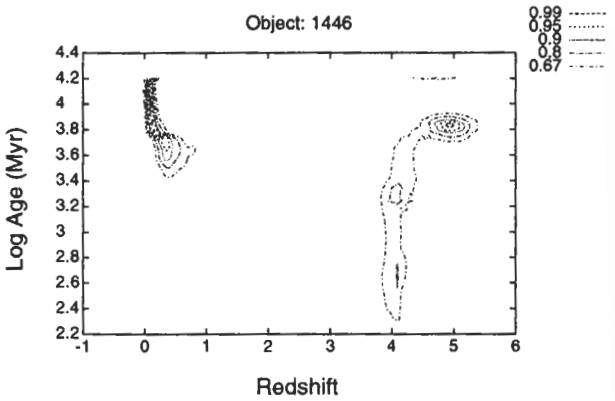

PEGASE models for RC J1503+0456

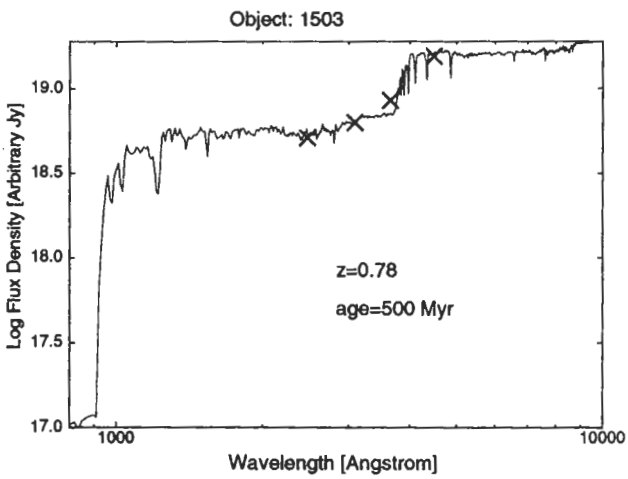

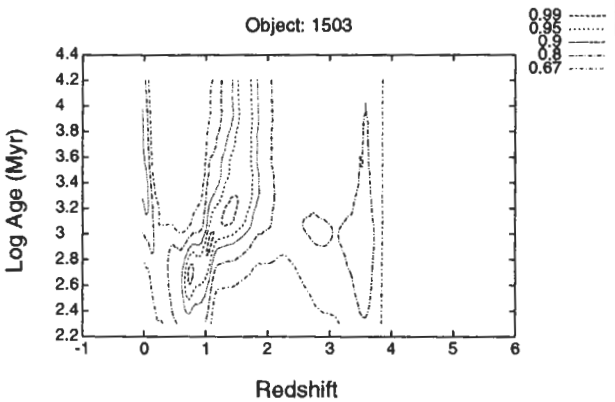

GISSEL models for RC J1503+0456

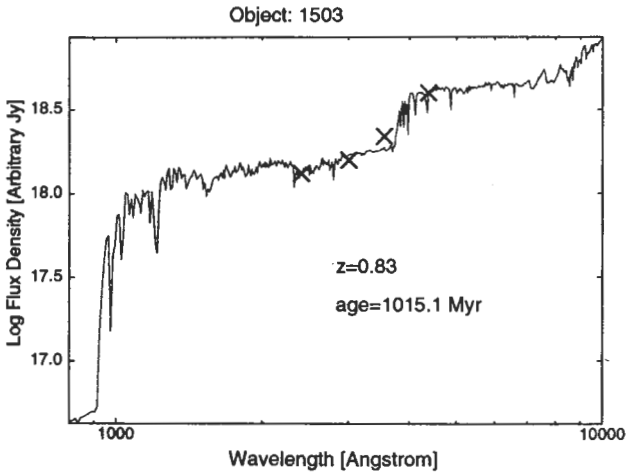

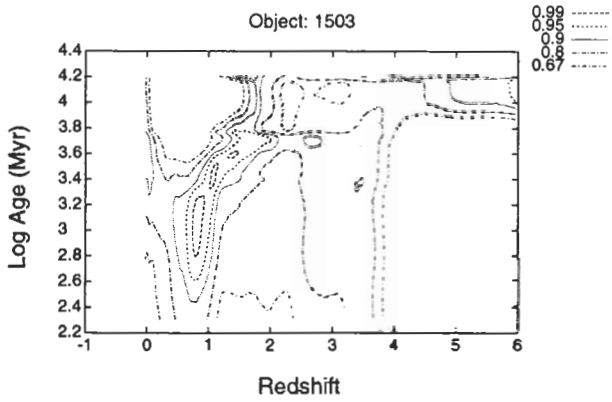

PEGASE models for RC J1510+0438

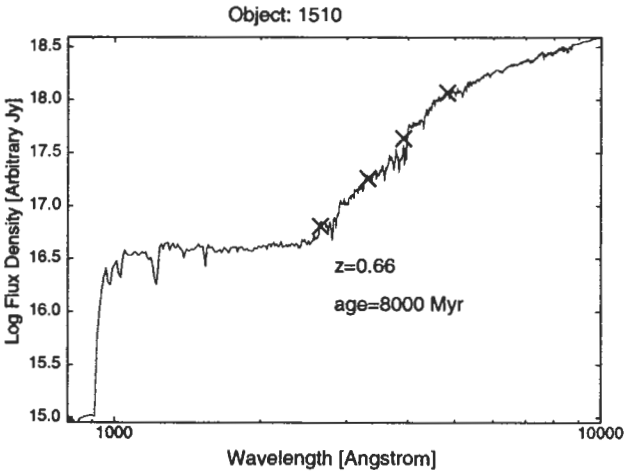

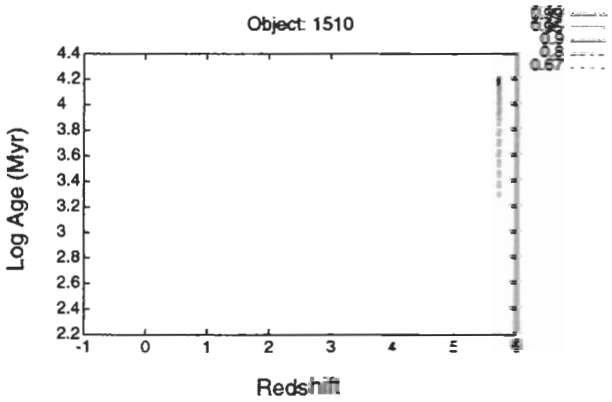

GISSEL models for RC J1510+0438

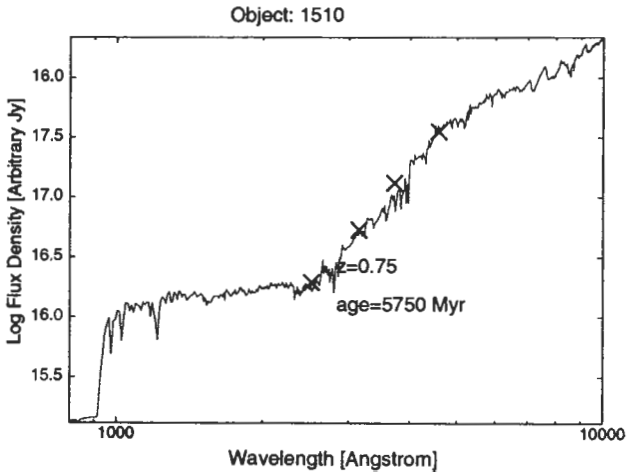

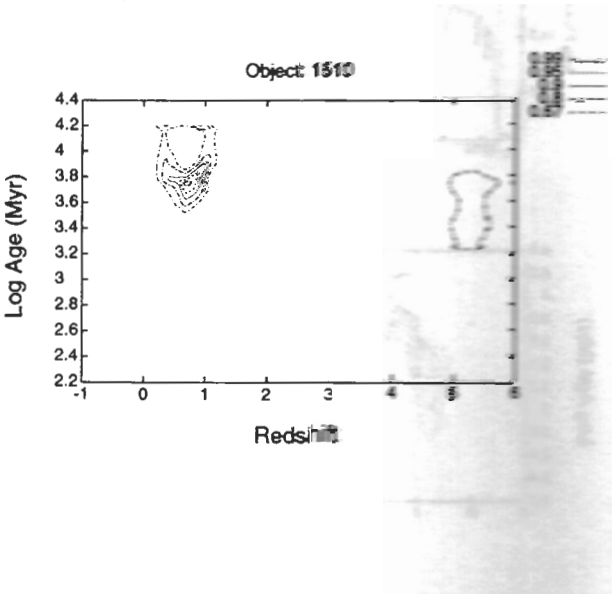

PEGASE models for RC J1551+0458

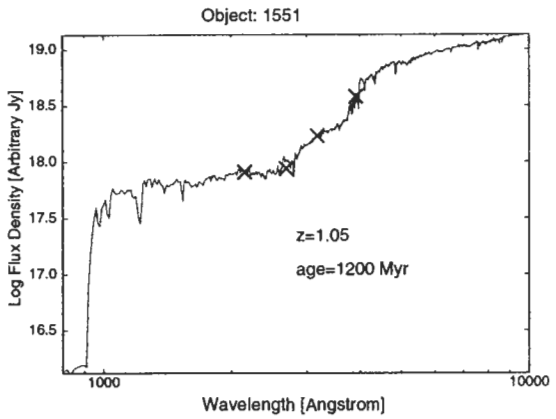

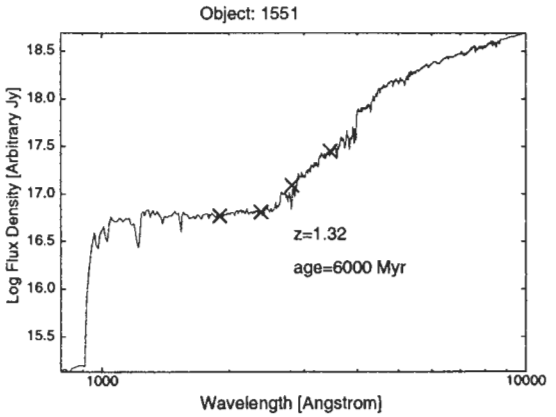

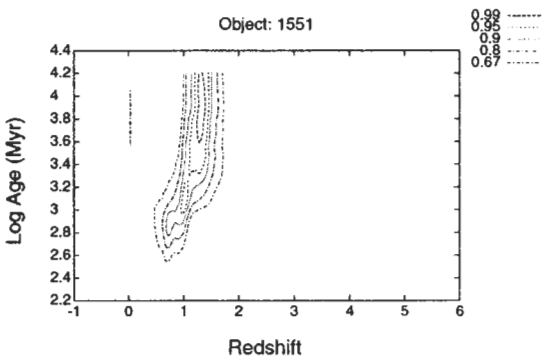

GISSEL models for RC J1551+0458

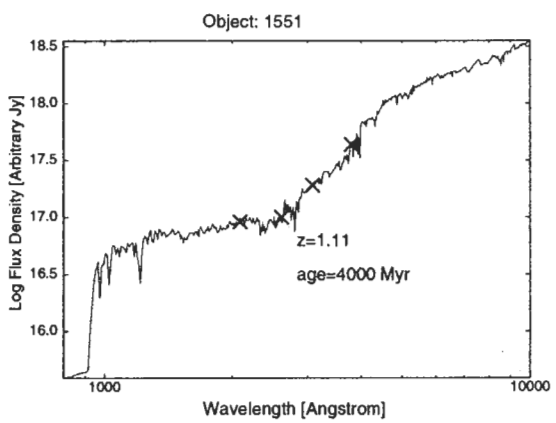

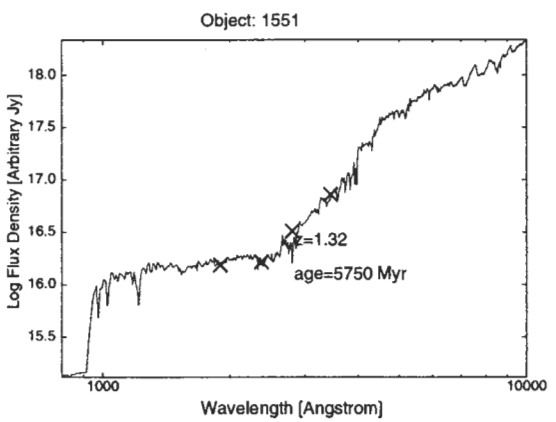

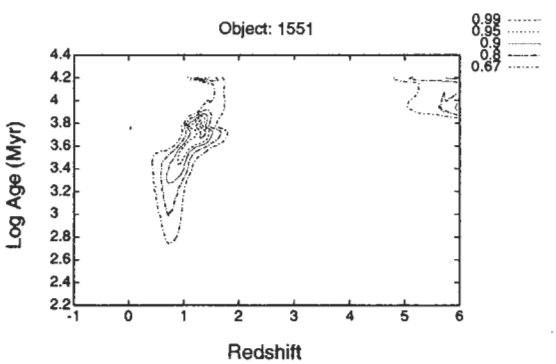

PEGASE models for RC J1626+0448

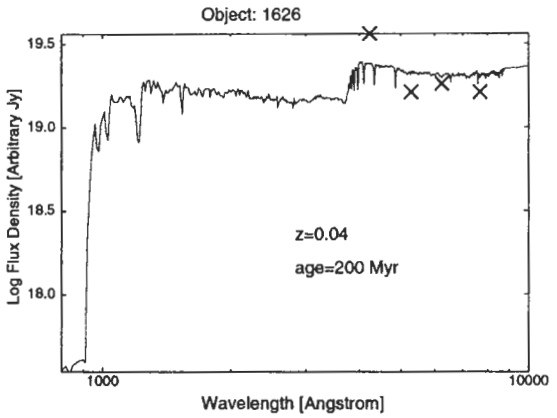

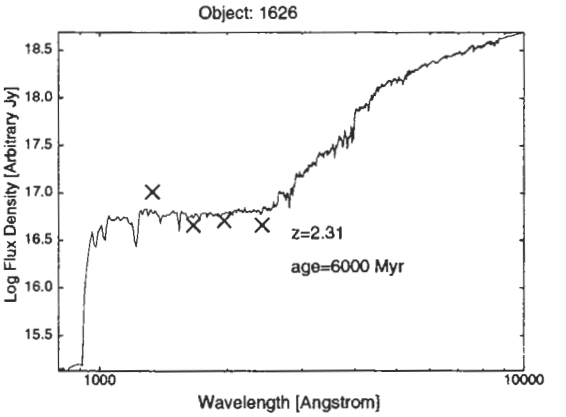

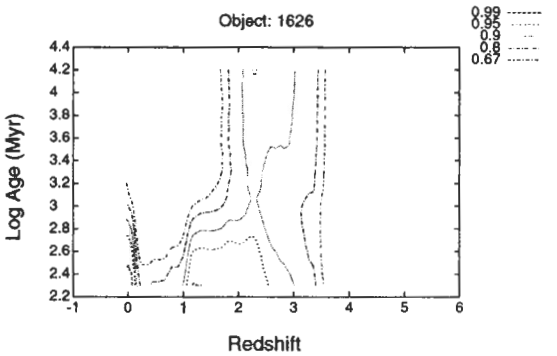

GISSEL models for RC J1626+0448

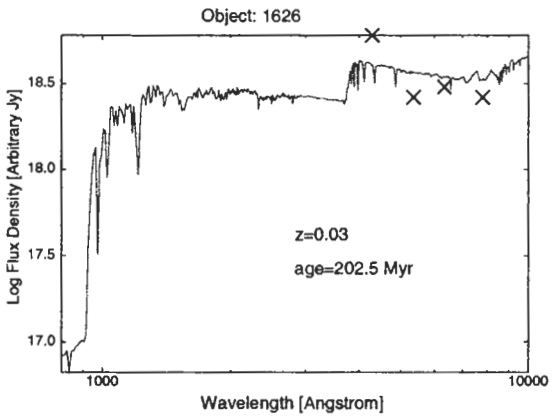

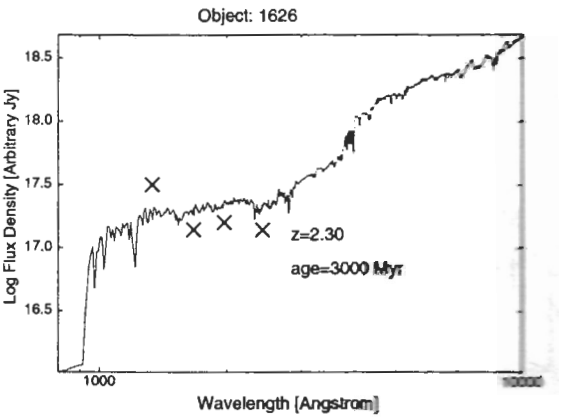

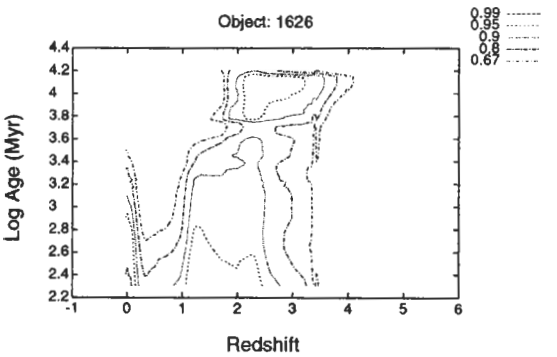

PEGASE models for RC J1638+0450

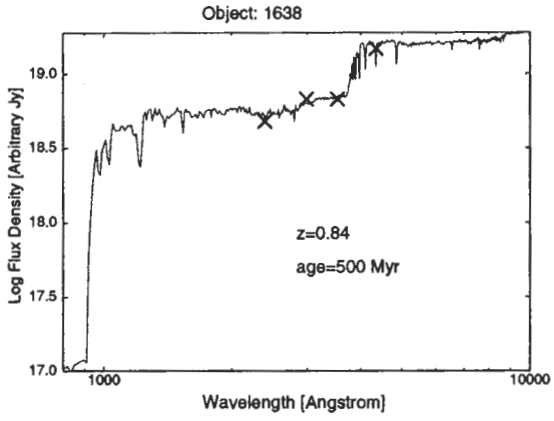

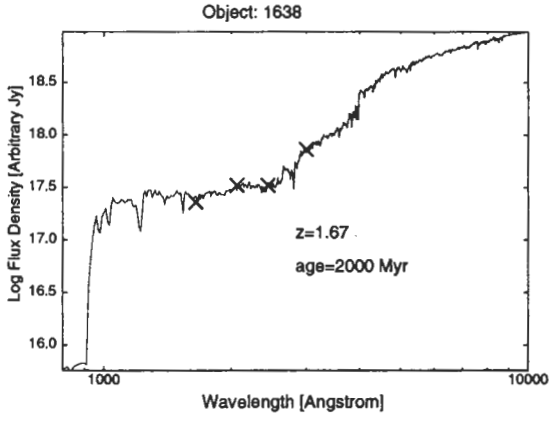

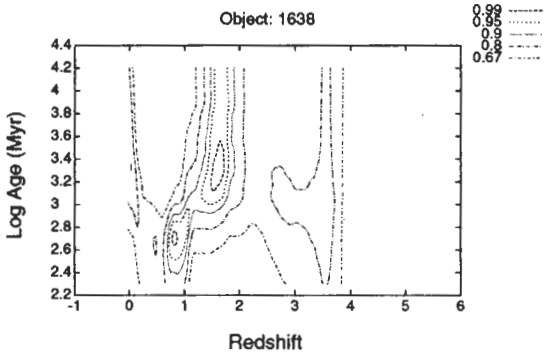

GISSEL models for RC J1638+0450

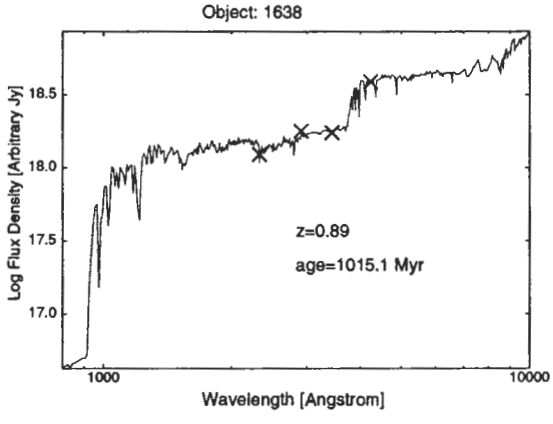

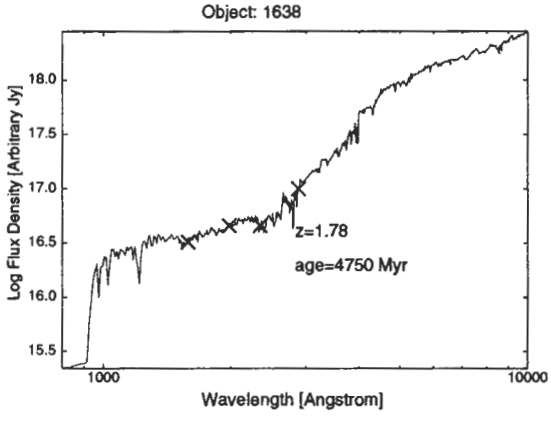

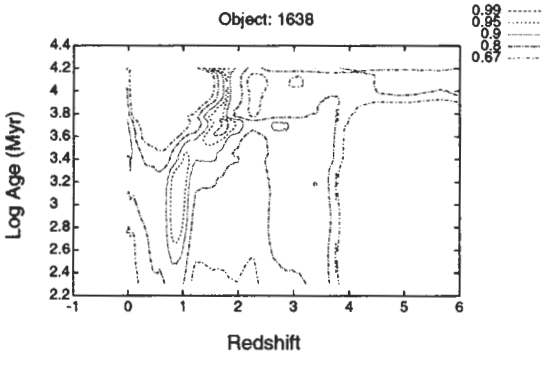

PEGASE models for RC J1646+0501

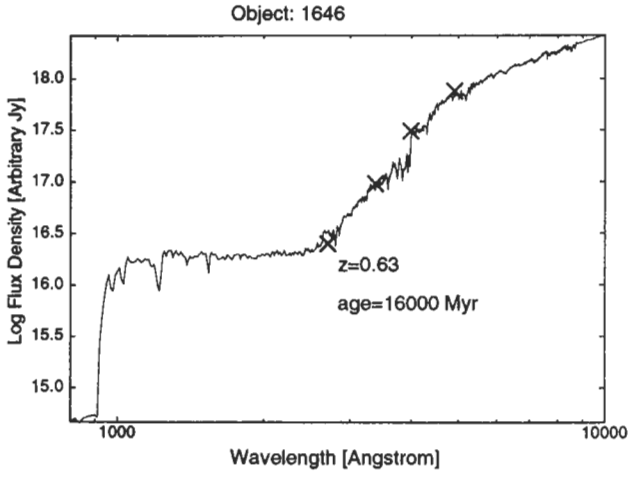

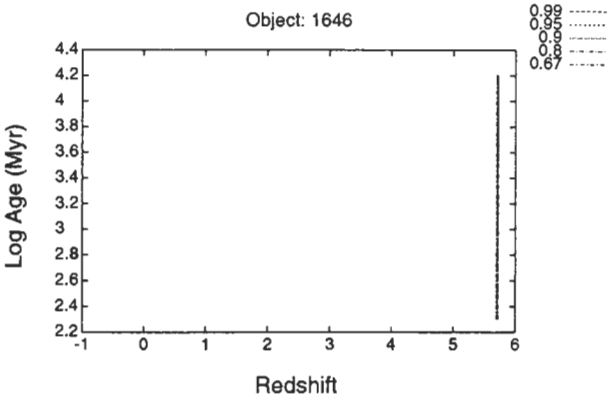

GISSEL models for RC J1646+0501

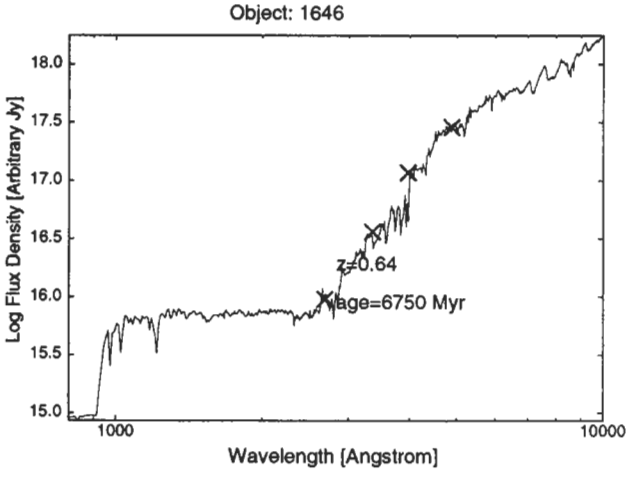

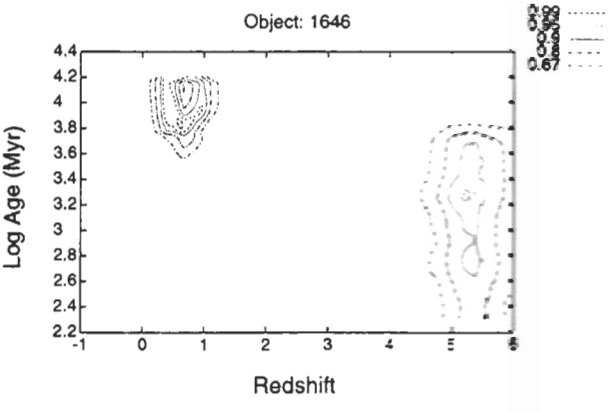

PEGASE models for RC J1703+0502

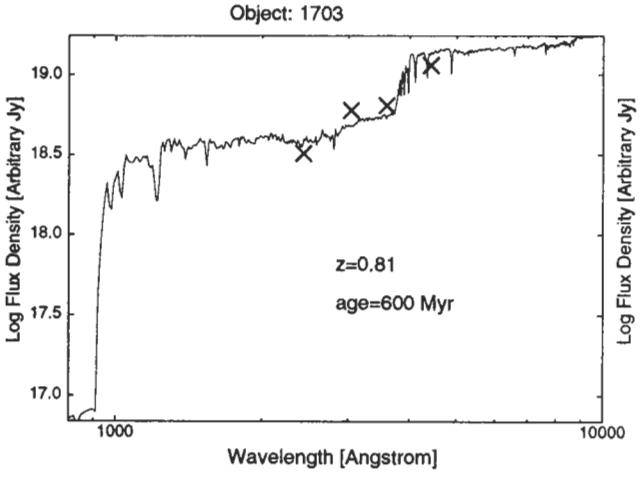

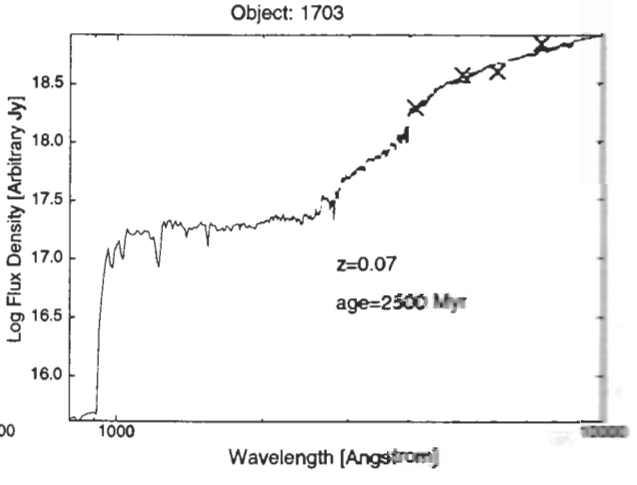

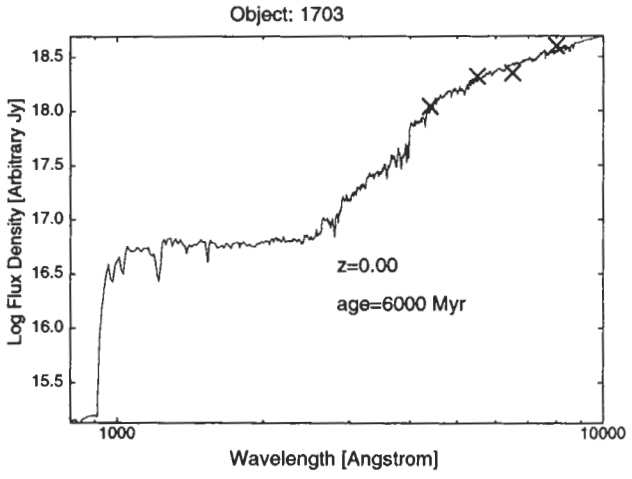

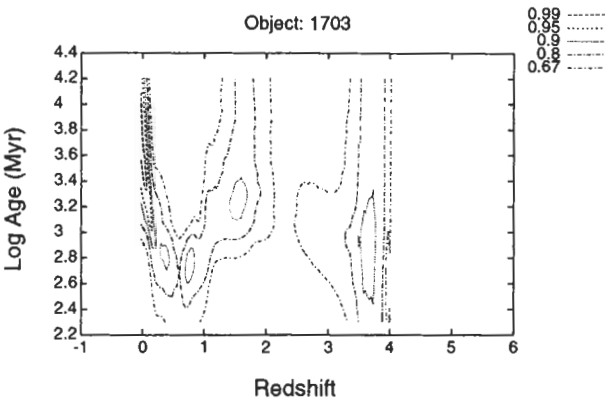

GISSEL models for RC J1703+0502

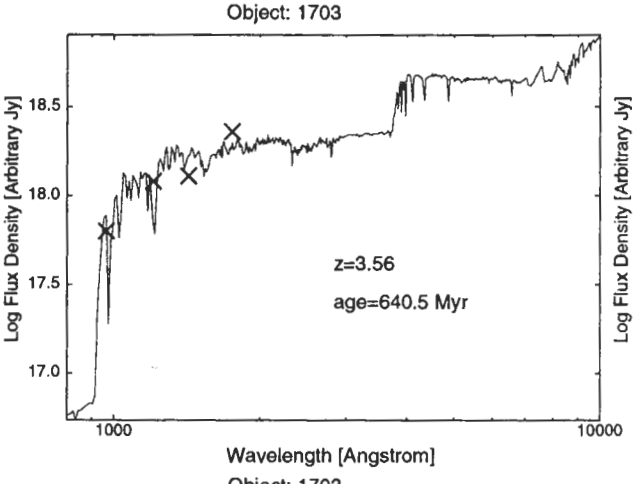

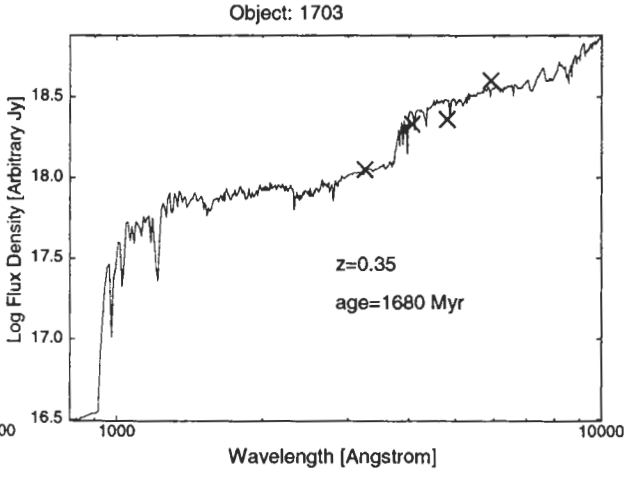

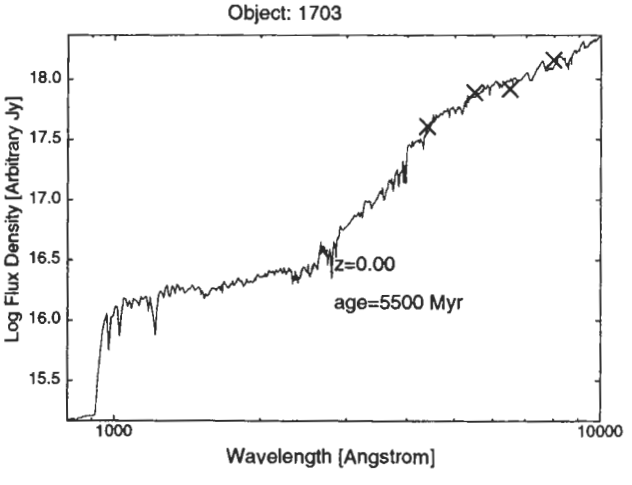

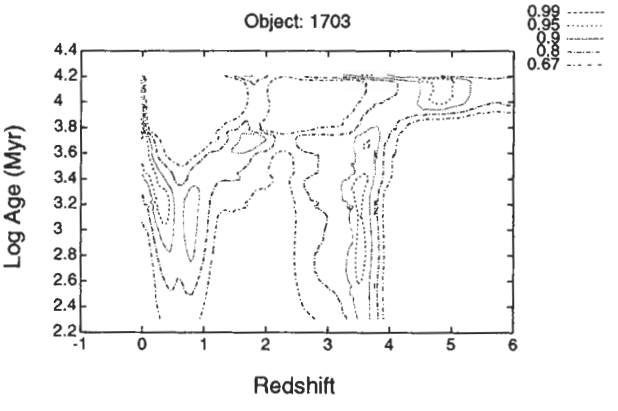

PEGASE models for RC J1706+0502

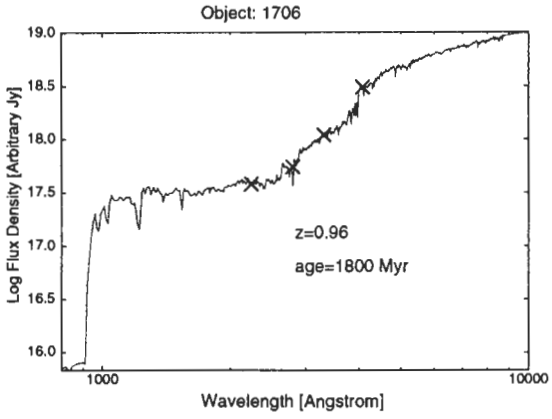

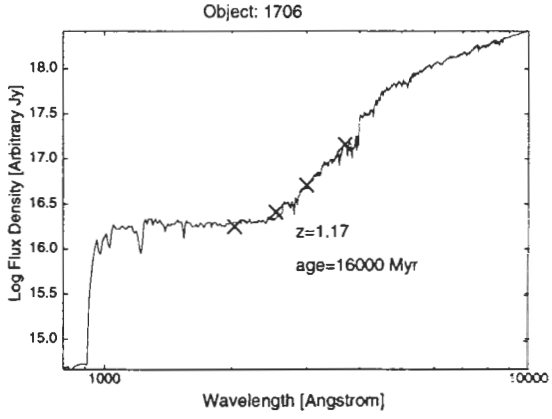

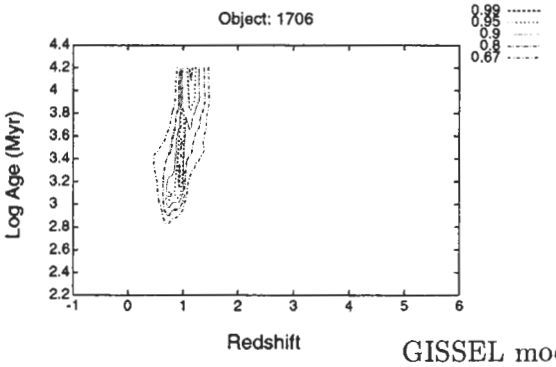

GISSEL models for RC J1706+0502

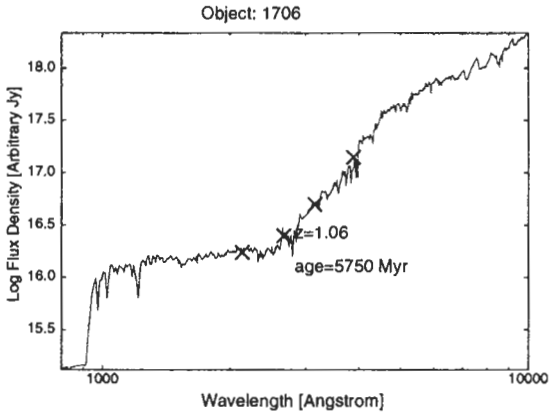

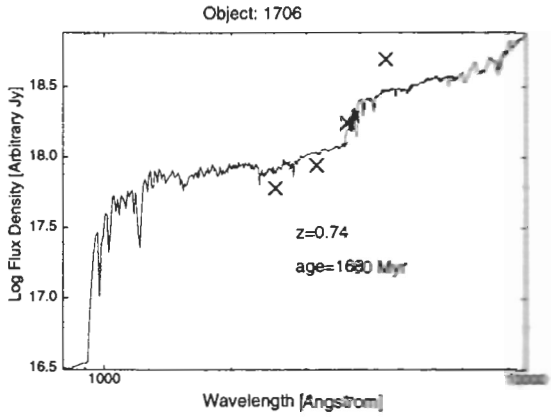

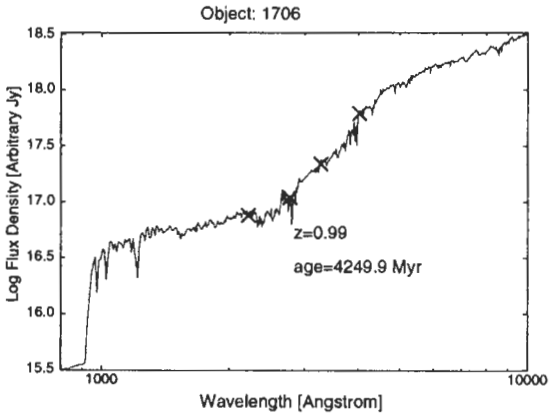

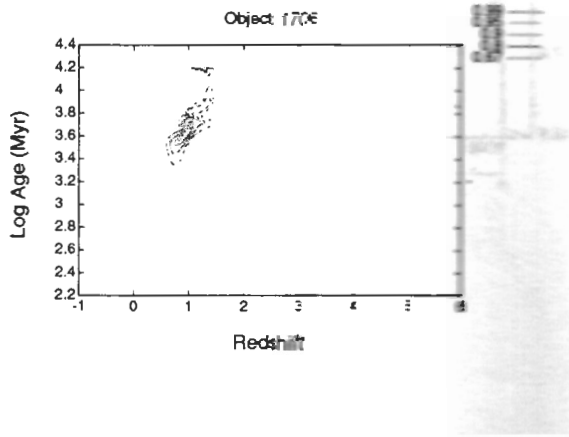

PEGASE models for RC J1722+0442

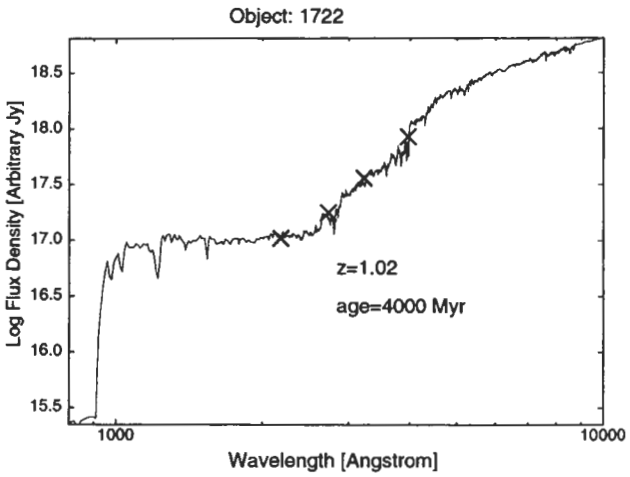

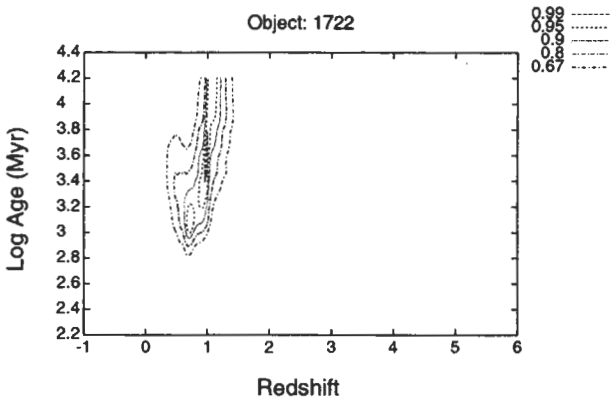

GISSEL models for RC J1722+0442

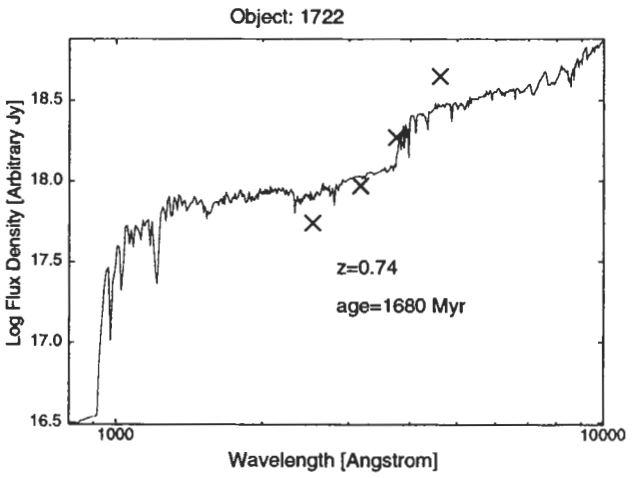

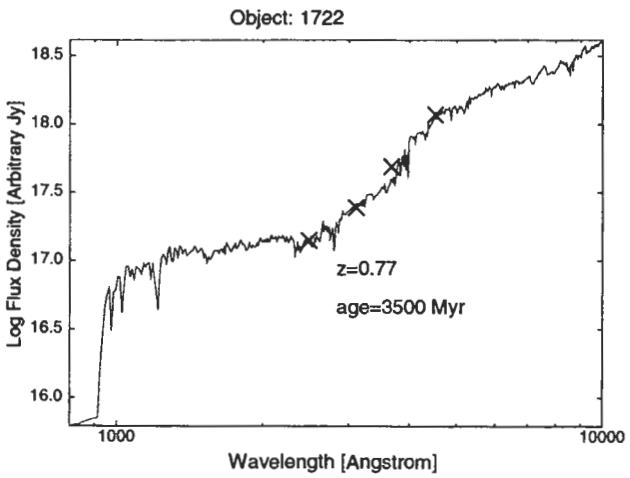

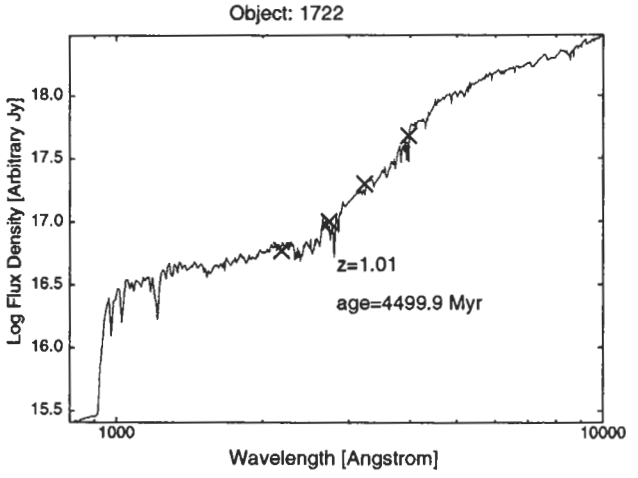

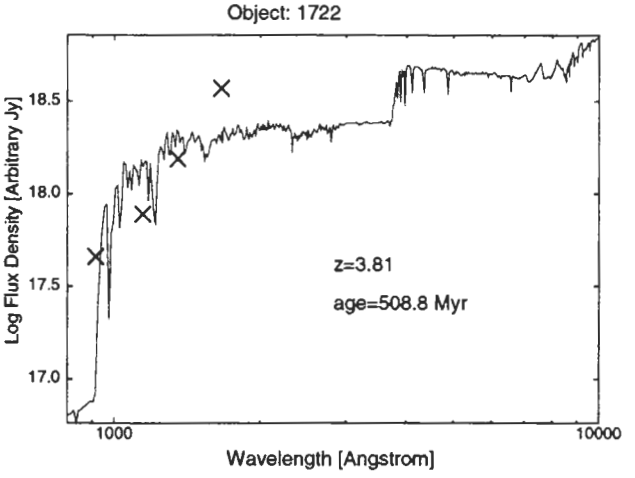

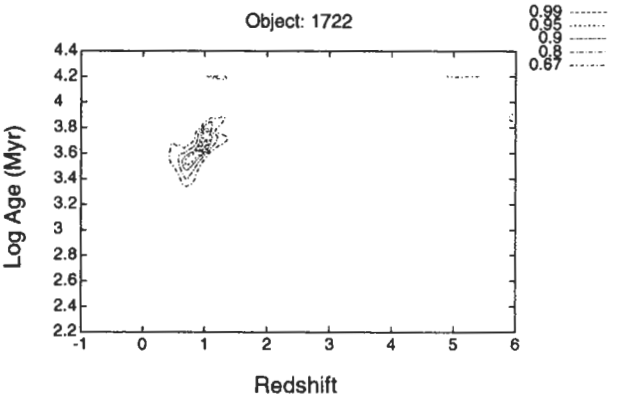

PEGASE models for RC J2029+0456

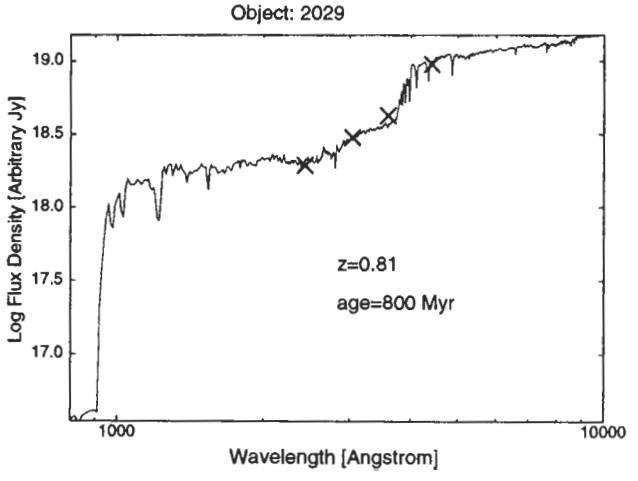

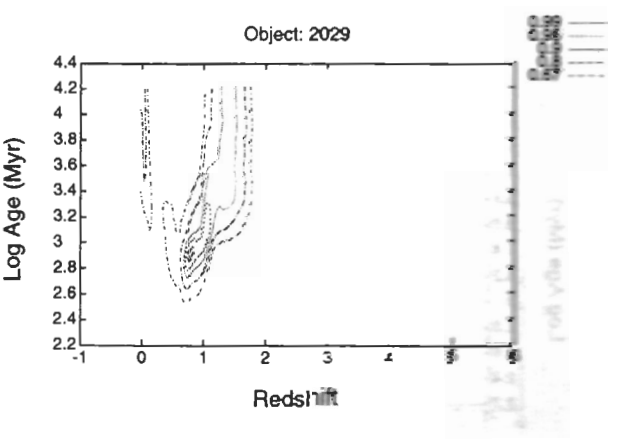

GISSEL models for RC J2029+0456

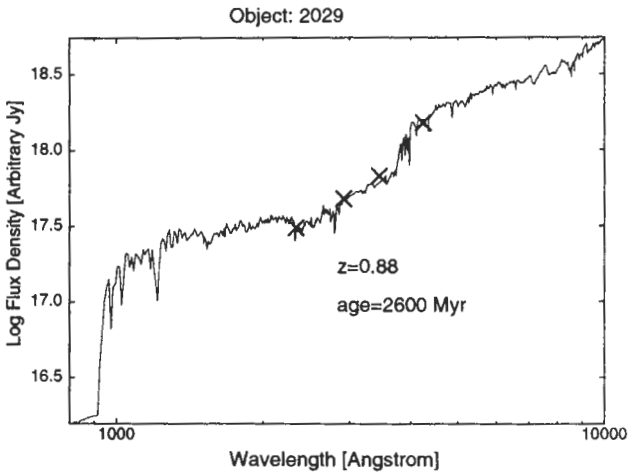

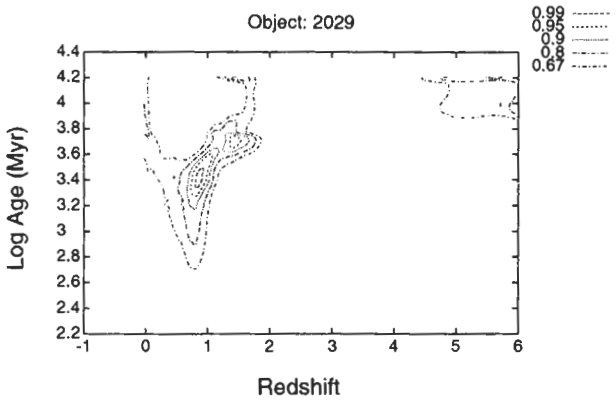

PEGASE models for RC J2219+0458

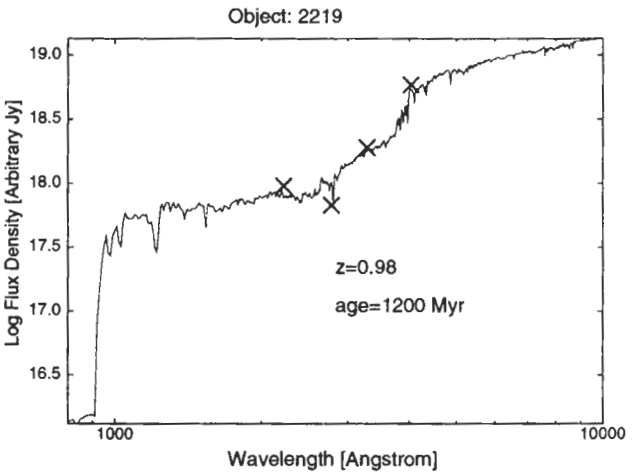

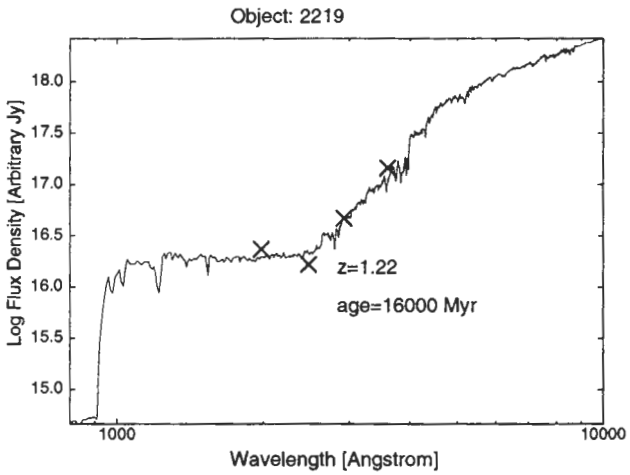

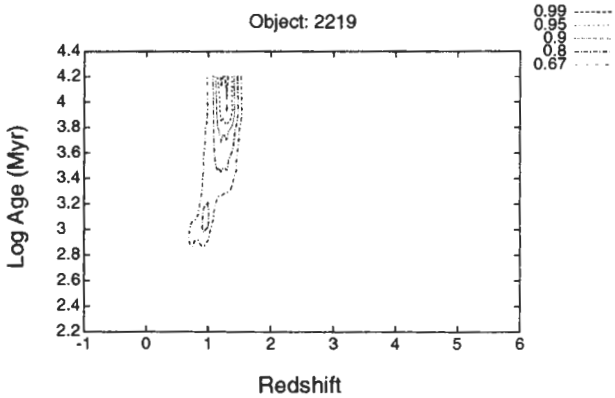

GISSEL models for RC J2219+0458

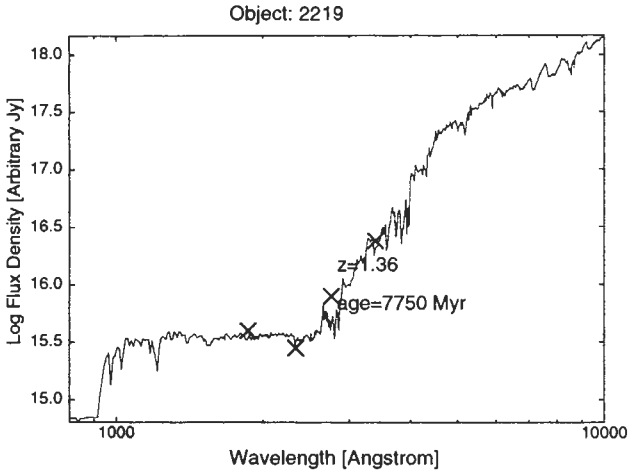

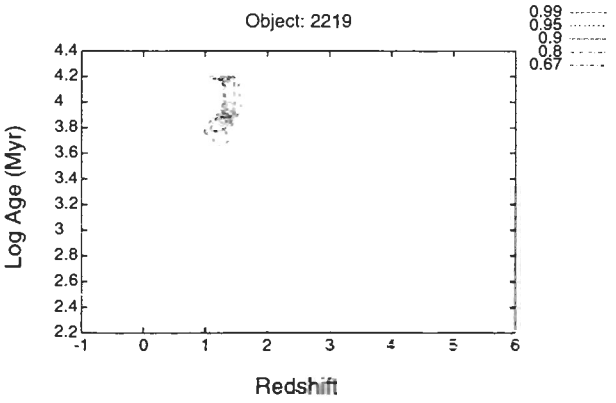

PEGASE models for RC J2224+0513

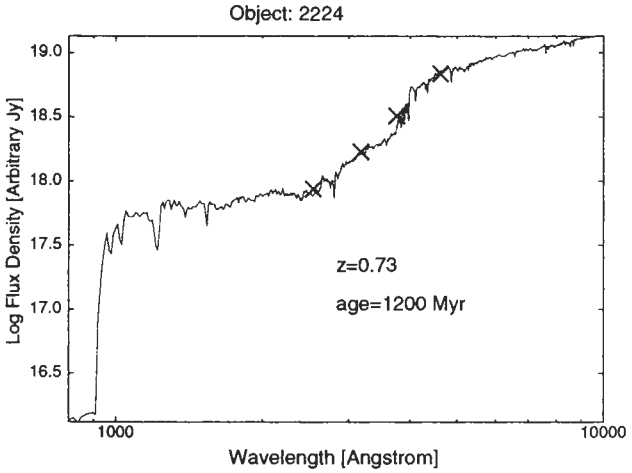

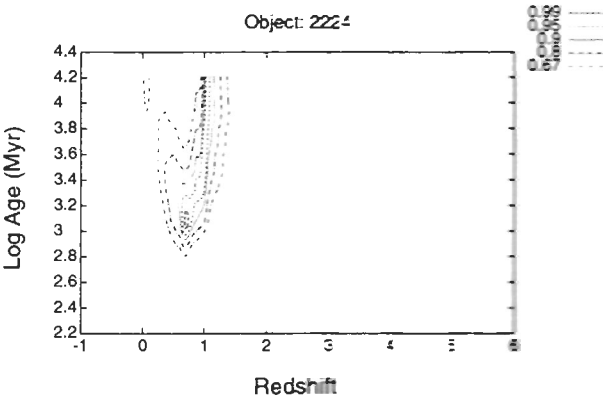

GISSEL models for RC J2224+0513

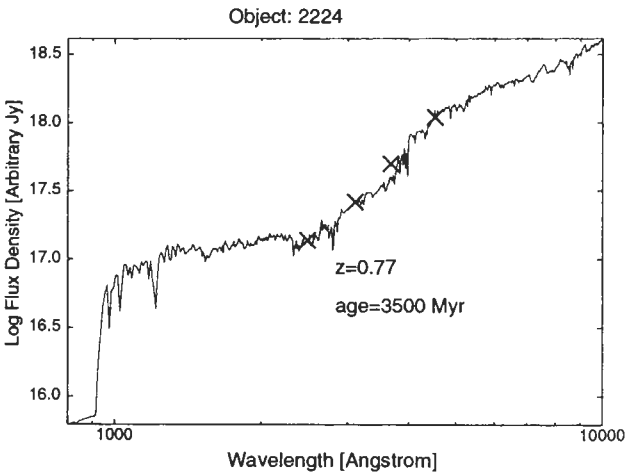

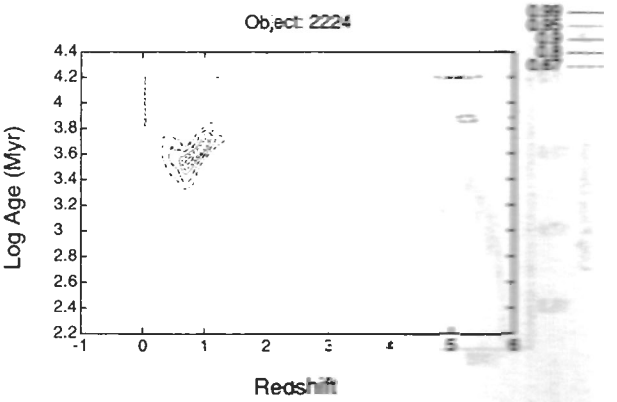

PEGASE models for RC J2247+0507

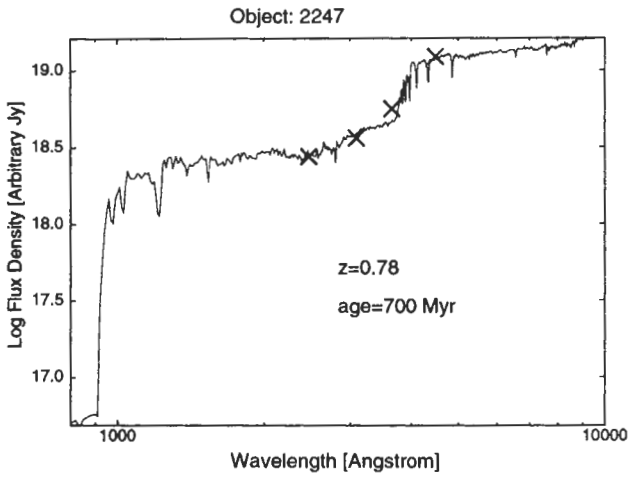

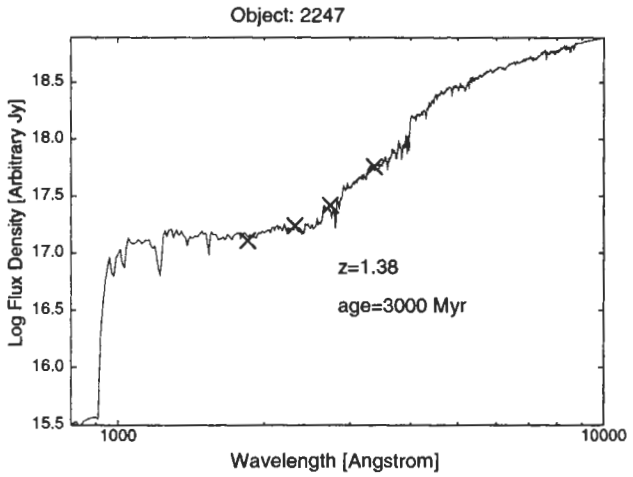

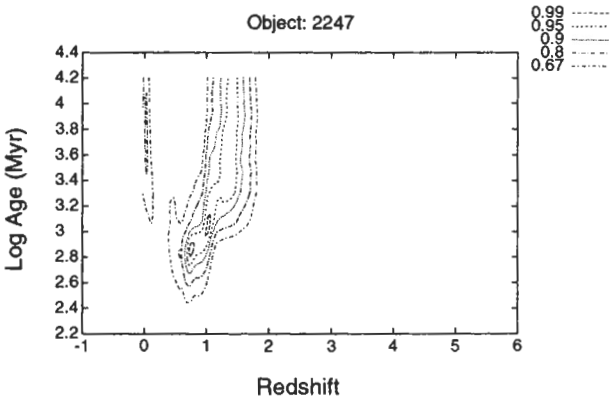

GISSEL models for RC J2247+0507

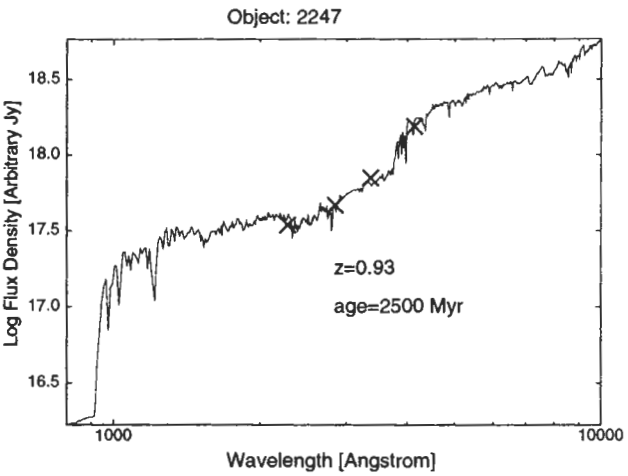

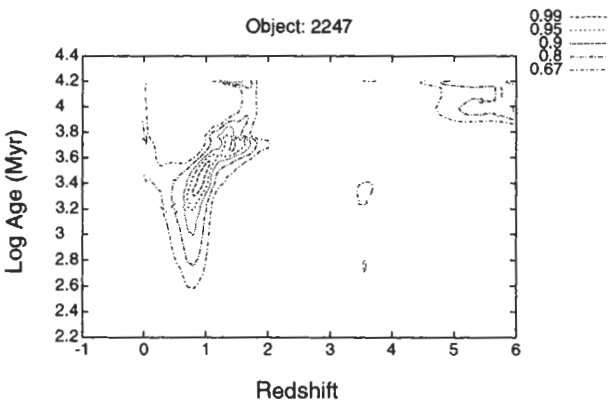

PEGASE models for RC J2348+0507

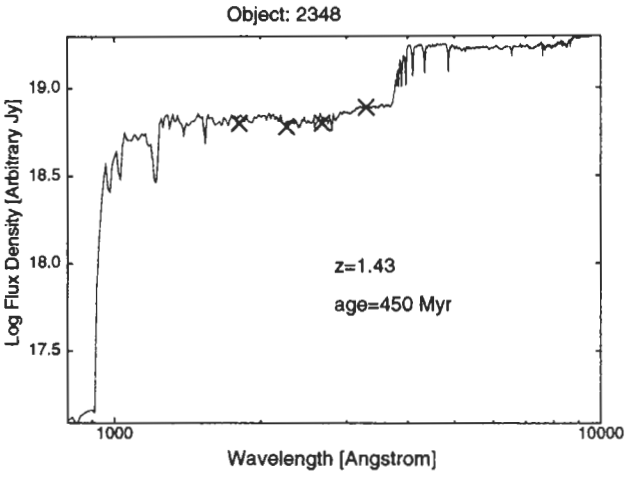

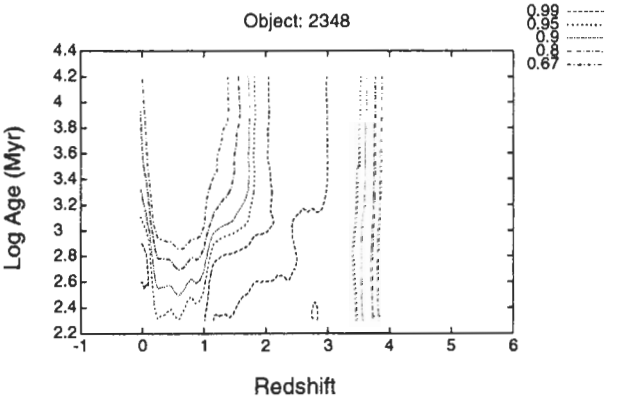

GISSEL models for RC J2348+0507